Folia Histochemica et Cytobiologica 2020, Vol. 58, No. 2, pp. 61–162

Folia Histochemica et Cytobiologica

Scientific quarterly devoted to problems of histochemistry, cytochemistry and cell & tissue biology

www.fhc.viamedica.pl

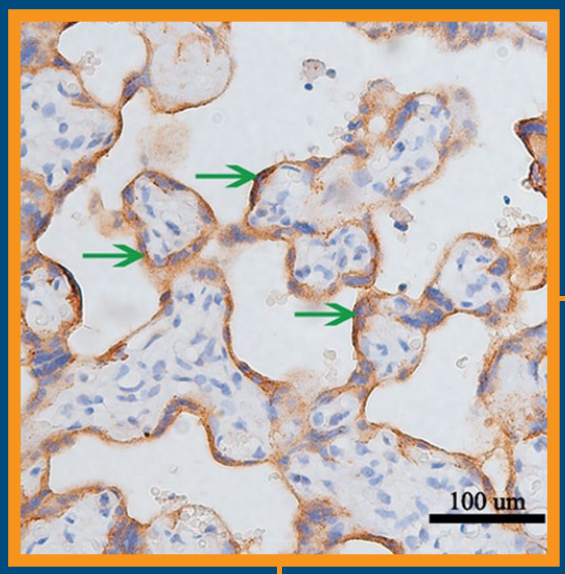

Vol. 58
No. 2
2020

ISSN 0239-8508

VIA MEDICA

Folia Histochemica et Cytobiologica

Scientific quarterly devoted to problems of histochemistry, cytochemistry and cell & tissue biology

www.journals.viamedica.pl/folia_histochemica_cytobiologica

Vol. 58
No. 2
2020

Official Journal of the Polish Society for Histochemistry and Cytochemistry

EDITORIAL OFFICE:
Department of Histology
Medical University of Gdansk
Debinki St. 1, 80–210 Gdansk, Poland
tel.: + 48 58 349 14 37
fax: + 48 58 349 14 19
e-mail: zkmiec@gumed.edu.pl
http://www.journals.viamedica.pl/folia_histochemica_cytobiologica

Folia Histochemica et Cytobiologica (pISSN 0239–8508, eISSN 1897–5631) is published quarterly, one volume a year, by the Polish Society for Histochemistry and Cytochemistry at VM Media sp. z.o.o VM Group sp.k., Gdansk.

Indexed in: Index Medicus/MEDLINE, Excerpta Medica/EMBASE, Chemical Abstracts/CAS, SCI Expanded, SciSearch, Biochemistry & Biophysics Citation Index, ISI Alerting Services, Biosis Previews Index Copernicus, Biological Abstracts, SCOPUS, Research Alert, ProQuest, EBSCO, DOAJ, Ulrich's Periodicals Directory.

POLISH SOCIETY FOR HISTOCHEMISTRY AND CYTOCHEMISTRY STATEMENT OF FOLIA HISTOCHEMICA ET CYTOBIOLOGICA EDITORIAL POLICY

Folia Histochemica et Cytobiologica is an international, English-language journal devoted to the rapidly developing fields of histochemistry, cytochemistry, cell and tissue biology.

The Folia Histochemica et Cytobiologica publishes papers that meet the needs and intellectual interests of medical professionals, basic scientists, college and university teachers and students. Prospective authors should read most recent issues of FHC to determine the appropriateness of a possible contribution. However, such an examination does not provide an infallible guide because editorial policy is always under review. Technical correctness is necessary, but it is not the only condition for acceptance. Clarity of exposition and potential interest of the readers are important considerations; it is the reader, not the author, who must receive the benefit of the doubt.

Folia Histochemica et Cytobiologica publishes review articles, original articles, short communications and proceedings of scientific congresses/symposia. Fields of particular interests include development and application of modern techniques in histochemistry and cell biology, cell biology and pathology, cell-microenvironment interactions, tissue organization and pathology.

Manuscripts announcing new theoretical or experimental results, or manuscripts questioning well-established and successful theories, are highly desirable and are a subject for evaluation by specialists. Manuscripts describing original research that clarifies past misunderstandings or allows a broader view of a subject are acceptable. Manuscripts that demonstrate new relations between apparently unrelated areas of fields of interests are appropriate. Manuscripts that show new ways of understanding, demonstrating, or deriving familiar results are also acceptable. Such manuscripts must provide some original cytobiological insight and not just a clever derivation.

Regularly, review or tutorial articles are published, often of a length greater than that of the average article. Most of these articles are a subject of a review; authors planning such articles are asked to consult with the editors at an early stage.

Most readers of a particular article will be specialists in the subject matter presented; the context within which the paper is presented should be established in the order given in Instructions for Authors. Manuscripts must be technically correct and must take proper cognizance of previous work on the same subject regardless of where it may have appeared. Such referencing is especially important for reminders of once well known ideas, proofs, or techniques that may have again become useful to readers. It is the responsibility of the author to provide adequate references; editors and referees will not do the literature search that should have been done by the authors. The references are a matter of review though.

Contributions considered include: Regular Articles (Papers), Short Communications, Review Articles, Conference Proceeding, Book Reviews and Technical Notes, which describe new laboratory methods or substantial improvements of the existing techniques. Regular articles should be about five journal pages or less in length. Short communications are usually confined to the discussion of a single concept and should be about two journal pages in length. Review articles are confined to a broad discussion and should contain the most recent knowledge about the subject.

Instructions concerning the preparation of manuscripts are given in the Information for Authors. Care in following those instructions will permit editors and referees to devote more time to thoughtful evaluation of contributions and will ultimately lead to a better, more interesting Journal.

SUBSCRIPTION

Folia Histochemica et Cytobiologica is available for paper subscription (print on demand).
To read and download articles for free as pdf document, visit http://czasopisma.viamedica.pl/fhc

Publisher: VM Media sp. z o.o. VM Group sp.k., Swietokrzyska St. 73, 80–180 Gdansk, http://www.viamedica.pl, wap.viamedica.pl

Illustration on the cover: *Expression of Angiogenic Factor with G Patch and FHA Domains 1 (AGGF1) in Placenta from Patients with Preeclampsia* (see: Lan-fen An *et al.*, pp. 83–89)

Folia Histochemica et Cytobiologica

Scientific quarterly devoted to problems of histochemistry, cytochemistry and cell & tissue biology

www.journals.viamedica.pl/folia_histochemica_cytobiologica

Vol. 58
No. 2
2020

Official Journal of the Polish Society for Histochemistry and Cytochemistry

ORIGINAL PAPERS

Immunocytochemical localization of tyrosine hydroxylase in the visual cortex of the microbat, *Rhinolophus ferrumequinum*
Myung-Jun Lee, Kyung-Min Kwon, Won-Tae Lee, Gil-Hyun Kim, Chang-Jin Jeon 61

Features of gonadal dysgenesis and Leydig cell impairment in testes with Sertoli cell-only syndrome
Daria Adamczewska, Jolanta Slowikowska-Hilczer, Katarzyna Marchlewska, Renata Walczak-Jedrzejowska 73

Expression of angiogenic factor with G patch and FHA domains 1 (AGGF1) in placenta from patients with preeclampsia
Lan-fen An, Shu-qi Chi, Jun Zhang, Hong-bo Wang, Wei-xiang Ouyang 83

Immunohistochemical detection of prolactin in clinically non–functioning pituitary adenomas
Katarzyna Winczyk, Joanna Toszek, Jacek Swietoslawski, Ewa Wojtczak, Marek Pawlikowski 90

Overexpression of Rictor protein and Rictor-*H. pylori* interaction has impact on tumor progression and prognosis in patients with gastric cancer
Fang Wang, Xiaoqi Lou, Yanfeng Zou, Dingtao Hu, Jiatao Liu, Jie Ning, Yang Jiao, Zuoyang Zhang, Feng Yang, Lulu Fan, Hanqing Yu, Wei Wei, Hua Wang, Guoping Sun 96

Downregulation of Polo-like kinase-1 (PLK-1) expression is associated with poor clinical outcome in uveal melanoma patients
Tomasz Berus, Anna Markiewicz, Katarzyna Kobylinska, Przemyslaw Biecek, Jolanta Orlowska-Heitzman, Bozena Romanowska-Dixon, Piotr Donizy 108

Gamma linolenic acid suppresses hypoxia-induced gastric cancer cell growth and epithelial-mesenchymal transition by inhibiting the Wnt/β-catenin signaling pathway
Yan Wang, Jian Shi, Liya Gong 117

Bisdemethoxycurcumin exerts a cell-protective effect *via* JAK2/STAT3 signaling in a rotenone-induced Parkinson's disease model *in vitro*
Duanqun He, Shuangxi Chen, Zijian Xiao, Heng Wu, Guijuan Zhou, Chenlin Xu, Yunqian Chang, Yihui Li, Gang Wang, Ming Xie 127

A close neuroanatomical relationship between the enkephalinergic (methionine-enkephalin) and tachykininergic (substance P) systems in the alpaca diencephalon
Pablo Sánchez, Manuel Lisardo Sánchez, Arturo Mangas, Luís Ángel Aguilar, Rafael Coveñas 135

Reactivity of astrocytes in the periaqueductal gray matter of rats treated with monosodium glutamate
Aleksandra Krawczyk, Jadwiga Jaworska-Adamu 147

The effect of dental gel formulation on human primary fibroblasts — an *in vitro* study
Barbara Sterczala, Julita Kulbacka, Jolanta Saczko, Marzena Dominiak 156

FOLIA HISTOCHEMICA ET CYTOBIOLOGICA
Vol. 58, No. 2, 2020
pp. 61–72

ORIGINAL PAPER

VIA MEDICA

Immunocytochemical localization of tyrosine hydroxylase in the visual cortex of the microbat, *Rhinolophus ferrumequinum*

Myung-Jun Lee, Kyung-Min Kwon, Won-Tae Lee, Gil-Hyun Kim, Chang-Jin Jeon*

Department of Biology, School of Life Sciences, BK21 Plus KNU Creative BioResearch Group, College of Natural Sciences, and Brain Science and Engineering Institute, Kyungpook National University, Daegu, 41566, South Korea

Abstract

Introduction. In order to enhance our understanding of bat vision, we investigated tyrosine hydroxylase (TH)-immunoreactive (IR) fibers in the visual cortex of the microbat.

Material and methods. The study was conducted on 12 freshly-caught adult bats (*Rhinolophus ferrumequinum*, both sexes, weighing 15–20 g). We used standard immunocytochemistry and confocal microscopy.

Results. TH-IR fibers were distributed throughout all layers of the visual cortex, with the highest density in layer I. Two types of TH-IR fibers were observed: small and large varicose fibers. TH-IR cells were not found in the microbat visual cortex. The microbat substantia nigra and ventral tegmental areas, previously identified sources of TH-IR fibers in the mammalian visual cortex, all contained strongly labeled TH-IR cells. The average diameters of TH-IR cells in the substantia nigra and the ventral tegmental areas were 14.39 ± 0.13 μm (mean ± SEM) and 11.85 ± 0.13 μm, respectively.

Conclusions. Our results suggest that the microbat has a well-constructed neurochemical organization of TH-IR fibers. This observation should provide fundamental insights into a better understanding of the nocturnal, echolocating bat visual system. *(Folia Histochemica et Cytobiologica 2020, Vol. 58, No. 2, 61–72)*

Key words: visual cortex; tyrosine hydroxylase; microbat; immunocytochemistry

Introduction

Bats are the only true flying mammals in the order Chiroptera and they help to maintain the healthy ecosystem with their pollination activities [1–4]. There are about 1,000 species of bats which are generally divided into two suborders: Megachiroptera (megabats, approximately 200 species), and Microchiroptera (microbats, approximately 800 species). Megabats, also called fruit bats, have large eyes with visual ability, while microbats have been known to have degenerated eyes with poor eyesight. Microbats primarily rely on sophisticated laryngeal echolocation, making high-frequency noises and listening to the returning echoes for navigation or prey detection [5–9].

It has been recognized, however, that many microbats also depend on vision. Thus, many functional elements of the retina have been found in the microbat including cone [10, 11] and rod photoreceptors [12], ultraviolet-sensitive cone photoreceptors [13, 14], and the functional opsin genes [15, 16], suggesting the possibility for photopic and scotopic vision. A recent study also described the distribution of the third class of mammalian photoreceptors, intrinsically photosensitive retinal ganglion cells (ipRGCs), in the microbat retina. The microbat has a much higher density of ipRGCs than diurnal animals, demonstrating the high species diversity between nocturnal and diurnal animals [17]. The AII [11, 12] and starburst [18] amacrine cells, which are the most well-understood amacrine

Correspondence address:
Prof. Chang-Jin Jeon, Neuroscience Lab.,
Department of Biology, College of Natural Sciences,
Kyungpook National University, 80, Daehak-ro,
Daegu, 41566, South Korea
phone: +82-53-950-5343, fax: +82-53-953-3066,
e-mail: cjjeon@knu.ac.kr

cells in many other mammalian species, have also been found in the microbat retina. Bipolar cells [12, 19] and ganglion cells [20] have also been identified in the microbat. In addition to the retina, various neuronal cells and fibers containing neurochemical components such as acetylcholine, nitric oxide, and calcium-binding proteins have been localized to the visual system of the microbat visual cortex [21–23] and in the superior colliculus [24], indicating the potential for visual perception and visuomotor integration.

Dopamine (DA), an important neurotransmitter in the nervous system, plays a widespread role in attention, arousal, learning, motivation, motor control, reinforcement, and reward [25–30]. Dopaminergic fibers and cells have been commonly found in the visual cortex of various mammals including rats [31–33], rabbits [34], whales [35], monkeys [31, 36], and humans [37]. Layer I contains the highest density of dopaminergic fibers [31, 35]. The visual cortex is known to receive inputs from dopaminergic neurons in the midbrain. The substantia nigra and ventral tegmental areas are also sources of dopaminergic fibers in the visual cortex [26, 27, 30, 38–40].

The greater horseshoe bat, *Rhinolophus ferrumequinum*, is an insectivorous microbat that mainly lives in caves. This species has a wide range in the Palearctic ecozone, occurring from North Africa and Southern Europe through South-west Asia, the Caucasus, Iran, Afghanistan, Pakistan, and the Himalayas, and all the way to South-eastern China, Korea, and Japan [41]. Our laboratory previously described the organization of the dopaminergic system in the microbat central visual system, and we have identified at least four types of TH-IR cells in the retina [18]. Thus, although echolocation is the primary method of navigation for microbat flight, it is also of interest to explore the functional organization of the central visual system to find possible implications for the role of vision in flight navigation [11, 17, 18, 23, 24, 42–44]. In the superior colliculus, TH-IR immunoreactivity was found within the fibers but not within the cells [24]. However, the distribution and morphology of dopaminergic fibers in the microbat visual cortex has not yet been investigated. As part of a larger effort to localize dopaminergic cells and fibers in the entire bat visual system, in this study we aimed to investigate the organization of dopaminergic systems in the microbat visual cortex and to compare the organization of the microbat visual cortex with that of other mammals. Our results provide some basic information about the neurochemical organization of TH-IRs immunoreactivities in relation to the functional role of visual ability in the nocturnal echolocating bat.

Materials and methods

Animal and tissue preparation. For this study, a total of 12 freshly-caught adult bats (*Rhinolophus ferrumequinum*, both sexes, weighing 15–20 g) were examined. All of the bats were captured in a cave in the district of Gimcheon, South Korea. After 5–6 h to transport and stabilize the bats, they were anesthetized with a mixture of ketamine hydrochloride (30–40 mg/kg; Yuhan, Seoul, Korea) and xylazine (3–6 mg/kg; Bayer, Leverkusen, Germany) prior to perfusion. The bats were then perfused intracardially with 4% paraformaldehyde (Sigma-Aldrich, St. Louis, MO, USA) and 0.3–0.5% glutaraldehyde (Sigma-Aldrich) in 0.1M sodium phosphate buffer (pH 7.4) containing 0.002% calcium chloride (Yakuri Pure Chemicals, Kyoto, Japan). Following a pre-rinse with approximately 30 ml of phosphate-buffered saline (PBS, pH 7.4) over a period of 3–5 min, each bat was perfused with 30–50 ml of fixative for 20–30 min via a syringe needle inserted through the left ventricle and aorta. The animal was decapitated and the head was placed in fixative for 2–3 h. The brain was then removed from the skull, stored for 2–3 h in the same fixative, and then left overnight in 0.1 M phosphate buffer (pH 7.4) containing 8% sucrose and 0.002% calcium chloride. The brain was then mounted onto a chuck and cut into 50 μm thick coronal sections using a Vibratome 3000 Plus Sectioning System (Vibratome, St. Louis, MO, USA). All animal experiments were approved by the Animal Care and Use Committee of Kyungpook National University (permission No. 2016-0151). The "Principles of laboratory animal care" (NIH publication No. 85-23, revised 1985) were followed throughout the research protocol period.

Horseradish peroxidase staining. The primary antibody used in this study was rabbit anti-tyrosine hydroxylase (TH; Pel-Freez, Rogers, AR, USA) [18, 24, 45]. Tissues were processed free floating in small vials at room temperature with gentle agitation. For immunocytochemistry, tissues were incubated in 1% sodium borohydride ($NaBH_4$; Sigma-Aldrich) for 30 min. Afterwards, the tissues were rinsed for 3 x 10 min in PBS, then incubated for 2 h in PBS with 4% normal goat serum (Vector Laboratories, Burlingame, CA, USA) with 0.5% Triton X-100 (Yakuri Pure Chemicals) added. Tissues were next incubated for 24 h in the primary antiserum (diluted 1:200) in PBS with 4% normal serum with 0.5% Triton X-100 added. Following three 10 min rinses in PBS, the tissues were incubated in a 1:200 dilution of biotinylated secondary IgG in a blocking solution. The secondary antibody used was biotinylated goat anti-rabbit (Vector Laboratories). The tissues were then rinsed three times for 10 min each in PBS and incubated for 2 h in a 1:50 dilution of avidin-biotinylated horseradish peroxidase complex (Vector Laboratories) in PBS. The tissues were

then rinsed in 0.25 M Tris buffer for 3 × 10 min. Finally, staining was visualized by reaction with 1,3'-diaminobenzidine tetrahydrochloride (DAB) and hydrogen peroxide in 0.25 M Tris buffer for 3–10 min using a DAB reagent set (Kirkegaard & Perry, Gaithersburg, MD, USA). All tissues were then rinsed in 0.25 M Tris buffer before mounting. As a negative control, some sections were incubated in the same solution without the addition of the primary antibody, and these control tissues showed no TH-IR immunoreactivity. Negative control and preabsorption tests for the specificity of this antibody conducted in the microbat central nervous system have been described in previous reports [24, 46]. Following the immunocytochemical procedures, the tissues were mounted on Superfrost Plus slides (Fisher, Pittsburgh, PA, USA) and dried overnight in a 37°C oven. The mounted sections were dehydrated, cleared, and coverslipped with Permount (Fisher).

Quantitative analysis. TH-IR fibers in the bat visual cortex were examined and photographed with a Zeiss Axioplan microscope (Carl Zeiss Meditec, Inc., Dublin, CA, USA). Among the 12 bats, we chose three animals and analyzed the quantitative data from nine best-labeled tissue sections (three tissue sections from each of three animals). Conventional or differential interference contrast (DIC) optic images were obtained using Zeiss AxioCam HRc digital camera with Zeiss Plan-Apochromat objectives and Zeiss AxioVision 4 software (Carl Zeiss Meditec, Inc.).

To quantify the density of IR fibers, we sampled sequential 210 × 210 μm fields and analyzed from nine sections in three bats (three tissue sections from each of three animals) across the superficial and deeper layers of the visual cortex. Line drawings showing the IR fibers were generated to clearly distinguish the distribution of the TH-IR fibers in the representative bat visual cortical section using Adobe Photoshop CS software (Adobe Systems Inc., San Jose, CA, USA).

In three animals, the morphological types and the average diameter and area of TH-IR neurons were analyzed. The morphological types were determined for 273 (SN) and 316 (VTA) neurons analyzed from nine sections in three bats and the average diameter and area of TH-IR neurons were determined for 210 (SN) and 236 (VTA) neurons analyzed from nine sections in three bats (three tissue sections from each of three animals). All analyses were performed using a 40× Zeiss Plan-Apochromat objective. To obtain the best images, we analyzed the cells under DIC optics. Only cell profiles containing a nucleus and at least one faintly visible nucleolus were included in the analysis. Since our goal was to obtain an estimate of each morphological cell type, no attempt was made to assess the total number of cells in each neuronal subpopulation. The average diameter and area of labeled neurons were computed using a digital camera (Carl Zeiss Meditec, Inc.). A cursor was moved manually around the outer contour of each cell using Zeiss AxioVison system. Images were adjusted with respect to brightness and contrast using Adobe Photoshop CS software (Adobe Systems Inc.).

Results

The distribution of TH-IR fibers in the microbat visual cortex

The laminar structure of the microbat visual cortex and the TH-IR immunoreactivity are shown in Figures 1A and 1B, respectively. These images demonstrate that the microbat visual cortex has well-developed dopaminergic fibers. TH-IR fibers were distributed throughout all layers of the microbat visual cortex. Figures 1C and 1D show highly magnified sections of the square regions in Figure 1B. Figure 1B is a dark-field photomicrograph, captured using 20× objective. Figure 1C, including the TH-IR fibers located within layers I–III, and Figure 1D, showing the TH-IR fibers located within layers IV–VI, are bright-field photomicrographs, captured using a 40× objective. A representation of the density of the TH-IR fibers is shown in Figure 1E. The dopaminergic fibers in the microbat visual cortex form a plexus of labeled fibers with differential densities in the different layers. Quantitative maps of fiber distribution indicate the density of the TH-IR fibers in each layer (Fig. 2). Figure 2 shows the laminar distribution pattern of the TH-IR fibers in the microbat visual cortex, which were analyzed using an image processing program developed at the National Institutes of Health. Three different sections each from three individual animals (total 9 sections, each represented by a different color in Fig. 2B) were analyzed in this study. Figure 2C shows a histogram of the density of the TH-IR fibers in the microbat visual cortex. The frequency of labeled fibers varies in each layer: 20.78 ± 0.70% (mean ± SEM) of the labeled fibers appear in layer I, 13.65 ± 0.42% in layer II, 15.89 ± 0.74% in layer III, 16.14 ± 0.63% in layer IV, 16.45 ± 0.66% in layer V, and 17.07 ± ± 0.74% in layer VI. Layer I had the highest density of TH-IR fibers, while layer II had the lowest TH-IR fiber density (Figs. 2B, 2C).

The morphology of TH-IR fibers in the microbat visual cortex

We identified at least two types of TH-IR varicose fibers in the microbat visual cortex: small varicose fibers (arrowheads in Figs. 3B, 3C and 3D) and large varicose fibers (arrows in Figs. 3A, 3B, 3D and 3E). Varicose fibers were distributed throughout the rostrocaudal section of the microbat visual cortex and numerous TH-IR varicosities were distributed irregularly along the fibers. The TH-IR fibers in the

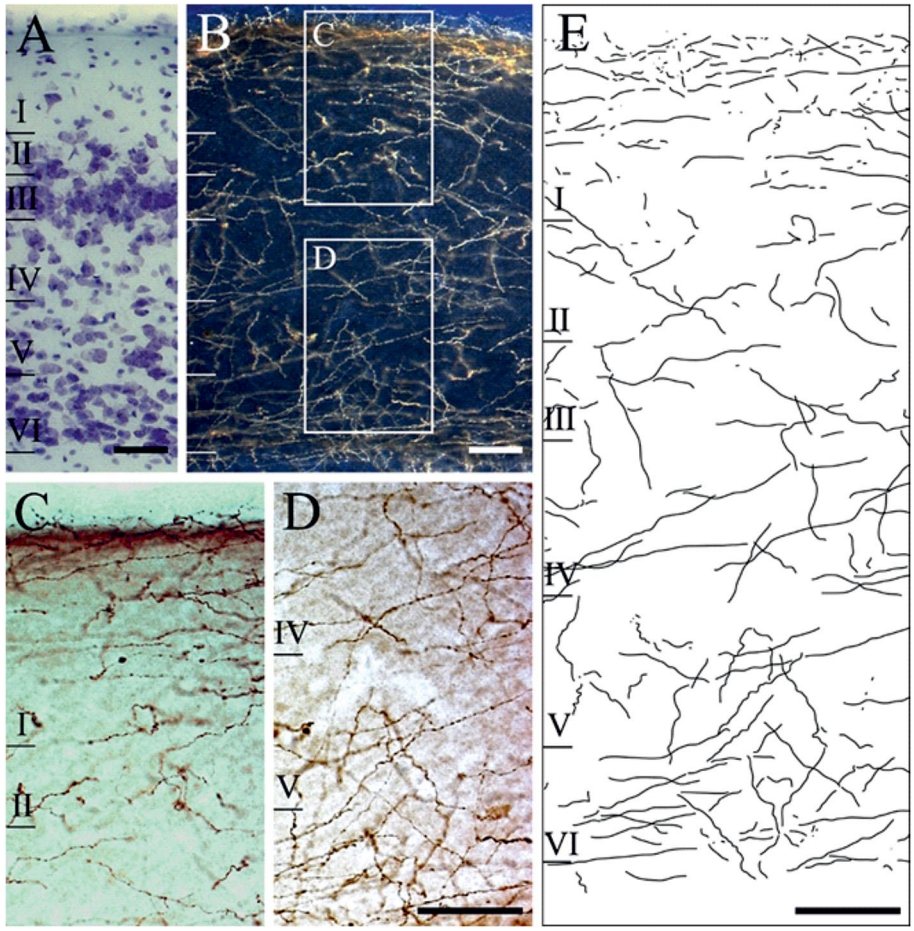

Figure 1. Distribution of TH-IR fibers in the microbat visual cortex. **A.** The approximate limits of the layers are indicated in the thionin-stained section. **B.** Low-magnification dark-field photomicrograph of TH-IR fibers in the microbat visual cortex. **C, D.** Medium magnification bright-field photomicrograph of TH-IR fibers showing the areas marked in (B). Varicose dopaminergic fibers generally observed in the microbat visual cortex. **E.** Drawing of the TH-IR fibers in the microbat visual cortex. Bar = 50 μm.

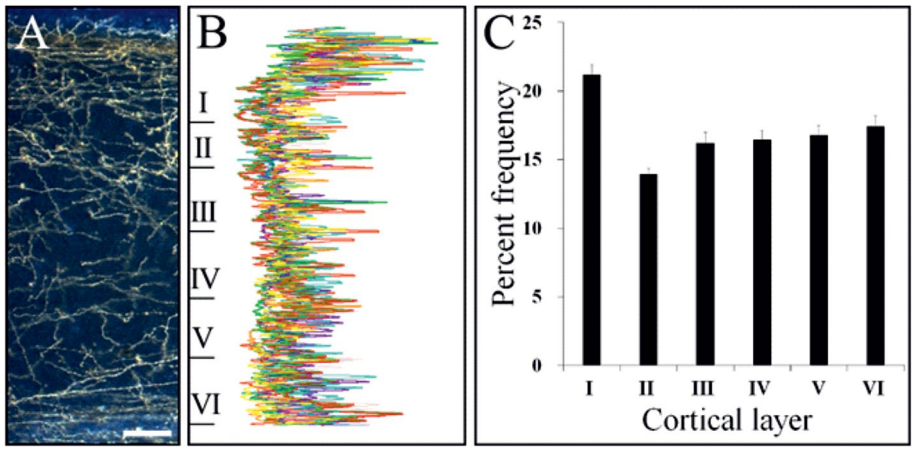

Figure 2. Intensity profile of TH-IR fibers in the visual cortex of the microbat. A plot of the intensity of the TH-IR fibers in different coronal sections of the microbat visual cortex, characterized using the image processing program Image J (NIH, Bethesda, MD, USA). **A.** Low-magnification dark-field photomicrograph of the microbat visual cortex shows well-labeled TH-IR fibers. **B.** Results of intensity graph analyses from nine coronal sections of the microbat visual cortex are shown. **C.** Density histogram of TH-IR fibers in the microbat visual cortex. Highest density was found in layer I. Bar = 50 μm.

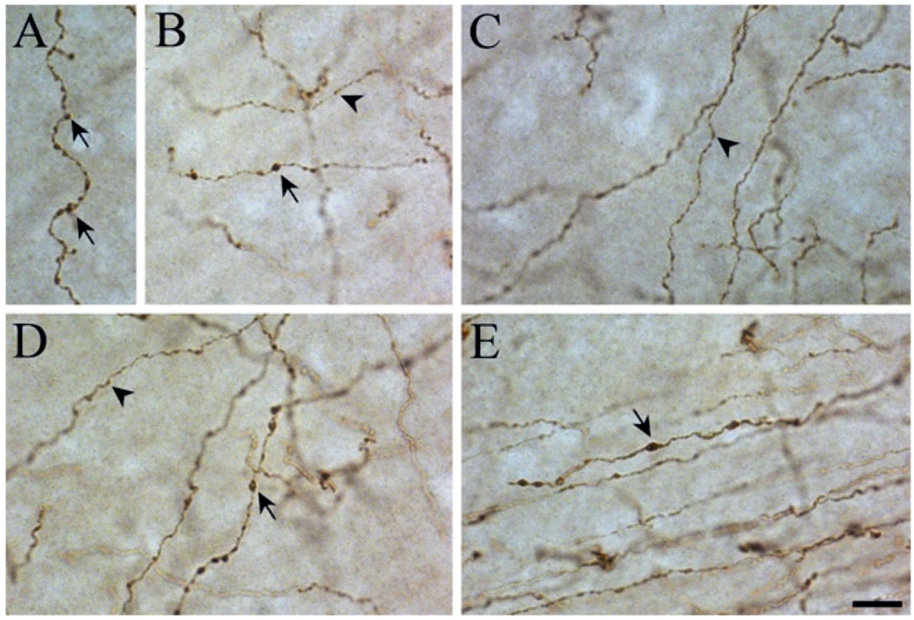

Figure 3. High-power differential interference contrast (DIC) photomicrographs of TH-IR fibers in the microbat visual cortex. **A, E.** Arrows indicate large varicosities in the microbat visual cortex. **C.** Arrowheads indicate small varicosities in the microbat visual cortex. **B, D.** TH-IR fibers with small (arrowheads) and large (arrows) varicosities in the microbat visual cortex. Bar = 10 μm.

microbat visual cortex exhibited various orientations, including vertical, horizontal, and oblique orientations. The microbat visual cortex does not appear to have dopaminergic neurons; no labeled neurons were found in this study.

Source of dopaminergic inputs to the microbat visual cortex

There are several subdivisions of dopaminergic neuron groups. The main groups of dopaminergic neurons are located in the following areas in the brain: A8 (retrorubral), A9 (substantia nigra), A10 (ventral tegmental area), A11 (caudal diencephalic group), A12 (tuberal cell group), A13 (zona incerta), A14 (hypothalamic nuclei), A15 (anterior hypothalamic group), and A16 (olfactory bulb) [46–48]. Among these, the substantia nigra and ventral tegmental areas are known to project dopaminergic fibers into the visual cortex [26, 27, 30, 38–40].

Substantia nigra

TH-IR neurons were distributed in the substantia nigra of the bat brain. Figure 4A represents an immunostained section containing the substantia nigra. Figure 4B, which is the magnified image of the area marked by a square in Figure 4A, shows intense labeling in various types of neurons in the substantia nigra. The large majority of the TH-IR neurons were round or oval cells, although other cell types were also observed, including stellate, horizontal fusiform, and vertical fusiform. Figure 5A shows representative multipolar round or oval cells. Figure 5B shows a small-sized stellate neuron. The stellate cells had polygon-shaped cell bodies with many dendrites coursing in all directions. Figure 5C shows a pyriform neuron with a pear-shaped cell body and a thick proximal dendrite directed toward the pial surface. The ascending process has many small branches, forming a dendritic bouquet. Figure 5D shows a vertical fusiform cell that displays a vertical fusiform cell body with a main, long process ascending towards the pial surface and a long descending process. Figure 5E shows a horizontal cell that displays a horizontally oriented small, fusiform cell body and horizontally oriented processes.

Quantitatively, 52.01 ± 3.06% (142 of 273 cells) of TH-IR neurons were round or oval, 15.82 ± 1.06% (51 of 273 cells) were vertical fusiform, 16.12 ± 0.74% (44 of 273 cells) were stellate, 11.72 ± 1.16% (32 of 273 cells) were horizontal cells, and 1.47 ± 0.12% (4 of 273 cells) were pyriform cells (Fig. 7). The average diameter of the 210 TH-IR neurons in the substantia nigra ranged from 8.41 to 20.13 μm, with a mean diameter of 14.39 ± 0.13 μm. The area of these cells ranged from 55.51 to 318.26 μm^2, with a mean area of 165.90 ± 3.23 μm^2 (Fig. 8).

Ventral tegmental area

Figure 4C presents an immunostained section containing the ventral tegmental area. Figure 4D is the magnified image of the area marked by square in Figure 4C

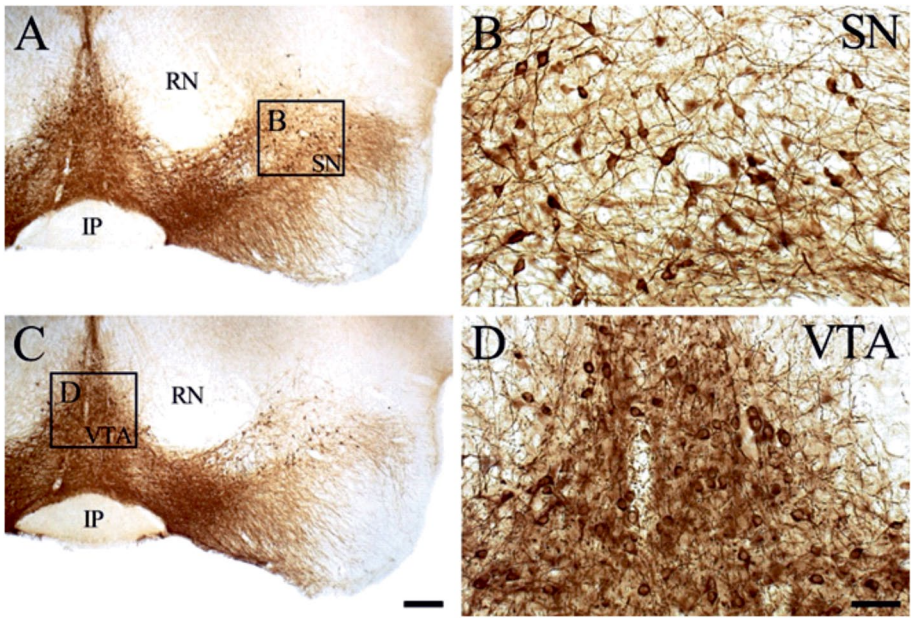

Figure 4. Photomicrographs show presumed sources of TH-IR fibers in the microbat visual cortex. **A.** Low-magnification photomicrograph of coronal sections showing the substantia nigra. **B.** High-magnification photomicrograph of the image in the square marked in (A). **C.** Low magnification photomicrograph of a coronal section showing the ventral tegmental area. **D.** High magnification photomicrograph of the image in the square marked in (C). RN — red nucleus; SN — substantia nigra; VTA — ventral tegmental area. Bars: C = 200 μm, D = 50 μm.

and shows intense labeling in various types of neurons in the ventral tegmental area. The majority of TH-IR neurons in the microbat ventral tegmental area were round or oval cells. Figure 6A shows several representative round or oval cells, and Figure 6B shows a large-sized stellate neuron with a polygon-shaped cell body and numerous dendrites coursing in all directions. Figure 6C shows a vertical fusiform cell that displays a vertical fusiform cell body with a main, long process ascending towards the pial surface and a long descending process. Figure 6D shows a horizontal cell that displays a horizontally oriented fusiform cell body and horizontally oriented processes. The pyriform cells (Fig. 6E) have pear-shaped cell bodies with a thick, proximal dendritic stump directed superficially towards the pial surface. Pyriform and horizontal cell types, however, were rare.

Quantitatively, 60.76 ± 3.47% (192 of 316 cells) of the TH-IR neurons were round or oval, 15.82 ± 0.82% (50 of 316 cells) were vertical fusiform, 8.23 ± 0.11% (26 of 316 cells) were stellate, 13.61 ± 1.55% (43 of 316 cells) were horizontal cells, and 1.58 ± 0.11% (5 of 316 cells) were pyriform cells (Fig. 7). The average diameter of the 236 TH-IR neurons in the ventral tegmental area ranged from 8.18 to 17.55 μm, with a mean diameter of 11.85 ± 0.13 μm. The area of these cells ranged from 52.61 to 242.04 μm^2, with a mean area of 113.62 ± 2.54 μm^2 (Fig. 8).

Discussion

This study demonstrates that TH–IR fibers are distributed in the microbat visual cortex. We identified at least two types of TH–IR varicose fibers, and the TH–IR cells identified in the substantia nigra and ventral tegmental area are thought to be the sources of these TH-IR fibers.

The purpose of this study was to investigate if TH-IR fibers are distributed in the microbat visual cortex as previously observed in the visual cortex of other animals [31–37]. The results show that TH-IR fibers with varicosities are present throughout all layers of the microbat visual cortex. A dopaminergic fiber density gradient was observed in the microbat visual cortex: layer I had the most densely innervated lamina, while layer II was the least innervated lamina. Dopaminergic fibers have been found in the visual cortex of many other mammals including rats [31–33], rabbits [34], whales [35], monkeys [31, 36], and humans [37]. In the rat visual cortex, dopaminergic fibers were located in layers I–III and in layer VI [31]. In the rabbit visual cortex, layers I–II and layer IV are the most heavily innervated [34]. In the whale visual cortex, most of the dopaminergic fibers were primarily located in layer I [35], and a similar pattern was found in the monkey visual cortex [31]. Thus,

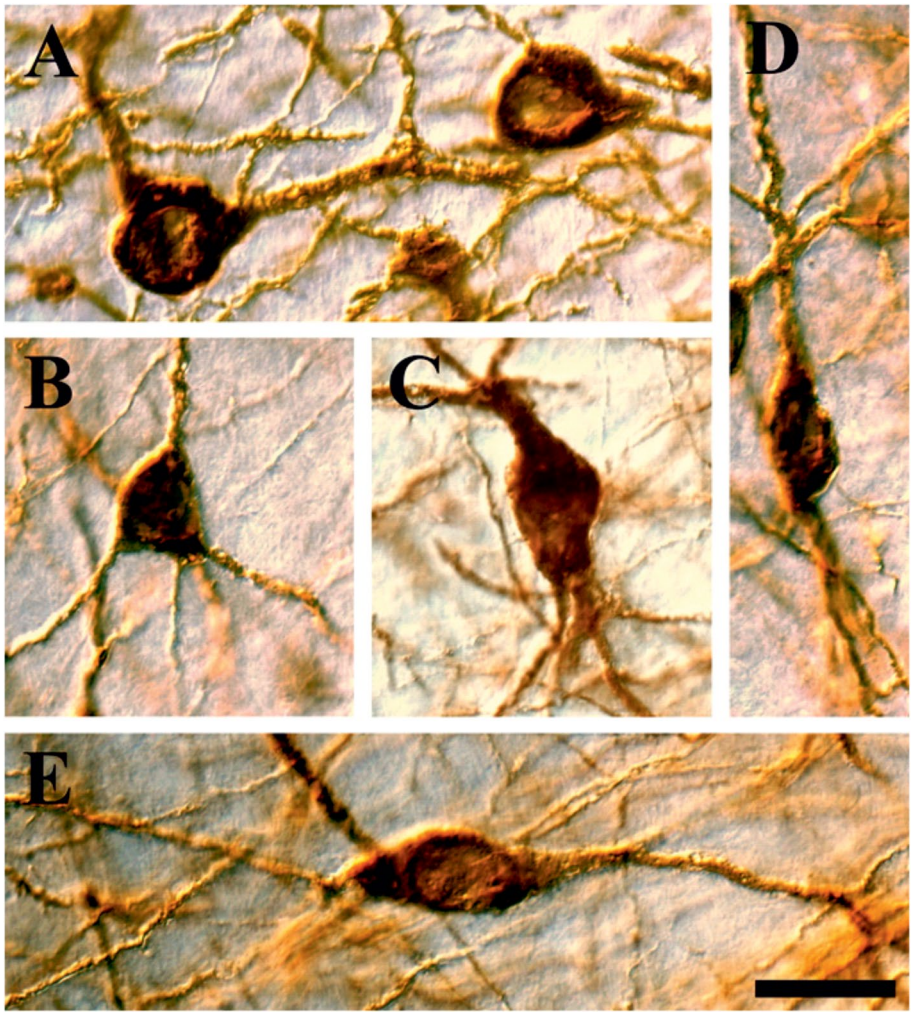

Figure 5. High-power differential interference contrast (DIC) photomicrographs of TH-IR cell types in the microbat substantia nigra. **A.** Round cells. At least three processes in various directions are seen (right side). The majority of TH-IR neurons were round or oval cells with many dendrites coursing in all directions. **B.** A multipolar stellate cell. Stellate neurons had polygon-shaped cell bodies with many dendrites coursing in all directions. **C.** A pyriform cell with a thick primary dendrite oriented toward the pial surface. This ascending process has many small branches, forming a dendritic bouquet. **D.** A vertical fusiform cell with a vertical fusiform cell body and vertically oriented processes. **E.** A horizontal fusiform cell with a horizontal fusiform cell body and horizontally oriented processes. Bar = 20 μm.

although the pattern of dopaminergic innervation has not been studied extensively across diverse animal species, the distribution pattern of the TH-IR fibers in the microbat visual cortex is similar to that of most of the mammals studied to date.

We found TH-IR varicosities throughout the microbat visual cortex, and identified at least two different types: small and large varicose TH-IR fibers. Varicose dopaminergic fibers are common in several brain regions in mammals [24, 31, 32, 35], including the visual cortex of rats [31, 32], whales [35], and monkeys [36]. In our previous study on the distribution of TH in microbats, we also identified two types of varicose dopaminergic fibers in the superior colliculus [24]. As differences in shape, diameter, and synaptic microstructure of varicosities are thought to affect synaptic profiles [49], we propose that the dopaminergic output may be influenced by the morphology of the varicose dopaminergic fibers. However, electron microscopy studies will be required to confirm the synaptic profiles of the TH-IR fibers in the microbat visual cortex.

We did not find TH-IR neurons in the microbat visual cortex, and our results are similar to those of previously studies of mammals such as monkeys [35] and rabbits [34]. However, the TH-IR neurons were found in rat, whale, and human visual cortex [32, 37]. In rat visual cortex, the TH-IR neurons are located

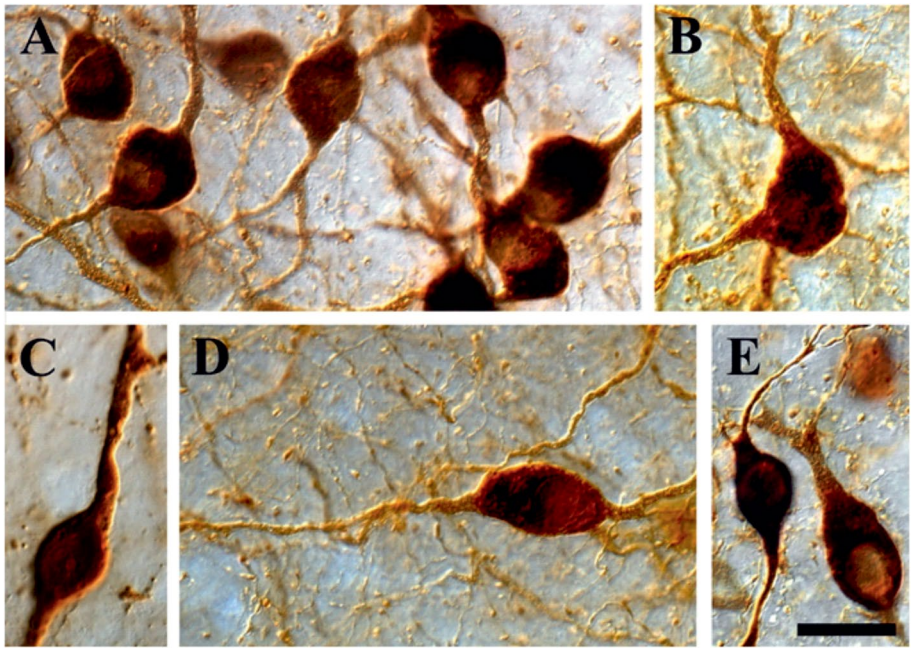

Figure 6. High-power differential interference contrast (DIC) photomicrographs of TH-IR cell types in the microbat ventral tegmental area. **A.** Several round or oval cells can be identified in this Figure. The majority of TH-IR cells were round or oval cells. **B.** A multipolar stellate cell. Stellate neurons had polygon-shaped cell bodies with many dendrites coursing in all directions. **C.** A vertical fusiform cell with a vertical fusiform cell body and vertically oriented processes. **D.** A horizontal fusiform cell with a horizontal fusiform cell body and horizontally oriented processes. **E.** Pyriform cells with a thick primary dendrite oriented toward the pial surface. This ascending process had small branches, forming a dendritic bouquet. Bar = 20 μm.

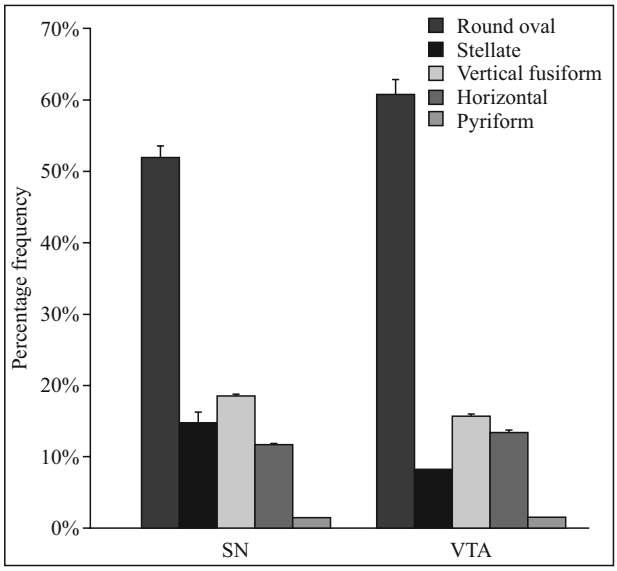

Figure 7. Histogram of the distribution of TH-IR neurons in the microbat substantia nigra and ventral tegmental area. In both areas, round or oval neurons presented the highest concentration of TH-IR cells, whereas the pyriform neurons comprised the smallest proportion. SN — substantia nigra; VTA — ventral tegmental area.

in layers I–VI. Most of these TH-IR neurons have bipolar or multipolar morphology and either fusiform or oval-shaped cell bodies [32]. In the whale visual cortex, TH-IR neurons are mainly observed in layer I [35]. TH-IR neurons in the visual cortex are mainly considered to be interneurons, and have been found to coexpress GABA or its biosynthetic enzyme glutamic acid decarboxylase (GAD) [50]. The functional significance of these inter-species differences in the presence of dopaminergic neurons in the visual cortex has not yet been understood. However, these patterns may reflect variations in the connections and synaptic loops of the dopaminergic system in the animal visual cortex. Another study demonstrated that dopamine modulates GABA release from interneurons *via* the D2-like dopamine receptors in the prefrontal cortex [51]. Thus, dopaminergic fibers may synapse with GABAergic interneurons and modulate GABA levels in the microbat visual cortex.

In the midbrain, TH-IR neurons found in the substantia nigra and ventral tegmental area form several dopaminergic pathways, such as the nigrostriatal, mesolimbic, and mesocortical pathways, that are

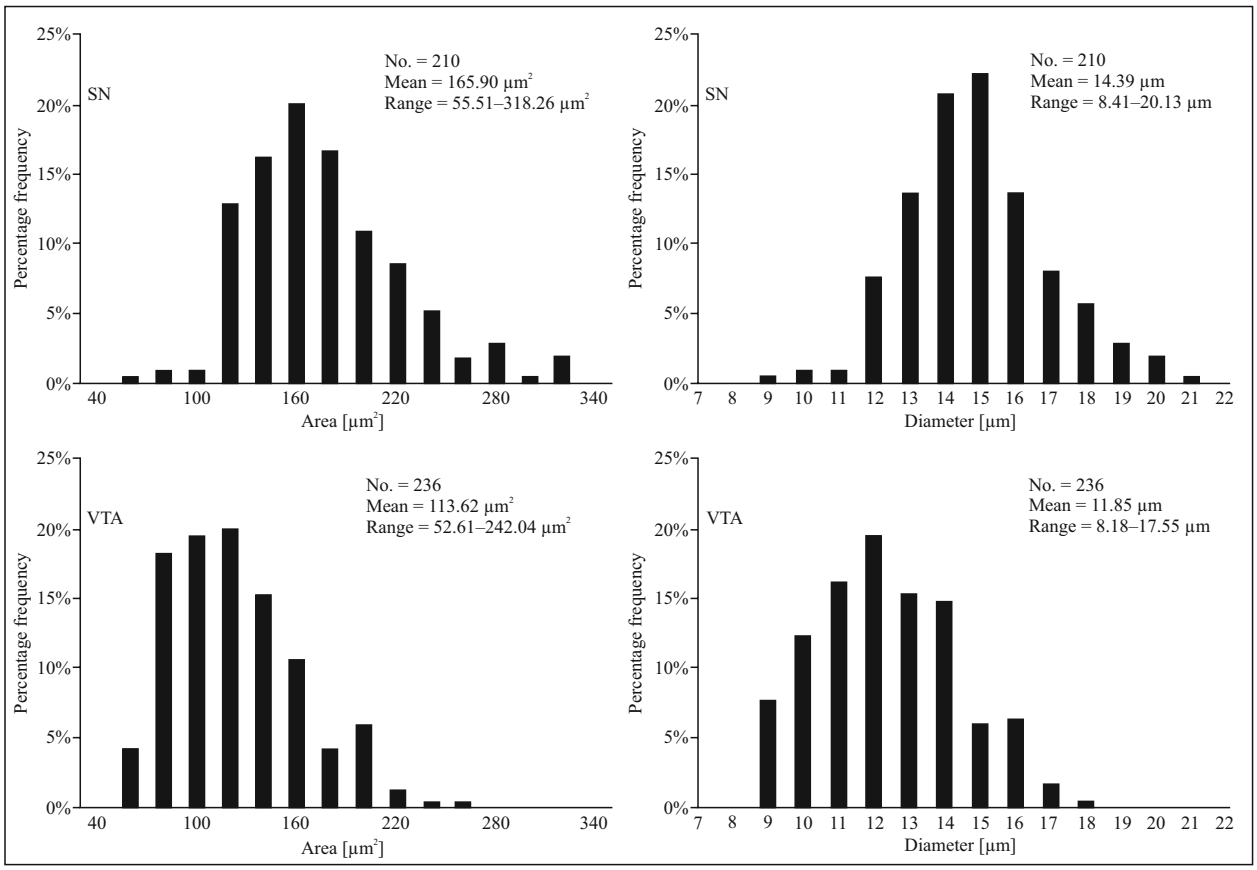

Figure 8. Histogram of TH-IR cell area and diameter in the microbat brain. The diameter of 210 TH-IR neurons in the substantia nigra ranged from 8.41 to 20.13 μm, with a mean of 14.39 ± 2.01 μm (mean ± SD). The area of these cells ranged from 55.51 to 318.26 μm^2, with a mean of 165.90 ± 46.86 μm^2. The diameter of 236 TH-IR neurons in the ventral tegmental area ranged from 8.18 to 17.55 μm, with a mean of 11.85 ± 2.03 μm. The area of these cells ranged from 52.61 to 242.04 μm^2, with a mean of 113.62 ± 39.11 μm^2. The best-stained cells were measured. SN — substantia nigra; VTA — ventral tegmental area.

Table 1. Quantitative data of tyrosine hydroxylase-immunoreactive cells in microbat substantia nigra and ventral tegmental area

	Animal number	Number of TH cells	Diameter ± SEM	
			(μm)	Area ± SEM (μm^2)
Substantia Nigra	1	72	14.76 ± 0.23	174.41 ± 5.65
	2	64	14.05 ± 0.21	157.47 ± 5.06
	3	74	14.32 ± 0.25	164.91 ± 5.81
	Average	70	14.39 ± 0.13	165.90 ± 3.23
Ventral Tegmental Area	1	77	11.00 ± 0.18	97.06 ± 3.27
	2	78	12.45 ± 0.23	125.18 ± 4.69
	3	81	12.09 ± 0.23	118.22 ± 4.50
	Average	78.66	11.85 ± 0.13	113.62 ± 2.54

known to project to the visual cortex. These pathways are associated with emotion-based behaviors and the control of voluntary motor movements. In previous studies identifying dopaminergic nuclei in megabats and microbats, TH-IR nuclei were found in the substantia nigra and ventral tegmental areas [24, 46–48, 52]. Morphometric analysis of the TH-IR cells in the substantia nigra showed a medium-large cellular area

(range 151.26–255.29 μm^2), while the TH-IR cells in the ventral tegmental area had a small-medium cellular area (range 92.70–187.67 μm^2) [52]. These results are similar to those observed in other mammals [53]. Our results also show that the TH-IR cells in the substantia nigra are larger than in the ventral tegmental area. In the present study we identified various cell types including round or oval, stellate, vertical fusiform, and horizontal cells. Although the presence of dopaminergic circuits need to be verified by retrograde trace injection, our current results and pervious findings [26, 27, 30, 38–40] suggest that dopaminergic cells found within the midbrain may be the source of the dopaminergic innervation in the microbat visual cortex. In addition, dopaminergic neurons of different soma sizes that originate in the midbrain are presumed to project varying sizes of dopaminergic fibers into the microbat visual cortex.

Dopaminergic neurons from the substantia nigra target layer I in the rat brain, while neurons originating in the ventral tegmental area and midline nuclei target layers V–VI [31]. Assuming that the central dopaminergic system in the microbat visual cortex is similar to that of the rat, it is possible that the pattern of TH-IR fiber distribution in the bat visual cortex represents region-specific laminar localization of dopaminergic afferents. The high density of TH-IR fibers in layer I of the bat visual cortex suggests that the bat visual cortex may receive much denser dopaminergic projections from the substantia nigra compared to the ventral tegmental area. However, the functional significance of the higher density of dopaminergic fibers in layer I of the visual cortex is not completely understood.

The functional role of TH-IR fibers in the visual cortex has not been fully elucidated yet. The dopaminergic system in the visual cortex may be involved in predicting reward information [54, 55]. Dopamine enhances the visual information content of oscillatory activity in the visual cortex [56]. In the bat, the striatal dopamine receptor-mediated pathway is an important factor in the production of bat echolocation pulses [57]. However, physiological studies of the role of dopamine in the visual cortex of bats have not been conducted. Our results demonstrate a well-organized dopaminergic system in the microbat visual cortex, which suggests that dopaminergic fibers in the visual cortex may play important roles such as predicting reward information and promoting the visual sensory information, as previously described in other mammals [54–56]. However, defining how dopamine modulates various brain functions in the microbat visual cortex requires further studies focusing on electrophysiological approaches.

In conclusion, our results show that well-organized TH-IR fibers are present in the microbat visual cortex. TH-IR cells were not observed in the microbat visual cortex. The microbat substantia nigra and ventral tegmental areas, which are known sources of dopaminergic fibers found in the mammalian visual cortex, contained many well-labelled TH-IR neurons. These results combined with previous studies of the microbat visual system may contribute valuable information to the theory that the microbat visual system has functional roles and is capable of visual processing.

Conflicts of Interest

The authors declare that there are no conflicts of interest.

Acknowledgements

We thank Essay Review for proofreading the manuscript.

References

1. Adams RA. Wing ontogeny, shifting niche dimensions, and adaptive landscapes. In: Adams RA, Pedersen SC, ed. Ontogeny, Functional Ecology, and Evolution of Bats. Cambridge: Cambridge University Press. ; 2000: 275–315.
2. Fenton MB, Simmons NB. Bats: A World of Science and Mystery. Chicago: University of Chicago Press; 2015.
3. Nowack RM. Walker's Mammals of the World. 6th ed. Baltimore: The Johns Hopkins University Press; 1999.
4. Simmons NB. Bat hylogeny: an evolutionary context for comarative studies. In Adams RA, Pedersen SC, ed. Ontogeny, Functional Ecology, and Evolution of Bats. Cambridge: Cambridge University Press; 2000: 9–58.
5. Altringham JD. Bats: Biology and Behaviour. New York: Oxford University Press; 1996.
6. Altringham JD. Bats: From Evolution to Conservation. 2nd ed. New York: Oxford University Press; 2011.
7. Jones G, Teeling EC. The evolution of echolocation in bats. Trends Ecol Evol. 2006; 21(3): 149–156, doi: 10.1016/j.tree.2006.01.001, indexed in Pubmed: 16701491.
8. Surlykke A, Boel Pedersen S, Jakobsen L. Echolocating bats emit a highly directional sonar sound beam in the field. Proc Biol Sci. 2009; 276(1658): 853–860, doi: 10.1098/rspb.2008.1505, indexed in Pubmed: 19129126.
9. Teeling EC. Bats (Chirotera). In Hedges SB, Kumar S, editors. The Time Tree of Life. Oxford University Press, Oxford 2009: 499–503.
10. Feller KD, Lagerholm S, Clubwala R, et al. Characterization of photoreceptor cell types in the little brown bat Myotis lucifugus (Vespertilionidae). Comp Biochem Physiol B Biochem Mol Biol. 2009; 154(4): 412–418, doi: 10.1016/j.cbpb.2009.08.006, indexed in Pubmed: 19720154.
11. Kim TJ, Jeon YK, Lee JY, et al. The photoreceptor populations in the retina of the greater horseshoe bat Rhinolophus ferrumequinum. Mol Cells. 2008; 26(4): 373–379, indexed in Pubmed: 18612246.
12. Müller B, Butz E, Peichl L, et al. The rod pathway of the microbat retina has bistratified rod bipolar cells and tristratified AII amacrine cells. J Neurosci. 2013; 33(3): 1014–1023, doi:

10.1523/JNEUROSCI.2072-12.2013, indexed in Pubmed: 23325239.
13. Müller B, Glösmann M, Peichl L, et al. Bat eyes have ultraviolet-sensitive cone photoreceptors. PLoS One. 2009; 4(7): e6390, doi: 10.1371/journal.pone.0006390, indexed in Pubmed: 19636375.
14. Winter Y, López J, Von Helversen O. Ultraviolet vision in a bat. Nature. 2003; 425(6958): 612–614, doi: 10.1038/nature01971, indexed in Pubmed: 14534585.
15. Xuan F, Hu K, Zhu T, et al. Immunohistochemical evidence of cone-based ultraviolet vision in divergent bat species and implications for its evolution. Comp Biochem Physiol B Biochem Mol Biol. 2012; 161(4): 398–403, doi: 10.1016/j.cbpb.2012.01.005, indexed in Pubmed: 22269122.
16. Zhao H, Xu D, Zhou Y, et al. Evolution of opsin genes reveals a functional role of vision in the echolocating little brown bat (Myotis lucifugus). Biochem Syst Ecol. 2009; 37(3): 154–161, doi: 10.1016/j.bse.2009.03.001.
17. Jeong MJ, Kim HG, Jeon CJ. The organization of melanopsin-immunoreactive cells in microbat retina. PLoS One. 2018; 13(1): e0190435, doi: 10.1371/journal.pone.0190435, indexed in Pubmed: 29304147.
18. Park EB, Jeon JY, Jeon CJ. Identification of protein kinase C α- and tyrosine hydroxylase-immunoreactive cells in the microbat retina. Histol Histopathol. 2018; 33(10): 1059–1073, doi: 10.14670/HH-18-001, indexed in Pubmed: 29741202.
19. Butz E, Peichl L, Müller B. Cone bipolar cells in the retina of the microbat Carollia perspicillata. J Comp Neurol. 2015; 523(6): 963–981, doi: 10.1002/cne.23726, indexed in Pubmed: 25521284.
20. Pettigrew JD, Dreher B, Hopkins CS, et al. Peak density and distribution of ganglion cells in the retinae of microchiropteran bats: implications for visual acuity. Brain Behav Evol. 1988; 32(1): 39–56, doi: 10.1159/000116531, indexed in Pubmed: 3191381.
21. Glezer II, Hof PR, Leranth C, et al. Calcium-binding protein-containing neuronal populations in mammalian visual cortex: a comparative study in whales, insectivores, bats, rodents, and primates. Cereb Cortex. 1993; 3(3): 249–272, doi: 10.1093/cercor/3.3.249, indexed in Pubmed: 8324371.
22. Gu YN, Kim HG, Jeon CJ. Localization of nitric oxide synthase-containing neurons in the bat visual cortex and colocalization with calcium-binding proteins. Acta Histochem Cytochem. 2015; 48(4): 125–133, doi: 10.1267/ahc.14066, indexed in Pubmed: 26379314.
23. Kim HG, Gu YN, Lee KP, et al. Immunocytochemical localization of the calcium-binding proteins calbindin D28K, calretinin, and parvalbumin in bat visual cortex. Histol Histopathol. 2016; 31(3): 317–327, doi: 10.14670/HH-11-680, indexed in Pubmed: 26536416.
24. Jeong SJ, Jeon CJ. Localization of choline acetyltransferase and tyrosine hydroxylase immunoreactivities in the superior colliculus of the microbat. Histol Histopathol. 2017; 32(6): 609–626, doi: 10.14670/HH-11-826, indexed in Pubmed: 27681043.
25. Abraham AD, Neve KA, Lattal KM. Dopamine and extinction: a convergence of theory with fear and reward circuitry. Neurobiol Learn Mem. 2014; 108: 65–77, doi: 10.1016/j.nlm.2013.11.007, indexed in Pubmed: 24269353.
26. Chinta SJ, Andersen JK. Dopaminergic neurons. Int J Biochem Cell Biol. 2005; 37(5): 942–946, doi: 10.1016/j.biocel.2004.09.009, indexed in Pubmed: 15743669.
27. Jacob SN, Nienborg H. Monoaminergic neuromodulation of sensory processing. Front Neural Circuits. 2018; 12: 51, doi: 10.3389/fncir.2018.00051, indexed in Pubmed: 30042662.
28. Overton PG, Vautrelle N, Redgrave P. Sensory regulation of dopaminergic cell activity: Phenomenology, circuitry and function. Neuroscience. 2014; 282: 1–12, doi: 10.1016/j.neuroscience.2014.01.023, indexed in Pubmed: 24462607.
29. Schultz W. Multiple dopamine functions at different time courses. Annu Rev Neurosci. 2007; 30: 259–288, doi: 10.1146/annurev.neuro.28.061604.135722, indexed in Pubmed: 17600522.
30. Wise RA. Dopamine, learning and motivation. Nat Rev Neurosci. 2004; 5(6): 483–494, doi: 10.1038/nrn1406, indexed in Pubmed: 15152198.
31. Berger B, Gaspar P, Verney C. Dopaminergic innervation of the cerebral cortex: unexpected differences between rodents and primates. Trends Neurosci. 1991; 14(1): 21–27, doi: 10.1016/0166-2236(91)90179-x, indexed in Pubmed: 1709528.
32. Kosaka T, Hama K, Nagatsu I. Tyrosine hydroxylase-immunoreactive intrinsic neurons in the rat cerebral cortex. Exp Brain Res. 1987; 68(2): 393–405, doi: 10.1007/BF00248804, indexed in Pubmed: 2891559.
33. Phillipson OT, Kilpatrick IC, Jones MW. Dopaminergic innervation of the primary visual cortex in the rat, and some correlations with human cortex. Brain Res Bull. 1987; 18(5): 621–633, doi: 10.1016/0361-9230(87)90132-8, indexed in Pubmed: 2440529.
34. Wang XH, Levitt P, Jenkins AO, et al. Normal development of tyrosine hydroxylase and serotonin immunoreactive fibers innervating anterior cingulate cortex and visual cortex in rabbits exposed prenatally to cocaine. Brain Research. 1996; 715(1-2): 221–224, doi: 10.1016/0006-8993(96)00012-1, indexed in Pubmed: 8739642.
35. Hof P, Glezer I, Revishchin A, et al. Distribution of dopaminergic fibers and neurons in visual and auditory cortices of the harbor porpoise and pilot whale. Brain Res Bull. 1995; 36(3): 275–284, doi: 10.1016/0361-9230(94)00202-c, indexed in Pubmed: 7697381.
36. Lewis DA, Campbell MJ, Foote SL, et al. The distribution of tyrosine hydroxylase-immunoreactive fibers in primate neocortex is widespread but regionally specific. J Neurosci. 1987; 7(1): 279–290, doi: 10.1523/JNEUROSCI.07-01-00279.1987, indexed in Pubmed: 2879896.
37. Gaspar P, Berger B, Febvret A, et al. Tyrosine hydroxylase-immunoreactive neurons in the human cerebral cortex: a novel catecholaminergic group? Neurosci Lett. 1987; 80(3): 257–262, doi: 10.1016/0304-3940(87)90464-2, indexed in Pubmed: 2891090.
38. Björklund A, Dunnett SB. Dopamine neuron systems in the brain: an update. Trends Neurosci. 2007; 30(5): 194–202, doi: 10.1016/j.tins.2007.03.006, indexed in Pubmed: 17408759.
39. Nieoullon A, Cheramy A, Glowinski J. Release of dopamine evoked by electrical stimulation of the motor and visual areas of the cerebral cortex in both caudate nuclei and in the substantia nigra in the cat. Brain Res. 1978; 145(1): 69–83, doi: 10.1016/0006-8993(78)90797-7, indexed in Pubmed: 638784.
40. Törk I, Turner S. Histochemical evidence for a catecholaminergic (presumably dopaminergic) projection from the ventral mesencephalic tegmentum to visual cortex in the cat. Neurosci Lett. 1981; 24(3): 215–219, doi: 10.1016/0304-3940(81)90159-2, indexed in Pubmed: 6168976.
41. Piraccini, R. Rhinolophus ferrumequinum. The IUCN Red List of Threatened Species. 2016. Available at: https://dx.doi.org/10.2305/IUCN.UK.2016-2.RLTS.T19517A21973253.en. Accessed June 8, 2018.
42. Jeon YK, Kim TJ, Lee JY, et al. AII amacrine cells in the inner nuclear layer of bat retina: identification by parvalbumin immunoreactivity. Neuroreport. 2007; 18(11): 1095–1099, doi: 10.1097/WNR.0b013e3281e72afe, indexed in Pubmed: 17589306.

43. Kim GH, Kim HG, Jeon CJ. Immunocytochemical localization of choline acetyltransferase in the microbat visual cortex. Acta Histochem Cytochem. 2018; 51(5): 153–165, doi: 10.1267/ahc.18018, indexed in Pubmed: 30510329.
44. Park EB, Gu YN, Jeon CJ. Immunocytochemical localization of cholinergic amacrine cells in the bat retina. Acta Histochem. 2017; 119(4): 428–437, doi: 10.1016/j.acthis.2017.04.009, indexed in Pubmed: 28483062.
45. Jang YJ, Yu SH, Lee ES, et al. Two types of tyrosine hydroxylase-immunoreactive neurons in the zebrafish retina. Neurosci Res. 2011; 71(2): 124–133, doi: 10.1016/j.neures.2011.07.002, indexed in Pubmed: 21784111.
46. Kruger JL, Dell LA, Bhagwandin A, et al. Nuclear organization of cholinergic, putative catecholaminergic and serotonergic systems in the brains of five microchiropteran species. J Chem Neuroanat. 2010; 40(3): 210–222, doi: 10.1016/j.jchemneu.2010.05.007, indexed in Pubmed: 20566329.
47. Dell LA, Kruger JL, Bhagwandin A, et al. Nuclear organization of cholinergic, putative catecholaminergic and serotonergic systems in the brains of two megachiropteran species. J Chem Neuroanat. 2010; 40(2): 177–195, doi: 10.1016/j.jchemneu.2010.05.008, indexed in Pubmed: 20566331.
48. Maseko BC, Manger PR. Distribution and morphology of cholinergic, catecholaminergic and serotonergic neurons in the brain of Schreiber's long-fingered bat, Miniopterus schreibersii. J Chem Neuroanat. 2007; 34(3-4): 80–94, doi: 10.1016/j.jchemneu.2007.05.004, indexed in Pubmed: 17560075.
49. Jeon CJ, Spencer R, Mize R. Organization and synaptic connections of cholinergic fibers in the cat superior colliculus. J Comp Neurol. 1993; 333(3): 360–374, doi: 10.1002/cne.903330305, indexed in Pubmed: 8349848.
50. Raghanti MA, Spocter MA, Stimpson CD, et al. Species-specific distributions of tyrosine hydroxylase-immunoreactive neurons in the prefrontal cortex of anthropoid primates. Neuroscience. 2009; 158(4): 1551–1559, doi: 10.1016/j.neuroscience.2008.10.058, indexed in Pubmed: 19041377.
51. Grobin AC, Deutch AY. Dopaminergic regulation of extracellular gamma-aminobutyric acid levels in the prefrontal cortex of the rat. J. Pharmacol. Exp. Ther. 1998; 285(1): 350–357, indexed in Pubmed: 9536031.
52. Medeiros HH, Santana MA, Leite MD, et al. The cytoarchitectonic and TH-immunohistochemical characterization of the dopamine cell groups in the substantia nigra, ventral tegmental area and retrorubral field in a bat (Artibeus planirostris). Neurosci Res. 2016; 112: 37–46, doi: 10.1016/j.neures.2016.06.005, indexed in Pubmed: 27349153.
53. Calvey T, Patzke N, Kaswera-Kyamakya C, et al. Organization of cholinergic, catecholaminergic, serotonergic and orexinergic nuclei in three strepsirrhine primates: Galago demidoff, Perodicticus potto and Lemur catta. J Chem Neuroanat. 2015; 70: 42–57, doi: 10.1016/j.jchemneu.2015.10.002, indexed in Pubmed: 26562782.
54. Shuler MG, Bear MF. Reward timing in the primary visual cortex. Science. 2006; 311(5767): 1606–1609, doi: 10.1126/science.1123513, indexed in Pubmed: 16543459.
55. Tan CO. Anticipatory changes in regional cerebral hemodynamics: a new role for dopamine? J Neurophysiol. 2009; 101(6): 2738–2740, doi: 10.1152/jn.00141.2009, indexed in Pubmed: 19321643.
56. Zaldivar D, Goense J, Lowe SC, et al. Dopamine is signaled by mid-frequency oscillations and boosts output layers visual information in visual cortex. Curr Biol. 2018; 28(2): 224–235.e5, doi: 10.1016/j.cub.2017.12.006, indexed in Pubmed: 29307559.
57. Tressler J, Schwartz C, Wellman P, et al. Regulation of bat echolocation pulse acoustics by striatal dopamine. J Exp Biol. 2011; 214(Pt 19): 3238–3247, doi: 10.1242/jeb.058149, indexed in Pubmed: 21900471.

Submitted: 20 January, 2020
Accepted after reviews: 9 May, 2020
Available as AoP: 2 June, 2020

FOLIA HISTOCHEMICA ET CYTOBIOLOGICA
Vol. 58, No. 2, 2020
pp. 73–82

ORIGINAL PAPER

VIA MEDICA

Features of gonadal dysgenesis and Leydig cell impairment in testes with Sertoli cell-only syndrome

Daria Adamczewska, Jolanta Slowikowska-Hilczer, Katarzyna Marchlewska, Renata Walczak-Jedrzejowska

Department of Andrology and Reproductive Endocrinology, Medical University of Lodz, Lodz, Poland

Abstract

Introduction. There is evidence that disturbed spermatogenesis is associated with impaired Leydig cell function and that it may be the result of testicular dysgenesis during fetal/infant development. Sertoli cell-only syndrome (SCOS) is defined by complete lack of germ cells in the seminiferous epithelium. The pathogenesis of SCOS is still not well understood. The aim of the study is to evaluate testes with SCOS focusing on morphometric signs of testicular dysgenesis and markers of Leydig cell (LC) function in relation to hormonal status of studied infertile men.

Materials and methods. Forty-nine testicular biopsies of patients with SCOS and 15 controls with normal spermatogenesis (NOR) were studied. In each biopsy the seminiferous tubule diameter (STD), thickness of tubular membrane (TM), area fraction of intertubular space (AFIS) were measured and semi-quantitative assessment of the LC number was performed (LC-score). The results of histological examination were correlated with serum levels of FSH, LH, testosterone (T) and T/LH ratio.

Results. In SCOS group testicular volume (median [M]: 16.0 *vs.* 29.5; $p < 0.001$) and STD (M: 141.7 *vs.* 190.2; $p < 0.001$) were lower, while TM (M: 9.8 *vs.* 6.4; $p < 0.001$) and AFIS (M: 47.6 *vs.* 27.6; $p < 0.001$) were significantly higher in comparison to NOR group. LC-score was higher in SCOS than in NOR group (M: 2.2 *vs.* 1.1; $p < 0.001$). Abnormal AFIS and STD were present in 43% of SCOS biopsies and among them in 81% the increased LC-score was found. In SCOS group, the subjects had significantly higher levels of both gonadotropins (FSH, M: 19.9 *vs.* 3.4; $p < 0.001$; LH, M: 7.1 *vs.* 4.2; $p < 0.001$). Total serum testosterone level did not differ between studied groups; however, T/LH ratio was significantly lower in SCOS group (M: 2.3 *vs.* 3.8; $p < 0.001$). Negative correlation between LC-score and STD was observed in SCOS group ($r = –0.48$; $p < 0.001$). AFIS correlated positively with serum FSH level in NOR ($r = 0.53$; $p < 0.05$) and SCOS ($r = 0.41$; $p < 0.05$) group, while with LH, and negatively with T/LH ratio, only in SCOS (LH, $r = 0.37$; $p < 0.05$; T/LH, $r = –0.36$; $p < 0.05$) group.

Conclusions. We have shown that substantial number of testes from subjects with SCOS presented abnormal morphometric features, which are recognized as the signs of testicular dysgenesis. Additionally, an increased number of Leydig cells simultaneously with abnormal T/LH ratio were found, which suggests an impaired function of these cells. Increased serum levels of LH and also FSH, may reflect dysfunction of Leydig cells. It seems that reproductive hormones levels reflect also the condition of testicular structure, and that FSH may be related to the changes in intertubular space area independently of impaired Leydig cell function. *(Folia Histochemica et Cytobiologica 2020, Vol. 58, No. 2, 73–82)*

Key words: Sertoli cell-only syndrome; testicular dysgenesis syndrome; Leydig cells; FSH; LH; testosterone; testicular biopsy; histology; morphometric assessment

Correspondence address:
Renata Walczak-Jedrzejowska, MSc, PhD, DSc
Department of Andrology and Reproductive Endocrinology,
Medical University of Lodz,
Pomorska str. 251, CKD UM, 92–213 Lodz, Poland
ORCID: 0000-0002-4267-5714
phone: +48 42 272 53 91
e-mail: renata.walczak-jedrzejowska@umed.lodz.pl

Introduction

Infertility is a problem that affects approximately 15% of couples trying to conceive after at least one year of regular, unprotected intercourses. The male factor is believed to contribute alone or in combination with female factor to difficulties in achieving pregnancy in 50% of cases [1]. Male infertility can be caused by wide range of conditions identified at pre-testicular, testicular and post-testicular level. It can results from anatomical or genetic abnormalities, endocrine, systematic or neurological diseases, infections, trauma, iatrogenic injury or gonadotoxins [2]. Also other factors such as excessive oxidative stress, improper lifestyle habits and sperm DNA fragmentation have been recently extensively studied as one of the mechanisms of male infertility [3–5].

The most severe form of human male infertility is Sertoli cell-only syndrome (SCOS), sometimes called germinal aplasia, a condition that is defined by a complete lack of germ cells, but preserved Sertoli cells in the seminiferous tubules [6]. It is estimated that about 5–10% of infertile men may have SCOS; however, its incidence may reach 39% in patients with non-obstructive azoospermia (NOA) [7]

The pathogenesis of the syndrome is still not well understood. Presumably, in congenital germ cell aplasia, primordial germ cells do not migrate from the yolk sac into embryonic gonad [8, 9]. The SCOS may also result from factors damaging spermatogenic epithelium such as toxic exposure, including chemotherapy, irradiation or hormonal factors. Cryptorchidism or viral orchitis have also been associated with the appearance of SCOS [6, 10]. Among genetic factors the most frequent are chromosomal abnormalities (*e.g.* Klinefelter syndrome) as well as deletions in AZF (azoospermia factor) region of the Y chromosome [11].

It is well recognized that significant proportion of patients with SCOS had elevated levels of follicle stimulating hormone (FSH) [7, 12]. However, in some cases FSH concentrations are within normal range what may indicate selective malfunction of seminiferous tubules [13]. Usually, the patients present normal levels of luteinizing hormone (LH) and testosterone (T), but some of them may present a decreased T/LH ratio resulting from slightly increased LH level and low-normal or decreased T level [7, 12, 14]. As hormone levels do not always distinguish normal testicular function from impaired spermatogenesis, the final diagnosis can be made only by testicular biopsy.

In cases of primary SCOS seminiferous tubules may have only slightly reduced diameter and normal tubular wall thickness. Contrary, in cases of secondary (acquired) SCOS, the tubular wall may be thickened, the seminiferous tubules diameter reduced and Sertoli cells may show signs of degeneration [6]. Not uncommon histological feature of SCOS is increased number of Leydig cells, which together with reduced T/LH is recognized as a marker of impaired Leydig cells function [7, 12, 15]. It was shown that the T/LH ratio might be lower in men with disturbed spermatogenesis when compared to men with normal spermatogenesis [12, 14, 16]. Additionally, the cut-off value at 2 for T/LH ratio was recently established based on data from a cohort of 127 subjects with normal spermatogenesis [16]. This Leydig cell dysfunction may reflect the lack of paracrine signals from the disturbed tubular compartment or may be a consequence of testicular dysgenesis during fetal/infant development [14, 15, 17, 18]. Additionally, apart from increased number of Leydig cells, the morphometric features such as decreased seminiferous diameter, increased tubular wall thickness and wide intertubular space may account for the signs of disturbed testicular organogenesis (dysgenesis) [19, 20].

Although testicular biopsy is the key tool in diagnostic work-up of azoospermic men, very often the process of evaluation of testicular tissue is focused primarily on the spermatogenic compartment with poor description of intertubular space and morphometric features of testicular tubule.

The aim of this study is to evaluate testes of patients with SCOS focusing on morphometric features of testicular dysgenesis and markers of Leydig cell function in relation to hormonal status of studied infertile men.

Materials and methods

The study protocol was approved by the Bioethics Committee of the Medical University of Lodz, Poland (No. RNN/14/15/EC).

Subjects and clinical data. To this retrospective study we included 49 men (age 19.6–43.8, median 31 years) with histological diagnosis of SCOS and 15 subjects (age 23.4–38.2, median 29.5 years) with normal spermatogenesis (NOR) observed in histological analysis as controls. All subjects were diagnosed because of azoospermia in semen analysis during the period 2005–2010. The most frequent andrological finding among SCOS subjects was history of cryptorchidism (18%; 9/49). Other alterations such as atrophy of contralateral testis, testicular microlithiasis found on ultrasonography or germ cell tumor in the contralateral testis were observed in 14% of the subjects (7 out of 49).

The paraffin embedded testicular biopsies as well as the subjects' medical history were available in the Department of

Andrology and Reproductive Endocrinology of the Medical University of Lodz. Testicular biopsies were taken in the II Department of Urology, Medical University of Lodz.

The bilateral biopsy was taken only in 5 cases. The histological pattern was consistent on both sides, thus the mean value was calculated from data obtained from histological and morphometric assessment of both testes.

Before testicular biopsy the subjects underwent physical examination and the testes volume was measured by ultrasonography. Hormonal measurements were performed in 55 subjects (SCOS = 40 and NOR = 15) as a part of their diagnostic workup. Serum concentrations of FSH, LH, total testosterone (T) were determined using enhanced chemiluminescence method for VITROS ECi Immunodiagnostic System with MicroWell technology utilizing commercially available VITROS Reagent Packs for the hormones according to manufacturer instruction (Ortho-Clinical Diagnostics Johnson and Johnson, UK). Hormonal determinations were performed in the laboratory of the Clinical Hospital of Medical University of Lodz. Additionally, ratio T/LH was calculated.

None of the subjects had hypogonadotropic hypogonadism, any chronic disease, Klinefelter syndrome or history of hormonal treatment. However, the patients did not have genetic analysis of AZF deletions. Although currently AZF deletions are examined routinely, 10 years earlier they were not tested in every patient.

Tissue preparation and histological analysis. All testicular biopsies were handled at the histological laboratory of the Department of Andrology and Reproductive Endocrinology, Medical University of Lodz. The subjects tissue samples were fixed in Bouin's solution, embedded in paraffin, cut at 5 μm-thick serial sections and transferred onto microscopic slides. After dewaxing and rehydration, the sections were stained with hematoxylin and eosin.

Histological analysis of spermatogenesis included a qualitative and quantitative evaluation of seminiferous epithelium in 50 tubules and calculation of the modified Johnsen Score (JS) was performed to confirm the histological pattern of complete SCOS and NOR in the biopsies.

Morphometric analysis. Morphometric measurements of seminiferous tubules diameter (STD), the thickness of tubular membrane (TM) as well as the areal fraction of the biopsy occupied by intertubular space (AFIS) were performed with utilization of an image analysis system. The system consists of an Eclipse E600 light microscope with a connected camera Nikon DS-Fi1c and software NIS-Elements AR Ver. 3.2 for image analysis (Nikon, Tokyo, Japan). Slides were viewed and documented at 100× and 200× total magnification (objective 10×).

The measurements of STD and TM were performed in tubules with a circular shape. For each tubule the length of two diameters was measured. Measurements were taken from 25 tubules for each testis, at 200× magnification, and then the mean value was calculated.

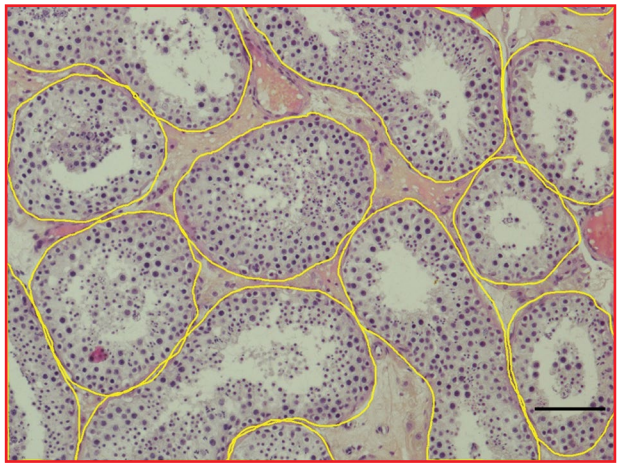

Figure 1. Seminiferous tubule delineation in a testis biopsy from the control group. The image shows seminiferous tubules cross-sections outlined in yellow using NIS-Elements AR ver. 3.2 software (Nikon). The frame used to cover the specific area of testis cross-section is marked in red and corresponds to 567240 μm^2 of the microscopic image. Magnification 100×, scale bar — 100 μm.

To measure AFIS, the microscopic image of the biopsy was visualized on a computer screen where, with the use of an image analysis software, a standardized frame of a known size was placed. The size of the frame was 870 × 652 μm which corresponds to an area of 567 240 μm^2 covered in the microscopic image of the biopsy at a 100× magnification. For each testicular biopsy an area of every single seminiferous tubule or its part present inside the frame was manually delineated (Fig. 1). The total area of intertubular space (IS) was then calculated by subtraction of the total area of seminiferous tubules from the frame area. In each case the data were collected from 10 images per each slide which corresponds to analyzed area of 5.7 mm^2. Finally, the AFIS was calculated as a percentage of the analyzed biopsy area occupied by IS.

The normal values of STD, TM and AFIS were defined upon the data of previous studies [19, 21, 22]. The following values were recognized as parameters of testicular dysgenesis: STD < 150 μm, TM (> 10 μm) and AFIS (> 40%).

Assessment of Leydig cells. Semi-quantitative assessment of Leydig cells number was performed by scoring created by Guminska *et al*. (2007) according to which a specific point value was assigned to number of Leydig cells observed in a particular IS as follow:

— 0 Leydig cells — 0 points;
— 1–5 Leydig cells — 1 point;
— 6–10 Leydig cells — 2 points;
— 11–30 Leydig cells — 3 points;
— > 30 Leydig cells (nodules of Leydig cells) — 4 points.

Leydig cells, arranged both as isolated cells or clusters, were recognized by their morphological features and location in the interstitial tissue. The morphological features included: 1) eccentric, regular round or oval nucleus, usually with one or two prominent nucleoli, 2) the nucleus surrounded by abundant eosinophilic cytoplasm. The cells are usually located adjacent to the seminiferous tubules or near blood vessels.

In each biopsy specimen 100 triangular IS were evaluated and a mean number of points was calculated. Leydig cells score (LC-score) > 2 points was considered as abnormal [21, 23].

Statistical analysis. The Statistica 13.1 software (StatSoft, Kraków, Poland) licensed by Medical University of Lodz was used for statistical analysis. To test the normality of obtained data the Shapiro-Wilk test was used. Due to a non-normal distribution of the majority of variables, non-parametric statistics were used. Medians and percentiles (2.5–97.5) were used for descriptive data. Between group differences were tested by Mann-Whitney U test. Nonparametric Spearman's rank correlation coefficient (r_s) was used to evaluate statistical relationship between continuous variables. The value of r_s was interpreted as follows: < 0.2 — lack of linear dependence, 0.2–0.4 — weak dependence, > 0.4–0.7 — moderate dependence, > 0.7–0.9 — strong dependence, > 0.9 — very strong dependence. A p value below 0.05 was considered statistically significant.

Results

Histological and morphometric analysis

The evaluation of spermatogenesis confirmed the histological pattern of complete SCOS (JS ≤ 2) and NOR (JS ≥ 8) in our subjects biopsies. Representative microphotographs of testicular tissue from SCOS and NOR subjects are shown in Figure 2.

The data concerning subjects' age, both testicles volume, morphometric analysis and LC-score are presented in Table 1. There was no difference in age between the subjects from the studied groups. In SCOS group the testes volume as well as STD were significantly lower when compared to NOR group ($p < 0.001$; $p < 0.001$, respectively). On the contrary, other morphometric features, *i.e.* TM and AFIS, were significantly higher ($p < 0.001$; $p < 0.001$, respectively). We found that abnormal morphometric features, which are recognized as parameters of testicular dysgenesis (STD < 15 μm, TM > 10 μm, AFIS > 40%), were present in biopsies of 12/49 SCO subjects (25%), whereas only 3/49 biopsies in this group (6%) presented normal values. In the remaining 69% of biopsies with SCOS we found two (15/49; 30%) or one (19/49; 39%) abnormal morphometric features. The most frequent was STD (31/49; 64%), then AFIS (30/49; 61%), and the least frequent — TM (23/49; 47%). In the NOR group all biopsy presented normal value for all the studied morphometric parameters.

The Leydig cell score was significantly higher in SCOS group ($p < 0.001$) when compared to NOR group. The LC-score above 2, which is consider abnormal, was present in 26/49 (53%) of SCOS biopsies, and in none biopsy in NOR group. Moreover, larger cluster of LC (LC-score between 3 and 4 points) was observed in 18/49 of SCOS biopsies (36%).

Hormonal levels

The hormone levels and ratios are presented in Table 2. In SCOS group the subjects had significantly higher levels of gonadotropins in comparison to the control group (FSH, $p < 0.001$; LH, $p < 0.001$). The total serum T concentration did not differ between the studied groups; however, the T/LH ratio was significantly decreased in SCOS group ($p < 0.001$). Considering the cut-off value for T/LH ratio, which was established by Lardone *et al.* [16], 13/40 (35%) subjects from SCOS group had T/LH < 2, and the remaining 27/40 (65%) had T/LH ≥ 2. All NOR subjects had T/LH ≥ 2.

Increased areal fraction of intertubular space (AFIS) and decreed seminiferous tubule diameter (STD) with concomitant appearance of increased Leydig cell score in SCOS patients

To answer the question if increased Leydig cell number appears concomitantly with increased AFIS and decreased tubule diameter we checked the incidence of concomitant appearance of all three features in the analyzed biopsies. We found that abnormal AFIS (> 40%) and STD (< 150 μm) values were present in 43% of biopsies with SCOS (21/49) and among them in 81% (17/21) we found an increased LC-score (> 2). On the other hand, we found that normal values for both AFIS (≤ 40%) and STD (≥ 150 μm) were present in 16% (8/49) of SCOS biopsies and almost in all cases, except one, the LC-score was normal (≤ 2) (88%; 7/8). In cases where AFIS value was abnormal and STD normal (20%; 10/49) we found that in only three biopsies (30%; 3/10) the LC-score was abnormal. Similar results were found in biopsies where AFIS value was normal and STD abnormal (20%; 10/49). In biopsies of those patients the abnormal LC-score was also present in 30% of biopsies (3/10).

Relationshisps between morphometric parameters and serum hormone concentrations

Relationships between morphometric features of testicular dysgenesis and serum levels of FSH, LH, T, as well as the parameters of Leydig cells function (T/LH ratio and LC-score) are shown in Table 3.

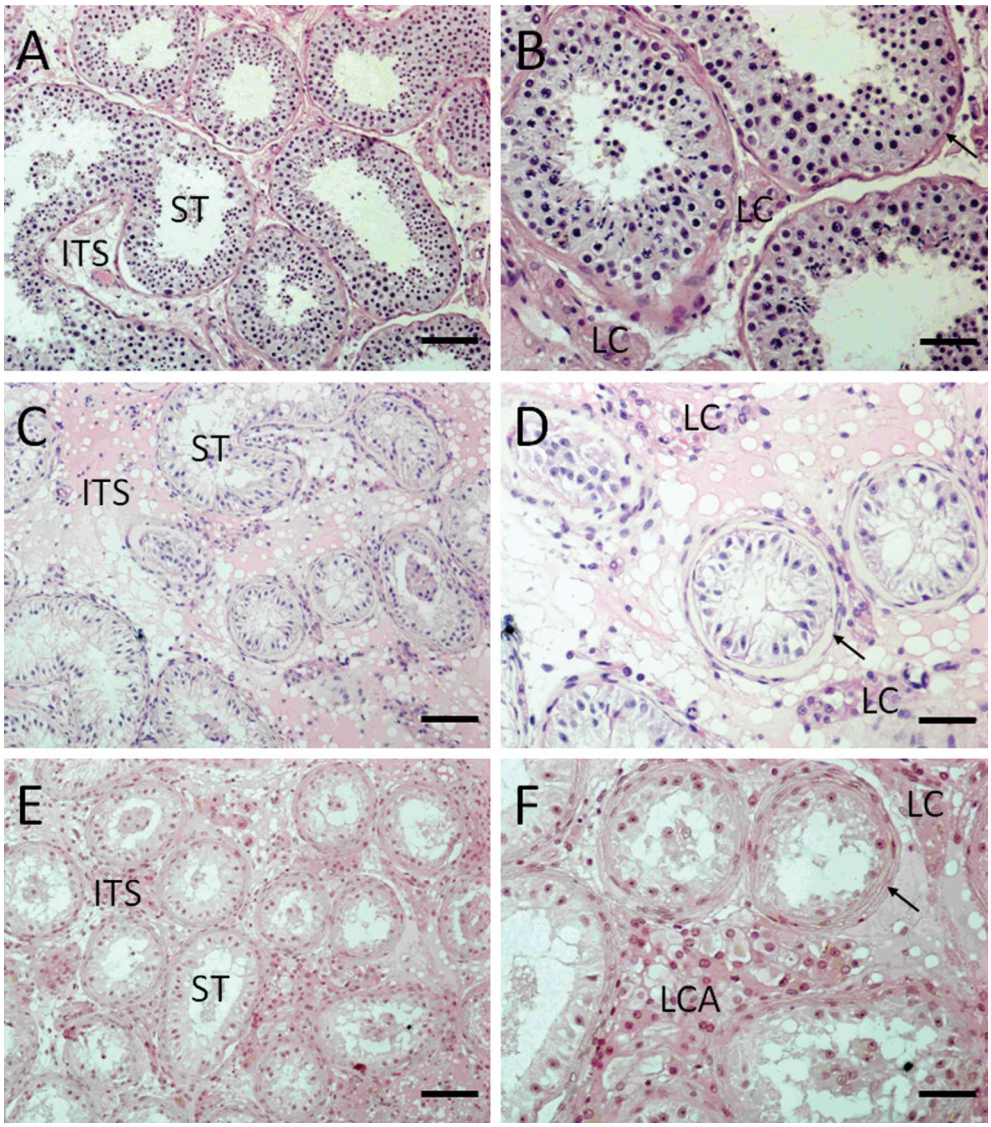

Figure 2. Histological structure of testicular biopsies from the control and SCOS group. **A.** Normal spermatogenesis: overview of well-developed seminiferous tubules (ST) that show a clear lumen, all stages of germ cell maturation and normal intertubular space (ITS). **B.** Enlargement of A: visible Leydig cells (LC) clusters of normal size; tubular basement membrane of normal thickness (arrow). **C.** Sertoli cell-only syndrome: overview of underdeveloped STs with small diameters; tubules contain only mature Sertoli cells, ITS is wide. **D.** Enlargement of C: in ITS visible LC cluster of normal size; thickness of tubular basement membrane is increased (arrow). **E.** Sertoli cell-only syndrome: overview of underdeveloped ST with small diameter; tubules contain only mature Sertoli cells, ITS is slightly wider than in (A). **F.** Enlargement of C: in ITS visible large LC cluster (aggregation) (LCA); thickness of basement membrane is increased (arrow). Magnifications and scale bars: A, C, E — 100×, bar — 100 μm; B, D, F — 200×, bar — 50 μm.

Considering collectively all the normal subjects and patients FSH and LH levels correlated negatively with STD ($p < 0.001$) and positively with TM ($p < 0.001$), AFIS ($p < 0.001$) and LC-score ($p < 0.001$). In SCOS group FSH and LH levels correlated positively with AFIS ($p < 0.05$) and LC-score ($p < 0.05$) while in NOR group the only observed correlation was between FSH levels and AFIS ($p < 0.05$).

The T/LH ratio correlated positively with STD ($p < 0.05$) and negatively with TM $p < 0.001$), AFIS ($p < 0.001$) and LC-score ($p < 0.01$) when considered all the subjects. Those correlations were not observed in the NOR group while in SCOS group T/LH ratio correlated negatively only with AFIS ($p < 0.05$). In all the subjects, LC-score correlated negatively with STD ($p < 0.001$) and positively with AFIS ($p < 0.001$) but not with TM. There were no statistically significant

Table 1. Comparison of age, both testes volume and histological morphometric features between SCOS and NOR groups

	SCOS n = 49	NOR (control) n = 15
	Median (2.5–97.5 percentile)	
Age	31 (19.6–43.8)	29.5 (23.4–38.2)
Both testes volume [mL]	**16.0 (5.7–30.0)**[a]	30.0 (22.8–40.6)
Morphometry		
STD [μm]	**141.7 (93.4–187.8)**[a]	190.2 (178.0–224.1)
TM [μm]	**9.8 (5.7–17.5)**[a]	6.4 (4.6–9.8)
AFIS (%)	**47.6 (25.3–79.6)**[a]	27.6 (20.3–39.6)
LC-score (points)	**2.2 (1.0–4.0)**[a]	1.1 (1.0–1.8)

SCOS — Sertoli cell-only syndrome; NOR — normal spermatogenesis; STD — seminiferous tubule diameter; TM — tubular membrane thickness; AFIS — areal fraction of intertubular spaces; LC — Leydig cells; [a]p < 0.001; SCOS *vs.* NOR (Mann-Whitney U test)

Table 2. Comparison of serum hormonal profile between SCOS and NOR groups

	SCOS n = 40	NOR (control) n = 15
	Median (2.5–97.5 percentile)	
FSH [mIU/mL]	**19.9 (7.1–34.4)**[a]	3.4 (1.8–6.4)
LH [mIU/mL]	**7.1 (2.2–26.3)**[a]	4.2 (2.4–6.4)
Testosterone (T) nmol/L	14.6 (7.8–27.4)	13.2 (8.5–25.7)
T/LH ratio	2.3 (0.3–5.3)a	3.8 (2.3–6.6)

SCOS — Sertoli cell-only syndrome; NOR — normal spermatogenesis; [a]p — < 0.001 — SCOS *vs.* NOR (Mann-Whitney U test)

Table 3. Spearman's rank correlations (r_s) between morphometric features, hormone values and parameters of Leydig cell dysfunction in all subjects, SCOS and NOR groups

	Total			
n = 55	**STD [μm]**	**TM [μm]**	**AFIS (%)**	**LC-score**
FSH [mIU/mL]	**–0.61**[c]	**0.53**[c]	**0.53**[c]	**0.50**[c]
LH [mIU/mL]	**–0.30**[c]	**0.37**[c]	**0.46**[c]	**0.47**[c]
Testosterone (T) [nmol/L]	–0.01	–0.10	–0.01	0.19
T/LH ratio	**0.22**[a]	**–0.34**[c]	**–0.42**[c]	**–0.26**[b]
LC-score	**–058**[c]	0.21	**0.40**[c]	–
	NOR (control)			
n = 15	**STD [μm]**	**TM [μm]**	**AFIS (%)**	**LC-score**
FSH [mIU/mL]	0.17	–0.06	**0.53**[a]	–0.33
LH [mIU/mL]	–0.51	0.05	0.21	0.15
Testosterone (T) [nmol/L]	–0.16	–0.39	0.26	0.02
T/LH ratio	0.33	–0.34	0.30	0.09
LC-score	–0.40	0.01	–0.04	**–**
	SCOS			
n = 40	**STD [μm]**	**TM [μm]**	**AFIS (%)**	**LC-score**
FSH [mIU/mL]	–0.19	0.17	**0.41**[a]	**0.40**[a]
LH [mIU/mL]	–0.12	0.31	**0.37**[a]	**0.40**[a]
Testosterone (T) [nmol/L]	–0.015	–0.04	–0.05	0.17
T/LH ratio	0.02	–0.25	**–0.36**[a]	–0.19
LC-score	**–0.48**[c]	0.06	0.28	–

SCOS — Sertoli cells only syndrome; NOR — normal spermatogenesis; STD — seminiferous tubule diameter; TM — tubular membrane thickness; AFIS — areal fraction of intertubular space; LC — Leydig cells; [a]p < 0.05; [b]p < 0.01; [c]p < 0.001

correlations between LC-score and morphometric features in control group, while in SCOS LC-score negatively correlated with STD (p < 0.001) but not with AFIS or TM; however, the correlation between AFIS and LC-score was close to statistical significance (p < 0.056) (Table 3). Additionally, STD correlated negatively with AFIS (r = –0.61, p < 0.001) in the whole group and this association was also noticed in

SCOS group ($r = -0.43$, $p < 0.002$), but not in the NOR group.

Discussion

In the present study we performed histological evaluation of testicular tissue with the pattern of SCOS and normal spermatogenesis focusing on detailed assessment of morphometric features of seminiferous tubules and intertubular space, as well as Leydig cell function. Moreover, we looked for associations between analyzed histological parameters and hormonal profile of the subjects.

As expected, the majority of our SCOS subjects had evident signs of testicular impairment presented by increased FSH and LH serum levels. We did not observed any abnormal levels of T when compared with men presenting normal spermatogenesis. Some earlier studies reported decreased serum levels of T in men with infertility; however, in most of those studies the patients were recruited by their seminal parameters or fertility status [14, 24, 25]. Similarly to our results, the decrease in T levels was not found in some other studies, where the subjects were selected and grouped according to histological pattern of testicular biopsy [7, 12, 16, 26]. The observed discrepancies may be explained by the fact that there is an extensive overlap between fertile and infertile men hormones' levels which may mask, to some extent, the differences between studied groups depending on selection criteria. Moreover, it appears that in some cases a type of control group may also be the reason for the discrepancies (seminal normozoospermia *vs* obstructive azoospermia with normal spermatogenesis in histological evaluation) [12]. We cannot also exclude that our group of patients, similarly to those in other histological studies mentioned above, is too small to reveal some minor differences between groups, which have been shown in larger populations [14].

However, despite the lack of differences in T levels between groups in the present study, we observed prominent decrease in T/LH ratio in SCOS group. This finding is in line with previous observations that impaired spermatogenesis is associated with decreased T/LH ratio, which is believed to be a result of Leydig cell dysfunction manifested by increased LH level and low-normal or decreased T level [7, 14–16, 24, 26–28].

It is well documented, that in the testes with disturbed spermatogenesis the increase in Leydig cell number may be observed [7, 12, 15]. There is evidence from animal models that increased number and impaired function of Leydig cells present in adulthood are the result of disturbed testicular organogenesis due to exposure to endocrine disruptors during fetal life [29, 30]. Thus, it has been suggested that in some of the infertile men the impaired function of Leydig cells as well as their hyperplasia may be symptoms of testicular dysgenesis [14, 15].

Apart from the increased number of Leydig cells and the hormonal symptoms of their functional impairment, features of disturbed testicular organogenesis may be also observed [19, 31, 32]. In the present study we have shown that morphometric features of testicular dysgenesis were present in 25% of testes with SCOS. The incidence of decreased STD or increased AFIS were the most frequent and constituted more than 60% of all cases and in 43% they appeared concomitantly.

It was shown previously that the degree of spermatogenic impairment correlates with the prevalence of dysgenetic features such as decreased STD, increased TM, AFIS and increased number of Leydig cells [19]. We observed that the increased TM was seen in almost half of the testes with SCOS. The results are in line with previous studies reporting that impaired spermatogenesis is associated with alterations of TM thickness due to increased accumulation of extracellular matrix and that the degree of the pathology correlates well with disturbances of spermatogenesis [33–36]. There are reports that thickening of the lamina propria is not secondary to germ cell loss and it seems to be always associated with the maturation of Sertoli cells, like in human cryptorchid testes or in Klinefelter syndrome [37, 38]. In dysgenetic testes preserved until adulthood the thickness of TM increases with the advancing age, while STD remains at the pre-pubertal level [19]. In cryptorchid testes the thickening of TM was observed already in 1–3-year-old boys, and it was associated with the inhibited maturation and disturbed functional relationships between Sertoli, Leydig and peritubular cells [39, 40]. The thickening of TM was also reported in patients suffering from seminoma, varicocele, orchitis or cancer of the prostate [35, 38, 41].

We also found increased point value of LC-score in SCOS in comparison with NOR group. Moreover, LC-score correlated positively with LH serum levels and negatively with T/LH ratio (when considered all subjects), what suggests a possible impairment of Leydig cell function, in line with previous reports [7, 12, 15]. It was suggested that impairment of spermatogenesis and Leydig cell function might reflect disturbed paracrine communication between the seminiferous epithelium and the Leydig cells, triggered by distorted function of the seminiferous epithelium, specifically Sertoli cells. However, it cannot be excluded that the parallel impairment of spermatogenesis and Leydig cells may reflect a congenital dysfunction of both

compartments caused by testicular dysgenesis during fetal/infant development [14]. It is hypothesized that the increased number of Leydig cells per clusters in biopsies with impaired spermatogenesis may be the result of smaller STD and thus 'shrinkage' of tubular compartment resulting in regrouping of Leydig cell to form larger cluster [15]. In such situation we should expect that concomitantly with decreased STD due to the impairment of spermatogenesis an increased AFIS might be seen with increased Leydig cell number. In fact, in majority of our SCOS biopsies (81%) presenting decreased STD and increased AFIS, we found an abnormal LC-score, which may support this hypothesis. However, there is still 19% of the SCOS biopsies where despite of decreased STD and increased AFIS the LC-score was normal. However, there is another possible explanation of increased Leydig cell number per cluster present in testes with impaired spermatogenesis. One can assume that it may be the result of prolonged proliferation of these cells during development caused probably by a lack of paracrine communication between impaired seminiferous epithelium and Leydig cells, with the secondary LH increase causing hyperstimulation of LCs [15]. Indeed, we observed that there are still some biopsies (40%) where despite increased LC-score only one from the morphometric parameters (AFIS or STD) was abnormal, suggesting that in these cases the formation of larger cluster of Leydig cells might not be connected with 'shrinkage' of tubular compartment. Moreover, we found that in all cases the LC-score negatively correlated with STD and, consequently, positively with AFIS. However, in SCOS group only the correlation between STD and LC-score was consistently observed. It may suggest that in some of the SCOS biopsies the presence of wide intertubular space may be an independent feature of disturbed testicular organogenesis. In addition, the presence of higher AFIS correlated positively with FSH levels in both study groups, while the positive correlation with LH and negative with T/LH was observed only in SCOS group.

In conclusion, we have shown that substantial number of testes from subjects with SCOS presented abnormal morphometric features which are recognized as the signs of testicular dysgenesis. Additionally, the finding of increased number of Leydig cells simultaneously with abnormal T/LH ratio suggests impaired function of these cells. Increased serum levels of LH, and also FSH, may reflect Leydig cells dysfunction. It seems that reproductive hormones levels reflect also the condition of testicular structure, and that FSH may be related to the changes in intertubular space area independently of impaired Leydig cell function.

Acknowledgments

This study was supported by grants funded by the National Science Centre, Poland (Grant number UMO-2014/13/B/NZ4/01198) and the Medical University of Lodz, Poland (Grant number: 503/1-089-03/503-11-002).

Competing interests

The authors declare that they have no competing interests.

Authors' contributions

DA wrote the draft of the manuscript; performed histological analysis of the biopsy, statistical analysis and interpretation of the results (a part of the results presented in the article were used in DA's Master Thesis, Medical University of Lodz; Faculty of Pharmacy; Department of Laboratory Medicine); JSH conceived and designed the study, analyzed clinical data, contributed in interpretation of the results, critically revised the manuscript; KM gave an intellectual content in preparing the manuscript; RWJ conceived and designed the study, performed histological analysis of the biopsy, statistical analysis and interpretation of the results, critically revised the manuscript. All authors read and approved the final manuscript.

References

1. Jungwirth A, Giwercman A, Tournaye H, et al. European Association of Urology Guidelines on Male Infertility: The 2012 Update. Eur Urol. 2012; 62(2): 324–332, doi: 10.1016/j.eururo.2012.04.048, indexed in Pubmed: PMID: 22591628.
2. Krausz C. Male infertility: Pathogenesis and clinical diagnosis. Best Pract Res Clin Endocrinol Metab. 2011; 25(2): 271–285, doi: 10.1016/j.beem.2010.08.006, indexed in Pubmed: 21397198.
3. Walczak-Jedrzejowska R, Wolski J, Slowikowska-Hilczer J. The role of oxidative stress and antioxidants in male fertility. Cent European J Urol. 2013; 65: 60–67, doi: 10.5173/ceju.2013.01.art19, indexed in Pubmed: 24578993.
4. Gill K, Jakubik J, Kups M, et al. The impact of sedentary work on sperm nuclear DNA integrity. Folia Histochem Cytobiol. 2015, doi: 10.5603/fhc.a2019.0002, indexed in Pubmed: 30869154.
5. Shi H, Liu J, Zhu P, et al. Expression of peroxiredoxins in the human testis, epididymis and spermatozoa and their role in preventing H2O2-induced damage to spermatozoa. Folia Histochem Cytobiol. 2018; 56(3): 141–150, doi: 10.5603/fhc.a2018.0019, indexed in Pubmed: 30187908.
6. Rajert-De Me, Grigor K, Skakkebaek N. Histoathological Evaluation of Testicular Biosy. In: Lenzi A, Simoni M, Huhtaniemi I, editors. Endocrinology of the Testis and Male Reroduction. Endocrinology. Cham, Switzerland: Sringer; 2017: 623–642.

7. Lardone MC, Piottante A, Valdevenito R, et al. Histological and hormonal testicular function in oligo/azoospermic infertile men. Andrologia. 2012; 45(6): 379–385, doi: 10.1111/and.12026, indexed in Pubmed: 23013062.
8. Halder A, Jain M, Kumar P. Primary Testicular Failure: An Overview. J Clin Diag Res. 2015; 3: 1–5, doi: 10.4172/2376-0311.1000e105.
9. Jain M, Kumar P, Iyer V, et al. Primary Testicular Failure. Basics of Human Andrology. 2017: 417–436, doi: 10.1007/978-981-10-3695-8_24.
10. Cheng Y, Chung C, Chen C, et al. Differential expression of microRNAs and their messengerRNA targets in men with normal spermatogenesis versus Sertoli cell-only syndrome. Urol Sci. 2017; 28(1): 42–49, doi: 10.1016/j.urols.2016.03.002.
11. Stouffs K, Gheldof A, Tournaye H, et al. Sertoli Cell-Only Syndrome: Behind the Genetic Scenes. BioMed Res Int. 2016; 2016: 1–7, doi: 10.1155/2016/6191307, indexed in Pubmed: 26925412.
12. Lardone MC, Castillo P, Valdevenito R, et al. P450-aromatase activity and expression in human testicular tissues with severe spermatogenic failure. Int J Androl. 2010; 33: 650-660, doi: 10.1111/j.1365-2605.2009.01002.x, indexed in Pubmed: 19906189.
13. Matsumoto AM, Bremner WJ, et al. Testicular disorders. In: Melmed S, Polonsky KS, Larsen PR, , editors. Williams Textbook of Endocrinology. 13 ed: Elsevier; 2017: 694–708.
14. Andersson AM, Jørgensen N, Frydelund-Larsen L, et al. Impaired Leydig Cell Function in Infertile Men: A Study of 357 Idiopathic Infertile Men and 318 Proven Fertile Controls. J Clin Endocrinol Metab. 2004; 89(7): 3161–3167, doi: 10.1210/jc.2003-031786, indexed in Pubmed: 15240588.
15. Holm M, Meyts ERD, Andersson AM, et al. Leydig cell micronodules are a common finding in testicular biopsies from men with impaired spermatogenesis and are associated with decreased testosterone/LH ratio. J Pathol. 2003; 199(3): 378––386, doi: 10.1002/path.1309, indexed in Pubmed: 12579540.
16. Lardone MC, Argandona F, Florez M, et al. Overexpression of CYP19A1 aromatase in Leydig cells is associated with steroidogenic dysfunction in subjects with Sertoli cell-only syndrome. Andrology. 2017; 5: 41-48, doi: 10.1111/andr.12289, indexed in Pubmed: 27769104.
17. Toppari J, Skakkebk N. Sexual differentiation and environmental endocrine disrupters. Baillieres Clin Endocrinol Metab. 1998; 12(1): 143–156, doi: 10.1016/s0950-351x(98)80529-6, indexed in Pubmed: 9890066.
18. Sharpe R. The ‚oestrogen hypothesis'- where do we stand now?1. Int J Androl. 2003; 26(1): 2–15, doi: 10.1046/j.1365-2605.2003.00367.x, indexed in Pubmed: 12534932.
19. Guminska A, Oszukowska E, Kuzanski W, et al. Less advanced testicular dysgenesis is associated by a higher prevalence of germ cell neoplasia. Int J Androl. 2009; 33(1): e153–e162, doi: 10.1111/j.1365-2605.2009.00981.x, indexed in Pubmed: 19719533.
20. Hoei-Hansen C, Holm M, Meyts ERD, et al. Histological evidence of testicular dysgenesis in contralateral biopsies from 218 patients with testicular germ cell cancer. J Pathol. 2003; 200(3): 370–374, doi: 10.1002/path.1372, indexed in Pubmed: 12845633.
21. Holstein AF, Roosen-Runge EC, Schirren CS. The testis biopsy. In: Holstein AF, Roosen-Runge EC, Schirren CS, editors. llustrated Pathology of Human Testes. Berlin: Grosse Verlag; 1988: 58–76.
22. Weinbauer GF, Gromoll J, Simoni M, et al. Physiology of testicular function. Andrology. Male Reroductive Health and Dysfunction. Berlin, Heidelberg, New York.: Sringer Verlag; 2010: 25–60.
23. Guminska A, Slowikowska-Hilczer J, Kuzanski W, et al. Features of impaired seminiferous tubule differentiation are associated with germ cell neoplasia in adult men surgically treated in childhood because of cryptorchidism. Folia Histochem Cytobiol. 2007; 45 : S163-168, doi: https://www.ncbi.nlm.nih. gov/pubmed/18292827, indexed in Pubmed; 18292827.
24. Giagulli VA, Vermeulen A. Leydig cell function in infertile men with idiopathic oligospermic infertility. J Clin Endocrinol Metab. 1988; 66(1): 62–67, doi: 10.1210/jcem-66-1-62, indexed in Pubmed: 2891722.
25. Bruno B, Villa S, Properzi G, et al. Hormonal and seminal parameters in infertile men. Andrologia. 2009; 18(6): 595–600, doi: 10.1111/j.1439-0272.1986.tb01837.x, indexed in Pubmed: 3101547.
26. Parada-Bustamante A, Molina C, Valencia C, et al. Disturbed testicular expression of the estrogen-metabolizing enzymes CYP1A1 and COMT in infertile men with primary spermatogenic failure: possible negative implications on Sertoli cells. Andrology. 2017; 5(3): 486–494, doi: 10.1111/andr.12346, indexed in Pubmed: 28334509.
27. Glass AR, Vigersky RA. Leydig cell function in idiopathic oligospermia. Fertil Steril. 1980; 34: 144-148, doi: https://www.ncbi.nlm.nih. gov/pubmed/6773819, indexed in Pubmed; 6773819.
28. Lardone MC, Argandoña F, Lorca M, et al. Leydig cell dysfunction is associated with post-transcriptional deregulation of CYP17A1 in men with Sertoli cell-only syndrome. MHR: Basic science of reproductive medicine. 2018; 24(4): 203–210, doi: 10.1093/molehr/gay006, indexed in Pubmed: 29438521.
29. Fisher JS. Human ‚testicular dysgenesis syndrome': a possible model using in-utero exposure of the rat to dibutyl phthalate. Hum Reprod. 2003; 18(7): 1383–1394, doi: 10.1093/humrep/deg273, indexed in Pubmed: 12832361.
30. Foster P. Effects of phthalate esters on the developing reproductive tract of male rats. Hum Reprod Update. 2001; 7(3): 231–235, doi: 10.1093/humupd/7.3.231, indexed in Pubmed: 11392369.
31. Chemes H, Muzulin P, Venara M, et al. Early manifestations of testicular dysgenesis in children: pathological phenotypes, karyotype correlations and precursor stages of tumour development. APMIS. 2003; 111(1): 12–24, doi: 10.1034/j.1600-0463.2003.1110104.x, indexed in Pubmed: 12760349.
32. Cools M, Aerde Kv, Kersemaekers AM, et al. Morphological and Immunohistochemical Differences between Gonadal Maturation Delay and Early Germ Cell Neoplasia in Patients with Undervirilization Syndromes. J Clin Endocrinol Metab. 2005; 90(9): 5295–5303, doi: 10.1210/jc.2005-0139, indexed in Pubmed: 15998778.
33. Sato Y, Nozawa S, Iwamoto T. Study of spermatogenesis and thickening of lamina propria in the human seminiferous tubules. Fertil Steril. 2008; 90(4): 1310–1312, doi: 10.1016/j.fertnstert.2007.10.019, indexed in Pubmed: 18304550.
34. Albrecht M. Insights into the nature of human testicular peritubular cells. Ann Anat. 2009; 191(6): 532–540, doi: 10.1016/j.aanat.2009.08.002, indexed in Pubmed: 19765961.
35. Volkmann J, Muller D, Feuerstacke C, et al. Disturbed spermatogenesis associated with thickened lamina propria of seminiferous tubules is not caused by dedifferentiation of myofibroblasts. Hum Reprod. 2011; 26(6): 1450–1461, doi: 10.1093/humrep/der077, indexed in Pubmed: 21467201.
36. Liu Y, Zhu Y, Di L, et al. Raman spectroscopy as an ex vivo noninvasive approach to distinguish complete and incom-

plete spermatogenesis within human seminiferous tubules. Fertil Steril. 2014; 102(1): 54–60.e2, doi: 10.1016/j.fertnstert.2014.03.035, indexed in Pubmed: 24767690.
37. Paniagua R, Martinez-Onsurbe P, Santamaria L, et al. Quantitative and ultrastructural alterations in the lamina propria and Sertoli cells in human cryptorchid testes. Int J Androl. 1990; 13(6): 470–487, doi: 10.1111/j.1365-2605.1990.tb01054.x, indexed in Pubmed: 1982882.
38. Martin R, Santamaría L, Nistal M, et al. The peritubular myofibroblasts in the testes from normal men and men with Klinefelter's syndrome. A quantitative, ultrastructural, and immunohistochemical study. J Pathol. 1992; 168(1): 59–66, doi: 10.1002/path.1711680111, indexed in Pubmed: 1453270.
39. Hadziselimovic F. Cryptorchidism. Ultrastructure of normal and cryptorchid testicular development. Berlin, Heidelberg, New York: Springer Verlag; 1977.
40. Müller J, Skakkebaek N. Abnormal Germ Cells in Maldescended Testes: A Study of Cell Density, Nuclear Size and Deoxyribonucleic Acid Content in Testicular Biopsies from 50 Boys. J Urol. 1984; 131(4): 730–733, doi: 10.1016/s0022-5347(17)50602-3, indexed in Pubmed: 6142966.
41. Santoro G, Romeo C, Impellizzeri P, et al. Ultrastructural and immunohistochemical study of basal lamina of the testis in adolescent varicocele. Fertil Steril. 2000; 73(4): 699–705, doi: 10.1016/s0015-0282(99)00611-1, indexed in Pubmed: 10731528.

Submitted: 24 February, 2020
Accepted after reviews: 12 May, 2020
Available as AoP: 2 June, 2020

FOLIA HISTOCHEMICA ET CYTOBIOLOGICA
Vol. 58, No. 2, 2020
pp. 83–89

ORIGINAL PAPER

VIA MEDICA

Expression of angiogenic factor with G patch and FHA domains 1 (AGGF1) in placenta from patients with preeclampsia

Lan-fen An, Shu-qi Chi, Jun Zhang, Hong-bo Wang*, Wei-xiang Ouyang*

Department of Obstetrics and Gynaecology, Union Hospital, Tongji Medical College, Huazhong University of Science and Technology, Wuhan 430022, China

Abstract

Introduction. Preeclampsia (PE) is a major contributor to maternal and foetal morbidity and mortality worldwide. It manifests as high blood pressure and proteinuria in women at more than 20 weeks of gestation. Abnormal levels of anti- and pro-angiogenesis factors are known to be associated with PE. In the present study, we aimed to determine the localisation of angiogenic factor with G patch and FHA domains 1 (AGGF1) in the placenta and to compare the expression levels of AGGF1 in the third-trimester placentas of preeclamptic and normotensive pregnancies.

Materials and methods. Placental tissue samples were collected from women with PE (n = 28) and without PE (n = 28). The normotensive controls without PE were matched for gestational age at delivery with the patients with PE. The expression levels of AGGF1 in the placental tissues were evaluated using immunohistochemistry, quantitative reverse transcription polymerase chain reaction and Western blot.

Results. The immunoexpression of AGGF1 was localised in the syncytiotrophoblast tissue. Notable, the mRNA and protein expression levels of AGGF1 were decreased in preeclamptic placentas as compared with the normotensive control group ($P < 0.05$).

Discussion. Our results suggest that the decreased AGGF1 in preeclamptic placentas may be related to the pathogenesis of preeclampsia. *(Folia Histochemica et Cytobiologica 2020, Vol. 58, No. 2, 83–89)*

Key words: angiogenesis; AGGF1; preeclampsia; placenta; syncytiotrophoblast; IHC; qPCR; WB

Introduction

Preeclampsia (PE), which affects 3–6% of all pregnancies, is a major contributor to maternal and foetal morbidity and mortality worldwide [1, 2]. It can be diagnosed by the combined presentation of high blood pressure and proteinuria after 20 weeks of gestation. The current definition of PE also includes maternal organ dysfunction [3, 4]. Despite advances in PE research, its aetiology and pathogenesis remain unclear [5].

Angiogenesis refers to the formation of new blood vessels from existing vasculature [6]. Placental angiogenesis can dramatically influence the outcome of pregnancies. During pregnancy, a vascular network is built between the mother and the foetus. Aberrant vascularization during this process may results in imbalance between pro-angiogenic and anti-angiogenic factors [7–10].

In pregnant women with PE, placental tissue overproduces two important anti-angiogenic proteins, which enter into maternal circulation: soluble endoglin (sEng) and soluble fms-like tyrosine kinase-1 (sFlt1). Furthermore, these patients have low circulat-

***Corresponding authors:** Wei-xiang Ouyang, Department of Obstetrics and Gynaecology, Union Hospital, Tongji Medical College, Huazhong University of Science and Technology, Wuhan, 430022, China
phone: +86-02785350522,
e-mail: oywx6222@163.com

***Co-Corresponding author:** Hong-bo Wang, Department of Obstetrics and Gynaecology, Union Hospital, Tongji Medical College, Huazhong University of Science and Technology, Wuhan, 430022, China
phone: +86-02785350617,
e-mail: hb_wang1969@sina.com

Table 1. Clinical characteristics of patients with preeclamptic and normotensive pregnancies

Parameters	Preeclamptic (n = 28)	Normotensive (n = 28)
Maternal age (years)	30.32 ± 5.54	29.86 ± 4.34
BMI in pregnancy [kg/m^2]	27.89 ± 3.25	26.58 ± 2.44
Gestational age (weeks)	36.77 ± 3.24	38.02 ± 1.07
SBP at delivery [mm Hg]	**155.9 ± 15.5***	113.8 ± 7.8
DBP at delivery [mm Hg]	**100.2 ± 21.4***	75.9 ± 7.50
Proteinuria†	**100% (28/28)***	0% (0/28)
Newborn weight [g]	**2683 ± 860***	3416 ± 289
1-Min Apgar score	**14.3% (4/28)***	0% (0/28)
5-Min Apgar score	**7.14% (2/28)***	0% (0/28)

Data are presented as mean ± SD or percentage (number/total). *P < 0.05 compared to normotensive control, Student's t-test. †Quantity of 24-hour protein excretion ≥ 300 mg/24 h is proteinuria positive and ≤ 300 mg/24 h is proteinuria negative. Abbreviations: BMI — body mass index in pregnancy; SBP — systolic blood pressure; DBP — diastolic blood pressure.

ing blood levels of two pro-angiogenic factors: vascular endothelial growth factor (VEGF) and placental growth factor (PlGF) [11, 12]. Zeisler *et al*. showed that the sFlt1/PlGF ratio is elevated in pregnant women before the clinical onset of PE. However, the predictive value of this ratio is not clear, although it can be used to predict the short-term absence of PE [13]. These angiogenesis factors are well-known biomarkers of PE and have been implicated in its pathophysiology [14, 15].

Angiogenic factor with G patch and FHA domains 1 (AGGF1, also known as VG5Q), a newly described angiogenic factor, is encoded on chromosome 5q13.3. The full-length AGGF1 complementary DNA (cDNA) encodes a protein with 714 amino acids, which contains a forkhead-associated domain (FHA), a G-patch domain, and a coiled-coil motif, the functions of these domains are unknown [16, 17]. Recent studies have shown that the purified AGGF1 protein can promote angiogenesis as potently as VEGF in chick embryos, and that the knockdown of AGGF1 expression can inhibit endothelial vessel formation [18, 19]. However, whether AGGF1 plays a role in the development of preeclampsia remains to be addressed.

The roles of many angiogenic factors in the development of PE have aroused wide concern in the past few decades. However, the expression pattern of AGGF1 in the placenta has not been investigated yet. In this study, we aimed to investigate the localisation of AGGF1 expression in the placenta and to analyse the difference in the expression patterns of AGGF1 in third-trimester placentas from preeclamptic and normotensive pregnancies.

Materials and methods

Ethical approval. The protocols for this study were approved by the Ethics Committee of Union Hospital, Tongji Medical College, Huazhong University of Science and Technology, Wuhan, China. All patient-derived tissue samples were obtained after receiving informed written consent from the patients.

Study populations. All placentas were obtained after caesarean sections performed at the Union Hospital between January 2016 and December 2016. The study groups consisted of 28 preeclamptic pregnancies and 28 normotensive pregnancies. All participants were at more than 28 weeks of gestation. PE is traditionally diagnosed if the patient presents with hypertension (blood pressure ≥ 140/90 mmHg) and proteinuria (≥ 300 mg/24 h) after week 20 of gestation. In the absence of proteinuria, hypertension combined with maternal organ dysfunction, such as thrombocytopenia, liver involvement, renal insufficiency, pulmonary oedema, or new-onset cerebral or visual symptoms can also be diagnosed with PE [3, 4]. Exclusion criteria for patients in this study included multiple pregnancies, tobacco use, cardiovascular diseases, diabetes mellitus, rupture of membranes, foetal structural or genetic anomalies, blood diseases, severe pre-existing metabolic disorders, and infectious diseases. Controls were normotensive women without any pregnancy-related complications or chronic problems. The clinical characteristics of the patients are summarized in Table 1.

Sample collection and preparation. Immediately after caesarean section, placental tissue (~10 g each) was collected from the area around the umbilical cord attachment site by cutting a vertical plane through the full thickness of an

apparently normal area, including both the maternal and foetal surfaces. Tissues with calcification or clots were excluded. The collected tissues were washed with sterile phosphate-buffered saline (PBS) and placed in 10% formalin and embedded in paraffin for immunohistochemical (IHC) analysis. The remaining parts of the placental segments were aliquoted and stored at –80°C for RNA and protein extraction.

Immunohistochemistry. The expression patterns of AGGF1 in the placental tissues were evaluated. The placental tissues embedded in paraffin were sectioned into slices 4 μm thick and incubated with rabbit polyclonal antibodies against AGGF1 (5.0 μg/ml; Abcam, Cambridge, MA, USA). The sections were then deparaffinised and rehydrated in graded ethanol before antigen retrieval was performed in citrate buffer (pH 6.0) for 3 min at full pressure using a pressure cooker. To inhibit the activity of endogenous peroxidase, the sections were then treated with 3% hydrogen peroxide for 5 min. Next, blocking was performed by incubating the sections in a solution of 0.01 mol/L Tris, 0.3% Triton X-100, and 10% normal goat serum for 30 min, after which they were incubated overnight at 4 °C with the primary antibody. After rinsing in phosphate-buffered saline (PBS), the sections were incubated with peroxidase-labelled anti-rabbit immunoglobulin G (IgG) for 30 min. Finally, all slides were incubated with DAB (Beyotime, Shanghai, China) before being rinsed with distilled water, counterstained with haematoxylin, dehydrated, and mounted. A Motic microscope (Motic, Xiamen, China) was used to visualise and photograph the slides. Semiquantitative evaluation of immunohistochemical (IHC) reaction was performed by two observers who were blinded to the identity of the slides. Remmele and Schicketanz immunoreactive score (IRS) and IHC score (IHS) were selected to analyse the data [20]. The IHSs were determined based on the staining intensity (SI) and the percentage of immunoreactive cells (PR). The SI scale was divided into four categories (0 = no staining, 1 = weak staining, 2 = moderate staining, and 3 = strong staining), and the PR scale was divided into five categories (0 = no staining, 1 = 1–10% staining, 2 = 11–50% staining, 3 = 51–80% staining, and 4 = 81–100% staining). A final semiquantitative score ranging from 0 to 12 points was calculated for each sample. Samples with IHS above 4 were considered positive, and those with IHS below 4 were considered negative.

RNA isolation and quantitative reverse transcription polymerase chain reaction (qRT-PCR). Total RNA was isolated from the placental tissues using RNAiso Plus (TaKaRa, Tokyo, Japan), according to the manufacturer's protocol. The RNA quality and purity were determined spectrophotometrically (NanoDrop; Thermo Fisher Scientific, CA, USA). Samples with optical density$_{260/280}$ ratios between 1.8 and 2.0 were chosen for the subsequent steps. One microgram of total RNA from each sample was reverse transcribed into cDNA in a 20-μl using PrimeScript™ RT Master Mix (TaKaRa), which was stored at –20°C for further analysis. Quantitative PCR was performed using the cDNA as the template. SYBR Premix Ex Taq II (TaKaRa) was used for the PCR. Each reaction mixture contained 5 μl 2× SYBR Taq II, 0.2 μM forward PCR primer, 0.2 μM reverse PCR primer, 0.2 μl 50 × ROX reference dye, 1 μl cDNA, and 3.4 μl sterile distilled water for a final volume of 10 μl. The qRT-PCR was performed using the pre-set PCR program in StepOnePlus™ Real-Time PCR System (Applied Biosystems, Waltham, MA, USA) to quantify mRNA expression levels, with GAPDH as internal control. Primers for the RT-PCRs were synthesized based on the GenBank database. The primer sequences were: GAPDH, forward primer: 5'-ACCACAGTCCATGCCATCAC-3', reverse primer: 5'-TCCACCACCCTGTTGCTGTA-3'; AGGF1, forward primer: 5'-AAACGTAGGAGCAGGTTGG-3', reverse primer: 5'-TGAGGATGGTTTGCCTGTCC-3'. The qRT-PCR consisted of a denaturation step at 95°C for 30 s, 40 cycles of an annealing step (95°C for 5 s, 65°C for 30 s, and 60°C for 45 s), and an extension step at 72°C for 60 s. The expression of target genes was established using the comparative cycle threshold (Ct; $2^{-\Delta\Delta CT}$) method.

Western blot. The placental tissues were homogenized on ice for 30 min in pre-cooled RIPA buffer. The homogenates were centrifuged at 12000 *g* for 15 min at 4°C and the supernatants were collected. After isolating the protein from the tissues, the concentration of lysates was determined in the samples using a bicinchoninic acid protein assay kit (Beyotime). After boiling the samples for 10 min, equal amounts of the proteins (30 μg) were separated using 10% SDS-PAGE and transferred to 0.45-μm polyvinyl difluoride (PVDF) membranes in 20% methanol and 0.1% SDS. These mixtures were then blocked for 1 h at room temperature with 0.1% TBST (20 mM Tris-HCL, 500 mM NaCl, and 0.05% Tween 20 at pH 7.5) with 5% fat-free dried milk power. The membranes were then separately incubated overnight at 4°C with rabbit polyclonal AGGF1 antibody (1.0 μg/ml; Abcam), and rabbit monoclonal GAPDH antibody (0.33 μg/ml; Affinity, Cincinnati, OH, USA). After washing and incubation with the secondary anti-rabbit antibody (0.2 μg/ml; Affinity) for 1 h at room temperature, the membranes were washed again and visualised using ECL-PLUS (Amersham Biosciences, Uppsala, Sweden). Finally, the intensity of the bands obtained was quantified using Image-Pro Plus (Media Cybernetics, Rockville, MD, USA).

Statistical analysis. All the data obtained were normally distributed, and all statistical analyses were performed

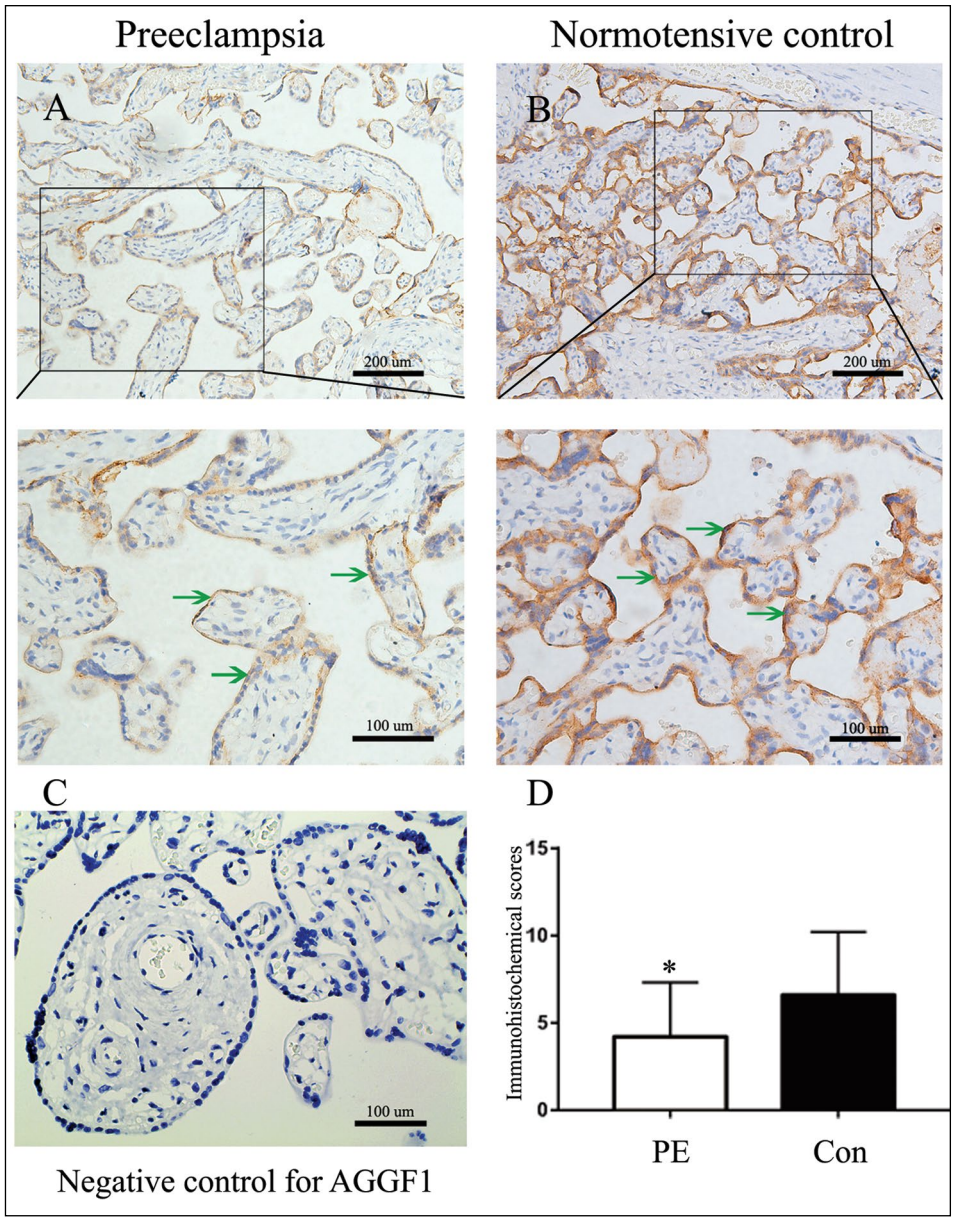

Figure 1. AGGF1 immunoreactivity in human placenta. Immunolocalisation of AGGF1 in placentas of patients with preeclampsia (**A**) and normotensive patients (**B**). (**C**). No AGGF1 immunoreactivity in tissue section of a patient with preeclampsia. (**D**). Immunohistochemical scores of AGGF1 in placentas of patients with preeclampsia (PE) and normotensive patients (Con) (4.21 ± 3.11 *vs*. 6.61 ± 3.59, respectively). Green arrows indicate syncytiotrophoblasts. The AGGF1 localises in the syncytiotrophoblastic layer of placental villi. *P = 0.0101, PE *vs.* Con. AGGF1 — Angiogenic factor with G patch and FHA domains 1.

using GraphPad Prism 5 (GraphPad Software Inc., San Diego, CA, USA). The results were presented as mean ± standard deviation (SD). Comparisons between groups were performed using Student's t-test. The chi-square test was used to analyse categorical variables. Statistical significance was defined as $P < 0.05$.

Results

Twenty-eight paired tissue samples were analysed by immunohistochemistry for AGGF1 expression. AGGF1 expression was localised in syncytiotrophoblasts. Positive expression of AGGF1 was found in both normotensive (18/28) and preeclamptic (9/28) samples. The immunohistochemical expression of AGGF1 in 32% of preeclamptic placentas (Fig. 1A) were dramatically decreased ($P < 0.05$) than those in normotensive ones (Fig. 1B). However, the majority (68%) of patients with preeclampsia did present AGGF1 immunoreactivity (Fig. 1C). Immunohistochemical scores of AGGF1 in two groups were shown in Figure 1D.

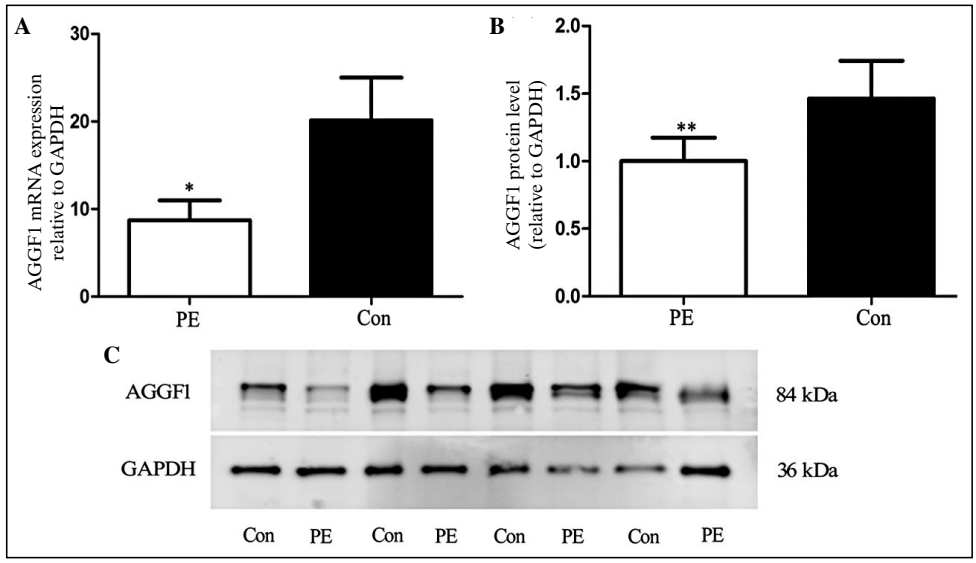

Figure 2. mRNA and protein expression levels of AGGF1 in placental tissues of patients with preeclampsia (PE) and normotensive patients (Con) assessed by qRT-PCR and Western blot. **A**. AGGF1 mRNA levels were lower in preeclamptic than control placentas (8.70 ± 2.28 *vs*. 20.13 ± 4.88 respectively, P = 0.0385). **B**. AGGF1 protein levels, as assessed by Western blot, were lower in preeclamptic than control placentas (1.00 ± 0.08 *vs.* 1.46 ± 0.14, respectively, P = 0.0054). **C**. Representative Western blots show the expression levels of AGGF1 protein in the studied groups. Bands were observed at 84 and 36 kDa, corresponding to the sizes of AGGF1 and GAPDH, respectively. *P < 0.05; **P < 0.01, preeclamptic placenta tissue (PE) *vs.* normotensive placenta tissue (Con).

The mRNA levels of total AGGF1 were also significantly decreased in the PE group than in the normotensive controls (Fig. 2A). The presence of the AGGF1 protein in placental tissues was determined by Western blot (Fig. 2B). The AGGF1 antibody detected one major band at approximately 84 kDa, which is similar to the reported molecular weight of AGGF1 (Fig. 2C) [19]. Protein levels of AGGF1 were lower (P < 0.05) in preeclamptic placentas than in normotensive ones.

Discussion

The gene encoding AGGF1 has been discovered in 2004 [19], and its physiological relevance needs to be further studied, especially in relation to PE. In the present study, we demonstrated that AGGF1 expression was localised by immunohistochemistry in the syncytiotrophoblasts of 64.3% of normotensive term placenta and 32.1% of preeclamptic placenta. Moreover, the mRNA and protein expression levels of AGGF1 were significantly lower in placental tissues from pregnancies complicated with PE than in those from normotensive pregnancies in the whole studied groups of patients.

Placental development involves the cooperation and proper functioning of various cell types [21]. Trophoblast tissue, the most critical component of placenta, acts as the interface between foetal and maternal tissues. Both cytotrophoblast's cells and syncytiotrophoblast of the placental villi release numerous angiogenic factors and present also their receptors [22].

Decreased AGGF1 expression in preeclamptic syncytiotrophoblast tissue of some preeclampsia patients may not be a specific characteristic of PE, but it is possibly associated with abnormal placental ischaemia and hypoxia in PE patients. Hypoxic regions are known to exist in and be important for the pathology of many diseases, including preeclampsia [23–25]. Placental ischaemia is considered a major pathogenic mechanism underlying PE and is known to result in hypoxia [26]. The ability of cells to adapt to hypoxia is important for survival in both physiological and pathophysiological states [27, 28].

Xu *et al*. reported that AGGF1 was down-regulated in human high-grade urothelial cancer cells after exposure to hypoxia, and this down-regulation may partly reduce hypoxia-induced apoptosis of the cancer cells [29]. However, the mRNA levels of AGGF1 were not different in hypoxic and normoxic conditions in cell cultures [29]. Conversely, Lu *et al*. reported that AGGF1 expression increased in response to hypoxia in endothelial cells that isolated from mouse hearts, which suggested that ischaemia induced AGGF1 expression in myocardial infarction mouse model [30]. Wang *et al*. reported that AGGF1 expression was up-regulated in hepatocellular carcinomas (HCCs),

compared to adjacent non-cancerous tissues and that a significant correlation (r = 0.548, 70 cases) was found between tumoural expression of VEGF and AGGF1 [31]. It has to be noted that these observations may be related to different cell types in various diseases or experimental models.

Our immunohistochemical analysis showed that the expression of AGGF1 was confined to the syncytiotrophoblast and was absent in the endothelial cells of the placenta. Previous studies have detected the AGGF1 protein in human umbilical vein endothelial cells and human microvascular endothelial cells [19]. AGGF1 is also known to be expressed in ovarian cancer cells, vascular smooth muscle cells, osteoblasts, HCCs, and human heart fibroblasts [19, 31]. In this study, we found no expression of AGGF1 in the endothelial cells of the placenta. This may be due to a differential expression in various organs or to the sensitivity of the technique.

Besides angiogenesis, AGGF1 has been suggested to be involved in multiple other functions. It has been suggested that AGGF1 can fully reverse the effects of hyperglycaemia on endothelial progenitor cells [32]. AGGF1 may also inhibit TNF-α-mediated monocyte adhesion to endothelial cells and affect the expression of adhesion molecules and chemokines [17]. In addition, AGGF1 has been shown to have anti-inflammatory effects, both *in vitro* and *in vivo*. As an anti-inflammatory agent, AGGF1 has been associated with TNF-alpha-induced endothelial activation and the regulation of liver fibrosis *via* TGF-beta signalling modulation [17, 33].

In summary, we preliminarily demonstrated that the AGGF1 expression was decreased in third-trimester preeclamptic placenta compared with normotensive term placenta. The exact role of decreased AGGF1 expression in PE remains unclear, and the molecular mechanisms remain to be defined.

Acknowledgments

We would like to thank all colleagues at Obstetrics and Gynaecology in the Union Hospital for sample collection. We have no financial relationships with any biotechnology, pharmaceutical, or other commercial entities that may be construed to have an interest in the subject matter or materials discussed in the manuscript.

The authors declare that they have no conflicts of interest related to this study.

References

1. Ananth CV, Keyes KM, Wapner RJ. Pre-eclampsia rates in the United States, 1980-2010: age-period-cohort analysis. BMJ. 2013; 347: f6564, doi: 10.1136/bmj.f6564, indexed in Pubmed: 24201165.
2. Saleem S, McClure EM, Goudar SS, et al. Global Network Maternal Newborn Health Registry Study Investigators. A prospective study of maternal, fetal and neonatal deaths in low- and middle-income countries. Bull World Health Organ. 2014; 92(8): 605–612, doi: 10.2471/BLT.13.127464, indexed in Pubmed: 25177075.
3. Mol B, Roberts C, Thangaratinam S, et al. Pre-eclampsia. The Lancet. 2016; 387(10022): 999–1011, doi: 10.1016/s0140-6736(15)00070-7.
4. American College of Obstetricians and Gynecologists, Task Force on Hypertension in Pregnancy. Hypertension in pregnancy. Report of the American College of Obstetricians and Gynecologists' Task Force on Hypertension in Pregnancy. Obstet Gynecol. 2013; 122(5): 1122–1131, doi: 10.1097/01.AOG.0000437382.03963.88, indexed in Pubmed: 24150027.
5. Hung TH, Skepper JN, Charnock-Jones DS, et al. Hypoxia-reoxygenation: a potent inducer of apoptotic changes in the human placenta and possible etiological factor in preeclampsia. Circ Res. 2002; 90(12): 1274–1281, doi: 10.1161/01.res.0000024411.22110.aa, indexed in Pubmed: 12089065.
6. Pratt A, Da Silva Costa F, Borg AJ, et al. Placenta-derived angiogenic proteins and their contribution to the pathogenesis of preeclampsia. Angiogenesis. 2015; 18(2): 115–123, doi: 10.1007/s10456-014-9452-3, indexed in Pubmed: 25433512.
7. Agarwal I, Karumanchi SA. Preeclampsia and the Anti-Angiogenic State. Pregnancy Hypertens. 2011; 1(1): 17–21, doi: 10.1016/j.preghy.2010.10.007, indexed in Pubmed: 21709826.
8. Moore Simas TA, Crawford SL, Solitro MJ, et al. Angiogenic factors for the prediction of preeclampsia in high-risk women. Am J Obstet Gynecol. 2007; 197(3): 244.e1–244.e8, doi: 10.1016/j.ajog.2007.06.030, indexed in Pubmed: 17826405.
9. Hertig A, Liere P. New markers in preeclampsia. Clin Chim Acta. 2010; 411(21-22): 1591–1595, doi: 10.1016/j.cca.2010.07.020, indexed in Pubmed: 20659441.
10. Romero R, Nien JK, Espinoza J, et al. A longitudinal study of angiogenic (placental growth factor) and anti-angiogenic (soluble endoglin and soluble vascular endothelial growth factor receptor-1) factors in normal pregnancy and patients destined to develop preeclampsia and deliver a small for gestational age neonate. J Matern Fetal Neonatal Med. 2008; 21(1): 9–23, doi: 10.1080/14767050701830480, indexed in Pubmed: 18175241.
11. Szpera-Gozdziewicz A, Breborowicz GH. Endothelial dysfunction in the pathogenesis of pre-eclampsia. Front Biosci (Landmark Ed). 2014; 19: 734–746, doi: 10.2741/4240, indexed in Pubmed: 24389217.
12. Maynard S, Epstein FH, Karumanchi SA. Preeclampsia and angiogenic imbalance. Annu Rev Med. 2008; 59: 61–78, doi: 10.1146/annurev.med.59.110106.214058, indexed in Pubmed: 17937587.
13. Zeisler H, Llurba E, Chantraine F, et al. Predictive Value of the sFlt-1:PlGF Ratio in Women with Suspected Preeclampsia. N Engl J Med. 2016; 374(1): 13–22, doi: 10.1056/NEJMoa1414838, indexed in Pubmed: 26735990.
14. Levine RJ, Lam C, Qian C, et al. CPEP Study Group. Soluble endoglin and other circulating antiangiogenic factors in preeclampsia. N Engl J Med. 2006; 355(10): 992–1005, doi: 10.1056/NEJMoa055352, indexed in Pubmed: 16957146.
15. Raymond D, Peterson E. A critical review of early-onset and late-onset preeclampsia. Obstet Gynecol Surv. 2011; 66(8): 497–506, doi: 10.1097/OGX.0b013e3182331028, indexed in Pubmed: 22018452.
16. Liu Yu, Yang H, Song L, et al. AGGF1 protects from myocardial ischemia/reperfusion injury by regulating myocardial apoptosis and angiogenesis. Apoptosis. 2014; 19(8): 1254–1268, doi: 10.1007/s10495-014-1001-4, indexed in Pubmed: 24893993.

17. Hu FY, Wu C, Li Y, et al. AGGF1 is a novel anti-inflammatory factor associated with TNF-α-induced endothelial activation. Cell Signal. 2013; 25(8): 1645–1653, doi: 10.1016/j.cellsig.2013.04.007, indexed in Pubmed: 23628701.
18. Timur AA, Driscoll DJ, Wang Q. Biomedicine and diseases: the Klippel-Trenaunay syndrome, vascular anomalies and vascular morphogenesis. Cell Mol Life Sci. 2005; 62(13): 1434–1447, doi: 10.1007/s00018-005-4523-7, indexed in Pubmed: 15905966.
19. Tian XL, Kadaba R, You SA, et al. Identification of an angiogenic factor that when mutated causes susceptibility to Klippel-Trenaunay syndrome. Nature. 2004; 427(6975): 640–645, doi: 10.1038/nature02320, indexed in Pubmed: 14961121.
20. Remmele W, Schicketanz KH. Immunohistochemical determination of estrogen and progesterone receptor content in human breast cancer. Pathology - Research and Practice. 1993; 189(8): 862–866, doi: 10.1016/s0344-0338(11)81095-2.
21. Gude NM, Roberts CT, Kalionis B, et al. Growth and function of the normal human placenta. Thromb Res. 2004; 114(5-6): 397–407, doi: 10.1016/j.thromres.2004.06.038, indexed in Pubmed: 15507270.
22. Geva E, Ginzinger DG, Zaloudek CJ, et al. Human placental vascular development: vasculogenic and angiogenic (branching and nonbranching) transformation is regulated by vascular endothelial growth factor-A, angiopoietin-1, and angiopoietin-2. J Clin Endocrinol Metab. 2002; 87(9): 4213–4224, doi: 10.1210/jc.2002-020195, indexed in Pubmed: 12213874.
23. Redman CW, Sargent IL. Latest advances in understanding preeclampsia. Science. 2005; 308(5728): 1592–1594, doi: 10.1126/science.1111726, indexed in Pubmed: 15947178.
24. Taweevisit M, Thorner PS. Hemoglobin Bart hydrops fetalis: A model for studying vascular changes in placental hypoxia. Placenta. 2016; 44: 98–103, doi: 10.1016/j.placenta.2016.06.009, indexed in Pubmed: 27452444.
25. Conrad KP, Benyo DF. Placental cytokines and the pathogenesis of preeclampsia. Am J Reprod Immunol. 1997; 37(3): 240–249, doi: 10.1111/j.1600-0897.1997.tb00222.x, indexed in Pubmed: 9127646.
26. Spradley FT, Tan AY, Joo WS, et al. Placental Growth Factor Administration Abolishes Placental Ischemia-Induced Hypertension. Hypertension. 2016; 67(4): 740–747, doi: 10.1161/HYPERTENSIONAHA.115.06783, indexed in Pubmed: 26831193.
27. López-Barneo J, Macías D, Platero-Luengo A, et al. Carotid body oxygen sensing and adaptation to hypoxia. Pflugers Arch. 2016; 468(1): 59–70, doi: 10.1007/s00424-015-1734-0, indexed in Pubmed: 26373853.
28. Hung TH, Skepper J, Burton G. In Vitro Ischemia-Reperfusion Injury in Term Human Placenta as a Model for Oxidative Stress in Pathological Pregnancies. The American Journal of Pathology. 2001; 159(3): 1031–1043, doi: 10.1016/s0002-9440(10)61778-6.
29. Xu Y, Zhou M, Wang J, et al. Role of microRNA-27a in down-regulation of angiogenic factor AGGF1 under hypoxia associated with high-grade bladder urothelial carcinoma. Biochim Biophys Acta. 2014; 1842(5): 712–725, doi: 10.1016/j.bbadis.2014.01.007, indexed in Pubmed: 24462738.
30. Lu Q, Yao Y, Hu Z, et al. Angiogenic Factor AGGF1 Activates Autophagy with an Essential Role in Therapeutic Angiogenesis for Heart Disease. PLoS Biol. 2016; 14(8): e1002529, doi: 10.1371/journal.pbio.1002529, indexed in Pubmed: 27513923.
31. Wang W, Li GY, Zhu JY, et al. Overexpression of AGGF1 is correlated with angiogenesis and poor prognosis of hepatocellular carcinoma. Med Oncol. 2015; 32(4): 131, doi: 10.1007/s12032-015-0574-2, indexed in Pubmed: 25796501.
32. Yao Y, Li Y, Song Q, et al. Angiogenic Factor AGGF1-Primed Endothelial Progenitor Cells Repair Vascular Defect in Diabetic Mice. Diabetes. 2019; 68(8): 1635–1648, doi: 10.2337/db18-1178, indexed in Pubmed: 31092480.
33. Zhou B, Zeng S, Li L, et al. Angiogenic factor with G patch and FHA domains 1 (Aggf1) regulates liver fibrosis by modulating TGF-β signaling. Biochim Biophys Acta. 2016; 1862(6): 1203–1213, doi: 10.1016/j.bbadis.2016.02.002, indexed in Pubmed: 26850475.

Submitted: 10 December, 2019
Accepted after reviews: 18 June, 2020
Available as AoP: 30 June, 2020

FOLIA HISTOCHEMICA ET CYTOBIOLOGICA
Vol. 58, No. 2, 2020
pp. 90–95

ORIGINAL PAPER

VIA MEDICA

Immunohistochemical detection of prolactin in clinically non-functioning pituitary adenomas

Katarzyna Winczyk, Joanna Toszek, Jacek Swietoslawski, Ewa Wojtczak, Marek Pawlikowski

Department of Neuroendocrinology, Medical University of Lodz

Abstract

Introduction. Approximately one third of pituitary adenomas are manifested neither by specific symptoms of hormone overproduction nor by elevated blood levels of pituitary hormones. However, these tumours, diagnosed before surgical intervention as clinically non-functioning pituitary adenomas (CNFPAs) express in majority different pituitary hormones, as can be revealed by means of immunohistochemical examination. One of the pituitary hormones which may be expressed in CNFPAs is prolactin (PRL) but the clinical and pathological data on this condition are very scarce.

Material and methods. Sixty two pituitary adenomas, diagnosed before surgery as CNFPAs, were immunoassayed with antibodies against PRL, growth hormone (GH), luteinizing hormone (LH), follicle stimulating hormone (FSH), thyrotropin (TSH), alpha subunit (alpha-SU), corticotropin (ACTH) and dopamine receptor type 2. In a proportion of the patients the presurgical concentrations of insulin-like growth factor 1 (IGF-1) were estimated by means of enzyme-amplified chemiluminescence assay.

Results. Twenty-three (37.1%) of the examined CNFPAs presented the positive immunoreaction with anti-PRL antibody. Most cases concerned women. Only in two cases (one woman and one man), PRL was the unique hormone expressed in the tumour. In the remaining adenomas PRL immunopositivity was accompanied by GH expression — 17, LH or free βLH — 13, FSH — 2, free α subunit — 4 or by ACTH — 5 tumours. Seven (30.43%) of them were recurrent in comparison with 12.8% PRL-immunonegative recurrent CNFPAs. Dopamine receptors were positively immunostained in all the investigated PRL-immunopositive and all PRL-immunonegative adenomas.

Conclusions. Our data confirm the observations that monohormonal silent prolactinomas are very rare but frequently silent PRL often co-expressed with GH or LH. Although in the whole population of patients with CNFPAs both sexes are equally represented, in the case of silent prolactinomas the female sex is prevalent. The observation of the higher rate of recurrent tumours within PRL-immunopositive adenomas *versus* PRL-immunonegative CNFPAs has to be confirmed on the larger material. *(Folia Histochemica et Cytobiologica 2020, Vol. 58, No. 2, 90–95)*

Key words: clinically non-functioning pituitary adenomas; immunohistochemistry; silent prolactinoma; GH; LH; dopamine receptors; insulin-like growth factor-1

Introduction

The pituitary adenomas usually relate to excess of pituitary hormones and lead to specific clinical symptoms of hormone over-secretion. However, the relatively high number of them (approximatively one third) are neither accompanied by increased hormone blood levels nor by clinical symptoms of pituitary hyperfunction. These tumours are diagnosed before surgery as clinically non-functioning pituitary adenomas (CNFPAs). Most of them present the immunohistochemical expression of different pituitary hormones, despite a lack of the clinical evidence of the hormone overproduction and increase of respective hormone levels in blood. Such tumours are called „silent" pituitary adenomas [1–7]. The majority of CNFPAs (70––80%) express gonadotropins or their subunits [1–10].

Correspondence address: Prof. Katarzyna Winczyk MD, PhD
Department of Neuroendocrinology,
Medical University of Lodz
251/A1 Pomorska Str., 92–213 Lodz, Poland
phone: +48 42 201 42 99
e-mail: katarzyna.winczyk@umed.lodz.pl

Silent corticotropinomas (corticotroph adenomas not manifested by Cushing's disease) and somatotroph adenomas without acromegaly (silent somatotropinomas) are less frequent but not exceedingly rare [1–7, 11–19]. In contrast, silent thyrotropin-expressing [1–7, 20] and prolactin-expressing pituitary adenomas are considered as very rare and the data concerning the clinical and pathological characterization of the latter of them are very scarce [5, 7, 21, 22]. The aim of the present study is to partially fill this gap.

Material and methods

Sixty-two pituitary adenomas were surgically removed in the Department of Neurosurgery and Surgery of Peripheral Nerves, Medical University of Lodz, Lodz, Poland. All the excised tumours were diagnosed before surgery as CNFPAs and after operation examined by immunohistochemistry. The samples were fixed in Bouin-Holland fixative or formalin and embedded in paraffin wax. The paraffin sections were immunoassayed generally as described before [23] with antibodies against prolactin (PRL, polyclonal, Dako, Glostrup, Denmark), growth hormone (GH, polyclonal, Dako, or Immunon, USA), luteinizing hormone (LH, monoclonal, Dako), follicle stimulating hormone (FSH, monoclonal, Dako), thyrotropin (TSH, monoclonal, Immunotech, France), alpha-subunit (alpha-SU, monoclonal, Immunotech, Marseille, France), corticotropin (ACTH, polyclonal, SigmaAldrich, St. Louis, MO, USA) and dopamine receptor type 2 (RD2 polyclonal, Merck Millipore, Darmstadt, Germany). The primary antibodies were applied in a working dilution of 1:100. The visualization of immunostaining was performed using Envision kit (Dako) with the use of 3,3' diaminobenzidine (DAB) as chromogen. A presence of more than 5% of immunopositive cells was considered as important. For a negative control, the primary antibody was omitted in the immunostaining procedure. The sections were viewed by a light microscope.

In a proportion of patients (37) with pituitary adenoma, the concentrations of insulin-like growth factor 1 (IGF-1) were estimated in blood serum by means of enzyme-amplified chemiluminescence immunoassay (EACLIA) on the Immulite 1000 analyser (Siemens, Warsaw, Poland) before surgery. The analytical sensitivity of the used assay was between 20 ng/mL and 1,600 ng/mL. Intra-assay coefficients of variation (CV), depending on the concentration included in ranges from 3.1% to 4.3% ng/mL and inter-assay CV was between 5.8% and 8.4% ng/mL.

The study was approved by the Bioethical Committee of the Medical University of Lodz, Lodz, Poland, decision RNN/99/15/KE.

Statistical analysis. The data obtained from the experiment was recorded on Excel (MS Office 2019) worksheets Basic descriptive statistics (mean ± SEM) were calculated. A statistical analysis was performed using programs included in the statistical package Statistica 13.1 (Statsoft, Krakow, Poland). The differences between mean values were evaluated by Student's t test and for sets of categorical data Pearson's chi square test was applied. The quantitative parameters were expressed as mean value ± standard deviation. Statistical differences between the tested values were considered as significant level of $p < 0.05$.

Results

The tumours derived from 62 patients (33 women and 29 man, mean age 57.4 ± 11.8 y) and diagnosed before surgery as CNFPAs. The immunohistochemical examination of removed pituitary adenomas was performed. Among them 23 (37.1%) presented the positive immunoreaction of the at least 10% adenoma cells with anti-prolactin antibody (Fig. 1A). These cases concerned 16 women and 7 men (69.6% and 30.4%, respectively) and gender difference were statistically significant — $p < 0.01$ (Fig. 2). The prevalence of feminine sex is specific for PRL-expressing CNFPA because the whole group of CNFPA included almost the same number of women and men. The PRL-positive and PRL-negative patients did not differ significantly in age (PRL-positive mean ± SEM 56.52 ± 2.26 y; PRL-negative 58.95 ± 1.90 y). Only in two cases (one woman and one man), the PRL was the unique hormone expressed in the tumour. In the remaining adenomas PRL immunopositivity was accompanied by GH expression — 17, LH or free βLH — 13, FSH — 2, free α subunit — 4 or by ACTH — 5 tumours (Fig. 1B, C). Seven adenomas were recurrent (7/23, 30.43%) in PRL-immunopositive group and it is a higher value in comparison with PRL-immunonegative recurrent CNFPAs (5/39, 12.8%), but this difference is not statistically significant (Fig. 3).

Presence of dopamine D2 receptors (RD2)

RD2 were detected in 32 adenomas. In all PRL-immunopositive (21 cases) and all PRL-immunonegative (11 cases) examined tumours the positive immunostaining was found (Fig. 4).

Insulin-like growth factor (IGF-1) serum concentration

IGF-1 was measured in 37 patients with CNFPAs. In monohormonal silent prolactinoma, only in one case IGF-1 was measured (man, 45 y, 117 ng/mL — normal value). In the PRL-immunopositive adenomas (n = 15), the mean IGF-1 serum concentration was 115.3 ± 4.7 ng/mL. In PRL-immunonegative CNFPAs the mean IGF-1 concentration was slightly

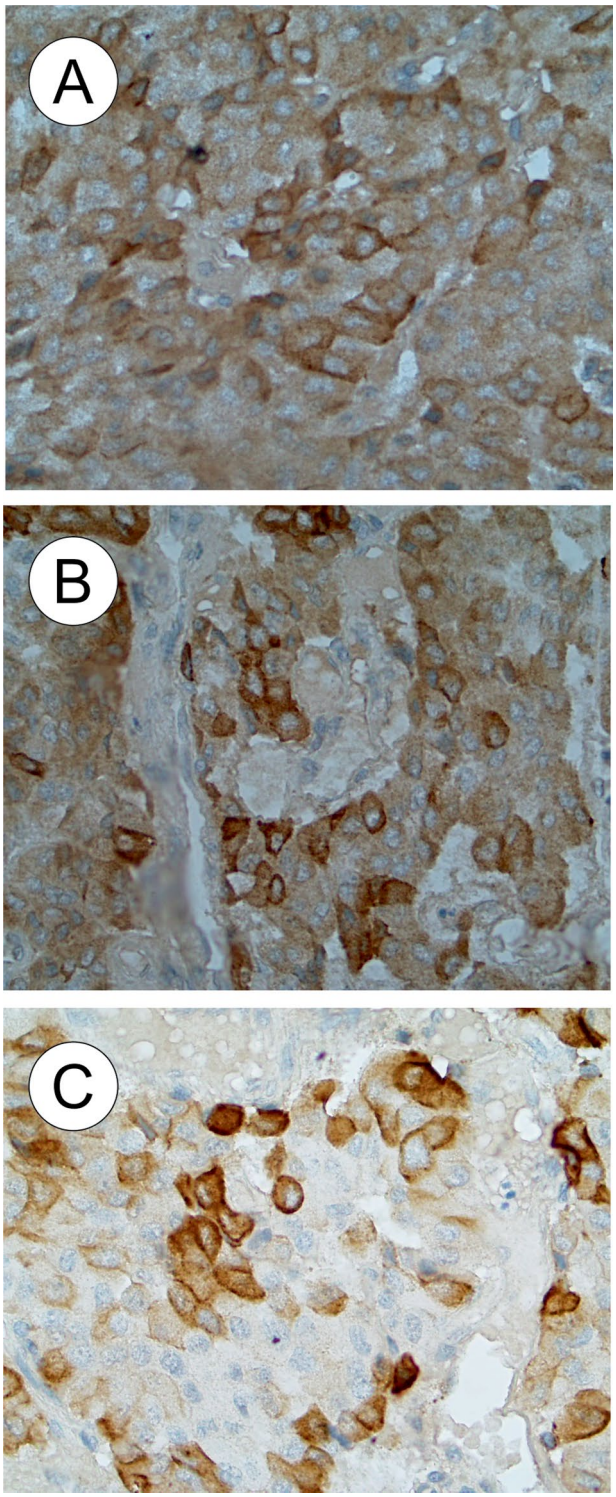

Figure 1. Immunohistochemical examination of clinically non-functioning pituitary adenoma in a 71-year-old man. Positive immunoreactions for: **A** — prolactin, **B** — growth hormone, **C** — alpha subunit. Original magnification 400×.

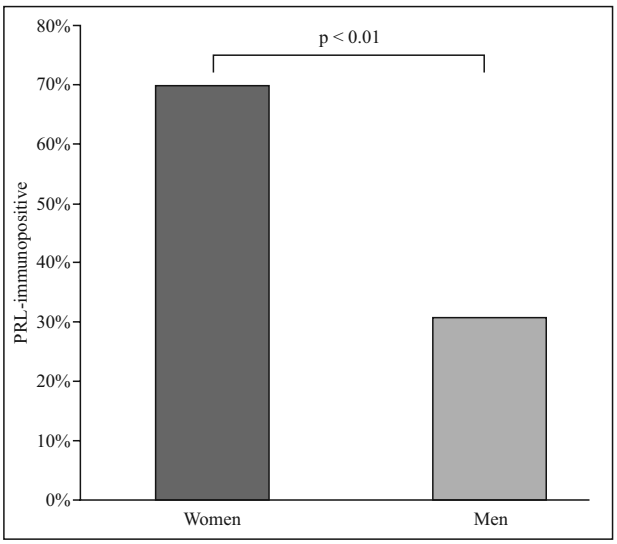

Figure 2. The percentage (%) of women (16/23) and man (7/23) with PRL-immunopositive pituitary adenomas.

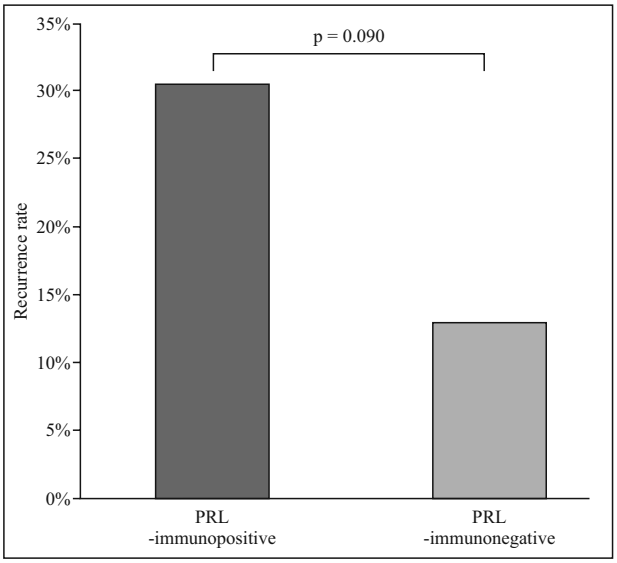

Figure 3. The number (%) of recurrences in PRL-immunopositive adenomas (7/23, 30.43%) and in PRL-immunonegative CNFPAs (5/39, 12.8%).

lower (102.1±17.5 ng/mL); however, the difference is not statistically significant ($p > 0.05$). Because PRL immunopositivity occurs often with co-expression of GH, we also compared IGF-1 serum levels in patients with GH-immunopositive and GH-immunonegative tumours. The difference was statistically significant (127.9 ± 20.75 ng/mL *vs.* 67.3±9.9 ng/mL, respectively, $p < 0.01$) (Fig. 5).

Discussion

Our data are concordant with the observations that monohormonal silent prolactinomas are exceedingly

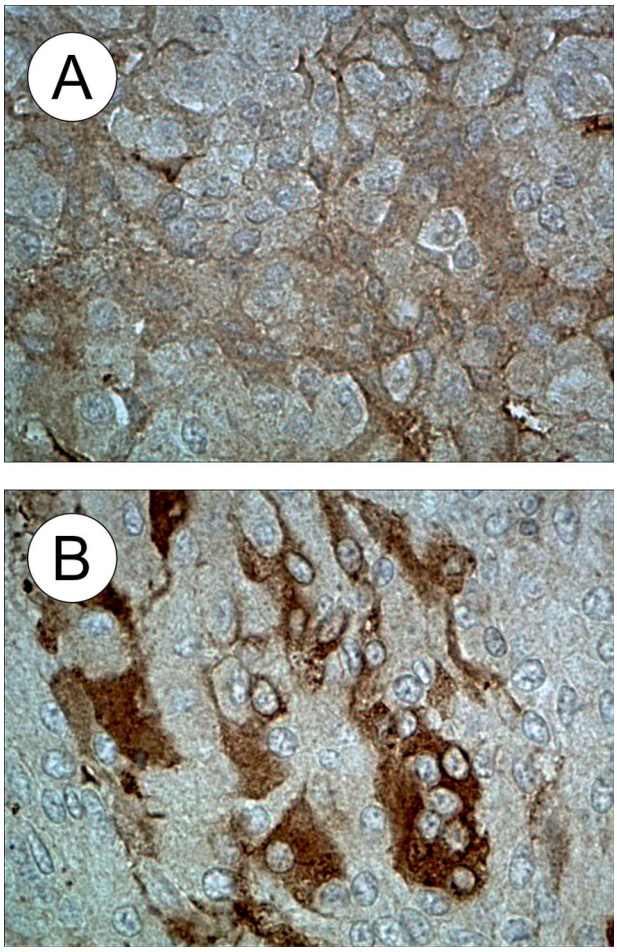

Figure 4. Positive immunostaining of dopamine receptors in PRL-immunopositive adenoma in a 60-year-old women) (**A**) and PRL-immunonegative adenoma in a 60-year-old man) (**B**). Original magnification 400×.

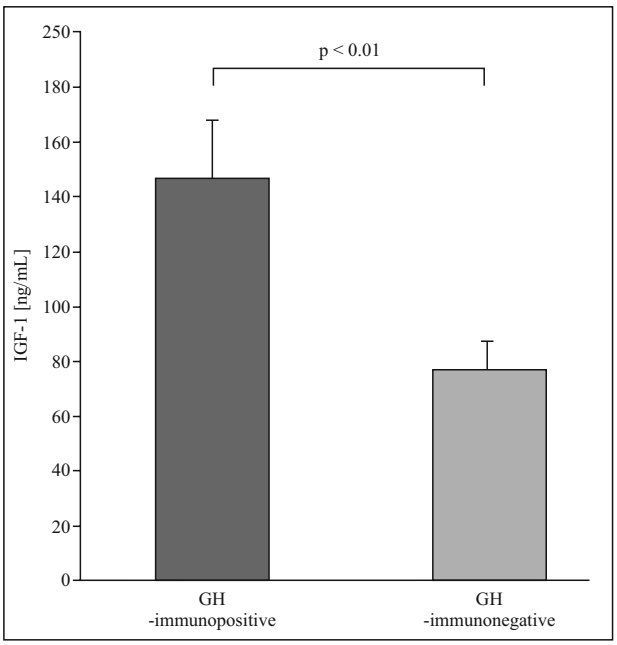

Figure 5. The mean IGF-1 serum levels in patients with PRL-immunopositive adenomas: comparison of the groups with GH-positive and GH-negative tumours.

rare [5, 7]. Moreover, they corroborate also with the findings that the PRL expression is frequently combined with either silent or active expression of GH [5, 7, 19]. This incidence is obvious because it is well known that lactotrophs and somatotrophs differentiate from the common progenitor cells under the influence of the same transcription factor (Pit-1). However, our novel observation is that the expression of PRL in CNFPA is frequently accompanied by gonadotropins, mostly by LH or free LH subunit. This combination is almost as frequent as that with GH. The prevalence of feminine sex and their high recurrence rate is also worth notice. The former observation may be related to the frequent expression of oestrogen receptors in this type of adenoma [24]. The latter finding is more difficult to explain. However, the recurrent PRL-expressing tumours observed in this study were not monohormonal prolactinomas but were combined mostly with GH (4/7) and with gonadotropins (mostly with LH, 5/7). The latter observation is concordant with the finding of Diri *et al.* [25] who found that that tumour recurrence rate is higher in LH-immunopositive in comparison with LH-immunonegative CNFPAs. Another factor that could be taken into consideration was a higher IGF-1 levels in silent GH-PRL adenoma than GH-immunonegative tumours (see below). Since the active prolactinomas are known to express the functional dopamine receptors and are in majority sensitive to pharmacological treatment by dopamine agonists, we wanted to see whether the silent prolactinomas express RD2 more frequently that PRL-immunonegative CNFPAs. Surprisingly, RD2 were detectable by immunohistochemistry in all cases of CNFPAs, irrespectively of the presence or absence of PRL immunostaining. This result is identical with that observed by Vieira *et al*. [26] who found the presence of RD2 mRNA as well as RD2 immunostaining in the all examined CNFPAs. The high frequency of RD2 in CNFPAs (approx. 70%) was also reported in the other studies [27, 28]. These results corroborate with the reported efficacy of the postoperative treatment of CNFPAs with dopamine agonists [27, 29, 30]. Our observation that the expression of RD2 concerns equally PRL-positive as PRL-negative CNFPAs suggests that the latter are also good candidates for the treatment with dopamine agonists. The last question worth to discuss is the relationship of PRL immu-

nopositivity and IGF-1 secretion. It was found that patients with PRL-expressing CNFPAs have slightly higher preoperative IGF-1 concentrations in blood in comparison with those with PRL-immunonegative tumours. However, this fact is probably connected with the frequent coexistence of PRL and GH also in the case of silent adenomas. In an earlier study of our team it was found that in acromegaly the IGF-1 preoperative levels are significantly higher in somatoprolactinomas than in 'pure' somatotropinomas [31]. This observation, together with the results of the present study, corroborate with the experimental investigations showing that IGF-1 enhances the proliferation of lactotrophs in murine pituitary cells *in vitro* [32] and may induce the differentiation of lactotrophs from their progenitor cells [33]. It was also shown that IGF-1 induces *in vitro* trans-differentiation of somatotrophs into lactotrophs in the rat pituitary cell line MtT/S [34, 35].

To sum up, the non-functioning PRL-expressing pituitary adenomas very rarely present themselves as monohormonal silent prolactinomas but are relatively frequent as combined PRL-GH or plurihormonal tumours expressing also other pituitary hormones (mostly LH). The higher recurrence rate of PRL-expressing CNFPAs, as observed in the present study, needs further studies on the larger material.

Acknowledgements

This study was supported by grant of Medical University of Lodz No. 503/3-015-04/503-51-001. The authors thank Professor Andrzej Radek, MD, PhD, and Professor Maciej Radek, MD, PhD for the providing of pituitary adenoma samples.

Conflict of interest

The authors declare no conflict of interest.

References

1. Wade AN, Baccon J, Grady MS, et al. Clinically silent somatotroph adenomas are common. Eur J Endocrinol. 2011; 165(1): 39–44, doi: 10.1530/EJE-11-0216, indexed in Pubmed: 21493729.
2. Mayson SE, Snyder PJ, Mayson SE, et al. Silent (clinically nonfunctioning) pituitary adenomas. J Neurooncol. 2014; 117(3): 429–436, doi: 10.1007/s11060-014-1425-2, indexed in Pubmed: 24676675.
3. Mayson SE, Snyder PJ. Silent pituitary adenomas. Endocrinol Metab Clin North Am. 2015; 44(1): 79–87, doi: 10.1016/j.ecl.2014.11.001, indexed in Pubmed: 25732644.
4. Mercado M, Melgar V, Salame L, et al. Clinically non-functioning pituitary adenomas: Pathogenic, diagnostic and therapeutic aspects. Endocrinol Diabetes Nutr. 2017; 64(7): 384–395, doi: 10.1016/j.endinu.2017.05.009, indexed in Pubmed: 28745610.
5. Manojlovic-Gacic E, Engström BE, Casar-Borota O. Histopathological classification of non-functioning pituitary neuroendocrine tumors. Pituitary. 2018; 21(2): 119–129, doi: 10.1007/s11102-017-0855-1, indexed in Pubmed: 29275530.
6. Ntali G, Wass JA. Epidemiology, clinical presentation and diagnosis of non-functioning pituitary adenomas. Pituitary. 2018; 21(2): 111–118, doi: 10.1007/s11102-018-0869-3, indexed in Pubmed: 29368293.
7. Drummond J, Roncaroli F, Grossman AB, et al. Clinical and Pathological Aspects of Silent Pituitary Adenomas. J Clin Endocrinol Metab. 2019; 104(7): 2473–2489, doi: 10.1210/jc.2018-00688, indexed in Pubmed: 30020466.
8. Pawlikowski M, Kunert-Radek J, Radek A. Gonadotropinoma - a frequent subtype of the pituitary adenoma. Endokrynol Pol. 2000; 51: 77–81.
9. Asa SL, Ezzat S. Gonadotrope Tumors. Prog Mol Biol Transl Sci. 2016; 143: 187–210, doi: 10.1016/bs.pmbts.2016.08.005, indexed in Pubmed: 27697203.
10. Pawlikowski M, Jaranowska M, Fryczak J, et al. Blood serum concentrations of gonadotropins and α-subunit in patients with gonadotropinomas in relation to the immunoreactivity of pituitary adenoma. Endokrynol Pol. 2018; 69(5): 526–529, doi: 10.5603/EP.a2018.0049, indexed in Pubmed: 30074232.
11. Reincke M, Allolio B, Saeger W, et al. A pituitary adenoma secreting high molecular weight adrenocorticotropin without evidence of Cushing's disease. J Clin Endocrinol Metab. 1987; 65(6): 1296–1300, doi: 10.1210/jcem-65-6-1296, indexed in Pubmed: 2824554.
12. Iino K, Oki Y, Matsushita F, et al. Immunohistochemical properties of silent corticotroph adenoma and Cushing's disease. Pituitary. 2007; 10(1): 35–45, doi: 10.1007/s11102-007-0010-5, indexed in Pubmed: 17410413.
13. Pawlikowski M, Kunert-Radek J, Radek M. "Silent" corticotropinoma. Neuro Endocrinol Lett. 2008; 29(3): 347–350, indexed in Pubmed: 18580839.
14. Guttenberg KB, Mayson SE, Sawan C, et al. Prevalence of clinically silent corticotroph macroadenomas. Clin Endocrinol (Oxf). 2016; 85(6): 874–880, doi: 10.1111/cen.13146, indexed in Pubmed: 27346850.
15. Kovacs K, Lloyd R, Horvath E, et al. Silent somatotroph adenomas of the human pituitary. Amer J Pathol. 1989; 134: 345–353.
16. Trouillas J, Sassolas G, Guigard MP, et al. Somatotropic adenomas without acromegaly. Pathol Res Pract. 1991; 187(8): 943–949, doi: 10.1016/s0344-0338(11)81065-4, indexed in Pubmed: 1792190.
17. Yamada S, Sano T, Stefaneanu L, et al. Endocrine and morphological study of a clinically silent somatotroph adenoma of the human pituitary. J Clin Endocrinol Metab. 1993; 76(2): 352–356, doi: 10.1210/jcem.76.2.8432778, indexed in Pubmed: 8432778.
18. Naritaka H, Kameya T, Sato Y, et al. Morphological characterization and subtyping of silent somatotroph adenomas. Pituitary. 1999; 1(3-4): 233–241, doi: 10.1023/a:1009942122673, indexed in Pubmed: 11081203.
19. Matsuno A, Itoh J, Itoh Y, et al. Histopathological analyses of silent pituitary somatotroph adenomas using immunohistochemistry, in situ hybridization and confocal laser scanning microscopic observation. Pathol Res Pract. 2001; 197(1): 13–20, doi: 10.1078/0344-0338-00003, indexed in Pubmed: 11209812.
20. Pawlikowski M, Kuta J, Fuss-Chmielewska J, et al. ‚Silent' somatotropinoma. Endokrynol Pol. 2012; 63(2): 88–91, indexed in Pubmed: 22538745.

21. Pawlikowski M, Pisarek H, Jaranowska M, et al. „Silent" thyrotropin (TSH) expression in acromegaly and clinically non-functioning pituitary adenomas. Endokrynol Pol. 2016; 67(5): 515–518, doi: 10.5603/EP.a2016.0056, indexed in Pubmed: 27403655.
22. Saeger W, Lüdecke DK, Buchfelder M, et al. Pathohistological classification of pituitary tumors: 10 years of experience with the German Pituitary Tumor Registry. Eur J Endocrinol. 2007; 156(2): 203–216, doi: 10.1530/eje.1.02326, indexed in Pubmed: 17287410.
23. Korol P, Jaranowska M, Pawlikowski M. Immunohistochemical demonstration of LH/CG receptors in non-neoplastic human adrenal cortex and adrenocortical tumors. Folia Histochem Cytobiol. 2019; 57(1): 23–27, doi: 10.5603/FHC.a2019.0003, indexed in Pubmed: 30924919.
24. Mavrakis AN, Tritos NA. Diagnostic and therapeutic approach to pituitary incidentalomas. Endocr Pract. 2004; 10(5): 438–444, doi: 10.4158/EP.10.5.438, indexed in Pubmed: 15760793.
25. Kaptain GJ, Simmons NE, Alden TD, et al. Estrogen receptors in prolactinomas: a clinico-pathological study. Pituitary. 1999; 1(2): 91–98, doi: 10.1023/a:1009903603495, indexed in Pubmed: 11081186.
26. Diri H, Ozaslan E, Kurtsoy A, et al. Is Positive Staining of Non-Functioning Pituitary Adenomas for Luteinizing Hormone Associated with a Poor Prognosis? Turk Neurosurg. 2017; 27(1): 8–13, doi: 10.5137/1019-5149.JTN.14889-15.1, indexed in Pubmed: 27593756.
27. Vieira Neto L, Widemberg LE, Moraes AB, et al. Dopamine receptor subtype 2 expression profile in nonfunctioning pituitary adenomas and in vivo response to cabergoline therapy. Clin Endocrinol (Oxf). 2015; 82: 739–746, doi: 10.1111/cen.12684, indexed in Pubmed: 25418156.
28. Pivonello R, Matrone C, Filippella M, et al. Dopamine receptor expression and function in clinically nonfunctioning pituitary tumors: comparison with the effectiveness of cabergoline treatment. J Clin Endocrinol Metab. 2004; 89(4): 1674–1683, doi: 10.1210/jc.2003-030859, indexed in Pubmed: 15070930.
29. Pawlikowski M. Immunohistochemical detection of dopamine D2 receptors in human pituitary adenomas. Folia Histochem Cytobiol. 2010; 48(3): 394–397, doi: 10.2478/v10042-010-0031-1, indexed in Pubmed: 21071344.
30. Cooper O, Greenman Y. Dopamine Agonists for Pituitary Adenomas. Front Endocrinol. 2018; 9, doi: 10.3389/fendo.2018.00469, indexed in Pubmed: 30186234.
31. Batista RL, Musolino NRC, Cescato VAS, et al. Cabergoline in the Management of Residual Nonfunctioning Pituitary Adenoma: A Single-Center, Open-Label, 2-Year Randomized Clinical Trial. Am J Clin Oncol. 2019; 42(2): 221–227, doi: 10.1097/COC.0000000000000505, indexed in Pubmed: 30540568.
32. Toszek J, Pawlikowski M, Jaranowska M, et al. Is preoperative level of insulin-like growth factor-1 (IGF-1) connected with immunohistochemical phenotype of pituitary adenoma in patients with acromegaly? Diagn Lab. 2019; 55: 1–6.
33. Oomizu S, Takeuchi S, Takahashi S. Stimulatory effect of insulin-like growth factor I on proliferation of mouse pituitary cells in serum-free culture. J Endocrinol. 1998; 157(1): 53–62, doi: 10.1677/joe.0.1570053, indexed in Pubmed: 9614357.
34. Hikake T, Hayashi S, Iguchi T, et al. The role of IGF1 on the differentiation of prolactin secreting cells in the mouse anterior pituitary. J Endocrinol. 2009; 203(2): 231–240, doi: 10.1677/JOE-09-0232, indexed in Pubmed: 19696100.
35. Inoue K, Sakai T. Conversion of growth hormone-secreting cells into prolactin-secreting cells and its promotion by insulin and insulin-like growth factor-1 in vitro. Exp Cell Res. 1991; 195(1): 53–58, doi: 10.1016/0014-4827(91)90499-k, indexed in Pubmed: 2055276.

Submitted: 14 February, 2020
Accepted after reviews: 15 June, 2020
Available as AoP: 29 June, 2020

FOLIA HISTOCHEMICA ET CYTOBIOLOGICA
Vol. 58, No. 2, 2020
pp. 96–107

ORIGINAL PAPER

VIA MEDICA

Overexpression of Rictor protein and Rictor-*H. pylori* interaction has impact on tumor progression and prognosis in patients with gastric cancer

Fang Wang[1], Xiaoqi Lou[1], Yanfeng Zou[2], Dingtao Hu[1], Jiatao Liu[3], Jie Ning[1], Yang Jiao[1], Zuoyang Zhang[4], Feng Yang[4], Lulu Fan[1], Hanqing Yu[1], Wei Wei[5], Hua Wang[1, 6], Guoping Sun[1*]

[1]Department of Oncology, the First Affiliated Hospital of Anhui Medical University, Hefei 230022, Anhui, China

[2]Department of Epidemiology and Biostatistics, School of Public Health, Anhui Medical University, Hefei 230032, Anhui, China

[3]Department of Pharmacy, the First Affiliated Hospital of Anhui Medical University, Hefei 230022, Anhui, China

[4]Department of Pathology, the First Affiliated Hospital of Anhui Medical University, Hefei 230022, Anhui, China

[5]Institute of Clinical Pharmacology, Anhui Medical University, Hefei 230032, Anhui, China

[6]Institute for Liver Diseases of Anhui Medical University, Hefei 230032, Anhui, China

Abstract

Introduction. Growing evidence indicates that Rictor (Rapamycin-insensitive companion of mTOR) is overexpressed across several malignancies and associated with poor survival. However, only limited data indicate that Rictor plays a role in gastric cancer (GC). We sought to explore the prognostic value of Rictor in GC and present interaction analysis between Rictor expression and *H. pylori* status regarding their effects over the prognosis of GC patient.

Materials and methods. 250 GC tissues and 124 lymph node metastases were collected for the detection of Rictor by immunohistochemistry. Cox regression model was used to assess the association between Rictor expression and patient prognosis. Functional experiments were examined in transfected cells using Rictor siRNA. Additive and multiplicative interactions of Rictor and *H. pylori* were evaluated.

Results. In this study, the positive rate of Rictor was 51.6% (129/150) in GC tissues. Multivariate analyses showed that Rictor was independent unfavorable predictor for OS (HR = 1.554, 95% CI = 1.076–2.244, P = 0.019) and DFS (HR = 1.556, 95% CI = 1.081–2.240, P = 0.017). Patients with upregulated Rictor in the primary tumor and lymph node metastases had the worst prognosis. We observed significant additive and multiplicative interactions between Rictor expression and *H. pylori* status for OS and DFS ($P < 0.05$). Our in vitro experiment showed that knockdown of Rictor could suppress cell proliferation, induce apoptosis and inhibit tumor migration and invasion.

Conclusion. Our results demonstrate that Rictor, acting as an oncogene, might be a potential prognostic biomarker and therapeutic target in GC. We suggest that Rictor expression and *H. pylori* status may be a prognostic marker in gastric cancer. *(Folia Histochemica et Cytobiologica 2020, Vol. 58, No. 2, 96–107)*

Key words: gastric cancer; Rictor; *H. pylori*; prognosis; progression; IHC; siRNA

***Correspondence address:** Dr. Guoping Sun,
Department of Oncology,
the First Affiliated Hospital of Anhui Medical University,
218 Jixi Road, Hefei 230022, Anhui, China
phone: +86055162923615, fax +86055162923615
e-mail: sungp@ahmu.edu.cn

Introduction

Cancer remains one of the most important global threats in public health. Recent statistical reports document that gastric cancer (GC) ranks as the fifth most common cancer and the third leading cause of cancer death [1]. Despite progress in the clinical management of GC, treatment of the disease remains challenging owing to the complexity of the disease and difficulty in early diagnosis. For early staged GC, the only curative treatment option is surgical resection [2]. Unfortunately, for patients with advanced-stage due to the poor prognosis, it remains a major clinical concern. The effects of conventional therapies, including chemotherapy and radiation, on survival benefits are limited. Targeted therapeutic strategies, such as angiogenesis and epidermal growth factor receptor (EGFR) inhibitors have exhibited significant antitumor activity [3]. The process of tumorigenesis involves diverse gene alterations, including epigenetic changes, oncogene activation, inactivation of tumor suppressor genes, and abnormal expression of cancer-related genes. Therefore, there is an urgent need for the discovery of novel genes that govern the progression of GC and novel therapeutic targets.

The mammalian target of rapamycin (mTOR) is known as a conserved serine-threonine protein kinase. It could regulate cell growth, metabolism as well as survival [4], and functions through two complexes: mTORC1 and mTORC2 [5]. Rapamycin insensitive companion of mTOR (Rictor) is an essential subunit of mTORC2 complex [6]. Rictor plays a vital role in the feedback loops and cross-talk in the PI3K/AKT/ /mTOR signal transduction pathway. Since Akt activation is essential for many events of the metastatic pathway in cancer, Rictor could serve as a novel therapeutic target. Targeted inhibition of mTORC2 activity through Rictor gene silencing could promote cisplatin-induced apoptosis and prevent cell migration in osteosarcoma and breast cancer [7–8]. Rictor upregulation was associated with invasive behavior and poor prognosis in several malignancies [9–11]. Currently, only a limited number of reports exist regarding the roles of Rictor in GC [10].

There is evidence that *H. pylori* infection is identified as a beneficial prognostic indicator for GC, indicating different growth patterns between *H. pylori* (+) and *H. pylori* (–) GC [12–13]. Meanwhile, the infection of *H. pylori* is associated with mTOR signaling [14–15]. Relatively little is known about whether there is an interaction between Rictor expression and *H. pylori* status in the prognosis of GC.

The objective of the current study was to explore the functional significance of Rictor in primary carcinomas and lymph node metastases, as well as the prognostic value in GC. Here, we also presented interaction analysis between Rictor expression and *H. pylori* status regarding their effects over GC patient prognosis. In addition, we characterized the role of Rictor in GC proliferation, migration, invasion and apoptosis.

Materials and methods

Patients and tissue specimens. This study was conducted in the First Affiliated Hospital of Anhui Medical University, and 250 pathologically diagnosed GC patients who underwent surgery from November 2007 to November 2009 were recruited. The current and our previous studies [12] were conducted based on the same study population, and it should be noted that there can be overlap between the patients of the two studies. We excluded patients with Siewert type I cardia adenocarcinoma and patients who received neoadjuvant treatment before surgery in the study.

In order to collect prognosis data, patients who underwent surgical resection were followed up according to a standard scheme [16]. At the first 2 years after the surgery, patients were followed up every 3 months. At the following 2 years, patients were followed up every 6 months, then yearly afterward. The follow-up program consisted of clinical examination, hematologic analyses, measurement of tumor markers, abdominal ultrasonography and chest radiography (once half a year), and endoscopy of the upper digestive tract (once a year). Computed tomography (CT) or positron emission tomography (PET)/CT was conducted for the surveillance of patients to detect recurrence after surgery. The follow-up plan lasted from the surgery until the date of death or the last date of follow-up via hospital visit or telephone. The follow-up deadline was August 15, 2018. Overall survival (OS) and disease-free survival (DFS) of patients were calculated. Overall survival (OS) was recorded from pathological diagnosis/recruitment to the date of death or the date of last follow-up. Disease-free survival (DFS) was recorded from the date of pathological diagnosis/ /recruitment to the date of disease recurrence or the date of last follow-up. The Ethics Committee of Anhui Medical University approved the study, and all of the participants enrolled in the study gave the written informed consent.

Immunohistochemistry. The H&E stained sections of each tumor were reexamined by a pathologist (ZZY) for histological analyses. Formalin-fixed paraffin-embedded (FFPE) sections of 250 GC tissues and 124 lymph node metastases were obtained for the detection of Rictor by immunohistochemical (IHC) method. Firstly, all the tissue sections were dewaxed with xylene, followed by antigen retrieving in a microwave for 20 min. In order to block endogenous peroxidase activity, we have immersed each slide in 3% hydrogen peroxide for 10 min. Then, these

slides were incubated with the primary mouse monoclonal anti-Rictor antibody (1:700 diluted sc-271081, Santa Cruz Biotechnology, Santa Cruz, CA, USA) at 4°C overnight. Thereafter, at room temperature (RT), these slides were incubated with horseradish peroxidase (HRP) labeled goat anti-mouse/anti-rabbit immunoglobulin (PV-6000, ZSGB Biotechnology, Beijing, China) for 20 min. Finally, the slides were stained with 3,3'-diaminobenzidine (DAB). The Rictor protein level was determined using semi-quantitative IHC detection system [17]. Assessment of IHC staining was performed by two pathologists (YF and ZZY) independently. We chose 10 high power fields (HPF) for each the tissue section and calculated the average number of positive cells. We assessed the percentage of positively stained cells (none = 0, less than 10% = 1, 10% to 50% = 2, greater than 50% = 3) as well as the staining intensity (none = 0, light yellow = 1, pale brown = 2, dark brown = 3). Finally, an immunoreactivity score was calculated using the sum of the percentage score and intensity score, ranging from 0 to 6. The immunoreactivity score of 0–2 was considered negative for Rictor immunostaining, otherwise positive [10].

IHC assay was performed on 250 pairs of GC and non-cancerous (located at least 5 cm from the tumor) tissues for the detection of *H. pylori*. The methods have been described in our previous studies [12]. We considered the patients as *H. pylori* positive if either the tumor or non-tumoral tissues was categorized as positive. Otherwise, if both the tumor and non-tumoral tissues were categorized as negative, we considered the patients as *H. pylori* negative.

Cell culture and transfection. BGC-823 and SGC-7901 human GC cell lines were purchased from the Cell Resource Centre, Shanghai Institute of Biochemistry and Cell Biology, Chinese Academy of Sciences, Shanghai, China. The cells were grown in the RPMI 1640 medium (Invitrogen, Carlsbad, CA, USA) to which 10% fetal bovine serum, penicillin (100 μ/ml) and streptomycin (100 mg/ml) were added. All cells were cultured at 37° and with a humidified atmosphere of 5% CO_2. We used RNA interference (siRNA) (final concentration of 100 nM, GenePharma, Shanghai, China) for Rictor knock-down. According to the manufacturer's protocol, we have plated BGC-823 and SGC-7901 cells in 6-well or 96-well plates at a density of 2×10^5 or $5\sim 6 \times 10^3$ cells per well for transfection, respectively. When cells grew to 40% ~ 60% confluence, they were transfected with 100 nM Rictor siRNA or the corresponding negative control (100 nM, GenePharma) using Lipofectamine 3000 transfection agent (Invitrogen). For example, in 6-well plates, 10 μl of Rictor siRNA was absorbed by RNA free enzyme gun head (Axygen, Tewksbury, MA, USA) and dissolved in 125 μl of Opti-MEM reduced serum culture medium (No:31985-062, GIBCO BRL, Grand Island, NY, USA) for transfection, and gently mixed. 7.5 μl Lipofectamine 3000 transfection agent was absorbed by RNA free enzyme gun head and dissolved in 125 μl of Opti-MEM reduced serum culture medium for transfection, and gently mixed. The reagent was blown and left at RT for 5 min. Then, the transfection mixture was added into the six-well plate. The transfected cells were incubated under 5% CO_2 at 37° for subsequent experiments.

Western blotting. Western blot assays were conducted to screen the specific Rictor siRNA sequence. RIPA buffer and protease inhibitors were used to extract lysates from cultured cells 48 h post-transfection. We have loaded the same amount of cell lysate for electrophoresis. Protein samples were separated using 6% SDS-PAGE. Then, we transferred the samples onto PVDF membranes (Millipore, Bedford, MA, USA) on ice overnight for about 14 h with constant pressure of 70 V, following by blocking with 5% non-fat milk for 2 h at RT. We incubated the membranes with mouse monoclonal anti-Rictor antibody (1:1000; ab56578, Abcam, Cambridge, MA, USA) overnight at 4°C. The membranes were then incubated with HRP-conjugated secondary antibody for 2 h at 37°C. Visualization was performed by using ECL substrate. We used β-actin as the loading control.

Cell viability assay. CCK-8 assay (Bestbio, Beijing, China) was used to measure effects of Rictor siRNA on cell viability. Cell suspensions (100 μl, 3×10^3 cells/well) were seeded into 96-well plates and transfected. After transfection, 10 μl of the CCK-8 reagent was added into each well at 24 h, 48 h and 72 h and the plates were incubated for another 1 h at 37°C. Then we used a microplate reader to record the absorbance at 450 nm. We performed at least three independent experiments. For each time point, each experimental group included six replicate wells.

Transwell cell migration/invasion assays. Transwell assay was used to determine the abilities of cell migration and invasion. We used 24-well plates with poly-carbonate transwell filters (Corning Incorporated, Corning, NY, USA) for the assay. For cell invasion, the membrane of the chamber was pre-coated with 60 μl extracellular Matrigel (Cat. no. 356234, BD Biosciences, San Jose, CA, USA). The extracellular Matrigel was freshly 1:7 diluted with serum-free medium to form a matrix barrier. At 37°C, it was incubated for 3 h before invasion assay. 48 h after the transfection, SGC-7901 cells and BGC-823 cells were harvested, and resuspended in serum-free medium to a concentration of 1×10^5 cells per well. These cells were loaded into each upper chamber with a volume of 100 μl and 750 μl of RPMI-1640 medium containing 10% FBS was added to the lower chamber. They were incubated for 24 h/48 h (SGC-7901 cell/BGC-823 cell) to measure the effects of Rictor siRNA on cell migration potential and incubated for 72 h to assess the effects of Rictor siRNA on cell invasion potential. Then, a cotton swab was used to scrape off the upper surface of the well. We fixed

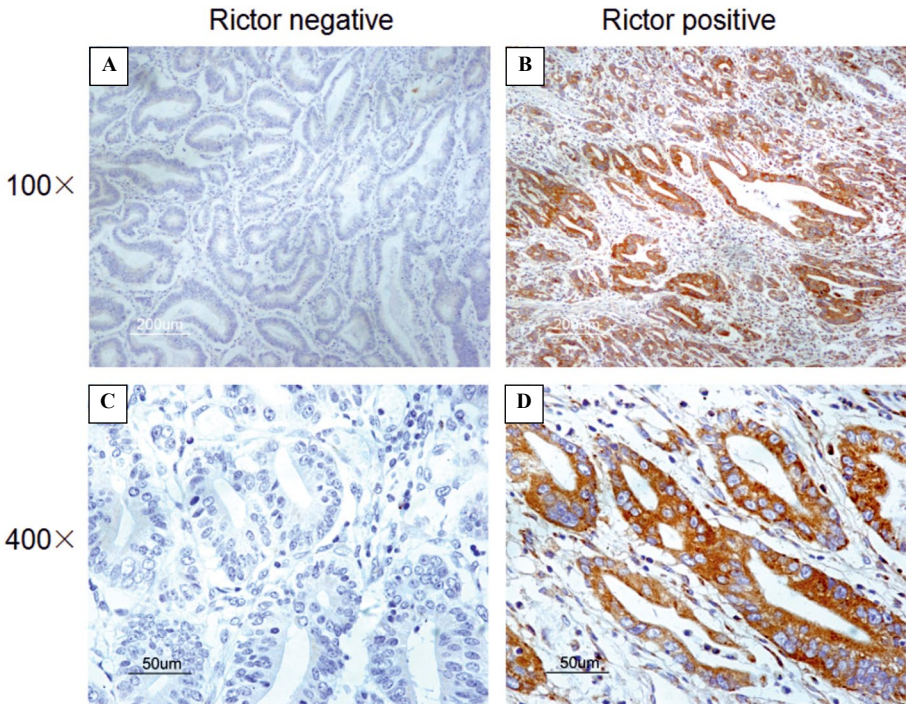

Figure 1. Immunoreactivity of Rictor in gastric cancer tissues. **A.** Negative expression of Rictor in gastric tumor specimens. **B.** Positive expression of Rictor in gastric tumor specimens. **C.** Negative expression of Rictor in gastric tumor specimens. **D.** Positive expression of Rictor in gastric tumor specimens. Magnifications: A and B — 100× C and D — 400×.

cells in 90% ethanol, stained with 0.1% crystal violet and then counted these cells on the lower surface of the well. We randomly selected five low-magnification areas (×100) to calculate the cell numbers.

Apoptosis assays. Annexin-V fluorescein isothiocyanate (FITC)/propidium iodide (PI) apoptosis kit (Bestbio) was used for apoptosis assays by flow cytometry. Cells were collected 48 h after transfection and centrifuged at 300 *g* for 5 min. Then, cells were washed twice in phosphate-buffered saline (PBS) and centrifuged in the same condition. Subsequently, these cells were re-suspended in 400 μl 1 × Binding Buffer. Afterwards, in the dark, these cells were stained with 5 μl Annexin-V FITC and 10 μl PI at 4°C for 15 min. The cells were then subjected to flow cytometry (Cytomics FC 500, Beckman Coulter, Brea, CA, USA) analysis, and quantified by using FlowJo (Version 7.6.2, http://www.flowjo.com/index.php).

Statistical analysis. Assays were independently performed at least three times and one representative experiment data were displayed. The statistical analyses of data were carried out by using SPSS version 13.0 software (SPSS Inc., Chicago, IL, USA). Correlations between Rictor expression level and clinicopathological characteristics of patients were identified by using Chi-square test. For continuous variables, differences among groups were identified by using *t*-test or ANOVA. OS and DFS were assessed by using Kaplan-Meier method. Log-rank test was used to compare the survival distributions between different groups. Univariate and multivariate Cox proportional hazard regression models were used to assess the prognostic value of Rictor in GC. The additive interactions were estimated by using direct counting and Chi-square test. We performed the tests using a 2 × 2 factorial design in order to calculate the attributable proportion (AP) and relative excess risk (RERI) [18–19]. The multiplicative interactions were estimated by using Cox's proportional hazards regression models. *P* value less than 0.05 indicated significantly difference.

Results

Rictor expression in gastric cancer

The expression of Rictor protein in GC tissues was detected by using IHC method. We found that 129 of 250 (51.6%) cancer tissues presented Rictor immunoreactivity (Rictor-IR) which was observed only in the cytoplasm of tumor cells (Fig. 1). Correlations between Rictor status and clinicopathological characteristics of the patients are shown in Table 1. The expression of Rictor was correlated with lymph node metastasis (χ^2 = 9.251, P = 0.002) and TNM stage (χ^2 = 10.840, P = 0.013). The rate of Rictor-IR was 38.2% for stage I, 48.0% for stage II, 62.1% for stage III, 75.0% for stage IV, respectively. The positive

Table 1. Relationships between Rictor expression and clinicopathological factors of patients

Factors	Cases	Rictor positive/n (%)	χ^2-value	P-value
Gender				
Male	191	96 (50.3)	0.580	0.446
Female	59	33 (55.9)		
Age (years)				
≤ 61	125	66 (52.8)	0.144	0.704
> 61	125	63 (50.4)		
WHO Grading				
Well differentiated	7	2 (28.6)	5.038	0.081
Moderately differentiated	78	34 (43.6)		
Poorly differentiated	165	93 (56.4)		
Lauren classification				
Intestinal	161	81(50.3)	0.422	0.810
Diffuse	73	40 (54.8)		
Mixed	16	8 (50.0)		
Location				
Proximal (cardia or fundus)	57	25 (43.9)	1.771	0.183
Distal (corpus, antrum or pylorus)	193	104 (53.9)		
Depth of invasion				
T1	40	15 (37.5)	4.888	0.180
T2	14	6 (42.9)		
T3	170	95 (55.9)		
T4	26	13 (50.0)		
Lymph node				
Negative	126	53 (42.1)	9.251	**0.002**
Positive	124	76 (61.3)		
TNM stage				
I	68	26 (38.2)	10.840	**0.013**
II	75	36 (48.0)		
III	103	64 (62.1)		
IV	4	3 (75.0)		
***H. pylori* status**				
Negative	98	58 (59.2)	3.712	0.054
Positive	152	71 (46.7)		

Abbreviations: WHO — World Health Organization; *H. pylori* — *Helicobacter pylori*.

staining rate of Rictor in GC patients with more advanced stage was significantly higher than in those with low grade stage. The positive staining rate of Rictor was 76 of 124 (61.3%) in lymph node metastasis group, compared to 53 of 126 (42.1%) in non-lymph node metastasis group. We also observed a relatively higher positive rate of Rictor in tissues with poor differentiation ($\chi^2 = 5.038$, P = 0.081) and in tissues without *H. pylori* infection than in tissues with *H. pylori* infection ($\chi^2 = 3.712$, P = 0.054); however, these differences did not reach statistical significance. We did not find significant correlations between Rictor expression and gender, age, Lauren classification, tumor location as well as depth of invasion in GC patients (all P > 0.05). Our results indicated that high Rictor expression was correlated with more

aggressive behavior including advanced stage and lymphatic metastasis.

Prognostic value of Rictor in gastric cancer

We explored the role of Rictor expression in prognosis of GC. The log-rank test was used to assess the association between Rictor expression and the prognosis of patients after surgery. The median OS in patients with positive Rictor status was 78.3 months (95% confidence interval (CI) = 28.8–127.8), while the mean OS was 94.7 months (95% CI = 87.2–102) in patients with negative Rictor status (P = 0.008). The median DFS in patients with positive Rictor status was 65.2 months (95% CI = 28.5–102.0), while the mean DFS was 90.5 months (95% CI = 82.3–98.7) in patients with negative Rictor status (P = 0.006). The OS and DFS curves are shown in Figure 2.

Then, we determined the relationship of Rictor status with DFS and OS in GC patients with surgical resection by using Cox proportional hazard model (Table 2). Univariate analyses indicated that Rictor status was associated with the OS of GC patients, showing that patients with Rictor-IR had relatively shorter survival time (HR = 1.617, 95% CI = 1.131–2.311, P = 0.008). Univariate analyses also showed that patients with Rictor (+) had relatively shorter DFS (HR = 1.631, 95% CI = 1.147–2.319, P = 0.006). When adjusting for gender, age, TNM stage, WHO grading, Lauren classification, invasion depth, tumor location and lymph node metastases, multivariate analyses showed that positive Rictor status was independent predictor for OS (HR = 1.554, 95% CI = 1.076–2.244, P = 0.019) and DFS (HR = 1.556, 95% CI = 1.081–2.240, P = 0.017). Our results revealed that Rictor IHC status may be associated with the prognosis of GC.

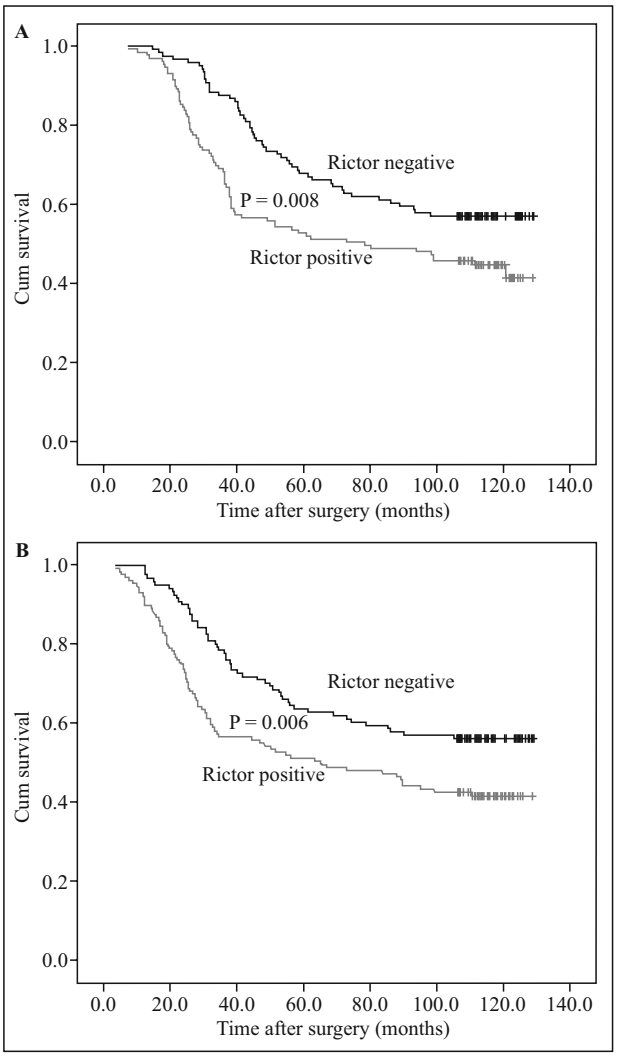

Figure 2. Overall survival (**A**) and Disease-free survival (**B**) in the entire group of 250 gastric cancer patients with respect to Rictor expression assessed by immunohistochemistry.

Rictor expression in primary carcinomas and corresponding lymph node metastases related to clinical outcome

Furthermore, we performed IHC analysis of Rictor on 124 lymph node metastases specimens. In 47 cases, Rictor-IR was found both in primary carcinomas and lymph node metastases whereas in 32 cases we did not detect Rictor-IR in these locations. In 45 cases, the expression of Rictor was found either in primary carcinomas or lymph node metastases. The Rictor-IRs in primary carcinomas and lymph node metastases were consistent ($\kappa = 0.369$, $P < 0.001$).

Then, patients were divided into three groups depending on the status of Rictor-IR in primary carcinomas and lymph node metastases. Univariate analysis revealed obvious survival differences among the three groups, but not significantly different (P = 0.090) (Fig. 3). The median OS of patients with Rictor-IR in both primary carcinomas and lymph node metastases was 33.6 months (95% CI = 22.7–44.4), 68.3 months (95% CI = 30.0–107.0) in patients with lack of Rictor-IR in both primary carcinomas and lymph node metastases (P = 0.036). The median OS of patients with Rictor-IR was 48.9 months (95% CI = 25.1–72.7) in either primary carcinomas or lymph node metastases. Rictor expression both in the primary carcinomas and lymph node metastases was correlated with the worst prognosis of GC patients (Fig. 3).

Additive and multiplicative interaction analysis of Rictor expression and H. pylori infection involved in the prognosis of patients with gastric cancer

H. pylori infection was considered as an independent protective factor for GC patients in our previous studies

Table 2. Univariate and multivariate Cox regression analysis of Rictor expression and survival of patients

Survival	Univariate analysis		Multivariate analysis[a]	
	HR (95% CI)	P-value	HR (95% CI)	P-value
OS				
Rictor negative	1.0 [Reference]	–	1.0 [Reference]	–
Rictor positive	1.617 (1.131–2.311)	**0.008**	1.554 (1.076–2.244)	**0.019**
DFS				
Rictor negative	1.0 [Reference]	–	1.0 [Reference]	–
Rictor positive	1.631 (1.147–2.319)	**0.006**	1.556 (1.081–2.240)	**0.017**

[a]Adjusted for gender, age, TNM stage, WHO grading, Lauren classification, tumor location, depth of invasion and lymph node metastasis. Abbreviations: HR — hazard ratio; CI — confidence interval; OS — overall survival; DFS — disease-free survival.

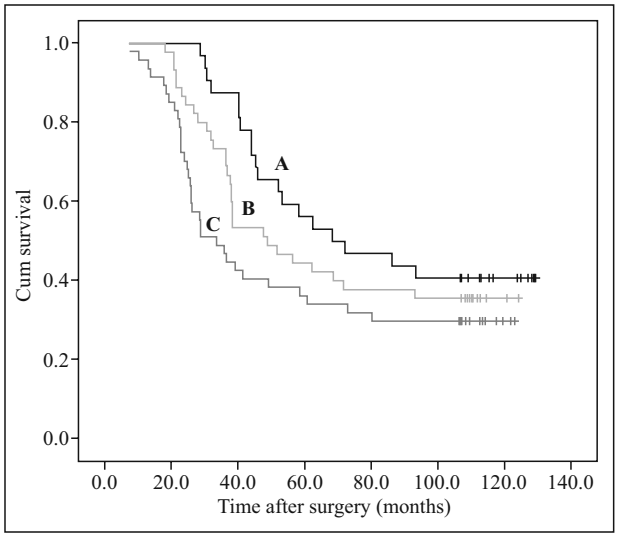

Figure 3. Overall survival of 124 gastric cancer patients with lymph node metastases according to different Rictor status in primary tumor and lymph node metastases (P = 0.090). **A.** Rictor was negative in both primary tumor and lymph node metastases. **B.** Rictor was positive in either primary tumor or lymph node metastases. **C.** Rictor was positive in both primary tumor and lymph node metastases. P = 0.276 (A *vs.* B), P = 0.036 (A *vs.* C), P = 0.209 (B *vs.* C).

[12, 20]. The update survival data resulted in similar findings. In order to explore the interaction between Rictor expression and *H. pylori* infection involved in patient prognosis, additive and multiplicative models were used for analysis. The results of interaction analysis for OS and DFS are shown in Table 3. A significant additive interaction was observed between Rictor expression and *H. pylori* status for OS (HR = 2.586, 95% CI = 1.613–4.146, P < 0.0001) and DFS (HR = 2.662, 95% CI = 1.680–4.218, P < 0.0001). The AP due to interaction was 0.343 for OS and 0.393 for DFS. The RERI due to interaction was 0.886 for OS and 1.047 for DFS. When adjusting for other prognostic factors including gender, age, TNM stage, WHO grading, Lauren classification, invasion depth, tumor location and lymph node metastasis, an additive interaction was still observed between Rictor expression and *H. pylori* status for OS (HR = 2.506, 95% CI = 1.532–4.098, P = 0.0003) and DFS (HR = 2.550, 95% CI = 1.573–4.134, P = 0.0001). The AP due to interaction was 0.413 for OS and 0.433 for DFS. The RERI due to interaction was 1.035 for OS and 1.104 for DFS. We have also observed significant multiplicative interaction between Rictor expression and *H. pylori* status for OS (HR = 2.165, 95% CI = 1.475–3.179, P < 0.0001) and DFS (HR = 2.276, 95% CI = 1.576–3.306, P < 0.0001) by Cox's proportional hazards regression. When adjusting for other prognostic factors including gender, age, TNM stage, WHO grading, Lauren classification, tumor location, invasion depth as well as lymph node metastasis, the results showed a consistent tendency toward a multiplicative interaction between Rictor expression and *H. pylori* status for OS (HR = 2.197, 95% CI = 1.472–3.277, P < 0.001) and DFS (HR = 2.255, 95% CI = 1.525–3.333, P < 0.0001).

Effects of Rictor on gastric cancer cell proliferation, migration, invasion and apoptosis

To evaluate the implication of Rictor in GC cell proliferation, migration, invasion and apoptosis, specific siRNAs against Rictor were generated for Rictor silencing. As shown in Figure 4A, Rictor expression was inhibited in the cell lines BGC-823 and SGC-7901 by using RNA interference technology. A panel of three Rictor siRNA sequences was transiently transfected into GC cells, screening for the sequence providing the greatest Rictor knockdown. Western blot analysis revealed a dramatically reduction of Rictor protein expression in GC cells 48 h post transfection with siRictor, especially for sequence siRic.3, which was used for all further studies.

Table 3. Proportional hazard models depicting the additive and multiplied interaction between Rictor expression and *H. pylori* status involved in gastric cancer patients' prognosis

Model with interaction term	HR (95%CI)	P-value	HR[a] (95%CI)	P[a]-value
Overall survival (OS)				
Additive				
H. pylori+/Rictor–	1.0 [Reference]	–	1.0 [Reference]	–
H. pylori–/Rictor–	1.355 (0.775–2.369)	0.287	1.230 (0.694–2.181)	0.479
H. pylori+/Rictor+	1.345 (0.830–2.180)	0.229	1.241 (0.760–2.027)	0.389
***H. pylori*–/Rictor+**	2.586 (1.613–4.146)	**< 0.0001**	2.506 (1.532–4.098)	**0.0003**
Multiplied				
*H. pylori**Rictor	2.165 (1.475–3.179)	**< 0.0001**	2.197 (1.472–3.277)	**< 0.001**
Disease-free survival (DFS)				
Additive				
H. pylori+/Rictor–	1.0 [Reference]	–	1.0 [Reference]	–
H. pylori–/Rictor–	1.322 (0.759–2.305)	0.325	1.235 (0.700–2.181)	0.466
H. pylori+/Rictor+	1.294 (0.801–2.088)	0.292	1.210 (0.743–1.972)	0.443
***H. pylori*–/Rictor+**	2.662 (1.680–4.218)	**< 0.0001**	2.550 (1.573–4.134)	**0.0001**
Multiplied				
***H. pylori**Rictor**	2.276 (1.576–3.306)	**< 0.0001**	2.255 (1.525–3.333)	**< 0.0001**

[a]Adjusted for other prognostic factors: sex, age, TNM stage, WHO grading, Lauren classification, tumor location, depth of invasion and lymph node metastasis. Abbreviations: HR — hazard ratio; CI — confidence interval; OS — overall survival; DFS — disease-free survival; H.pylori — Helicobacter pylori.

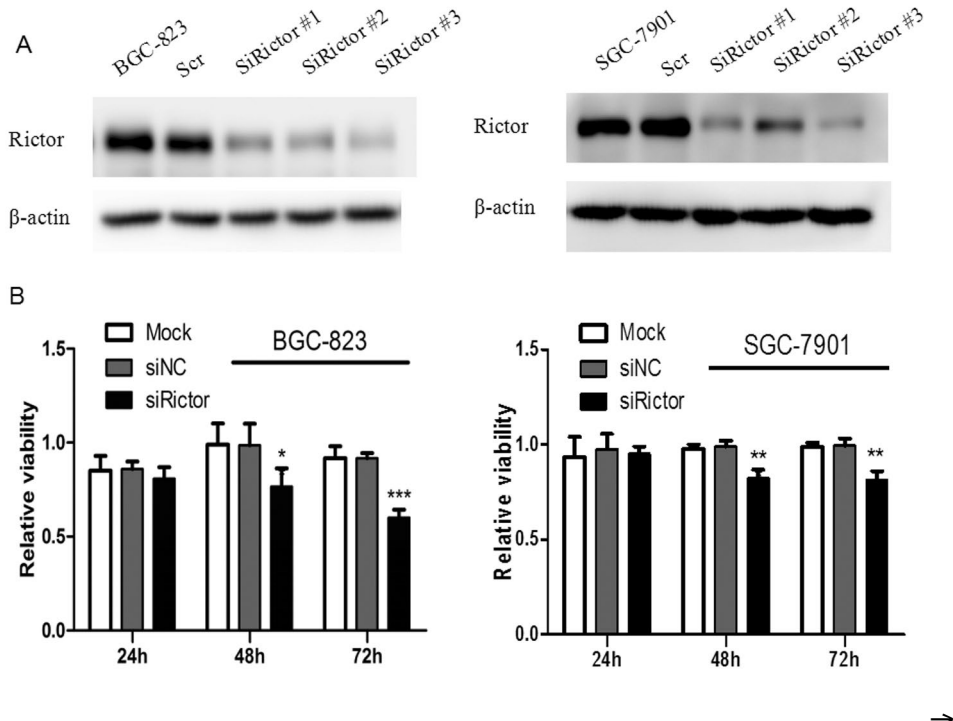

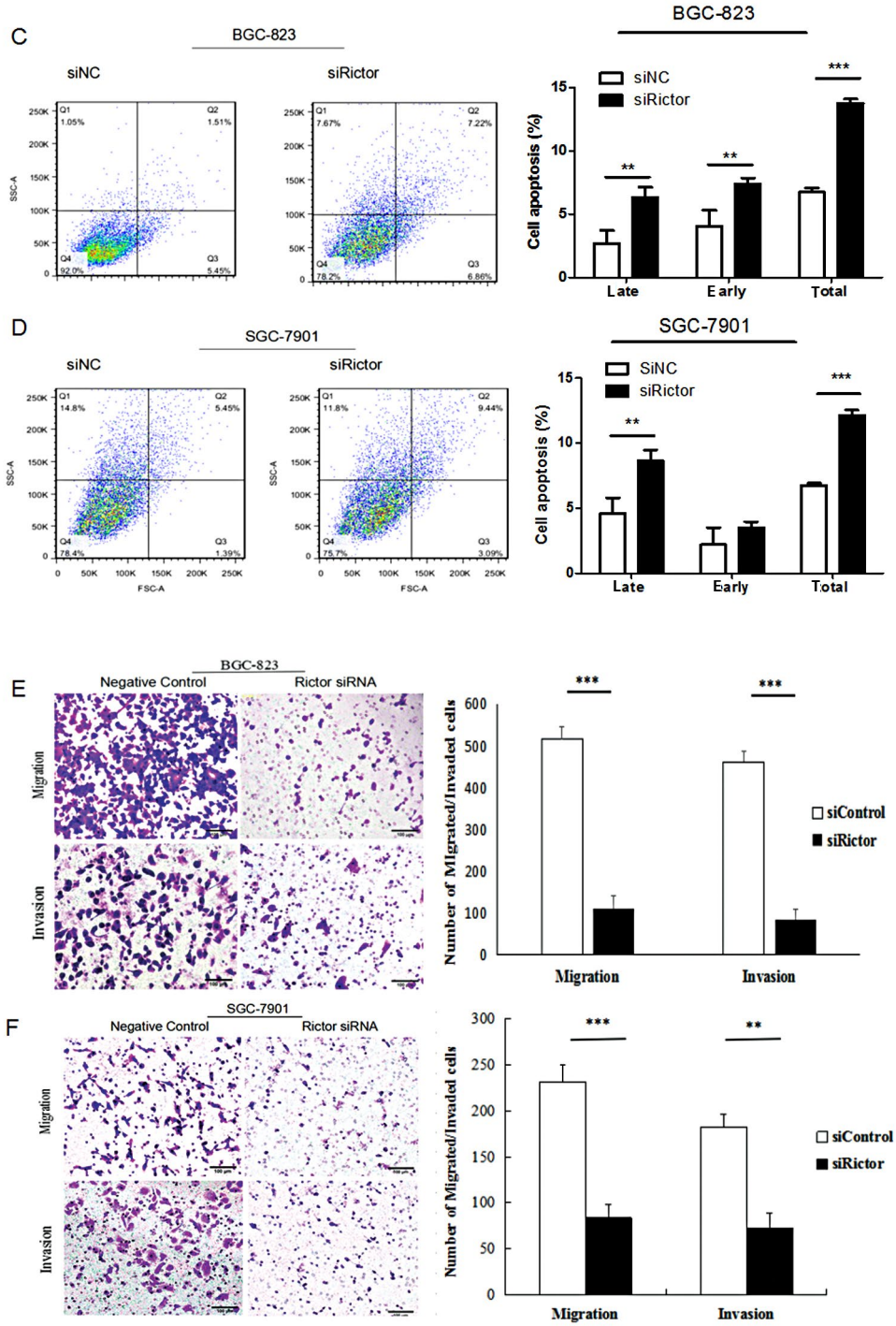

Figure 4. Functional effects of Rictor siRNA on gastric cancer cell proliferation, apoptosis, migration and invasion. **A.** Knockdown of Rictor by siRNA was confirmed by Western blot in BGC-823 and SGC-7901 cells. β-actin served as an internal control. **B.** Suppression of Rictor significantly inhibited gastric cancer cell proliferation. **C–D.** Suppression of Rictor significantly induced cell apoptosis. **E–F.** Suppression of Rictor significantly inhibited the migration and invasion of BGC-823 and SGC-7901 cells. Figure is representative of 3 experiments with similar results. Data represent the mean ± SEM. Bars represent mean and whiskers SD. *P < 0.05, **P < 0.01, ***P < 0.001.

We next examined the biological effects of siRNA--mediated Rictor knockdown on GC cells. CCK-8 assay was used to investigate the functions of Rictor regarding GC cell proliferation (Fig. 4B). Compared with the control group, the proliferation rate in BGC-823 cells transfected with siRictor was significantly

decreased at 48 h and 72 h of incubation ($P < 0.05$). Similarly, the proliferation rate in SGC-7901 cells transfected with siRictor also showed a significant decrease at 48 h and 72 h of incubation ($P < 0.05$). All of these data showed that knockdown of Rictor could impair the growth of GC cells.

Annexin V staining and cytometry analysis were used to assess the effects of Rictor on GC cell apoptosis. Knocking down Rictor expression significantly promoted cell apoptosis in BGC-823 and SGC-8901 cells (Fig. 4C, D). These results indicated that Rictor may act as an oncogene involved in the promotion of GC cell proliferation and inhibition of GC cell apoptosis.

Transwell assays were used to explore the influence of Rictor on GC cell migration and invasion. Migration and invasion assays indicated that pore transfer capacity of GC cells was significantly decreased in cells transfected with siRictor compared to control group (Fig. 4E, F). These results revealed that Rictor played a promotion role in the migration and invasion of GC cells.

Discussion

In this study, Rictor was identified to be often upregulated in GC tissues. We found that overexpression of Rictor was associated with tumor stage and lymph node metastasis. A relatively higher positive rate of Rictor was observed in tissues with poor differentiation and negative *H. pylori* status. Through long period of follow-up, univariate and multivariate analyses revealed that the patients with positive Rictor status had relatively shorter survival time. Patients with Rictor upregulated both in the primary carcinomas and lymph node metastases had the worst prognosis. The additive and multiplicative interactions between Rictor expression and *H. pylori* status involved in patient prognosis were identified for the first time. Our in vitro experiment showed that knockdown of Rictor could suppress GC cell proliferation, induce apoptosis and inhibit tumor migration and invasion. Collectively, our findings demonstrated that Rictor, acting as an oncogene, may be a potential prognostic biomarker and therapeutic target in GC.

In previous studies, elevated Rictor expression was associated with some clinicopathological factors such as age, invasion depth, tumor size, pathological stage, lymph node metastasis and tumor thrombus in some malignancies [9–11]. Consistent with these findings, we also found the association between Rictor expression and TNM stage as well as lymph node metastasis. Rictor was significantly upregulated in advanced-stage GC tissues and lymph node metastases. In the current work, we explored the survival time of different groups of patients depending on the status of Rictor on primary carcinomas and lymph node metastases. Rictor immunoreactivity in primary carcinomas as well as in the corresponding metastatic lymph nodes correlated with the worst clinical outcome. These results suggest that Rictor may be involved in the process of cancer metastases, indicating the pattern of more aggressive behavior which can be harbored on metastases.

To our knowledge, only a few studies [10, 11] focused on the relationship between Rictor expression and GC prognosis. In the study of Bian *et al.*, Rictor expression was not an independent prognostic indicator when adjusting other factors [10]. In our study, we had the chance to explore such an association based on a cohort of GC patients. Several years ago, the GC cohort was established at the study department, and we collected and preserved the gastric tumor as well as normal tissues of GC patients who underwent surgery [12]. Based on the same study population, a long follow-up was possible and the prognosis data of the patients were prospectively recorded. Our data has shown Rictor as an independent unfavorable prognostic indicator for OS and DFS both in univariate and multivariate analysis.

This is the first study to show a synergistic relationship between Rictor overexpression and negative *H. pylori* status in predicting patient prognosis. The current study demonstrated significant additive and multiplicative interactions between Rictor expression and *H. pylori* status. This was suggestive of a much poorer survival for patients whose GC tissues were Rictor positive (+) and *H. pylori* negative (–). In our previous study, *H. pylori* (+) and *H. pylori* (–) GC tissues exhibited different biological behavior and prognosis, indicating different genetic alterations. It can be speculated that Rictor overexpression as potential oncogenic driver for *H. pylori* negative GC. Future studies will be needed to investigate whether patients with GC can be stratified based on Rictor amplification and *H. pylori* infection status to derive clinical benefits from target therapies. The molecular mechanisms need to be further elucidated.

Rictor is a key component of mTORC2, functions in actin cytoskeleton, cell proliferation and survival. Existing evidence has demonstrated the oncogenic roles of mTORC2/Rictor in regulating cancer cell migration, invasion and metastasis in breast, prostate, colorectal cancers and gliomas [21–25]. Cui *et al*. has identified that over-activation of mTORC2 in glioma could promote proliferation and migration of neoplastic cells [23]. Tumor growth of pancreatic cancer can be impaired by the inhibition of mTORC2 component RICTOR [26]. Cheng *et al*. found that patients with

a new subset of lung cancer with Rictor amplification could benefit from mTOR1/2 inhibitors [27]. Similar results were identified across solid tumors by Kim *et al*., which led to further pre-clinical and clinical investigation with AZD2014 in Rictor-amplified GC [28]. Other authors showed that inhibition of mTORC2/ /Rictor in colon cancer reduced cell proliferation *in vitro* and the formation of tumor xenografts *in vivo* [21]. These studies suggested the importance of Rictor in various cancers. In the study, we confirmed the effects of Rictor on GC cells. Consistent with the role of Rictor as a potential cancer promoter, the results showed that the invasion and migration abilities of GC cells were decreased whereas apoptosis of tumor cells was increased when Rictor was knocked down. The proliferation ability of GC cells was also impaired by inhibition of Rictor. It has been viewed as a promising approach for targeting Rictor in GC therapy, since Rictor may play important role in GC development.

Taken together, Rictor may be an unfavorable prognostic factor for GC patients. To our knowledge, this report is the first to demonstrate significant additive and multiplicative interactions between Rictor expression and *H. pylori* status in predicting patient prognosis. In addition, the present study provided the evidence that Rictor functions as an oncogene that facilitates GC cell proliferation and promotes cell migration and invasion. The results suggest therapeutic potential of targeting Rictor in gastric cancer.

Acknowledgments

This study was supported by the National Natural Science Foundation of China (grant number: 81602115 to F. Wang, grant number: 81572430, 81872047 to G. Sun and grant number: 81522009 to H. Wang), the Foundation of Supporting Program for the Excellent Young Faculties in Universities of Anhui Province in China (gxyq2019012).

Conflict of interest

The authors declare no conflict of interest.

References

1. Bray F, Ferlay J, Soerjomataram I, et al. Global cancer statistics 2018: GLOBOCAN estimates of incidence and mortality worldwide for 36 cancers in 185 countries. CA Cancer J Clin. 2018; 68(6): 394–424, doi: 10.3322/caac.21492, indexed in Pubmed: 30207593.
2. Toiyama Y, Tanaka K, Kitajima T, et al. Serum angiopoietin-like protein 2 as a potential biomarker for diagnosis, early recurrence and prognosis in gastric cancer patients. Carcinogenesis. 2015; 36(12): 1474–1483, doi: 10.1093/carcin/bgv139, indexed in Pubmed: 26420253.
3. Yuan DD, Zhu ZX, Zhang X, et al. Targeted therapy for gastric cancer: Current status and future directions (Review). Oncol Rep. 2016; 35(3): 1245–1254, doi: 10.3892/or.2015.4528, indexed in Pubmed: 26718131.
4. Betz C, Hall MN. Where is mTOR and what is it doing there? J Cell Biol. 2013; 203(4): 563–574, doi: 10.1083/jcb.201306041, indexed in Pubmed: 24385483.
5. Guertin DA, Sabatini DM. Defining the role of mTOR in cancer. Cancer Cell. 2007; 12(1): 9–22, doi: 10.1016/j.ccr.2007.05.008, indexed in Pubmed: 17613433.
6. Sarbassov DD, Ali SM, Kim DH, et al. Rictor, a novel binding partner of mTOR, defines a rapamycin-insensitive and raptor-independent pathway that regulates the cytoskeleton. Curr Biol. 2004; 14(14): 1296–1302, doi: 10.1016/j.cub.2004.06.054, indexed in Pubmed: 15268862.
7. Li H, Lin J, Wang X, et al. Targeting of mTORC2 prevents cell migration and promotes apoptosis in breast cancer. Breast Cancer Res Treat. 2012; 134(3): 1057–1066, doi: 10.1007/s10549-012-2036-2, indexed in Pubmed: 22476852.
8. Wang X, Lai P, Zhang Z, et al. Targeted inhibition of mTORC2 prevents osteosarcoma cell migration and promotes apoptosis. Oncol Rep. 2014; 32(1): 382–388, doi: 10.3892/or.2014.3182, indexed in Pubmed: 24840134.
9. Jiang WJ, Feng RX, Liu JT, et al. RICTOR expression in esophageal squamous cell carcinoma and its clinical significance. Med Oncol. 2017; 34(3): 32, doi: 10.1007/s12032-017-0894-5, indexed in Pubmed: 28132115.
10. Bian Y, Wang Z, Xu J, et al. Elevated Rictor expression is associated with tumor progression and poor prognosis in patients with gastric cancer. Biochem Biophys Res Commun. 2015; 464(2): 534–540, doi: 10.1016/j.bbrc.2015.07.001, indexed in Pubmed: 26159923.
11. Wen SY, Li CH, Zhang YL, et al. Rictor is an independent prognostic factor for endometrial carcinoma. Int J Clin Exp Pathol. 2014; 7(5): 2068–2078, indexed in Pubmed: 24966915.
12. Wang F, Sun GP, Zou YF, et al. Helicobacter pylori infection predicts favorable outcome in patients with gastric cancer. Curr Oncol. 2013; 20(5): e388–e395, doi: 10.3747/co.20.1417, indexed in Pubmed: 24155636.
13. Meimarakis G, Winter H, Assmann I, et al. Helicobacter pylori as a prognostic indicator after curative resection of gastric carcinoma: a prospective study. Lancet Oncol. 2006; 7(3): 211–222, doi: 10.1016/s1470-2045(06)70586-1.
14. Li Na, Tang B, Jia YP, et al. CagA Protein Negatively Regulates Autophagy and Promotes Inflammatory Response via c-Met-PI3K/Akt-mTOR Signaling Pathway. Front Cell Infect Microbiol. 2017; 7: 417, doi: 10.3389/fcimb.2017.00417, indexed in Pubmed: 28983474.
15. Hu G, Guo L, Ye G. Helicobacter pylori infection impairs gastric epithelial barrier function via microRNA-100-mediated mTOR signaling inhibition. Mol Med Rep. 2018; 18(1): 587–594, doi: 10.3892/mmr.2018.8971, indexed in Pubmed: 29749451.
16. Marrelli D, Pinto E, Stefano ADe, et al. Clinical utility of CEA, CA 19-9, and CA 72-4 in the follow-up of patients with resectable gastric cancer. Am J Surg. 2001; 181(1): 16–19, doi: 10.1016/s0002-9610(00)00549-3, indexed in Pubmed: 11248169.
17. Gulhati P, Cai Q, Li J, et al. Targeted inhibition of mammalian target of rapamycin signaling inhibits tumorigenesis of colorectal cancer. Clin Cancer Res. 2009; 15(23): 7207–7216, doi: 10.1158/1078-0432.CCR-09-1249, indexed in Pubmed: 19934294.
18. Andersson T, Alfredsson L, Källberg H, et al. Calculating measures of biological interaction. Eur J Epidemiol. 2005;

20(7): 575–579, doi: 10.1007/s10654-005-7835-x, indexed in Pubmed: 16119429.
19. Hughes T, Adler A, Kelly JA, et al. BIOLUPUS Network. Evidence for gene-gene epistatic interactions among susceptibility loci for systemic lupus erythematosus. Arthritis Rheum. 2012; 64(2): 485–492, doi: 10.1002/art.33354, indexed in Pubmed: 21952918.
20. Wang F, Liu J, Zou Y, et al. MicroRNA-143-3p, up-regulated in H. pylori-positive gastric cancer, suppresses tumor growth, migration and invasion by directly targeting AKT2. Oncotarget. 2017; 8(17): 28711–28724, doi: 10.18632/oncotarget.15646, indexed in Pubmed: 28404925.
21. Roulin D, Cerantola Y, Dormond-Meuwly A, et al. Targeting mTORC2 inhibits colon cancer cell proliferation in vitro and tumor formation in vivo. Mol Cancer. 2010; 9: 57, doi: 10.1186/1476-4598-9-57, indexed in Pubmed: 20226010.
22. Gulhati P, Bowen KA, Liu J, et al. mTORC1 and mTORC2 regulate EMT, motility, and metastasis of colorectal cancer via RhoA and Rac1 signaling pathways. Cancer Res. 2011; 71(9): 3246–3256, doi: 10.1158/0008-5472.CAN-10-4058, indexed in Pubmed: 21430067.
23. Cui Y, Zhao J, Yi L, et al. microRNA-153 Targets mTORC2 Component Rictor to Inhibit Glioma Cells. PLoS One. 2016; 11(6): e0156915, doi: 10.1371/journal.pone.0156915, indexed in Pubmed: 27295037.
24. Guan B, Wu K, Zeng J, et al. Tumor-suppressive microRNA-218 inhibits tumor angiogenesis via targeting the mTOR component RICTOR in prostate cancer. Oncotarget. 2017; 8(5): 8162–8172, doi: 10.18632/oncotarget.14131, indexed in Pubmed: 28030804.
25. Werfel TA, Wang S, Jackson MA, et al. Selective mTORC2 Inhibitor Therapeutically Blocks Breast Cancer Cell Growth and Survival. Cancer Res. 2018; 78(7): 1845–1858, doi: 10.1158/0008-5472.CAN-17-2388, indexed in Pubmed: 29358172.
26. Schmidt KM, Hellerbrand C, Ruemmele P, et al. Inhibition of mTORC2 component RICTOR impairs tumor growth in pancreatic cancer models. Oncotarget. 2017; 8(15): 24491––24505, doi: 10.18632/oncotarget.15524, indexed in Pubmed: 28445935.
27. Cheng H, Zou Y, Ross JS, et al. RICTOR Amplification Defines a Novel Subset of Patients with Lung Cancer Who May Benefit from Treatment with mTORC1/2 Inhibitors. Cancer Discov. 2015; 5(12): 1262–1270, doi: 10.1158/2159-8290.CD-14-0971, indexed in Pubmed: 26370156.
28. Kim ST, Kim SY, Klempner SJ, et al. Rapamycin-insensitive companion of mTOR (RICTOR) amplification defines a subset of advanced gastric cancer and is sensitive to AZD2014-mediated mTORC1/2 inhibition. Ann Oncol. 2017; 28(3): 547–554, doi: 10.1093/annonc/mdw669, indexed in Pubmed: 28028034.

Submitted: 8 January, 2020
Accepted after reviews: 16 June, 2020
Available as AoP: 25 June, 2020

FOLIA HISTOCHEMICA ET CYTOBIOLOGICA
Vol. 58, No. 2, 2020
pp. 108–116

ORIGINAL PAPER

VIA MEDICA

Downregulation of Polo-like kinase-1 (PLK-1) expression is associated with poor clinical outcome in uveal melanoma patients

Tomasz Berus[1], Anna Markiewicz[2], Katarzyna Kobylinska[3], Przemyslaw Biecek[3], Jolanta Orlowska-Heitzman[4], Bozena Romanowska-Dixon[2], Piotr Donizy[5]

[1]Department of Ophthalmology, 4th Military Clinical Hospital with Polyclinic, Wroclaw, Poland

[2]Department of Ophthalmology and Ocular Oncology, the Jagiellonian University, Medical College, Krakow, Poland

[3]Faculty of Mathematics, Informatics and Mechanics University of Warsaw, Warsaw, Poland

[4]Department of Pathomorphology, the Jagiellonian University, Medical College, Krakow, Poland

[5]Department of Pathomorphology and Oncological Cytology, Wroclaw Medical University, Wroclaw, Poland

Abstract

Introduction. Uveal melanoma (UM) is the most common primary eye tumour in adults. Distant metastases are seen in 50% of cases regardless of treatment, which contributes to high mortality rates. Polo-like kinase-1 (PLK-1) is a protein regulator of mitotic entry and cytokinesis. Increased PLK-1 expression has been shown in different tumours, which makes its inhibition a potential treatment target. To date, no study has been published to discuss the prognostic role of PLK-1 expression in patients with uveal melanoma.

Material and methods. We assessed by immunohistochemistry PLK-1 expression in uveal melanoma cells collected in 158 patients treated by primary enucleation. We determined the correlation between PLK-1 levels evaluated by the immunoreactivity scale (IRS) method and detailed clinical as well as histological parameters. Additionally, we determined the association between PLK-1 expression levels and long-term prognosis.

Results. Elevated PLK-1 expression in tumour cells, defined as IRS >2, was observed in 70% (111/158) of cases, whereas low expression or no expression was seen in the remaining 30% (47/158) of patients. There was a significant correlation between low PLK-1 expression and a higher clinical tumour stage (pT, $p = 0.04$) as well as a higher AJCC prognostic stage group ($p = 0.037$). We observed an inverse correlation between PLK-1 expression and tumour cell pigment content ($p = 0.0019$). There was no correlation between PLK-1 expression and other histological parameters such as mitotic rate or histological subtype. The Kaplan-Meier's analysis demonstrated that low PLK-1 expression was associated with significantly reduced overall survival ($p = 0.0058$). A similar trend, albeit not significant, was observed for disease-free survival ($p = 0.088$).

Conclusions. Downregulated PLK-1 expression is a negative prognostic factor in uveal melanoma. It warrants further, multicentre research on prognostic role of PLK-1 expression and possibility of PLK-1 inhibition in uveal melanoma. *(Folia Histochemica et Cytobiologica 2020, Vol. 58, No. 2, 108–116)*

Key words: uveal melanoma; polo-like kinase-1; prognostic factor; IHC

Introduction

Uveal melanoma (UM) is the most common primary eye tumour in adults. The incidence in the general population is below 10 cases per million population per year [1]. We have previously discussed epidemi-

Correspondence address: Tomasz Berus, MD
Department of Ophthalmology
4th Military Clinical Hospital with Polyclinic,
Weigla 5, 50–981 Wroclaw, Poland
e-mail: tberus@op.pl

ology and prognostic factors in uveal melanoma in a comprehensive review [2]. Depending on the clinical course of disease, chances for vision preservation and patient expectations, primary tumours can be effectively treated with brachytherapy, proton beam irradiation, transpupillary thermotherapy, local resection, endoresection, or enucleation. Regardless of the selected treatment modality, almost 50% of affected patients develop distant metastases, which contributes to very high mortality rates [2]. Conventional chemotherapy, isolated hepatic perfusion, immunoembolisation, surgery and checkpoint inhibitors have very limited efficacy in metastatic UM with the median overall survival (OS) of 1.07 years (range: 0.59–2.50 years) across all treatment modalities [3].

Polo-like kinase-1 (PLK-1) is a serine/threonine-protein kinase consisting of a highly conservative N-terminal kinase domain (KD) of 252 amino-acids and a C-terminal Polo-box domain (PBD), that is, two conserved polo-box regions of 30 amino-acids connected via a short linker. An interaction with peptides phosphorylated by other kinases involved in the cell cycle changes the PBD conformation. Acting like a clip, it docks PLK-1 at its accurately selected target site during the appropriate stage of cell division [4, 5], whereby PLK-1 becomes a master regulator of mitosis and cytokinesis [6].

PLK-1 has been implicated in Cdk1-cyclin B activation at mitotic entry, centrosome maturation, bipolar spindle formation, activation of anaphase promoting complex/cyclosome (APC/C), accumulation of spindle assembly checkpoint (SAC) proteins at kinetochores, sister chromatid separation, as well as cytokinesis [7–9]. Furthermore, PLK-1 has recently been shown to play a role in microtubule dynamics, DNA replication, chromosome dynamics, p53 regulation, and recovery from the G2 DNA-damage checkpoint [10].

PLK-1 overexpression has been demonstrated in a number of human tumours, where it often correlates with increased cellular proliferation and poor prognosis [11–18], *e.g.* in skin melanoma [19, 20]. Therefore, it is currently considered a prooncogenic factor, which exerts its effect by affecting cell cycle checkpoints and causing genetic instability. As such, it is the target of cancer therapies [21], which seems potentially plausible also in UM [22].

The aim of this study was to assess the PLK-1 expression in UM as well as its correlation with detailed clinical and pathological parameters, and long-term survival.

Material and methods

Patients. The study group consisted of 158 patients with uveal melanoma treated by primary enucleation at the Department of Ophthalmology and Ocular Oncology, Medical College, Jagiellonian University in Krakow, Poland, diagnosed in 2002–2011. Patients were enrolled in the study based on the availability of their medical records and tissue specimens, which included paraffin blocks and histological slides. Comprehensive clinical data was retrieved from the archived medical records, and details of diagnostic and therapeutic procedures performed were sourced out from the Ocular Oncology Outpatient Clinic, University Hospital, Krakow, Poland. The study was reviewed and approved by the ethical committees of the Jagiellonian University, Krakow, Poland (decision no. 122.6120.58.216), and the Wroclaw Medical University, Wroclaw, Poland (decision no. KB-500/2017).

Records were reviewed for clinical and pathological data including age, sex, affected eye, largest basal diameter and thickness of the tumour, tumour staging (pT and AJCC prognostic stage group), tumour location relative to the equator, ciliary body involvement, clinical tumour pigmentation and shape, concomitant glaucoma and/or retinal detachment, histological subtype, scleral and/or optic nerve infiltration, as well as tumour necrosis. Additionally, detailed histological parameters, such as mitotic rate, presence of tumour-infiltrating lymphocytes (TILs), nuclear pseudoinclusions (NPIs), intranuclear grooves, multinucleated giant cells and haemorrhage, as well as tumour cell pigmentation level were considered. The largest basal diameter and thickness of the tumour were described in line with the guidelines of the American Joint Committee on Cancer (AJCC) [23].

Immunohistochemistry. Paraffin blocks with tissues of 158 primary uveal melanomas were cut with a microtome to prepare 4 μm-thick sections which were subsequently mounted on sialinized slides (Agilent DAKO, Santa Clara, CA, USA). The slides then underwent automated dewaxing, rehydration and heat-induced epitope retrieval with EnVision Target Retrieval Solution (Agilent DAKO) for 30 min at 97°C in PT Link Pre-Treatment Module for Tissue Specimens (DAKO). Automated immunohistochemical staining with anti-PLK-1 (rabbit monoclonal antibody, 208G4; #4513; dilution 1:100; Cell Signalling Technology, Danvers, MA, USA) was performed in Autostainer Link 48 (DAKO) and Liquid Permanent Red (Agilent DAKO) was utilized as a detection system. Human colorectal adenocarcinoma was stained as positive control. Negative controls were processed using FLEX Rabbit Negative Control, Ready-to-Use (Agilent DAKO) in place of the primary antibody.

Evaluation of PLK-1 expression. The expression of PLK-1 in UM cells (Fig. 1) was determined using the semi-quantitative method. The two IHC reaction parameters used were the percentage of cells with a positive cytoplasmic reaction (the percentage of reactive tissue) and the intensity of cytoplasmic PLK-1 reaction. The Remmele and Stegner semiquantitative immunoreactive score (IRS) was used to compute

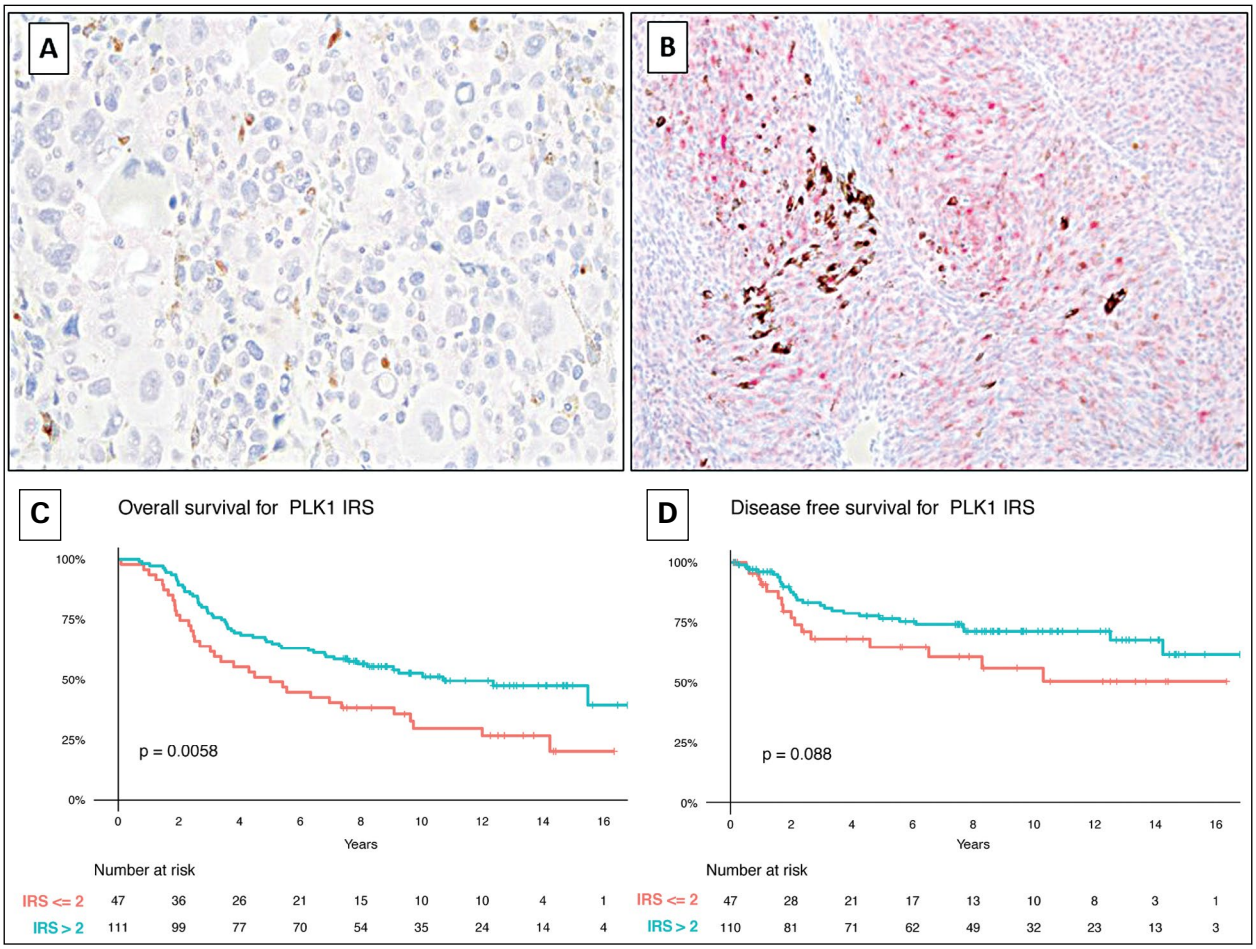

Figure 1. PLK-1 expression in uveal melanoma. **A.** Lack of PLK-1 immunoreactivity in neoplastic cells (400×). **B.** Enhanced expression of PLK-1 in uveal melanoma cells (200×). **C.** Kaplan-Meier analysis of the prognostic impact of PLK-1 expression in uveal melanoma patients. Downregulation of PLK-1 expression was significantly correlated with reduced overall survival (p = 0.0058). **D.** A similar trend as in (C), albeit not significant, was observed for disease-free survival (p = 0.088) (D).

the above parameters [24]. In the IRS, the percentage of reactive cells scores 0–4 points and staining intensity scores 0–3 points. The ultimate IRS is a product of multiplication of the above parameters, ranging between 0 and 12 points.

Tumoural pigmentation was assessed using a three-step scale: 0 – lack of melanin or melanin was present in < 10% of melanoma cells; 1 (low): melanin was present in 11–50% of melanoma cells; 2 (high): melanin was present in 51–100% melanoma cells.

Statistical analysis. Statistical analysis was performed using the R language [25] and the survminer tool [26]. For the purposes of correlation analysis, we assumed a dichotomous division of PLK-1 expression into low and high corresponding to semiquantitative IRS of ≤ 2 and > 2, respectively. In order to determine the overall survival (OS) and disease-free survival (DFS), Kaplan-Meier curves and the log-rank test were used; all analyses were carried out using the survival package for R [25, 26]. In order to determine the correlations between the PLK-1 expression and continuous variables, the Wilcoxon two-sample test was used. The correlations between PLK-1 expression and binary variables were determined using the Fisher's exact test while the correlations with other categorical variables were determined using the chi-square test. The p value below 0.05 was considered significant for all comparisons.

Results

PLK-1 immunoreactivity in uveal melanoma cells

High PLK-1 expression, defined as IRS > 2, was observed in 70% (111/158) of specimens, whereas low expression or no expression was seen in the remaining 30% (47/158) of specimens, including undetectable PLK-1 expression in 3.8% (6/158) of specimens (Fig. 1A–B). The mean IRS for PLK-1 expression in tumour cells was 4 (median: 4).

Correlations of PLK-1 expression with clinical parameters

There was a significant inverse correlation between PLK-1 expression and the basal tumour diameter ($p = 0.044$). Similarly, there was a significant correlation between low PLK-1 expression and higher clinical tumour stage (pT, $p = 0.040$) as well as AJCC prognostic stage group ($p = 0.037$). Interestingly, high PLK-1 expression was associated with more advanced age of patients ($p = 0.0019$), whereas low PLK-1 expression was associated with a higher incidence of retinal detachment secondary to UM ($p = 0.0076$) (Table 1).

Correlations of PLK-1 expression with histological parameters

There was an inverse correlation between PLK-1 expression and tumour cell pigment content ($p = 0.0019$) and a positive correlation between PLK-1 expression and the presence of nuclear grooves ($p = 0.017$). On the other hand, low PLK-1 expression significantly correlated with the presence of nuclear pseudoinclusions (NPIs) ($p = 0.0071$). There was no significant correlation between PLK-1 expression and other histological parameters such as mitotic rate or histological subtype (Table 2).

The effect of PLK-1 expression on long-term survival

The Kaplan-Meier's analysis demonstrated that low PLK-1 expression was associated with significantly reduced overall survival ($p = 0.0058$). A similar trend, albeit not significant, was observed for disease-free survival ($p = 0.088$) (Fig. 1C–D).

Discussion

PLK-1 is a protein with important roles in the regulation of the cell cycle. It is physiologically strongly expressed in tissues undergoing intensive proliferation, such as testes, thymus, and spleen, or during proliferative events such as in developing embryos *etc*. [27]. Hence, the question follows whether high PLK-1 expression in tumour cells is associated with oncogenesis or intense cell proliferation. Over 25 years of PLK-1-related research, a number of papers have been published to characterise its mechanism of action, both in the cell cycle and in cellular response to DNA damage [28–30].

PLK-1 and the p53 tumour suppressor protein are closely related in an inhibitory feedback loop, which is the fundamental mechanism whereby PLK-1 participates in oncogenesis [28]. High PLK-1 expression leading to cell cycle acceleration was demonstrated in tumour cells lacking functional p53. However, overexpression of PLK-1 inhibits the effect of p53. As a result, the cell is incapable of apoptosis in response to DNA damage and continues to function with increasing genomic instability and aneuploidy [29, 31–36]. PLK-1 depletion breaks the vicious circle restoring the p53 function. Importantly, it also triggers tumour cell apoptosis whilst preserving normal cells [37–39]. Apart from interaction with p53, PLK-1 may regulate tumorigenesis by modulating Myc stability [40, 41] and affecting PTEN [42] as well as other tumour suppressors [43].

This provides the theoretical basis for the research of PLK-1 inhibitors, which block kinase domain or PBD [4]. One of them, volasertib, was granted a Breakthrough Therapy designation by the FDA [44] and reached Phase III of clinical trials in patients aged 65 years and above with previously untreated acute myeloid leukaemia [45, 46]. Nevertheless, despite expectations based on preclinical study findings, no significant clinical success of PLK-1 inhibitors has been reported to date [47]. The search for more selective inhibitors is ongoing, as kinases, including those of the PLK family, can often exert opposing effects on tumour development [27, 47]. Using PLK-1 inhibitors in combination therapy as agents reducing cancer resistance to other therapies, seems promising at the moment [46, 47].

As pharmaceutical companies and researchers have been trying to find a therapeutic use of PLK-1 inhibitors, the kinase has also sparked significant controversies [48]. While PLK-1 overexpression is linked to uncontrolled cell proliferation and impaired response to DNA damage, its low expression impairs cell cycle processes, such as spindle assembly or centrosome maturation, leading to tumour progression [30]. Recent studies in mice not only confirmed these findings, but also demonstrated the potential of PLK-1 as a tumour suppressor [49–52]. This inhibition effect is possible in interaction with specific oncogenes (such as K-Ras, Her2 or APC^{min}) and may be caused by up- or down-regulation of PLK-1 expression [43], both of which can induce genetic instability and aneuploidy. Hence, the outcomes are likely determined by other factors rather than a stand-alone PLK-1 expression level, such as oncogenesis, tumour progression or potential protective/repair mechanisms.

De Cárcer [43] analysed data from the Cancer Genome Atlas (TGCA) [53] and the Kaplan Meier Plotter database [54, 55], demonstrating that PLK-1 overexpression may lead to different outcomes depending on tumour type. For example, it was linked to shorter overall survival (OS) in patients with lung, bladder, and kidney clear cell carcinoma, whereas in patients with thymoma, lung squamous cell carcino-

Table 1. Summary statistics for relation between expression of PLK-1 in uveal melanoma cells and clinical parameters

Clinical parameters	PLK-1 IRS		
	Low ≤ 2 (No. 47)	High > 2 (No. 111)	*p* value
Age in years (18–86)[a]	63 (58–72)	59 (51–64)	**0.0019**
Gender[c]			1.0
Female	24 (51%)	58 (52%)	
Male	23 (49%)	53 (48%)	
Side[c]			0.86
Right	22 (47%)	54 (49%)	
Left	25 (53%)	57 (51%)	
Largest basal tumour diameter (by AJCC)[b]			**0.044**
> 9–12 mm	2 (4%)	11 (10%)	
> 12–15 mm	3 (6%)	24 (22%)	
> 15–18 mm	13 (28%)	26 (23%)	
> 18 mm	29 (62%)	50 (45%)	
Greatest tumour height (by AJCC)[b]			0.75
≤ 3 mm	0 (0%)	1 (1%)	
> 3–6 mm	2 (4%)	12 (11%)	
> 6–9 mm	13 (28%)	28 (25%)	
> 9–12 mm	16 (34%)	40 (36%)	
> 12–15 mm	12 (26%)	24 (22%)	
> 15 mm	4 (9%)	6 (5%)	
Primary tumour (pT)[b]			**0.040**
2	1 (2%)	12 (11%)	
3	11 (23%)	39 (35%)	
4	35 (74%)	60 (54%)	
Stage[b]			**0.037**
IIA	0 (0%)	10 (9%)	
IIB	10 (21%)	33 (30%)	
IIIA	15 (32%)	37 (33%)	
IIIB	16 (34%)	26 (23%)	
IIIC	6 (13%)	5 (5%)	
Localization[b]			0.53
In front of the equator	39 (55%)	32 (49%)	
Equator	11 (15%)	8 (12%)	
Behind the equator	21 (30%)	25 (38%)	
Ciliary body involvement[c]			0.41
Ciliary body not involved	53 (63%)	56 (70%)	
Ciliary body involved	31 (37%)	24 (30%)	
Degree of pigmentation[b]			0.21
Amelanotic	4 (10%)	22 (21%)	
Mild pigmentation	16 (38%)	42 (39%)	
Intense pigmentation	22 (52%)	43 (40%)	
Shape[c]			0.73
Dome shape	23 (50%)	60 (55%)	
Mushroom shape	23 (50%)	50 (45%)	
Retinal detachment[c]			**0.0076**
No RD	3 (6%)	28 (25%)	
Coexistence of RD	44 (94%)	83 (75%)	
Glaucoma[c]			0.46
No glaucoma	39 (83%)	96 (87%)	
Coexistence of glaucoma	8 (17%)	14 (13%)	

[a]*p* value of Wilcoxon two sample test; [b]*p* value of chi^2 test; [c]*p* value of Fisher's exact test. Statistically significant results ($P < 0.05$) are shown in bold text.

Table 2. Summary statistics for relation between expression of PLK-1 in uveal melanoma cells and histopathological parameters

Histopathological parameters	PLK-1 IRS		
	Low ≤ 2 (No. 47)	High > 2 (No. 111)	*p* value
Histologic subtype[a]			0.46
Spindle cell melanoma	6 (13%)	23 (21%)	
Mixed cell melanoma	34 (72%)	75 (68%)	
Epithelioid cell melanoma	7 (15%)	13 (12%)	
Mitotic rate[b]			0.47
0–4	32 (70%)	70 (63%)	
5–31	14 (30%)	41 (37%)	
Scleral infiltration[b]			0.16
None or intrascleral infiltration	44 (94%)	109 (98%)	
Full-thickness infiltration	3 (6%)	2 (2%)	
Invasion of the optic nerve[a]			0.59
No invasion	38 (81%)	91 (82%)	
Optic nerve head invasion	9 (19%)	17 (15%)	
Optic nerve invasion	0 (0%)	3 (3%)	
Necrosis[b]			0.60
No necrosis	39 (85%)	92 (88%)	
Necrosis present	7 (15%)	12 (12%)	
Marked pleomorphism[b]			0.57
No marked pleomorphism	41 (87%)	101 (91%)	
Marked pleomorphism present	6 (13%)	10 (9%)	
TILs[b]			0.44
No TILs	43 (91%)	96 (86%)	
TILs present	4 (9%)	15 (14%)	
Multinucleated giant cells[b]			0.54
No multinucleated giant cells	34 (72%)	86 (77%)	
Multinucleated giant cells present	13 (28%)	25 (23%)	
NPIs[b]			**0.0071**
No NPIs	21 (45%)	76 (68%)	
NPIs present	26 (55%)	35 (32%)	
Intranuclear grooves[b]			**0.017**
No intranuclear grooves	43 (91%)	82 (74%)	
Intranuclear grooves present	4 (9%)	29 (26%)	
Haemorrhage[b]			0.082
No haemorrhage	33 (70%)	93 (84%)	
Haemorrhage present	14 (30%)	18 (16%)	
Pigmentation[a]			**0.0019**
Lack of melanin	2 (4%)	12 (11%)	
Low pigmentation	18 (38%)	68 (61%)	
High pigmentation	27 (57%)	31 (28%)	

[a]*p* value of chi^2 test; [b]*p* value of Fisher's exact test. Statistically significant results ($P < 0.05$) are shown in bold font.

ma or rectal adenocarcinoma, higher PLK-1 levels seemed to be associated with significantly longer OS [43]. Interestingly, PLK-1 overexpression did not affect survival prognosis in patients with ovarian cancer, stomach adenocarcinoma and cervical squamous cell carcinoma [43]. Nevertheless, the effect of PLK-1 expression on long-term follow-up in patients with uveal melanoma was not assessed in that study.

In our research, contrary to most mentioned above reports, indicating PLK-1 as a prognostic factor for poor prognosis, we observed high PLK-1 expression in smaller UM tumours and in patients with lower clinical tumour stage (pT and AJCC). Furthermore, the Kaplan-Meier survival analysis demonstrated that high PLK-1 expression was associated with significantly shorter overall survival, with a similar trend in disease-free survival.

PLK-1 is one of the 50 most overexpressed genes of primary cutaneous melanoma (CM) and its metastases as compared with melanocytic nevi [56]. The expression of PLK-1 is dynamically regulated during CM cell cycle and is vital for cell survival. The level of PLK-1 varies with tumour thickness and has prognostic value for CM. High PLK-1 expression was significantly correlated with unfavourable clinical outcome [20]. Also for thin melanomas (< 0.75 mm), which should have an excellent prognosis, high expression of PLK-1 is a reliable marker for identifying patients at high risk of metastasis [19]. Kinetochore complex component (NDC80), a downstream effector in the PLK-1 signalling pathways, involved in the occurrence of many tumours and highly expressed in a variety of cancer types, is also associated with poor overall survival in metastatic CM [57, 58]. Therefore, determining PLK-1 expression, in addition to the Breslow thickness, can help identify patients with aggressive tumours.

Specific inhibition of PLK-1 using the commercially available inhibitor BI 2536 leads to a dose- and time-dependent decrease in CM cell viability and induction of apoptosis [56]. Moreover it shows an additive effect with simultaneous inhibition of the mitogen-activated protein kinase (MAPK) signalling pathway or inhibition of mitogen-activated protein kinase/extracellular signal-regulated kinase (MEK). Therefore, combination of MAPK/MEK and PLK-1 inhibition could be a potentially attractive therapeutic strategy in CM [56, 59–61].

Unfortunately, many differences between CM and UM mean that other therapeutic strategies need to be sought in uveal melanoma. One of proposed explanations is ocular immune privilege, which may likely alter signalling pathways in UM compared to skin melanoma [62]. The studies assessing biological drugs in UM have not shown good results to date [62]. Although PLK-1 inhibitors appear promising in oncology, and PLK-1 has been identified as one of UM-specific therapeutic targets [22], our results support the need for multicentre studies on prognostic significance of PLK-1 expression in uveal melanoma and in vitro studies to determine the effect of inducing or inhibiting PLK-1 expression in UM cells.

Funding

A statutory subsidy by the Polish Ministry of Science and Higher Education as part of grants ST.B130.18.030 and SUB.B130.20.022 (record numbers in the Simple system). PBi was financially supported by the Polish National Science Centre under Opus Grant number 2017/27/B/ST6/0130.

References

1. Singh AD, Turell ME, Topham AK. Uveal melanoma: trends in incidence, treatment, and survival. Ophthalmology. 2011; 118(9): 1881–1885, doi: 10.1016/j.ophtha.2011.01.040, indexed in Pubmed: 21704381.
2. Berus T, Halon A, Markiewicz A, et al. Clinical, Histopathological and Cytogenetic Prognosticators in Uveal Melanoma — A Comprehensive Review. Anticancer Res. 2017; 37(12): 6541–6549, doi: 10.21873/anticanres.12110, indexed in Pubmed: 29187428.
3. Rantala ES, Hernberg M, Kivelä TT. Overall survival after treatment for metastatic uveal melanoma: a systematic review and meta-analysis. Melanoma Res. 2019; 29(6): 561–568, doi: 10.1097/CMR.0000000000000575, indexed in Pubmed: 30664106.
4. Elia AEH, Rellos P, Haire LF, et al. The molecular basis for phosphodependent substrate targeting and regulation of Plks by the Polo-box domain. Cell. 2003; 115(1): 83–95, doi: 10.1016/s0092-8674(03)00725-6, indexed in Pubmed: 14532005.
5. Archambault V, Lépine G, Kachaner D. Understanding the Polo Kinase machine. Oncogene. 2015; 34(37): 4799–4807, doi: 10.1038/onc.2014.451, indexed in Pubmed: 25619835.
6. Combes G, Alharbi I, Braga LG, et al. Playing polo during mitosis: PLK1 takes the lead. Oncogene. 2017; 36(34): 4819–4827, doi: 10.1038/onc.2017.113, indexed in Pubmed: 28436952.
7. Petronczki M, Lénárt P, Peters JM. Polo on the Rise-from Mitotic Entry to Cytokinesis with Plk1. Dev Cell. 2008; 14(5): 646–659, doi: 10.1016/j.devcel.2008.04.014, indexed in Pubmed: 18477449.
8. Lénárt P, Petronczki M, Steegmaier M, et al. The small-molecule inhibitor BI 2536 reveals novel insights into mitotic roles of polo-like kinase 1. Curr Biol. 2007; 17(4): 304–315, doi: 10.1016/j.cub.2006.12.046, indexed in Pubmed: 17291761.
9. Barr FA, Silljé HHW, Nigg EA. Polo-like kinases and the orchestration of cell division. Nat Rev Mol Cell Biol. 2004; 5(6): 429–440, doi: 10.1038/nrm1401, indexed in Pubmed: 15173822.
10. Liu XS, Song B, Liu X. The substrates of Plk1, beyond the functions in mitosis. Protein Cell. 2010; 1(11): 999–1010, doi: 10.1007/s13238-010-0131-x, indexed in Pubmed: 21153517.
11. Wolf G, Hildenbrand R, Schwar C, et al. Polo-like kinase: a novel marker of proliferation: Correlation with estrogen-receptor expression in human breast cancer. Pathology — Research and Practice. 2000; 196(11): 753–759, doi: 10.1016/s0344-0338(00)80107-7.

12. Donizy P, Halon A, Surowiak P, et al. Augmented expression of Polo-like kinase 1 is a strong predictor of shorter cancer-specific overall survival in early stage breast cancer at 15-year follow-up. Oncol Lett. 2016; 12(3): 1667–1674, doi: 10.3892/ol.2016.4890, indexed in Pubmed: 27602103.
13. Tokumitsu Y, Mori M, Tanaka S, et al. Prognostic significance of polo-like kinase expression in esophageal carcinoma. Int J Oncol. 1999; 15(4): 687–692, doi: 10.3892/ijo.15.4.687, indexed in Pubmed: 10493949.
14. Wolf G, Elez R, Doermer A, et al. Prognostic significance of polo-like kinase (PLK) expression in non-small cell lung cancer. Oncogene. 1997; 14(5): 543–549, doi: 10.1038/sj.onc.1200862, indexed in Pubmed: 9053852.
15. Takai N, Miyazaki T, Fujisawa K, et al. Expression of polo-like kinase in ovarian cancer is associated with histological grade and clinical stage. Cancer Lett. 2001; 164(1): 41–49, doi: 10.1016/s0304-3835(00)00703-5, indexed in Pubmed: 11166914.
16. Macmillan JC, Hudson JW, Bull S, et al. Comparative expression of the mitotic regulators SAK and PLK in colorectal cancer. Ann Surg Oncol. 2001; 8(9): 729–740, doi: 10.1007/s10434-001-0729-6, indexed in Pubmed: 11597015.
17. Cheng MW, Wang BC, Weng ZQ, et al. Clinicopathological significance of Polo-like kinase 1 (PLK1) expression in human malignant glioma. Acta Histochem. 2012; 114(5): 503–509, doi: 10.1016/j.acthis.2011.09.004, indexed in Pubmed: 22000864.
18. Lin P, Wen DY, Dang YW, et al. Comprehensive and Integrative Analysis Reveals the Diagnostic, Clinicopathological and Prognostic Significance of Polo-Like Kinase 1 in Hepatocellular Carcinoma. Cell Physiol Biochem. 2018; 47(3): 925––947, doi: 10.1159/000490135, indexed in Pubmed: 29843122.
19. Kneisel L, Strebhardt K, Bernd A, et al. Expression of polo-like kinase (PLK1) in thin melanomas: a novel marker of metastatic disease. J Cutan Pathol. 2002; 29(6): 354–358, doi: 10.1034/j.1600-0560.2002.290605.x, indexed in Pubmed: 12135466.
20. Strebhardt, K. Prognostic Value of Pololike Kinase Expression in Melanomas. JAMA: The Journal of the American Medical Association. 2000; 283(4): 479–480, doi: 10.1001/jama.283.4.479.
21. Otto T, Sicinski P. Cell cycle proteins as promising targets in cancer therapy. Nat Rev Cancer. 2017; 17(2): 93–115, doi: 10.1038/nrc.2016.138, indexed in Pubmed: 28127048.
22. Bailey FP, Clarke K, Kalirai H, et al. Kinome-wide transcriptional profiling of uveal melanoma reveals new vulnerabilities to targeted therapeutics. Pigment Cell Melanoma Res. 2018; 31(2): 253–266, doi: 10.1111/pcmr.12650, indexed in Pubmed: 28972303.
23. Grossniklaus HE, Finger PT, Harbour JW, et al. Protocol for the Examination of Specimens From Patients With Uveal Melanoma, https://documents.cap.org/protocols/cp-uveal-melanoma-17protocol-4000.pdf (2017, accessed 12 March 2020).
24. Remmele W, Stegner HE. [Recommendation for uniform definition of an immunoreactive score (IRS) for immunohistochemical estrogen receptor detection (ER-ICA) in breast cancer tissue]. Pathologe. 1987; 8(3): 138–140, indexed in Pubmed: 3303008.
25. R Core Team. R: A language and environment for statistical computing. R Foundation for Statistical Computing, Vienna, Austria, https://www.r-project.org/ (2019, accessed 12 March 2020).
26. Kassambara A, Kosinski M, Biecek P. survminer: Drawing Survival Curves using 'ggplot2'. R package version 0.4.6., https://cran.r-project.org/package=survminer (2019, accessed 12 March 2020).
27. Strebhardt K. Multifaceted polo-like kinases: drug targets and antitargets for cancer therapy. Nat Rev Drug Discov. 2010; 9(8): 643–660, doi: 10.1038/nrd3184, indexed in Pubmed: 20671765.
28. Eckerdt F, Yuan J, Strebhardt K. Polo-like kinases and oncogenesis. Oncogene. 2005; 24(2): 267–276, doi: 10.1038/sj.onc.1208273, indexed in Pubmed: 15640842.
29. Takai N, Hamanaka R, Yoshimatsu J, et al. Polo-like kinases (Plks) and cancer. Oncogene. 2005; 24(2): 287–291, doi: 10.1038/sj.onc.1208272, indexed in Pubmed: 15640844.
30. Weng Ng WT, Shin JS, Roberts TL, et al. Molecular interactions of polo-like kinase 1 in human cancers. J Clin Pathol. 2016; 69(7): 557–562, doi: 10.1136/jclinpath-2016-203656, indexed in Pubmed: 26941182.
31. Liu XS, Li H, Song B, et al. Polo-like kinase 1 phosphorylation of G2 and S-phase-expressed 1 protein is essential for p53 inactivation during G2 checkpoint recovery. EMBO Rep. 2010; 11(8): 626–632, doi: 10.1038/embor.2010.90, indexed in Pubmed: 20577264.
32. Yang X, Li H, Zhou Z, et al. Plk1-mediated phosphorylation of Topors regulates p53 stability. J Biol Chem. 2009; 284(28): 18588–18592, doi: 10.1074/jbc.C109.001560, indexed in Pubmed: 19473992.
33. Chen J, Dai Gu, Wang YQ, et al. Polo-like kinase 1 regulates mitotic arrest after UV irradiation through dephosphorylation of p53 and inducing p53 degradation. FEBS Lett. 2006; 580(15): 3624–3630, doi: 10.1016/j.febslet.2006.05.047, indexed in Pubmed: 16753148.
34. Dias SS, Hogan C, Ochocka AM, et al. Polo-like kinase-1 phosphorylates MDM2 at Ser260 and stimulates MDM2-mediated p53 turnover. FEBS Lett. 2009; 583(22): 3543–3548, doi: 10.1016/j.febslet.2009.09.057, indexed in Pubmed: 19833129.
35. Ando K, Ozaki T, Yamamoto H, et al. Polo-like kinase 1 (Plk1) inhibits p53 function by physical interaction and phosphorylation. J Biol Chem. 2004; 279(24): 25549–25561, doi: 10.1074/jbc.M314182200, indexed in Pubmed: 15024021.
36. McKenzie L, King S, Marcar L, et al. p53-dependent repression of polo-like kinase-1 (PLK1). Cell Cycle. 2010; 9(20): 4200–4212, doi: 10.4161/cc.9.20.13532, indexed in Pubmed: 20962589.
37. Liu X, Erikson RL. Polo-like kinase (Plk)1 depletion induces apoptosis in cancer cells. Proc Natl Acad Sci U S A. 2003; 100(10): 5789–5794, doi: 10.1073/pnas.1031523100, indexed in Pubmed: 12732729.
38. Liu X, Lei M, Erikson RL. Normal cells, but not cancer cells, survive severe Plk1 depletion. Mol Cell Biol. 2006; 26(6): 2093–2108, doi: 10.1128/MCB.26.6.2093-2108.2006, indexed in Pubmed: 16507989.
39. Guan R, Tapang P, Leverson JD, et al. Small interfering RNA-mediated Polo-like kinase 1 depletion preferentially reduces the survival of p53-defective, oncogenic transformed cells and inhibits tumor growth in animals. Cancer Res. 2005; 65(7): 2698–2704, doi: 10.1158/0008-5472.CAN-04-2131, indexed in Pubmed: 15805268.
40. Ren Y, Bi C, Zhao X, et al. PLK1 stabilizes a MYC-dependent kinase network in aggressive B cell lymphomas. J Clin Invest. 2018; 128(12): 5517–5530, doi: 10.1172/JCI122533, indexed in Pubmed: 30260324.
41. Xiao D, Yue M, Su H, et al. Polo-like Kinase-1 Regulates Myc Stabilization and Activates a Feedforward Circuit Promoting Tumor Cell Survival. Mol Cell. 2016; 64(3): 493–506, doi: 10.1016/j.molcel.2016.09.016, indexed in Pubmed: 27773673.

42. Choi BH, Pagano M, Dai W. Plk1 protein phosphorylates phosphatase and tensin homolog (PTEN) and regulates its mitotic activity during the cell cycle. J Biol Chem. 2014; 289(20): 14066–14074, doi: 10.1074/jbc.M114.558155, indexed in Pubmed: 24706748.
43. Cárcer Gde. The Mitotic Cancer Target Polo-Like Kinase 1: Oncogene or Tumor Suppressor? Genes. 2019; 10(3): 208, doi: 10.3390/genes10030208.
44. Boehringer Ingelheim's investigational volasertib receives FDA Breakthrough Therapy designation, https://www.boehringer-ingelheim.us/press-release/boehringer-ingelheims-investigational-volasertib-receives-fda-breakthrough-therapy (accessed 1 February 2020).
45. Volasertib in Combination With Low-dose Cytarabine in Patients Aged 65 Years and Above With Previously Untreated Acute Myeloid Leukaemia, Who Are Ineligible for Intensive Remission Induction Therapy (POLO-AML-2), https://clinicaltrials.gov/ct2/show/NCT01721876?term=polo-aml-2&rank=1 (accessed 1 February 2020).
46. Van den Bossche J, Lardon F, Deschoolmeester V, et al. Spotlight on Volasertib: Preclinical and Clinical Evaluation of a Promising Plk1 Inhibitor. Med Res Rev. 2016; 36(4): 749–786, doi: 10.1002/med.21392, indexed in Pubmed: 27140825.
47. Gutteridge RE, Ndiaye MA, Liu X, et al. Plk1 Inhibitors in Cancer Therapy: From Laboratory to Clinics. Mol Cancer Ther. 2016; 15(7): 1427–1435, doi: 10.1158/1535-7163.MCT-15-0897, indexed in Pubmed: 27330107.
48. Lu LY, Yu X. The balance of Polo-like kinase 1 in tumorigenesis. Cell Div. 2009; 4: 4, doi: 10.1186/1747-1028-4-4, indexed in Pubmed: 19161615.
49. Lu LY, Wood JL, Minter-Dykhouse K, et al. Polo-like kinase 1 is essential for early embryonic development and tumor suppression. Mol Cell Biol. 2008; 28(22): 6870–6876, doi: 10.1128/MCB.00392-08, indexed in Pubmed: 18794363.
50. Wierer M, Verde G, Pisano P, et al. PLK1 signaling in breast cancer cells cooperates with estrogen receptor-dependent gene transcription. Cell Rep. 2013; 3(6): 2021–2032, doi: 10.1016/j.celrep.2013.05.024, indexed in Pubmed: 23770244.
51. de Cárcer G, Venkateswaran SV, Salgueiro L, et al. Plk1 overexpression induces chromosomal instability and suppresses tumor development. Nat Commun. 2018; 9(1): 3012, doi: 10.1038/s41467-018-05429-5, indexed in Pubmed: 30069007.
52. Raab M, Sanhaji M, Matthess Y, et al. PLK1 has tumor-suppressive potential in APC-truncated colon cancer cells. Nat Commun. 2018; 9(1): 1106, doi: 10.1038/s41467-018-03494-4, indexed in Pubmed: 29549256.
53. The Cancer Genome Atlas Program, https://www.cancer.gov/about-nci/organization/ccg/research/structural-genomics/tcga (accessed 1 February 2020).
54. Győrffy B, Lanczky A, Eklund AC, et al. An online survival analysis tool to rapidly assess the effect of 22,277 genes on breast cancer prognosis using microarray data of 1,809 patients. Breast Cancer Res Treat. 2010; 123(3): 725–731, doi: 10.1007/s10549-009-0674-9, indexed in Pubmed: 20020197.
55. The Kaplan Meier plotter, www.kmplot.com (accessed 1 February 2020).
56. Jalili A, Moser A, Pashenkov M, et al. Polo-like kinase 1 is a potential therapeutic target in human melanoma. J Invest Dermatol. 2011; 131(9): 1886–1895, doi: 10.1038/jid.2011.136, indexed in Pubmed: 21654832.
57. Zhang Z, Zhang G, Gao Z, et al. Comprehensive analysis of differentially expressed genes associated with PLK1 in bladder cancer. BMC Cancer. 2017; 17(1): 861, doi: 10.1186/s12885-017-3884-2, indexed in Pubmed: 29246203.
58. Chen J, Wu F, Shi Yu, et al. Identification of key candidate genes involved in melanoma metastasis. Mol Med Rep. 2019; 20(2): 903–914, doi: 10.3892/mmr.2019.10314, indexed in Pubmed: 31173190.
59. Schmit TL, Zhong W, Setaluri V, et al. Targeted depletion of Polo-like kinase (Plk) 1 through lentiviral shRNA or a small-molecule inhibitor causes mitotic catastrophe and induction of apoptosis in human melanoma cells. J Invest Dermatol. 2009; 129(12): 2843–2853, doi: 10.1038/jid.2009.172, indexed in Pubmed: 19554017.
60. Posch C, Cholewa BD, Vujic I, et al. Combined Inhibition of MEK and Plk1 Has Synergistic Antitumor Activity in NRAS Mutant Melanoma. J Invest Dermatol. 2015; 135(10): 2475–2483, doi: 10.1038/jid.2015.198, indexed in Pubmed: 26016894.
61. Chen HY, Villanueva J. Playing Polo-Like Kinase in NRAS-Mutant Melanoma. J Invest Dermatol. 2015; 135(10): 2352–2355, doi: 10.1038/jid.2015.253, indexed in Pubmed: 26358384.
62. Basile MS, Mazzon E, Fagone P, et al. Immunobiology of Uveal Melanoma: State of the Art and Therapeutic Targets. Front Oncol. 2019; 9: 1145, doi: 10.3389/fonc.2019.01145, indexed in Pubmed: 31750244.

Submitted: 12 March, 2020
Accepted after reviews: 22 June, 2020
Available as AoP: 30 June, 2020

FOLIA HISTOCHEMICA ET CYTOBIOLOGICA
Vol. 58, No. 2, 2020
pp. 117–126

ORIGINAL PAPER

VIA MEDICA

Gamma linolenic acid suppresses hypoxia-induced gastric cancer cell growth and epithelial-mesenchymal transition by inhibiting the Wnt/β-catenin signaling pathway

Yan Wang*, Jian Shi, Liya Gong

Department of Nutrition, The second hospital of Hebei Medical University, Shijiazhuang City, Hebei Province, 050000, China

Abstract

Introduction. Gastric cancer is one of the most common malignancies in China and the fifth most common cancer in the world. Gamma linolenic acid (GLA) was reported to have anti-inflammatory and anti-cancer effects. The purpose of this research was to investigate the effect and mechanism of GLA on gastric cancer cell growth under hypoxic conditions.

Material and methods. The hypoxia models of SGC-7901 and MGC-803 cells were established, and then were exposed to different concentrations of 50, 100 or 200 μM GLA. MTT assay, colony formation assay, wound healing assay and transwell assay were used to investigate the effects of GLA treatment on gastric cancer cell growth under hypoxia (1% O_2). The expression of apoptosis- and epithelial-mesenchymal transition (EMT)-related proteins was detected by qPCR and western blot.

Results. GLA treatment significantly decreased viability and inhibited colony formation ($p < 0.05, p < 0.01$) of SGC-7901 and MGC-803 cells under hypoxia. Western blotting analysis showed that GLA treatment decreased the expression of proliferating cell nuclear antigen (PCNA), microchromosome maintenance complex component 2 (MCM-2) and anti-apoptotic protein Bcl-2, while increased the expression of pro-apoptotic proteins (Bax and Cleaved Caspase-3) ($p < 0.05$ and $p < 0.01$). In addition, Wound healing analysis and Transwell assays showed that GLA treatment inhibited the migration and invasion of SGC-7901 and MGC-803 cells in a dose-dependent manner ($p < 0.01$). Western blotting analysis showed that GLA treatment increased the expression of epithelial marker proteins (γ-catenin and E-cadherin), while decreased the expression of stromal and extracellular matrix marker proteins (fibronectin, Snail and β-catenin) ($p < 0.01$). Further analyses showed that GLA treatment decreased the expression of β-catenin in Wnt/β-catenin pathway ($p < 0.01$). Moreover, exogenous Wnt3a reversed the inhibitory effect of GLA on β-catenin expression, and further reversed the inhibitory effect of GLA on gastric cancer cell growth and EMT markers ($p < 0.05, p < 0.01$).

Conclusion. These findings suggest that GLA should be tested in animal models and in clinical studies as a potentially effective bioactive phytochemical substance for the treatment of gastric cancer. *(Folia Histochemica et Cytobiologica 2020, Vol. 58, No. 2, 117–126)*

Key words: Gamma linolenic acid; gastric cancer; SGC-7901 cells; MGC-803 cells; hypoxia; cell growth; Wnt/β-catenin; EMT; apoptosis

Correspondence address: Yan Wang,
Department of Nutrition, The second hospital of Hebei Medical University, 215 Hepingxi Road, Shijiazhuang City, Hebei Province, China
phone: 86+0311-66002787
e-mail: YanWangart@163.com

Introduction

Gastric cancer is one of the most common malignancies in China and the fifth most common cancer in the world [1, 2]. Although great progress has been achieved in the survival rate after surgery, the recurrence and metastasis rates are still high [3]. Chemotherapy plays an important role in the treatment of gastric cancer. However, patients with distant metastasis or recurrent advanced gastric cancer are still incurable, and the median overall survival time of patients with metastatic disease is still not ideal [4]. In addition, the sensitivity of conventional radiotherapy is poor, which makes the 5-year survival rate of gastric cancer patients still less than 30% [5, 6]. In general, since current therapeutic methods are not sufficient for the treatment of patients with gastric cancer [7] many drugs are currently used as complementary strategies for the treatment of this malignancy [8–11]. For example, it has been reported that, arginine, glutamine, and omega-3 PUFA significantly improved the three-month survival rate of patients with gastric cancer [12].

In particular, gamma linolenic acid (GLA) is an omega-6 polyunsaturated fatty acid (PUFA) that is present in plant seed oils, such as *Borago offcinalis* [13], *Oenothera biennis* and *Ribes nigrum* [14]. As early as in 1980, PUFA has been shown to inhibit various cancer cells without affecting normal cells [15–17]. In the past few decades, extensive studies have confirmed the potential anticancer effect of these fatty acids [18–21]. For examples, *in vivo* experiments have shown that GLA exhibits a dose-dependent regulatory effect on an experimental study on hepatocellular carcinoma [22]. Further studies of underlying molecular mechanisms indicated that GLA may exert a chemical protective effect on DEN-induced liver cancer by altering hypoxic microenvironment, mitochondria-mediated death, apoptosis, and anti-inflammatory pathways [22]. In addition, Chas *et al.* used gas chromatography to establish a biochemical profile fatty acids (FA) in the adipose tissue and found that inflammatory breast cancer was associated with decreased levels of eicosapentaenoic acid (EPA) and GLA in breast cancer adipose tissue [23]. However, the role of GLA in the progression of gastric cancer remains unknown.

In this study, we investigated the effects of GLA on the viability, colony formation, migration and invasion *in vitro* in SGC-7901 and MGC-803 cells under hypoxia, and then comprehensively analyzed the epithelial-mesenchymal transition (EMT). The underlying mechanisms were also investigated. The results of our study suggest that GLA may be a potentially attractive bioactive phytochemical for the treatment of gastric cancer.

Materials and methods

Cell culture and treatment. The gastric epithelial cell line GES-1, human gastric cancer cell lines SGC-7901, and MGC-803 were purchased from Cancer Institute of Chinese Academy of Medical Sciences (Beijing, China). SGC-7901 and MGC-803 cells were seeded in RPMI 1640 (GIBCO) supplemented with 10% fetal bovine serum (FBS) (GIBCO, Grand Island, CA, USA), 100 μg/mL streptomycin and 100 μg/mL penicillin (Hyclone, Los Angeles, CA, USA), and cultured at 37°C and 5% CO_2 in a humid sterile incubator. Cells were seeded at a density of 1×10^6 cells into each 100 mm petri dish and cultured until the cells grew to approximately 90% confluence. SGC-7901 and MGC-803 cells hypoxia models were established as previously described [24]. Briefly, SGC-7901 and MGC-803 cells were exposed to 1% O_2, 5% CO_2, and 94% N_2 humidified atmosphere at 37°C under hypoxic conditions, respectively. SGC-7901 and MGC-803 cells were then treated with various concentrations of GLA (50, 100 and 200 μM; Sigma Aldrich, St Louis, MO, USA) under hypoxia.

Cell viability assay. The effect of GLA on the viability of GES-1, SGC-7901 and MGC-803 cells was detected by MTT assay. In brief, GLA was dissolved in RPMI 1640 medium at a concentration of 1 M as a stock solution, which was then mixed with fresh medium to achieve the desired final concentrations (50, 100, 200 μM). Cells were seeded in a 96-well plate at 5×10^3 cells per well under hypoxic conditions. Subsequently, the cells were exposed to different doses of GLA (50, 100 or 200 μM) or 200 ng/mL WNT3a (Abcam, cat.no. ab153563, Cambridge, MA, USA) [25]. The cells in blank control were treated with RPMI 1640 medium only. After incubation of the cells for 48 h, 20 μL of diluted (1 mg/ml) MTT (stock solution was made by dissolving MTT powder in 10 mg/mL of phosphate buffered saline) was added to the cells which were further incubated at 37°C for 4 h. Finally, the absorbance of each well at a wavelength of 570 nm was measured on a Microplate Reader (ELX800, BIO-TEK Instruments, Inc., Doraville, GA, USA). Each treatment was performed in triplicate.

Colony formation assay. GES-1, SGC-7901 and MGC-803 cells were used for colony formation analysis. Briefly, 5×10^5 cells were seeded in 60 mm culture dishes under hypoxia and treated with GLA (50, 100 or 200 μM) or/and Wnt3a (200 ng/ml dissolved immediately before use). After two weeks, cell colonies were stained with crystal violet.

Wound healing assay. Cell migratory ability was tested by wound healing assay. Under hypoxic conditions, 5×10^5 cells were seeded in each well of a 6-well plate and cultured to 90% confluence. Cells were exposed to different doses of GLA (50, 100 or 200 μM) or/and Wnt3a (200 ng/ml) and

cultured to monolayer cells at 37°C. Then the cells were scraped with the tip of a 1 mL sterile pipette. After 24 h, wound recovery was assessed under light microscopy.

Transwell assay. Cell invasive ability was detected by Transwell assay. Cells (3×10^4) were seeded into the transwell upper cavity covered with matrigel and RPMI 1640 medium was added to the lower chamber. Then, cells were treated with different doses of GLA (50, 100 or 200 μM) or/and Wnt3a (200 ng/ml) under hypoxic conditions. After 48 h, the cells in the lower chamber were fixed with methanol and stained with crystal violet. Finally, cell colonies were counted by taking pictures under a light microscope.

Western blotting. The levels of the studied proteins were measured by western blotting. After the cells were lysed in lysis buffer, a whole cell lysate was obtained. Total protein (50–90 μg) was separated on a 10% polyacrylamide gel (SDS-PAGE). Subsequently, the proteins in the gel were transferred to a nitrocellulose membrane and blocked with blocking buffer (1% Tween-20 and 1% BSA, Ph 7.6 in 20 mM TBS) at room temperature for 60 min, and then incubated with antibodies (all from Abcam, Cambridge Science Park, Cambridge, UK) against PCNA (1:1000; cat. no. ab92552), MCM-2 (1:200; cat. no. ab31159), Bcl-2 (1:1000; cat. no. ab185002), Bax (1:500; cat. no. ab53154), Cleaved Caspase-3 (1:500; cat. no. ab49822) or γ-catenin (1:1000; cat. no. ab184919), E-cadherin (1:500; cat. no. ab15148), fibronectin (1:1000; cat. no. ab32419), Snail (1:1000; cat. no. ab229701), β-catenin (1:5000; cat. no. ab32572), GAPDH (1:10000; cat. no. ab181602;) overnight at 4°C or for 3 h at room temperature. The membrane was washed 3 times with TBST (10 min each), and then incubated with anti-mouse or anti-rabbit secondary antibody (1: 1,000; cat. no. umbers 7076 and 14708; Cell Signaling Technology, Danvers, MA, USA) at 37°C for 60 min. The membrane was washed twice with TBST and once with TBS for 15 min each wash. The membrane was then incubated with alkaline phosphatase until an appropriate signal level was visible. The protein band was photographed by FluorChem® Imaging Systems (Alpha Innotech Corp., San Leandro, CA, USA). Quantification was performed spectrophotometrically using ImageJ (National Institutes of Health, Bethesda, MD, USA).

Quantitative real-time polymerase chain reaction (qRT--PCR). The mRNA levels of were measured by qRT-PCR. Total RNAs were isolated using Trizol reagents from cells, and then RNA (1 μg) was reverse transcribed into cDNA (a template for qPCR) using QuantScript RT Kit (Tiangen, Beijing, China). qPCR was conducted by FastFire qPCR PreMix (SYBR Green) (Tiangen) with GAPDH as a standard reference. The expression was calculated using $2^{-\Delta\Delta CT}$ method. The primers were as follows:

γ-catenin, F, 5'-GCTAACGTAAACGTGACTT-3'; R, 5'-ACAACTGCTAGCTGAAACGT-3'
E-cadherin, F, 5'-CCATTCGACCATAGCTCTC-3'; R, 5'-GGCAAATTCCGGTACGCCT-3'
Fibronectin, F, 5'-CTAGGTACGTAACGTGACG-3'; R, 5'-GCAATCAACTTACGTTCAC-3'
Snail, F, 5'-GGCCCTTTACAGTGCACC-3'; R, 5'-TTCGTCGACGCTGCACACTC-3'
β-catenin, F, 5'-TTTCAACGGGTACCCTGTC-3'; R, 5'-GCTAACTCGAATGCAACGT-3'

Statistical analysis. All data were expressed as mean ± SD from at least three independent experiments. Statistical analysis was carried out using SPSS software (version 15.0; IBM Corp., Armonk, NY, USA). ANOVA followed by *post hoc* was performed to evaluate the significance of differences in the mean values. p values < 0.05 were considered statistically significant.

Results

GLA inhibits the viability and colony formation and promotes apoptosis of gastric cancer cells under hypoxia

As shown in Figures 1A–C, GLA, at all 3 concentrations used, did not inhibit the viability, colony formation or apoptosis of GES-1 cells. Since hypoxia is the basic feature of tumor microenvironment, the SGC-7901 and MGC-803 cells were cultured under hypoxia to study the effects of GLA (50,100 or 200 μM) on cell growth, viability and colony formation. The results showed that, compared with the control group, GLA treatment for 72 h significantly decreased cell viability and inhibited colony formation (Fig. 1D and 1E, $p < 0.05, p < 0.01$). Western blot analysis showed that GLA treatment decreased the expression levels of cell proliferation-related proteins (PCNA and MCM-2) and anti-apoptotic protein (Bcl-2), while increased the expression of anti-apoptotic proteins, Bax and cleaved Caspase-3, in a dose-dependent manner (Fig. 1F, $p < 0.05, p < 0.01$).

GLA inhibits the migration and invasion of gastric cancer cells under hypoxia

The effect of GLA on the invasion and migration of gastric cancer cells was detected by transwell assay and wound healing assay, respectively. As shown in Figure 2A, the wound closure area in SGC-7901 and MGC-803 cells cultured under hypoxia was increased in a dose-dependent manner after GLA treatment compared with the control group (Fig. 2A, $p < 0.01$). The transwell assay showed that the invasion of SGC-7901 and MGC-803 cells treated with GLA was de-

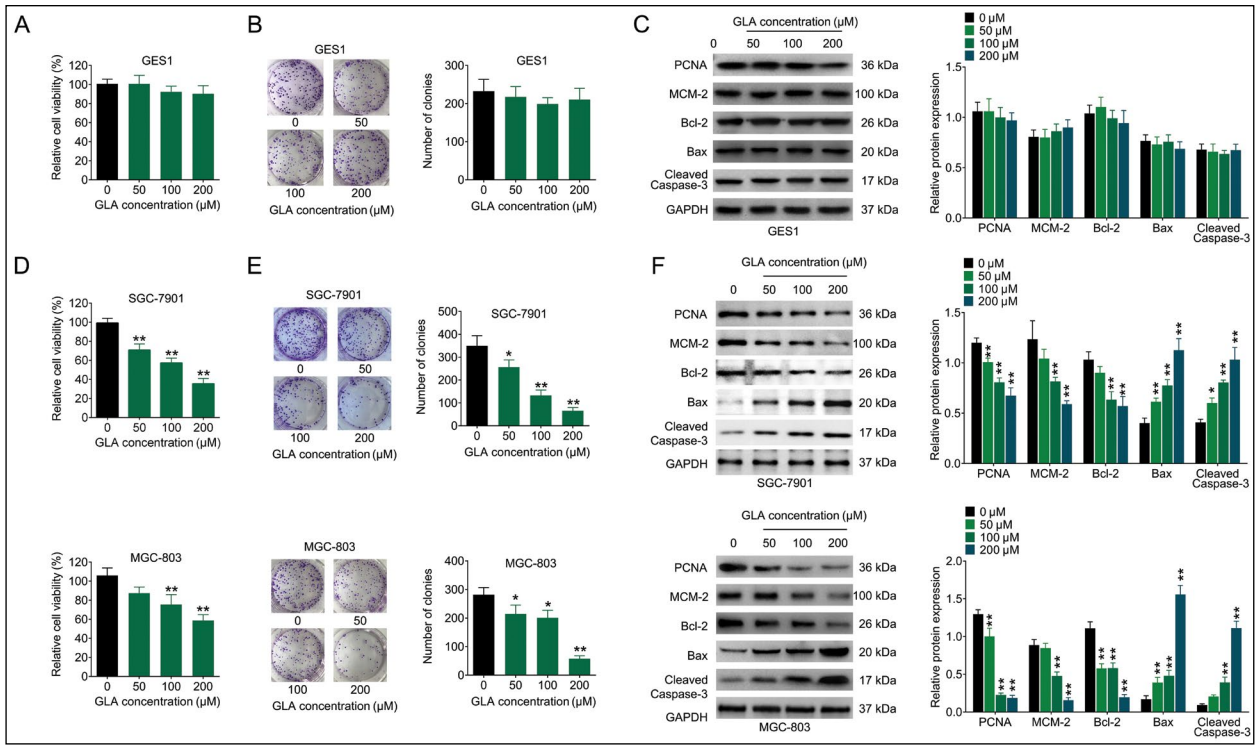

Figure 1. GLA inhibits the viability and colony formation and promotes apoptosis of gastric cancer cells under hypoxia. SGC-7901 and MGC-803 cells exposed to 1% O_2, 5% CO_2, and 94% N_2 humidified atmopshere at 37°C were treated with different doses of GLA (50, 100 and 200 μM), respectively. **A.** Viability of GES-1 cells was measured by MTT assay. **B.** The colony formation of GES-1 cells was detected by colony formation assay. **C.** The protein levels of PCNA, MCM-2, Bcl-2, Bax and Cleaved Caspase-3 in GES-1 cells were determined by Western blotting. **D.** Viability of SGC-7901 and MGC-803 cells was measured by MTT assay. **E.** The colony formation of SGC-7901 and MGC-803 cells was detected by colony formation assay. **F.** The protein levels of PCNA, MCM-2, Bcl-2, Bax and Cleaved Caspase-3 in SGC-7901 and MGC-803 cells were determined by Western blotting. n = 3, $*p < 0.05$, $**p < 0.01$ *vs.* control group (no GLA).

creased in a dose-dependent manner compared with the control group (Fig. 2B, $p < 0.01$).

GLA inhibits EMT and Wnt/β-catenin signaling pathways in gastric cancer cells

To reveal the effects of GLA on the invasion and migration of SGC-7901 and MGC-803 cells, cells were treated with different concentrations of GLA (50,100 or 200 μM) under hypoxic conditions for 72 h. After GLA treatment, the protein levels of epithelial cell markers (γ-catenin and E-cadherin) increased significantly, while the protein levels of the mesenchymal cell markers (fibronectin and Snail) were decreased in SGC-7901 and MGC-803 cells. Besides, GLA treatment also reduced the protein level of β-catenin protein in a dose-dependent manner compared to the control group (Fig. 3, $p < 0.01$).

GLA inhibits hypoxia-induced EMT in gastric cancer cells by inhibiting Wnt/β-catenin signal pathway

To further explore the molecular mechanism, SGC-7901 cells were treated with GLA (200 μM) and/or Wnt3a (200 ng/ml). As shown in Figure 4A, compared with cells that were treated only with GLA, Wnt3a significantly reversed the inhibitory effect of GLA on the protein levels of epithelial cells (γ-catenin, E-cadherin) and EMT markers (fibronectin and Snail) in SGC-7901 cells ($p < 0.05, p < 0.01$). Results from qRT-PCR analyses showed consistent results (Fig. 4B, $p < 0.05, p < 0.01$).

GLA inhibits the growth of gastric cancer cells under hypoxia through Wnt/β-catenin signal pathway

Finally, we analyzed the possible molecular mechanism underlying the regulatory role of GLA on the growth of the studied gastric cancer cells under hypoxia. As shown in Figure 5A, Wnt3a pre-treatment for 72 h significantly reversed the inhibitory effect of GLA on the viability of SGC-7901 cells ($p < 0.01$). Colony formation analysis showed that Wnt3a treatment also significantly reversed the inhibitory effect of GLA on the colony formation of SGC-7901 cells (Fig. 5B, $p < 0.01$). Wound healing assay and Transwell assay showed that compared with GLA treatment group,

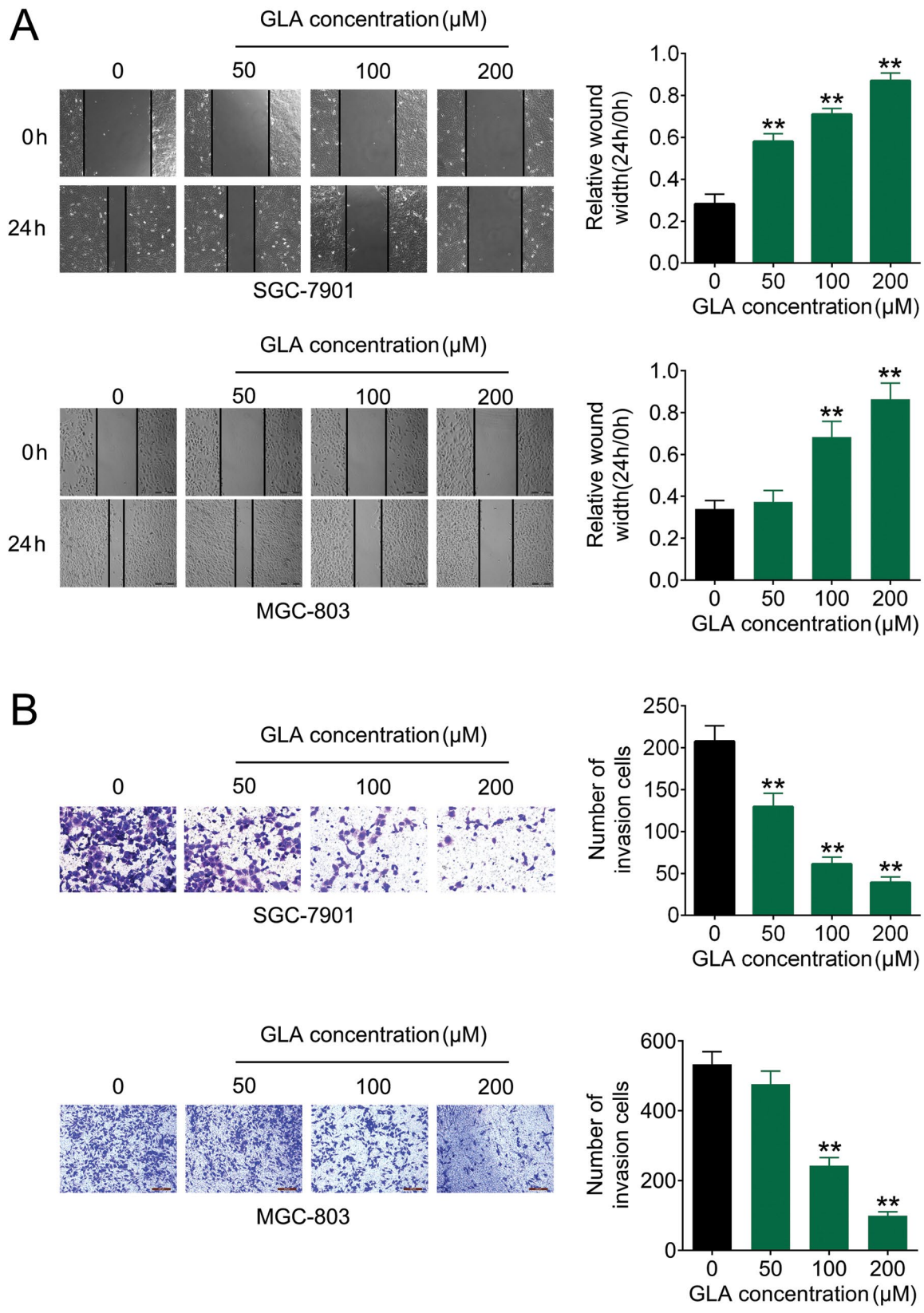

Figure 2. GLA inhibits the migration and invasion of gastric cancer cells under hypoxia. SGC-7901 and MGC-803 cells exposed to 1% O_2, 5% CO_2, and 94% N_2 humidified atmosphere at 37°C were treated with different doses of GLA (50, 100 or 200 μM). The migratory ability (**A**) and invasive ability (**B**) of SGC-7901 and MGC-803 cells were detected by wound-healing assays and transwell assay, respectively. n = 3, $^{*}p < 0.05$, $^{**}p < 0.01$ *vs.* control group (no GLA).

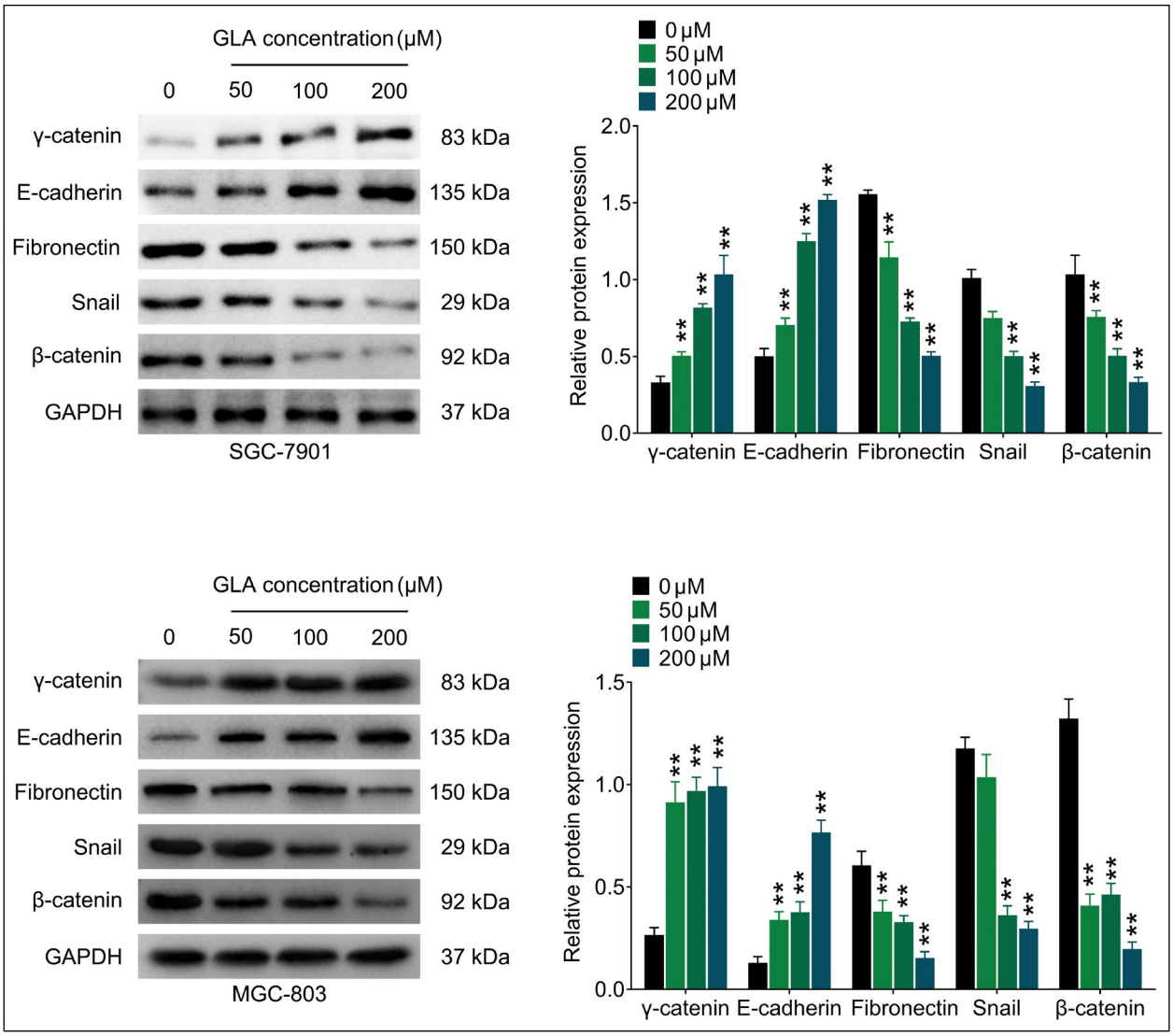

Figure 3. GLA inhibits EMT and Wnt/β-catenin signaling pathways in gastric cancer cells. SGC-7901 and MGC-803 cells exposed to 1% O_2, 5% CO_2, and 94% N_2 humidified atmosphere at 37°C were treated with different doses of GLA (50, 100 or 200 μM). The protein levels of γ-catenin, E-cadherin, fibronectin, Snail and β-catenin were determined by Western blotting in SGC-7901 and MGC-803 cells. n = 3, $^{*}p < 0.05$, $^{**}p < 0.01$ *vs.* control group (no GLA).

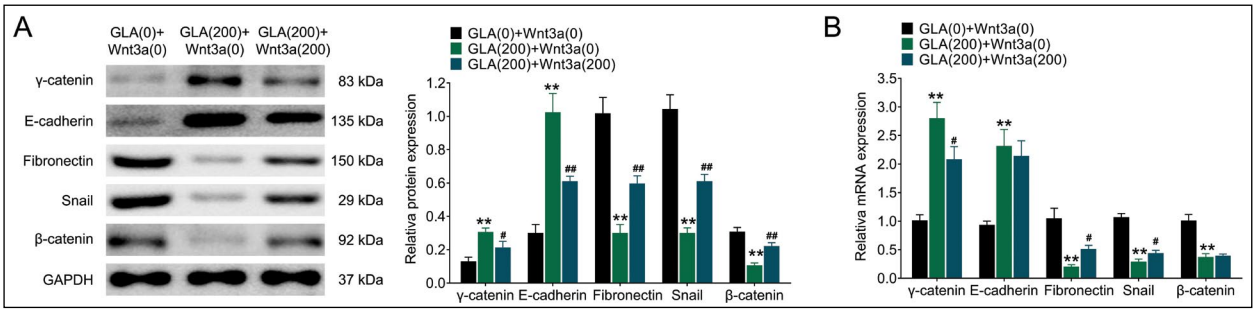

Figure 4. GLA inhibits hypoxia-induced EMT of gastric cancer cells by inhibiting Wnt/β-catenin signal pathway. SGC-7901 and MGC-803 cells exposed to 1% O_2, 5% CO_2, and 94% N_2 humidified atmosphere at 37°C were treated with GLA (200 μM) or/and Wnt3a (200 ng/ml). The protein levels of γ-catenin, E-cadherin, fibronectin, Snail and β-catenin in SGC-7901 and MGC-803 cells were determined by Western blotting and qPCR. n = 3, $^{**}p < 0.01$ *vs.* GLA (0 μM) + Wnt3a (0 μM); $^{\#}p < 0.05$ *vs.* GLA (200 μM) + Wnt3a (200 ng/ml).

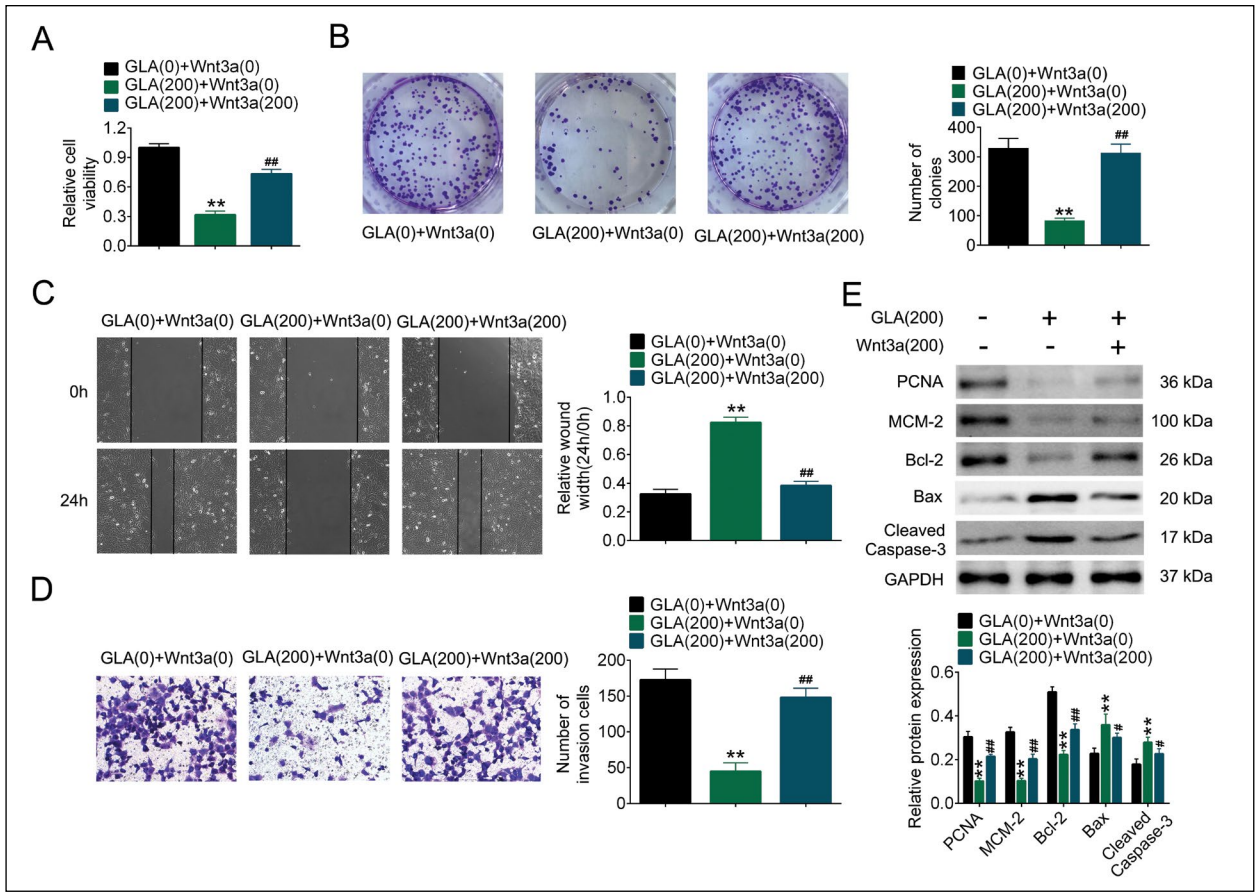

Figure 5. GLA inhibits the growth of gastric cancer cells under hypoxia through Wnt/β-catenin signal pathway. SGC-7901 and MGC-803 cells exposed to 1% O_2, 5% CO_2, and 94% N_2 humidified atmosphere at 37°C were treated with GLA (200 μM) or/and Wnt3a (200 ng/ml). **A.** Viability of SGC-7901 cells were measured by MTT assay. **B.** The colony formation assay of SGC-7901 cells was performed. Cell migratory ability (**C**) and cell invasive ability (**D**) of SGC-7901 cells were detected by wound-healing assays and Transwell assay, respectively. **E.** The protein levels of PCNA, MCM-2, Bcl-2, Bax and Cleaved Caspase-3 were determined by Western blotting. n = 3, $^{*}p < 0.05$, $^{**}p < 0.01$ *vs.* GLA (0 μM) + Wnt3a (0 μM); $^{\#}p < 0.05$, $^{\#\#}p < 0.01$ *vs.* GLA (200 μM) + Wnt3a (200 ng/ml).

preincubation with Wnt3a significantly reversed the inhibitory effects of GLA on the invasion and migration of SGC-7901 cells (Fig. 5C and 5D, $p < 0.01$). In addition, Western blotting showed that compared with GLA treatment group, Wnt3a treatment significantly reversed the inhibition of GLA on the expression of PCNA, MCM-2 and Bcl-2 and the expression of Bax and cleaved Caspase-3 in SGC-7901 cells (Fig. 5E, $p < 0.05$, $p < 0.01$).

Discussion

Despite the achievements in surgical resection and chemotherapy for the treatment of gastric cancer, its recurrence rate and metastasis rate are still high, and the median overall survival (OS) time of patients with metastatic disease is still very poor [3, 4]. GLA is a promising bioactive molecule that has anticancer activity in many types of cancer [18, 22, 26, 27], but its biological activity in gastric cancer is poorly understood. It has been reported that regular intake of GLA could reduce inflammation and inhibit the development of cancer [28–30]. Previous studies have also shown that GLA inhibited cell growth in the human neuroblastoma cell line [31], and decreased GLA levels are associated with the development of inflammatory breast cancer [23]. GLA inhibited DMBA-induced breast cancer by mediating mitochondrial death and apoptosis, reducing hypoxic microenvironment, hindering the synthesis of fatty acids from scratch, and mediating cholinergic anti-inflammatory pathway [32]. In this study, we found that GLA could inhibit the activity and growth of hypoxic-induced SGC-7901 and MGC-803 cells in a concentration-dependent manner, and reverse the migration, invasion and EMT SGC-7901 and MGC-803 cells induced by hypoxia. Further mo-

lecular mechanisms have shown that GLA treatment inhibited the progression of hypoxic gastric cancer by inducing the inactivation of Wnt/β-catenin signaling pathway. This preliminary study suggested that GLA could inhibit the progression of gastric cancer.

Hypoxia is a common marker for several types of human solid tumors and an adverse prognostic factor that associated with the development of EMT [33–35]. Hypoxia-induced EMT decreased the expression of E-cadherin and other epithelial markers and increased the expression of N-cadherin, vimentin, and other mesenchymal markers [36]. Jo *et al*. found that hypoxia can induce EMT process by up-regulation of N-cadherin and snail/slug and down-regulation of PCNA in liver cancer cells [37]. Tam *et al*. explored the effects of different oxygen levels on EMT induction and stemness maintenance and attempted to elucidate the signal transduction pathways in colorectal cancer cells. It was found that 10% O_2 may be an EMT-induced condition, and inhibition of JNK can be used as a therapeutic method to inhibit the metastasis of colorectal cancer cells [38]. Consistent with the above results, we found that GLA induced epithelial to mesenchymal transformation of gastric cancer cells by increasing epithelial cell markers (γ-catenin and E-cadherin), and decreasing mesenchymal cell markers (fibronectin and Snail) under hypoxia. Interestingly, GLA exerted a protective role in hypoxic-induced EMT in gastric cancer cells, because dose-dependent treatment with GLA reversed the hypoxia-induced growth of gastric cancer cells.

It is well-known that the regulatory mechanism underlying hypoxic-induced EMT is complex and complicated. For example, GRP78 promoted hypoxia-induced EMT in A549 cells by activating the smad2/3 and Src/MAPK pathways [39]. Celastrus orbiculatus extract significantly inhibited tumor metastasis and EMT by inhibiting the HIF-1 alpha/Twist1 signaling pathway in hypoxia-induced HepG2 cells [40]. Scutellarin reversed hypoxia-induced EMT in breast cancer cells through the PI3K/Akt and MAPK pathways [34]. Besides, it is also reported that Wnt signaling pathway promotes tumor progression and metastasis in various cancers [41]. Previous studies have shown that the Wnt/β-catenin pathway is activated in gastric cancer [42], and contributes to tumor malignancy in gastrointestinal stromal tumor [43]. In gastric cancer, a variety of biologically active substances have been shown to regulate the Wnt/β-catenin pathway, such as lycopene [44], sinomenine [45] and cardamom [46]. However, whether GLA can also modulate the progression of gastric cancer by regulating the Wnt/β-catenin pathway remains unknown. β-catenin is a main member of the Wnt signaling pathway. In general, Wnt /β-catenin signals promote tumor spread and development by activating downstream genes β-catenin, cyclin D and proto-oncogenes. In this study, GLA reduced the protein levels of β-catenin in SGC-7901 and MGC-803 cells under hypoxic conditions in a concentration-dependent manner, and thereby inhibited cell growth and EMT in gastric cancer. Notably, Wnt3a reversed the inhibitory effect of GLA on β-catenin expression, and further reversed the inhibitory effect of GLA on gastric cancer cell growth and EMT. These results indicated that Wnt/β-catenin signals were involved in the regulatory effects of GLA in gastric cancer cells.

In summary, our study showed that GLA inhibited hypoxia-induced cell growth and EMT by inhibiting the Wnt/β-catenin signaling pathway, thus demonstrating antitumor activity in gastric cancer cell lines. Therefore, GLA may be a potentially attractive bioactive phytochemical for the treatment of gastric cancer. Our findings provide a theoretical basis for GLA as a potential clinical drug for gastric cancer.

Competing interests

The authors declare that they have no competing interests, and all authors should confirm its accuracy.

Availability of data and materials

All data generated or analyzed during this study are included in this published article.

Authors' contributions

Yan Wang conceived and designed the experiments, Jian Shi analyzed and interpreted the results of the experiments, Liya Gong performed the experiments.

Informed consent

Written informed consent was obtained from a legally authorized representative(s) for anonymized patient information to be published in this article.

References

1. Wu C, Li M, Meng H, et al. Analysis of status and countermeasures of cancer incidence and mortality in China. Sci China Life Sci. 2019; 62(5): 640–647, doi: 10.1007/s11427-018-9461-5, indexed in Pubmed: 30900169.
2. Ferlay J, Soerjomataram I, Dikshit R, et al. Cancer incidence and mortality worldwide: sources, methods and major patterns in GLOBOCAN 2012. Int J Cancer. 2015; 136(5): E359–E386, doi: 10.1002/ijc.29210, indexed in Pubmed: 25220842.
3. Ferlay J, Shin HR, Bray F, et al. Estimates of worldwide burden of cancer in 2008: GLOBOCAN 2008. Int J Cancer. 2010; 127(12): 2893–2917, doi: 10.1002/ijc.25516, indexed in Pubmed: 21351269.

4. Ohtsu A. Chemotherapy for metastatic gastric cancer: past, present, and future. J Gastroenterol. 2008; 43(4): 256–264, doi: 10.1007/s00535-008-2177-6, indexed in Pubmed: 18458840.
5. Liu Na, Wang X. [Current status and research progress of perioperative chemotherapy in advanced gastric cancer]. Zhonghua Wei Chang Wai Ke Za Zhi. 2015; 18(10): 983–985, indexed in Pubmed: 26499140.
6. Allemani C, Weir HK, Carreira H, et al. CONCORD Working Group. Global surveillance of cancer survival 1995-2009: analysis of individual data for 25,676,887 patients from 279 population-based registries in 67 countries (CONCORD-2). Lancet. 2015; 385(9972): 977–1010, doi: 10.1016/S0140-6736(14)62038-9, indexed in Pubmed: 25467588.
7. Patrad E, Niapour A, Farassati F, et al. Combination treatment of all-trans retinoic acid (ATRA) and γ-secretase inhibitor (DAPT) cause growth inhibition and apoptosis induction in the human gastric cancer cell line. Cytotechnology. 2018; 70(2): 865–877, doi: 10.1007/s10616-018-0199-3, indexed in Pubmed: 29417442.
8. Makuuchi R, Sugisawa N, Kaji S, et al. Enhanced recovery after surgery for gastric cancer and an assessment of preoperative carbohydrate loading. Eur J Surg Oncol. 2017; 43(1): 210–217, doi: 10.1016/j.ejso.2016.07.140, indexed in Pubmed: 27554250.
9. Zhao J, Wang G, Jiang ZW, et al. Patients Administered Neoadjuvant Chemotherapy Could be Enrolled into an Enhanced Recovery after Surgery Program for Locally Advanced Gastric Cancer. Chin Med J (Engl). 2018; 131(4): 413–419, doi: 10.4103/0366-6999.225047, indexed in Pubmed: 29451145.
10. Tegels JJW, De Maat MFG, Hulsewé KWE, et al. Improving the outcomes in gastric cancer surgery. World J Gastroenterol. 2014; 20(38): 13692–13704, doi: 10.3748/wjg.v20.i38.13692, indexed in Pubmed: 25320507.
11. Shimizu N, Hatao F, Fukatsu K, et al. Results of a nationwide questionnaire-based survey on nutrition management following gastric cancer resection in Japan. Surg Today. 2017; 47(12): 1460–1468, doi: 10.1007/s00595-017-1552-4, indexed in Pubmed: 28600636.
12. Klek S, Scislo L, Walewska E, et al. Enriched enteral nutrition may improve short-term survival in stage IV gastric cancer patients: A randomized, controlled trial. Nutrition. 2017; 36: 46–53, doi: 10.1016/j.nut.2016.03.016, indexed in Pubmed: 28336107.
13. Tasset-Cuevas I, Fernández-Bedmar Z, Lozano-Baena MD, et al. Protective effect of borage seed oil and gamma linolenic acid on DNA: in vivo and in vitro studies. PLoS One. 2013; 8(2): e56986, doi: 10.1371/journal.pone.0056986, indexed in Pubmed: 23460824.
14. Guil-Guerrero JL, García-Maroto F, Campra-Madrid P, et al. Occurrence and characterization of oils rich in γ-linolenic acid Part II: fatty acids and squalene from Macaronesian Echium leaves. Phytochemistry. 2000; 54(5): 525–529, doi: 10.1016/s0031-9422(00)00139-4.
15. Bégin ME, Ells G, Das UN, et al. Differential killing of human carcinoma cells supplemented with n-3 and n-6 polyunsaturated fatty acids. J Natl Cancer Inst. 1986; 77(5): 1053–1062, indexed in Pubmed: 3464797.
16. Bégin ME. Effects of polyunsaturated fatty acids and of their oxidation products on cell survival. Chem Phys Lipids. 1987; 45(2-4): 269–313, doi: 10.1016/0009-3084(87)90069-7, indexed in Pubmed: 3319230.
17. Dai J, Shen J, Pan W, et al. Effects of polyunsaturated fatty acids on the growth of gastric cancer cells in vitro. Lipids Health Dis. 2013; 12: 71, doi: 10.1186/1476-511X-12-71, indexed in Pubmed: 23663688.
18. Menendez JA, Colomer R, Lupu R. Omega-6 polyunsaturated fatty acid gamma-linolenic acid (18:3n-6) is a selective estrogen-response modulator in human breast cancer cells: gamma-linolenic acid antagonizes estrogen receptor-dependent transcriptional activity, transcriptionally represses estrogen receptor expression and synergistically enhances tamoxifen and ICI 182,780 (Faslodex) efficacy in human breast cancer cells. Int J Cancer. 2004; 109(6): 949–954, doi: 10.1002/ijc.20096, indexed in Pubmed: 15027132.
19. Menéndez JA, Ropero S, del Barbacid MM, et al. Synergistic interaction between vinorelbine and gamma-linolenic acid in breast cancer cells. Breast Cancer Res Treat. 2002; 72(3): 203–219, doi: 10.1023/a:1014968415759, indexed in Pubmed: 12058962.
20. Robbins M, Ali K, McCaw R, et al. gamma-linolenic acid (GLA)-mediated cytotoxicity in human prostate cancer cells. Adv Exp Med Biol. 1999; 469: 499–504, doi: 10.1007/978-1-4615-4793-8_73, indexed in Pubmed: 10667374.
21. Wang X, Lin H, Gu Y. Multiple roles of dihomo-γ-linolenic acid against proliferation diseases. Lipids Health Dis. 2012; 11: 25, doi: 10.1186/1476-511X-11-25, indexed in Pubmed: 22333072.
22. Cui H, Han F, Zhang L, et al. Gamma linolenic acid regulates PHD2 mediated hypoxia and mitochondrial apoptosis in DEN induced hepatocellular carcinoma. Drug Des Devel Ther. 2018; 12: 4241–4252, doi: 10.2147/DDDT.S178519, indexed in Pubmed: 30587920.
23. Chas M, Goupille C, Arbion F, et al. Low eicosapentaenoic acid and gamma-linolenic acid levels in breast adipose tissue are associated with inflammatory breast cancer. Breast. 2019; 45: 113–117, doi: 10.1016/j.breast.2019.04.001, indexed in Pubmed: 30959386.
24. Zhao S, Min P, Liu L, et al. NEDD9 Facilitates Hypoxia-Induced Gastric Cancer Cell Migration via MICAL1 Related Rac1 Activation. Front Pharmacol. 2019; 10: 291, doi: 10.3389/fphar.2019.00291, indexed in Pubmed: 31019460.
25. Zhang Qi, Bai X, Chen W, et al. Wnt/β-catenin signaling enhances hypoxia-induced epithelial-mesenchymal transition in hepatocellular carcinoma via crosstalk with hif-1α signaling. Carcinogenesis. 2013; 34(5): 962–973, doi: 10.1093/carcin/bgt027, indexed in Pubmed: 23358852.
26. Xu Yi, Qi J, Yang X, et al. Free radical derivatives formed from cyclooxygenase-catalyzed dihomo-γ-linolenic acid peroxidation can attenuate colon cancer cell growth and enhance 5-fluorouracil's cytotoxicity. Redox Biol. 2014; 2: 610–618, doi: 10.1016/j.redox.2014.01.022, indexed in Pubmed: 25114837.
27. Yang X, Xu Yi, Gao Di, et al. Dihomo-γ-linolenic acid inhibits growth of xenograft tumors in mice bearing human pancreatic cancer cells (BxPC-3) transfected with delta-5-desaturase shRNA. Redox Biol. 2019; 20: 236–246, doi: 10.1016/j.redox.2018.10.001, indexed in Pubmed: 30384258.
28. Roy S, Rawat AK, Sammi SR, et al. Alpha-linolenic acid stabilizes HIF-1 α and downregulates FASN to promote mitochondrial apoptosis for mammary gland chemoprevention. Oncotarget. 2017; 8(41): 70049–70071, doi: 10.18632/oncotarget.19551, indexed in Pubmed: 29050261.
29. Rani A, Roy S, Singh M, et al. α-Chymotrypsin regulates free fatty acids and UCHL-1 to ameliorate N-methyl nitrosourea induced mammary gland carcinoma in albino wistar rats. Inflammopharmacology. 2016; 24(5): 277–286, doi: 10.1007/s10787-016-0280-5, indexed in Pubmed: 27671329.

30. Balakumar P, Taneja G. Fish oil and vascular endothelial protection: bench to bedside. Free Radic Biol Med. 2012; 53(2): 271–279, doi: 10.1016/j.freeradbiomed.2012.05.005, indexed in Pubmed: 22584102.
31. Saha B, Patro BS, Koli M, et al. -4,4'-Dihydroxystilbene (DHS) inhibits human neuroblastoma tumor growth and induces mitochondrial and lysosomal damages in neuroblastoma cell lines. Oncotarget. 2017; 8(43): 73905–73924, doi: 10.18632/oncotarget.17879, indexed in Pubmed: 29088756.
32. Roy S, Singh M, Rawat A, et al. GLA supplementation regulates PHD2 mediated hypoxia and mitochondrial apoptosis in DMBA induced mammary gland carcinoma. Int J Biochem Cell Biol. 2018; 96: 51–62, doi: 10.1016/j.biocel.2018.01.011, indexed in Pubmed: 29355756.
33. Murakami K, Wu Y, Imaizumi T, et al. DEC1 promotes hypoxia-induced epithelial-mesenchymal transition (EMT) in human hepatocellular carcinoma cells. Biomed Res. 2017; 38(4): 221–227, doi: 10.2220/biomedres.38.221, indexed in Pubmed: 28794399.
34. Lv WL, Liu Q, An JH, et al. Scutellarin inhibits hypoxia-induced epithelial-mesenchymal transition in bladder cancer cells. J Cell Physiol. 2019; 234(12): 23169–23175, doi: 10.1002/jcp.28883, indexed in Pubmed: 31127618.
35. Deng M, Xue YJ, Xu LR, et al. Chrysophanol Suppresses Hypoxia-Induced Epithelial-Mesenchymal Transition in Colorectal Cancer Cells. Anat Rec (Hoboken). 2019; 302(9): 1561–1570, doi: 10.1002/ar.24081, indexed in Pubmed: 30737895.
36. Ruan J, Zhang L, Yan L, et al. Inhibition of hypoxia-induced epithelial mesenchymal transition by luteolin in non-small cell lung cancer cells. Mol Med Rep. 2012; 6(1): 232–238, doi: 10.3892/mmr.2012.884, indexed in Pubmed: 22552526.
37. Jo H, Lee J, Jeon J, et al. The critical role of glucose deprivation in epithelial-mesenchymal transition in hepatocellular carcinoma under hypoxia. Sci Rep. 2020; 10(1): 1538, doi: 10.1038/s41598-020-58124-1, indexed in Pubmed: 32001727.
38. Tam SY, Wu VWC, Law HKW. JNK Pathway Mediates Low Oxygen Level Induced Epithelial-Mesenchymal Transition and Stemness Maintenance in Colorectal Cancer Cells. Cancers (Basel). 2020; 12(1), doi: 10.3390/cancers12010224, indexed in Pubmed: 31963305.
39. Zhu X, Lu X. MiR-423-5p inhibition alleviates cardiomyocyte apoptosis and mitochondrial dysfunction caused by hypoxia/reoxygenation through activation of the wnt/β-catenin signaling pathway via targeting MYBL2. J Cell Physiol. 2019; 234(12): 22034–22043, doi: 10.1002/jcp.28766, indexed in Pubmed: 31074036.
40. Qian YY, Shi YY, Lu SH, et al. Extracts of Celastrus Orbiculatus Inhibit Cancer Metastasis by Down-regulating Epithelial-Mesenchymal Transition in Hypoxia-Induced Human Hepatocellular Carcinoma Cells. Chin J Integr Med. 2019; 25(5): 334–341, doi: 10.1007/s11655-018-2562-9, indexed in Pubmed: 30046956.
41. Su J, Su Bo, Xia H, et al. RORα Suppresses Epithelial-to-Mesenchymal Transition and Invasion in Human Gastric Cancer Cells via the Wnt/β-Catenin Pathway. Front Oncol. 2019; 9: 1344, doi: 10.3389/fonc.2019.01344, indexed in Pubmed: 31867273.
42. Wang Xi, Lu B, Dai C, et al. Caveolin-1 Promotes Chemoresistance of Gastric Cancer Cells to Cisplatin by Activating WNT/β-Catenin Pathway. Front Oncol. 2020; 10: 46, doi: 10.3389/fonc.2020.00046, indexed in Pubmed: 32117718.
43. Zeng S, Seifert AM, Zhang JQ, et al. Wnt/β-catenin Signaling Contributes to Tumor Malignancy and Is Targetable in Gastrointestinal Stromal Tumor. Mol Cancer Ther. 2017; 16(9): 1954–1966, doi: 10.1158/1535-7163.MCT-17-0139, indexed in Pubmed: 28611108.
44. Kim M, Kim SH, Lim JW, et al. Lycopene induces apoptosis by inhibiting nuclear translocation of β-catenin in gastric cancer cells. J Physiol Pharmacol. 2019; 70(4), doi: 10.26402/jpp.2019.4.11, indexed in Pubmed: 31741457.
45. Yuan H, Zhang J, Li F, et al. Sinomenine exerts antitumour effect in gastric cancer cells via enhancement of miR-204 expression. Basic Clin Pharmacol Toxicol. 2019; 125(5): 450–459, doi: 10.1111/bcpt.13285, indexed in Pubmed: 31243880.
46. Hou G, Yuan X, Li Yi, et al. Cardamonin, a natural chalcone, reduces 5-fluorouracil resistance of gastric cancer cells through targeting Wnt/β-catenin signal pathway. Invest New Drugs. 2020; 38(2): 329–339, doi: 10.1007/s10637-019-00781-9, indexed in Pubmed: 31102118.

Submitted: 14 November, 2019
Accepted after reviews: 8 June, 2020
Available as AoP: 1 July, 2020

FOLIA HISTOCHEMICA ET CYTOBIOLOGICA
Vol. 58, No. 2, 2020
pp. 127–134

ORIGINAL PAPER

VIA MEDICA

Bisdemethoxycurcumin exerts a cell-protective effect *via* JAK2/STAT3 signaling in a rotenone-induced Parkinson's disease model *in vitro*

Duanqun He[1, 3, #], Shuangxi Chen[1, #], Zijian Xiao[1], Heng Wu[1], Guijuan Zhou[1], Chenlin Xu[1], Yunqian Chang[1], Yihui Li[1], Gang Wang[2, *], Ming Xie[1, *]

[1]The First Affiliated Hospital, University of South China, Hengyang, Hunan 421001, PR China

[2]Department of Rehabilitation, Union Hospital, Tongji Medical College, Huazhong University of Science and Technology, Wuhan, Hubei 430022, PR China

[3]Shenzhen Baoan People's Hospital (Group), The Second People's Hospital, Shenzhen, Guangdong 518101, China

[#]These authors contributed equally to this study.

Abstract

Introduction. Oxidative stress and cell apoptosis have both been suggested to be closely associated with the pathogenesis of Parkinson's disease (PD). Previously, bisdemethoxycurcumin (BDMC) has been shown to exhibit several desirable characteristics as a candidate neuroprotective agent, including antioxidant and anti-inflammatory activities in the nervous system. However, whether BDMC can exert cell-protective roles in an *in vitro* model of PD remains unknown.

Material and methods. SH-SY5Y cells were pretreated with BDMC, with or without AG490 and SI-201, for 30 min, followed by a co-incubation with rotenone for 24 h. Subsequently, a cell viability assay and western blotting was performed, and SOD and GSH activities were analyzed.

Results. The results revealed that the pretreatment with BDMC enhanced the cell survival, antioxidative stress capacity and the phosphorylation levels of JAK/STAT3 in SH-SY5Y cells treated with rotenone. However, following the incubation with AG490 and SI-201, inhibitors of the JAK/STAT3 signaling pathway, BDMC was unable to exert cell-protective roles in SH-SY5Y cells treated with rotenone.

Conclusions. In conclusion, the results suggested that BDMC may exert a cell-protective role in SH-SY5Y cells *in vitro* via JAK2/STAT3 signaling, thus suggesting the possible application of BDMC for the treatment of neurodegenerative diseases related to JAK2/STAT3 signaling. *(Folia Histochemica et Cytobiologica 2020, Vol. 58, No. 2, 127–134)*

Key words: oxidative stress; rotenone; SH-SY5Y cells; bisdemethoxycurcumin (BDMC); JAK/STAT3

Introduction

Parkinson's disease (PD), a common neurodegenerative disease [1], is mainly characterized by a substantial loss of dopaminergic neurons in the substantia nigra, which causes a reduction of striata dopamine, and promotes cognitive impairment and functional defects [2]. Both motor and non-motor symptoms are observed in patients with PD, who require assistance in performing all activities [3, 4]. It has been suggested that the excessive generation of reactive oxygen species (ROS), oxidative stress, neuroinflammation and mitochondrial dysfunction may all account for the loss of dopaminergic neurons and neuronal apoptosis [5–7]. However, the available current therapeutic strategies only provide symptomatic improvements due to the complex pathogenesis of PD. As a consequence,

Correspondence address: Ming Xie and Gang Wang, e-mail: c237423281@163.com; wangzuogang@21cn.com

there remains an urgent requirement to determine the pathological mechanisms of PD to discover novel potential therapeutic targets to effectively treat PD.

Bisdemethoxycurcumin (BDMC), a natural derivative of curcumin, has demonstrated higher polarity, hydrophilicity and water solubility compared with the parent compound curcumin [8]. It was also reported to exert considerable antioxidant, anti-inflammatory and antiproliferative activities [9], and it demonstrated more effective pharmacological properties than curcumin [10], which suggested that it may be a more promising drug for clinical use [11].

Oxidative stress is considered to be the main cause of dopaminergic neuron degeneration in PD [12, 13]. Attempts to target signaling pathways that may be associated with the pathological process of PD have been made to counteract oxidative stress and cell apoptosis, of which one of the signaling pathways is the Janus-activated kinase 2/signal transducer and activator of transcription 3 (JAK2/STAT3) signaling pathway. Briefly, the signaling pathway consists of ligands binding to the membrane receptor and inducing the formation of Janus-activated kinase 2 (JAK2) binding sites in the cytoplasm to phosphorylate JAK2. Subsequently, the exposure of the STAT3 anchor point leads to its phosphorylation and activation, resulting in the translocation of STAT3 from the cytoplasm to the nucleus, to promote the transcription and expression of target genes [11]. Phosphorylated STAT3 has been discovered to promote cell proliferation, anti-inflammatory properties and the inhibition of apoptosis [14], and it also exerted neurotrophic effects on newly generated neurons and synapses [15].

The aim of the present study was to investigate the effects and underlying mechanisms of BDMC in SH-SY5Y cells treated with rotenone, an agent used to mimic the behavioral and neuropathological conditions of PD. The results indicated that BDMC may exert a cell-protective role against rotenone-induced neurotoxicity in SH-SY5Y cells *via* JAK2/STAT3 signaling.

Materials and methods

BDMC. BDMC, which contains > 80% curcumin and > 94% curcuminoid content purity, was purchased from Sigma-Aldrich (St. Louis, MO, USA). For cell incubations, BDMC was dissolved in 0.2% DMSO.

Cell culture and treatments. SH-SY5Y cells were cultured as previously described [16]. It was previously reported that BDMC exerted protective effects against cytotoxicity in retinal pigment epithelial cells at a concentration of 15 μM [17]. Also, 100 nM rotenone induced neuronal loss, neuroinflammation, oxidative stress and NF-κB activity [18]. Therefore, the present study selected 15 μM BMDC (the protective concentration) and 100 nM rotenone (the neurotoxic concentration) for subsequent experiments. A total of 1×10^4 SH-SY5Y cells were seeded into 96-well cell culture plates (for the cell viability assay) or 24-well cell culture plates (for SOD, GSH and western blotting assays), and treated as follows: 1) Cells were pretreated with 15 μM BDMC for 30 min prior to a 24-h co-culture with 100 nM rotenone; 2) cells were pretreated with 10 μM AG490 and 15 μM BDMC for 30 min prior to a 24-h co-culture with rotenone; or 3) cells were pretreated with 100 nM S3I-201 and 15 μM BDMC for 30 min prior to a 24-h co-culture with rotenone. At the end of the treatment duration, a cell viability assay and western blotting were performed, and SOD and GSH activities were analyzed.

Cell viability assay. Cell viability assay was performed as previously described [19–21], with minor modifications. Briefly, at the indicated time points, SH-SY5Y cells were cultured in DMEM, supplemented with 10 μl 3-(4, 5-dimethyl-2-thiazolyl)-2, 5-diphenyl- 2-H-tetrazolium bromide (MTT; 500 μg/ml; cat. no. M1020; Beijing Solarbio Science & Technology, Co., Ltd., Shanghai, China) for 4 h. After aspirating the culture medium, 100 μl dimethyl sulfoxide (DMSO) was added to each well in the culture plates and the cells were incubated at 37°C for 30 min. Finally, the optical density was measured with a spectrophotometer at a wavelength of 410 nm.

Measurement of SOD activity. The WST-1 Cell Proliferation assay kit was used to detect SOD activity, according to the manufacturer's instructions (cat. no. A001-3-2; Jiancheng Biotech Ltd., Nanjing, China) [22, 23]. The xanthine-xanthine oxidase system was applied to produce superoxide ions, which can react with 2-(4-iodophenyl)-3-(4-nitrophenol-5-phenyltetrazolium chloride) to form a red formazan dye. The absorbance was determined at the wavelength of 550 nm. The protein concentration was determined using a BCA protein assay kit (QPBCA, Sigma-Aldrich; Merck KGaA, Saint Louis, MO, USA). The values were expressed as units/mg protein, with one unit of SOD defined as the amount of SOD inhibiting the rate of reaction by 50% at 25°C.

Measurement of GSH. Measurement of GSH content was performed according to a previously described method [24], with minor modifications. Briefly, SH-SY5Y cells in the culture medium were centrifuged at 500 × *g* for 10 min and washed with PBS twice. The collected SH-SY5Y cells were resuspended in protein removal reagent and vigorously vortexed. Subsequently, the samples were frozen rapidly and thawed with liquid nitrogen twice at 37°C, and then incubated at 4°C for 5 min. Following centrifugation at 10,000 × *g* for 10 min, the supernatants were collected. The

determination of GSH levels was performed using a GSH and GSSG assay kit (cat. no. S0053; Beyotime Institute of Biotechnology, Shanghai, China), according to the manufacturer's instructions.

Western blotting. Western blotting was performed as previously described [25–27], with minor modifications. Briefly, whole cell lysates were obtained using a RIPA lysis buffer mixture (Beijing Solarbio Science & Technology Co., Ltd.), supplemented with PMSF (1:200; Beijing Solarbio Science & Technology Co., Ltd.). The lysates were then combined with 25% LDS Sample buffer (Invitrogen; Thermo Fisher Scientific, Inc., Carlsbad, CA, USA) and heated at 95°C for 15 min. Protein samples were separated via 10% SDS-PAGE and transferred onto polyvinylidene difluoride (PVDF) membranes (EMD Millipore, Billerica, MA, USA) for 3 h at 300 mA. The membranes were blocked with 5% nonfat dry milk or BSA dissolved in Tris-HCl saline buffer containing 0.1% Tween-20 (TBST; pH 7.4). Subsequently, the blots were incubated overnight at 4°C with the following antibodies: Rabbit anti-p-STAT3 (1:500; cat. no. S2690; Sigma-Aldrich; Merck KGaA) and rabbit anti-p-JAK2 (1:500; cat. no. SAB4300124; Sigma-Aldrich; Merck KGaA). Following the primary antibody incubation, the membranes were washed three times for 5 min each in TBST and incubated with HRP-conjugated goat anti-rabbit secondary antibodies (1:1,000; Boster Biological Technology, Wuhan, China) diluted in TBST for 1 h. The membranes were washed three times in TBST for 5 min each at room temperature and proteins bands were visualized with an enhanced chemiluminescence (ECL) solution (Bio-Rad Laboratories, Inc., Hercules, CA , USA). The expression levels were semi-quantified using ImageJ 5.0 software (National Institutes of Health, Bethesda, MD, USA).

Statistical analysis. Data are presented as the mean ± SEM. Statistical comparisons between groups were performed using a Student's t test for independent samples on SPSS 18.0 software (SPSS, Inc., New York, NY, USA). $P < 0.05$ was considered to indicate a statistically significant difference.

Results

BDMC treatment enhances cell survival and the antioxidative stress ability in SH-SY5Y cells treated with rotenone

To investigate the effects of BDMC treatment on rotenone-induced SH-SY5Y cells, a cell viability assay was performed, and SOD and GSH activities were analyzed, following the pretreatment of cells with BDMC and the co-culture with rotenone.

The results of the cell viability assay revealed that compared with the control group, the cell survival rate was decreased in response to the treatment with 100 nM rotenone. Notably, compared with the rotenone-treated cells, BDMC treatment significantly increased the cell survival rate in a dose-dependent manner (Fig. 1A).

It was further discovered that compared with the control group, BDMC treatment did not increase the SOD levels (Fig. 1B), while the SOD levels were decreased in response to the treatment with rotenone. Moreover, compared with the rotenone-induced group, BDMC treatment significantly increased the SOD levels (Fig. 1B). A similar trend was observed for the GSH levels (Fig. 1C).

BDMC treatment enhances the phosphorylation levels of JAK/STAT3 in SH-SY5Y cells treated with rotenone

To investigate the effects of BDMC treatment on rotenone-induced SH-SY5Y cells, the phosphorylation levels of JAK2/STAT3 were evaluated following the pretreatment of cells with BDMC and the co-culture with rotenone.

The western blotting results revealed that compared with the control group (*i.e.* rotenone-treated cells), BDMC treatment did not upregulate the JAK2 and STAT3 phosphorylation levels. The JAK2 and STAT3 phosphorylation levels were downregulated in response to the treatment with rotenone. Moreover, compared with the rotenone-induced group, BDMC treatment significantly upregulated the JAK2 and STAT3 phosphorylation levels (Fig. 2A–C).

These results suggested that BDMC may inhibit the toxicity induced by rotenone in SH-SY5Y cells.

AG490, an inhibitor of the JAK/STAT3 signaling pathway, reverses the cell-protective effects of BDMC treatment in SH-SY5Y cells treated with rotenone

To investigate the effects of the JAK/STAT3 signaling pathway on the cell-protective role of BDMC in rotenone-induced SH-SY5Y cells, STAT3 phosphorylation levels, cell survival, and SOD and GSH activities were evaluated following the pretreatment with AG490 and BDMC, and the co-culture with rotenone.

The results of the cell viability assay demonstrated that BDMC treatment did not increase the cell survival of SH-SY5Y cells induced by rotenone following the inhibition of JAK/STAT3 signaling pathway (Fig. 3A).

In addition, it was observed that BDMC treatment did not increase the SOD levels in SH-SY5Y cells induced by rotenone following the inhibition of JAK/ /STAT3 signaling pathway (Fig. 3B). A similar trend for GSH levels was observed (Fig. 3C).

These results suggested that BDMC treatment may not inhibit the toxicity induced by rotenone in

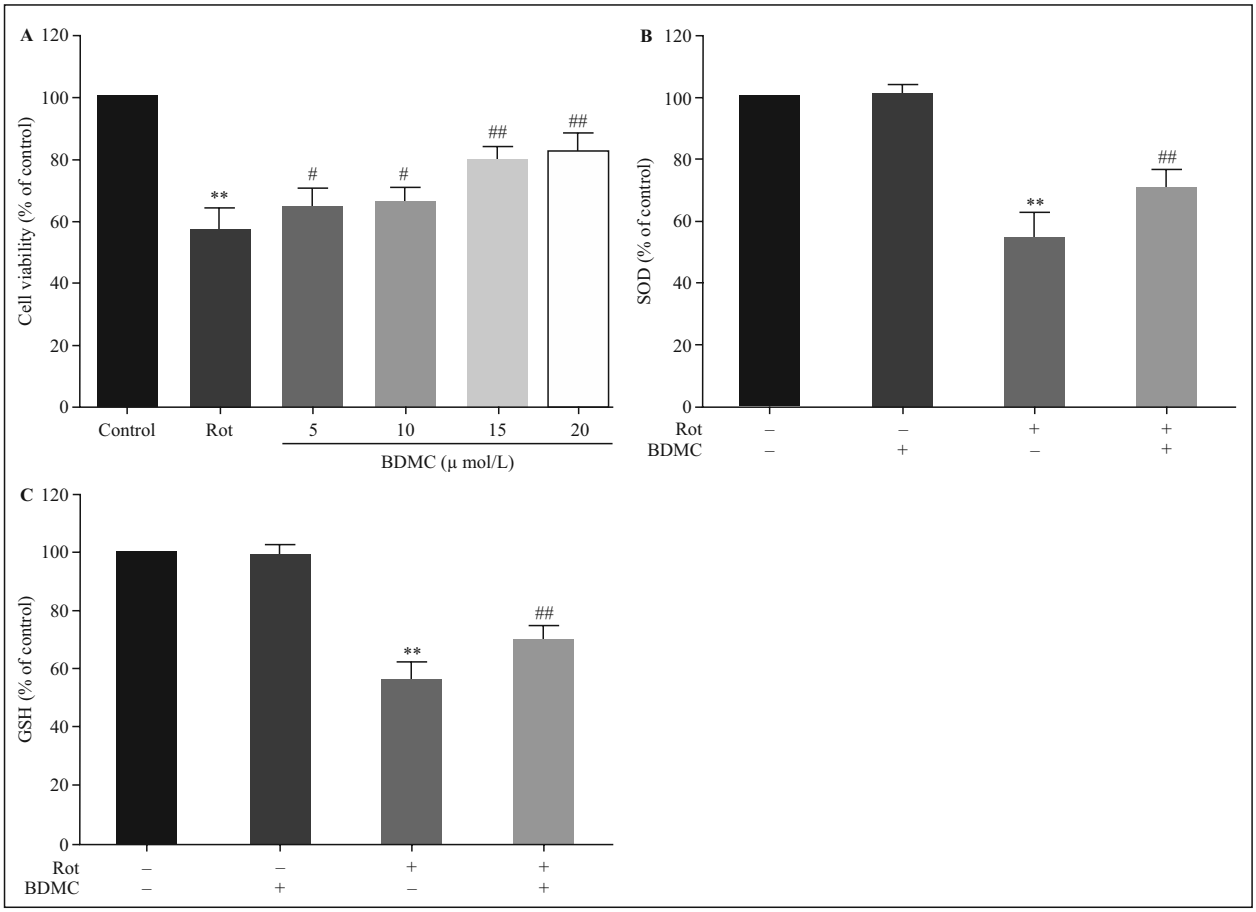

Figure 1. Determination of the effects of BDMC treatment on cell survival and oxidative stress in SH-SY5Y cells treated with rotenone. (**A**) A total of 1×10^4 SH-SY5Y cells were pretreated with BDMC (0, 5, 10, 15 or 20 μM) for 30 min prior to a 24-h co-culture with 100 nM rotenone, and the cell survival rate was calculated. A total of 1×10^4 SH-SY5Y cells were pretreated with 15 μM BDMC for 30 min prior to a 24-h co-culture with 100 nM rotenone, and (**B**) SOD and (**C**) GSH activities were measured. $^{**}P < 0.01$ *vs.* control; $^{\#\#}P < 0.01$, $^{\#}P < 0.05$ *vs*. rotenone-induced group from 5 independent experiments.

SH-SY5Y cells upon the inhibition of the JAK/STAT3 signaling pathway.

S3I-201, an inhibitor of the STAT3 signaling pathway, reverses the cell-protective effects of BDMC treatment in SH-SY5Y cells treated with rotenone

To investigate the effects of the JAK signaling pathway on the cell-protective role of BDMC in SH-SY5Y cells induced by rotenone, the phosphorylation levels of JAK, cell survival, and SOD and GSH activities were analyzed following the pretreatment of cells with S3I-201 and BDMC and the co-culture with rotenone.

The results of the cell viability assay revealed that BDMC treatment did not increase the cell survival of SH-SY5Y cells induced by rotenone following the inhibition of the JAK signaling pathway (Fig. 4A).

Furthermore, BDMC treatment did not increase the SOD levels in rotenone-induced SH-SY5Y cells following the inhibition of the JAK signaling pathway (Fig. 4B). A similar pattern was observed for GSH levels (Fig. 4C).

These results indicated that BDMC treatment may not inhibit the toxicity induced by rotenone in SH-SY5Y cells upon the inhibition of the JAK signaling pathway.

Discussion

In the present study, BDMC treatment was revealed to enhance the cell survival, antioxidative stress ability and the phosphorylation levels of JAK/STAT3 in SH-SY5Y cells treated with rotenone. Moreover, following the inhibition of the JAK/STAT3 signaling pathway, BDMC was unable to exert these cell-protective roles. Thus, the present study suggested that BDMC treatment may protect SH-SY5Y cells from the neurotoxicity induced by rotenone treatment via the JAK/STAT3 signaling pathway.

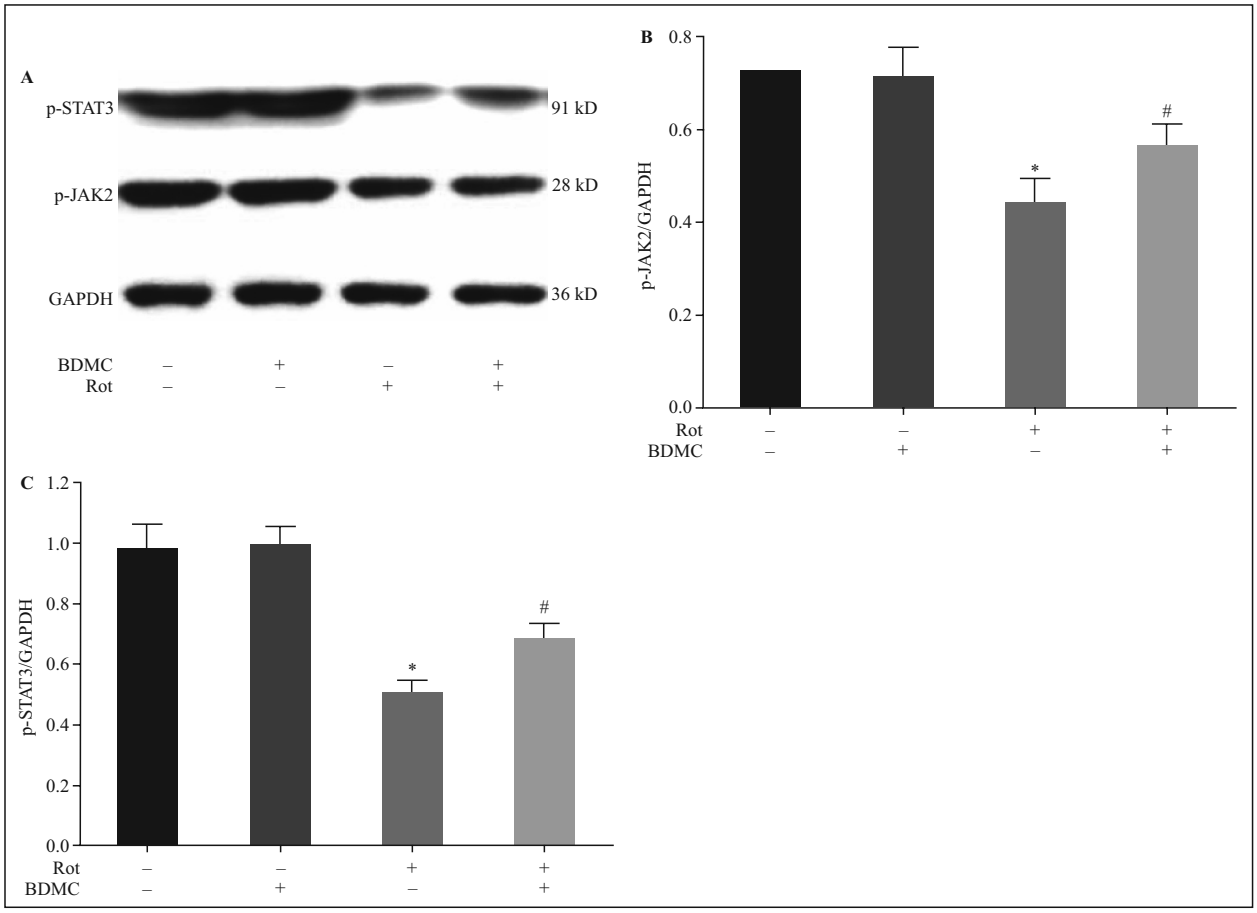

Figure 2. Determination of the effects of BDMC treatment on the JAK/STAT3 signaling pathway in SH-SY5Y cells treated with rotenone. (**A**) A total of 1×10^4 SH-SY5Y cells were pretreated with 15 μM BDMC for 30 min prior to a 24-h co-culture with 100 nM rotenone, and western blotting was performed. Representative western blots are shown. The phosphorylation levels of (**B**) JAK2 and (**C**) STAT3 were upregulated following the treatment with BDMC. $^*P < 0.05$ *vs*. control group; $^{\#}P < 0.05$ *vs*. rotenone-induced group from 5 independent experiments.

PD is a slow, progressive neurodegenerative disease that is associated with the degeneration of dopaminergic neurons [28]. The loss of dopamine accounts for numerous of the symptoms that accompany the disease, including motor dysfunction, mood alterations and cognitive impairment [29]. Due to difficulties in studying the progression of PD in humans, the treatment of the catecholaminergic neuroblastoma cell line SH-SY5Y with various neurotoxins has been widely used to construct a model closely mimicking PD *in vitro* [30–32]. In the present study, BDMC treatment was discovered to decrease the cell death of SH-SY5Y cells induced by rotenone.

Oxidative stress has been identified to account for the progressive death of the dopaminergic neurons [33]. The apoptotic death of nigrostriatal dopaminergic neurons is initiated by oxidative stress [34]. SOD and GSH are important antioxidants that scavenge oxygen free radicals, thus protecting against oxidative stress. In PD model rats, the levels of GSH, SOD and other free radical scavenging enzymes in the brain of the model rats were significantly reduced, further indicating that the rat model of PD demonstrated a reduced ability to scavenge oxygen free radicals; this led to the accumulation of ROS in the tissue cells, which in turn induced the continuous progression of PD [35]. In the present study, BDMC was discovered to protect against oxidative stress.

The activation of the JAK2/STAT3 signaling pathway serves as a protective mechanism against oxidative stress [36]. In the present study, the phosphorylation levels of the JAK2/STAT3 signaling pathway were identified to be upregulated in response to BDMC treatment, whereas following the inhibition of this pathway, BDMC was unable to exert its functional roles.

In conclusion, the findings of the present study suggested that BDMC treatment may alleviate the

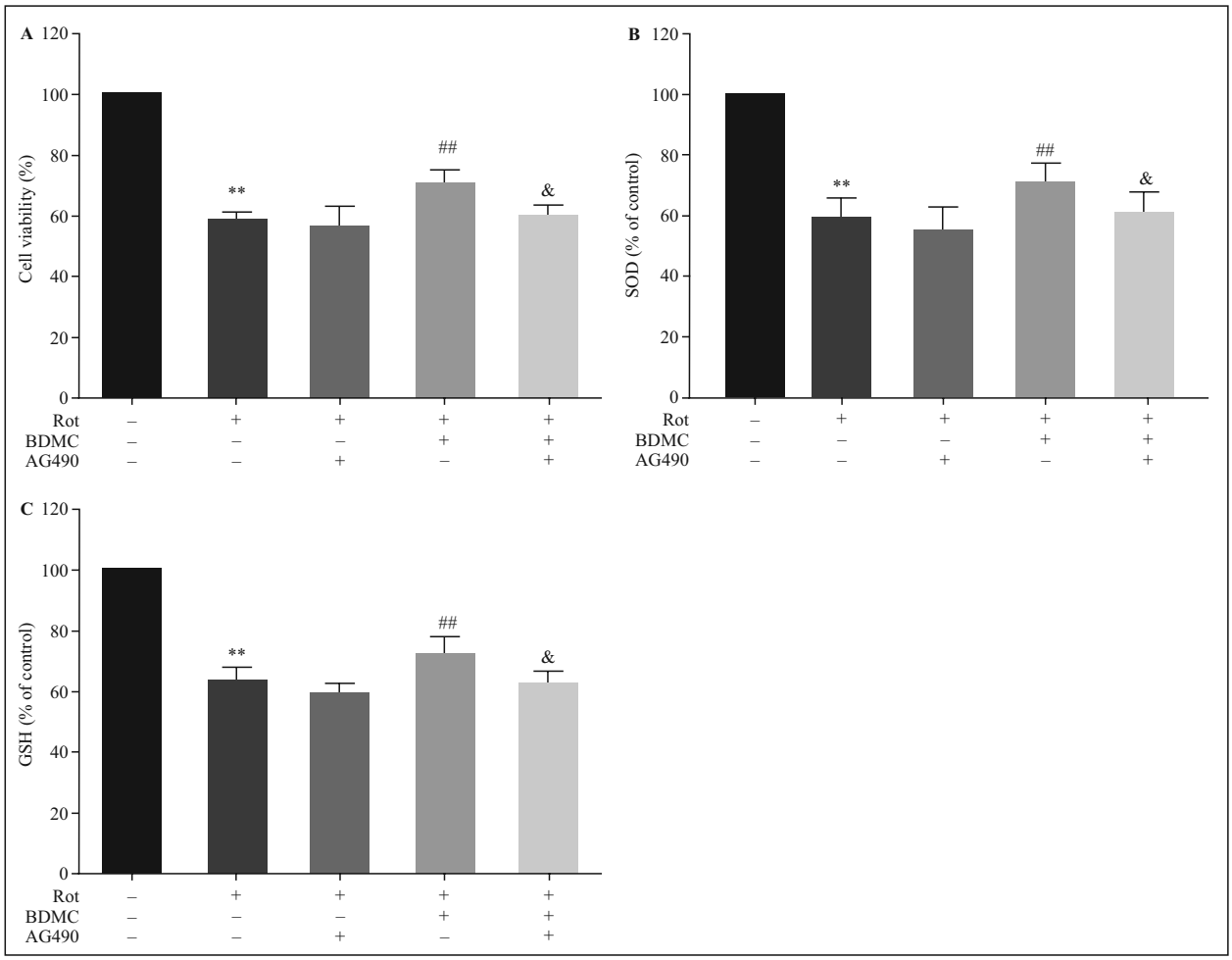

Figure 3. Determination of the effects of BDMC treatment on the cell survival and oxidative stress in SH-SY5Y cells treated with rotenone following the inhibition of the JAK/STAT3 signaling pathway. A total of 1×10^4 SH-SY5Y cells were co-pretreated with 10 μM AG490 (an inhibitor of the JAK/STAT3 signaling pathway) and 15 μM BDMC for 30 min prior to a 24-h co-culture with 100 nM rotenone. The (**A**) cell survival rate, (**B**) SOD activity and (**C**) GSH activity were not increased in response to the treatment with BDMC following the inhibition of the JAK/STAT3 signaling pathway. $^{**}P < 0.01$ *vs*. control group; $^{\#\#}P < 0.01$, $^{\#}P < 0.05$ *vs*. rotenone-induced group; $^{\&}P < 0.05$ *vs*. BDMC + rotenone-induced group from 5 independent experiments.

neurotoxicity of rotenone in SH-SY5Y cells by improving cell survival and exerting antioxidative stress properties. These effects were indicated to occur through the inhibition of the JAK/STAT3 signaling pathway, which may provide a foundation for BDMC treatment to be considered as a novel therapeutic strategy for the treatment of PD.

Acknowledgements

We thank the Hunan Provincial Natural Science Foundation of China (grant nos. 2019JJ40267, 2017JJ3273, 2018JJ2358), Hunan Health Commission project (grant nos. 20201911, 20200469, 20201963, C20180238) and Hengyang Science and technology project (grant no.2016KJ38) for support.

Declaration of competing interest

All authors declare no competing interests.

Disclosure of conflict of interest

None.

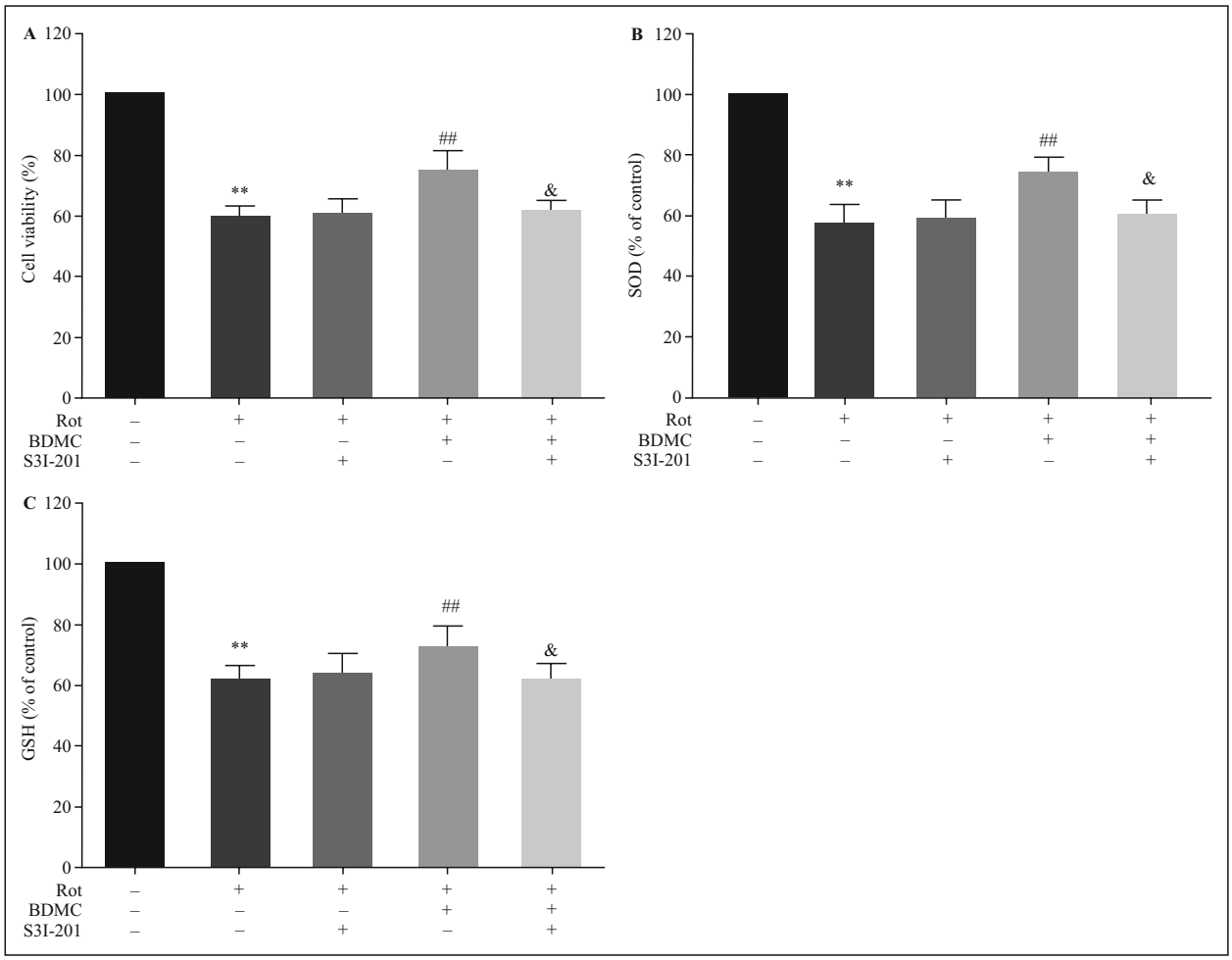

Figure 4. Determination of the effects of BDMC treatment on the cell survival and oxidative stress in SH-SY5Y cells treated with rotenone following the inhibition of the STAT3 signaling pathway. A total of 1×10^4 SH-SY5Y cells were co-pretreated with 100 nM S3I-201 (an inhibitor of the STAT3 signaling pathway) and 15 μM BDMC for 30 min prior to a 24-h co-culture with 100 nM rotenone. The (**A**) cell survival rate, (**B**) SOD activity and (**C**) GSH activity were not increased in response to the treatment with BDMC upon the inhibition of the STAT3 signaling pathway. $^{**}P < 0.01$ *vs*. control group; $^{\#\#}P < 0.01$, $^{\#}P < 0.05$ *vs*. rotenone-induced group; $^{\&}P < 0.05$ *vs*. BDMC + rotenone-induced group from 5 independent experiments.

References

1. Cao Xu, Cao L, Ding L, et al. A New Hope for a Devastating Disease: Hydrogen Sulfide in Parkinson's Disease. Mol Neurobiol. 2018; 55(5): 3789–3799, doi: 10.1007/s12035-017-0617-0, indexed in Pubmed: 28536975.
2. Keeney PM, Xie J, Capaldi RA, et al. Parkinson's disease brain mitochondrial complex I has oxidatively damaged subunits and is functionally impaired and misassembled. J Neurosci. 2006; 26(19): 5256–5264, doi: 10.1523/JNEUROSCI.0984-06.2006, indexed in Pubmed: 16687518.
3. Chaudhuri K, Schapira A. Non-motor symptoms of Parkinson's disease: dopaminergic pathophysiology and treatment. The Lancet Neurology. 2009; 8(5): 464–474, doi: 10.1016/s1474-4422(09)70068-7.
4. Xia R, Mao ZH. Progression of motor symptoms in Parkinson's disease. Neurosci Bull. 2012; 28(1): 39–48, doi: 10.1007/s12264-012-1050-z, indexed in Pubmed: 22233888.
5. Mattson MP. Apoptosis in neurodegenerative disorders. Nat Rev Mol Cell Biol. 2000; 1(2): 120–129, doi: 10.1038/35040009, indexed in Pubmed: 11253364.
6. Onyango IG. Mitochondrial dysfunction and oxidative stress in Parkinson's disease. Neurochem Res. 2008; 33(3): 589–597, doi: 10.1007/s11064-007-9482-y, indexed in Pubmed: 17940895.
7. Youn JK, Kim DW, Kim ST, et al. PEP-1-HO-1 prevents MPTP-induced degeneration of dopaminergic neurons in a Parkinson's disease mouse model. BMB Rep. 2014; 47(10): 569–574, doi: 10.5483/bmbrep.2014.47.10.286, indexed in Pubmed: 24499676.
8. Gagliardi S, Ghirmai S, Abel KJ, et al. Evaluation in vitro of synthetic curcumins as agents promoting monocytic gene expression related to β-amyloid clearance. Chem Res Toxicol. 2012; 25(1): 101–112, doi: 10.1021/tx200246t, indexed in Pubmed: 22029407.
9. Sandur SK, Pandey MK, Sung B, et al. Curcumin, demethoxycurcumin, bisdemethoxycurcumin, tetrahydrocurcumin and turmerones differentially regulate anti-inflammatory and anti-proliferative responses through a ROS-independent mechanism. Carcinogenesis. 2007; 28(8): 1765–1773, doi: 10.1093/carcin/bgm123, indexed in Pubmed: 17522064.

10. Ramezani M, Hatamipour M, Sahebkar A. Promising anti-tumor properties of bisdemethoxycurcumin: A naturally occurring curcumin analogue. J Cell Physiol. 2018; 233(2): 880–887, doi: 10.1002/jcp.25795, indexed in Pubmed: 28075008.
11. Basile V, Ferrari E, Lazzari S, et al. Curcumin derivatives: molecular basis of their anti-cancer activity. Biochem Pharmacol. 2009; 78(10): 1305–1315, doi: 10.1016/j.bcp.2009.06.105, indexed in Pubmed: 19580791.
12. Jenner P. Oxidative stress in Parkinson's disease. Ann Neurol. 2003; 53 Suppl 3: S26–36; discussion S36, doi: 10.1002/ana.10483, indexed in Pubmed: 12666096.
13. Reynolds A, Laurie C, Mosley RL, et al. Oxidative Stress and the Pathogenesis of Neurodegenerative Disorders. Int Rev Neurobiol. 2007: 297–325, doi: 10.1016/s0074-7742(07)82016-2, indexed in Pubmed: 17678968.
14. La Fortezza M, Schenk M, Cosolo A, et al. JAK/STAT signalling mediates cell survival in response to tissue stress. Development. 2016; 143(16): 2907–2919, doi: 10.1242/dev.132340, indexed in Pubmed: 27385008.
15. Hoffmann CJ, Harms U, Rex A, et al. Vascular signal transducer and activator of transcription-3 promotes angiogenesis and neuroplasticity long-term after stroke. Circulation. 2015; 131(20): 1772–1782, doi: 10.1161/CIRCULATIONAHA.114.013003, indexed in Pubmed: 25794850.
16. Eum WS, Shin MJ, Lee CH, et al. Neuroprotective effects of Tat-ATOX1 protein against MPP-induced SH-SY5Y cell deaths and in MPTP-induced mouse model of Parkinson's disease. Biochimie. 2019; 156: 158–168, doi: 10.1016/j.biochi.2018.10.010, indexed in Pubmed: 30352250.
17. Park SI, Lee EH, Kim SoRa, et al. Anti-apoptotic effects of Curcuma longa L. extract and its curcuminoids against blue light-induced cytotoxicity in A2E-laden human retinal pigment epithelial cells. J Pharm Pharmacol. 2017; 69(3): 334––340, doi: 10.1111/jphp.12691, indexed in Pubmed: 28155996.
18. Im JH, Yeo InJ, Hwang CJu, et al. PEGylated Erythropoietin Protects against Brain Injury in the MCAO-Induced Stroke Model by Blocking NF-κB Activation. Biomol Ther (Seoul). 2020; 28(2): 152–162, doi: 10.4062/biomolther.2019.147, indexed in Pubmed: 31813204.
19. Chen S, Hou Y, Zhao Z, et al. Neuregulin-1 Accelerates Functional Motor Recovery by Improving Motoneuron Survival After Brachial Plexus Root Avulsion in Mice. Neuroscience. 2019; 404: 510–518, doi: 10.1016/j.neuroscience.2019.01.054, indexed in Pubmed: 30731156.
20. Li J, Chen S, Zhao Z, et al. Effect of VEGF on Inflammatory Regulation, Neural Survival, and Functional Improvement in Rats following a Complete Spinal Cord Transection. Front Cell Neurosci. 2017; 11: 381, doi: 10.3389/fncel.2017.00381, indexed in Pubmed: 29238292.
21. Chen SX, He JH, Mi YJ, et al. A mimetic peptide of α2,6-sialyllactose promotes neuritogenesis. Neural Regen Res. 2020; 15(6): 1058–1065, doi: 10.4103/1673-5374.270313, indexed in Pubmed: 31823885.
22. Yuhai GU, Zhen Z. Significance of the changes occurring in the levels of interleukins, SOD and MDA in rat pulmonary tissue following exposure to different altitudes and exposure times. Exp Ther Med. 2015; 10(3): 915–920, doi: 10.3892/etm.2015.2604, indexed in Pubmed: 26622414.
23. Mao GX, Zheng LD, Cao YB, et al. Antiaging effect of pine pollen in human diploid fibroblasts and in a mouse model induced by D-galactose. Oxid Med Cell Longev. 2012; 2012: 750963, doi: 10.1155/2012/750963, indexed in Pubmed: 22577492.
24. Zhang Bo, Chen Na, Chen H, et al. The critical role of redox homeostasis in shikonin-induced HL-60 cell differentiation via unique modulation of the Nrf2/ARE pathway. Oxid Med Cell Longev. 2012; 2012: 781516, doi: 10.1155/2012/781516, indexed in Pubmed: 23119122.
25. Xu J, Hu C, Chen S, et al. Neuregulin-1 protects mouse cerebellum against oxidative stress and neuroinflammation. Brain Res. 2017; 1670: 32–43, doi: 10.1016/j.brainres.2017.06.012, indexed in Pubmed: 28623147.
26. Chen Sx, Hu Cl, Liao Yh, et al. L1 modulates PKD1 phosphorylation in cerebellar granule neurons. Neurosci Lett. 2015; 584: 331–336, doi: 10.1016/j.neulet.2014.11.012, indexed in Pubmed: 25445362.
27. Jiang Q, Chen S, Hu C, et al. Neuregulin-1 (Nrg1) signaling has a preventive role and is altered in the frontal cortex under the pathological conditions of Alzheimer's disease. Mol Med Rep. 2016; 14(3): 2614–2624, doi: 10.3892/mmr.2016.5542, indexed in Pubmed: 27486021.
28. Vogt Weisenhorn DM, Giesert F, Wurst W. Diversity matters - heterogeneity of dopaminergic neurons in the ventral mesencephalon and its relation to Parkinson's Disease. J Neurochem. 2016; 139 Suppl 1: 8–26, doi: 10.1111/jnc.13670, indexed in Pubmed: 27206718.
29. Olanow CW, Schapira AHV, Agid Y. Neuroprotection for Parkinson's disease: prospects and promises. Ann Neurol. 2003; 53 Suppl 3: S1–S2, doi: 10.1002/ana.10566, indexed in Pubmed: 12666093.
30. Xie Hr, Hu Ls, Li Gy. SH-SY5Y human neuroblastoma cell line: in vitro cell model of dopaminergic neurons in Parkinson's disease. Chin Med J (Engl). 2010; 123(8): 1086–1092, indexed in Pubmed: 20497720.
31. Xicoy H, Wieringa Bé, Martens GJM. The SH-SY5Y cell line in Parkinson's disease research: a systematic review. Mol Neurodegener. 2017; 12(1): 10, doi: 10.1186/s13024-017-0149-0, indexed in Pubmed: 28118852.
32. Morales-Garcia JA, Aguilar-Morante D, Hernandez-Encinas E, et al. Silencing phosphodiesterase 7B gene by lentiviral-shRNA interference attenuates neurodegeneration and motor deficits in hemiparkinsonian mice. Neurobiol Aging. 2015; 36(2): 1160–1173, doi: 10.1016/j.neurobiolaging.2014.10.008, indexed in Pubmed: 25457552.
33. Dexter DT, Jenner P. Parkinson disease: from pathology to molecular disease mechanisms. Free Radic Biol Med. 2013; 62: 132–144, doi: 10.1016/j.freeradbiomed.2013.01.018, indexed in Pubmed: 23380027.
34. Agrawal S, Singh A, Tripathi P, et al. Cypermethrin-induced nigrostriatal dopaminergic neurodegeneration alters the mitochondrial function: a proteomics study. Mol Neurobiol. 2015; 51(2): 448–465, doi: 10.1007/s12035-014-8696-7, indexed in Pubmed: 24760363.
35. Lee HJ, Shin SY, Choi C, et al. Formation and removal of alpha-synuclein aggregates in cells exposed to mitochondrial inhibitors. J Biol Chem. 2002; 277(7): 5411–5417, doi: 10.1074/jbc.M105326200, indexed in Pubmed: 11724769.
36. Zheng Wx, Wang F, Cao Xl, et al. Baicalin protects PC-12 cells from oxidative stress induced by hydrogen peroxide via anti-apoptotic effects. Brain Inj. 2014; 28(2): 227–234, doi: 10.3109/02699052.2013.860469, indexed in Pubmed: 24456060.

Submitted: 25 December, 2019
Accepted after reviews: 3 June, 2020
Available as AoP: 18 June, 2020

FOLIA HISTOCHEMICA ET CYTOBIOLOGICA
Vol. 58, No. 2, 2020
pp. 135–146

ORIGINAL PAPER

VIA MEDICA

A close neuroanatomical relationship between the enkephalinergic (methionine-enkephalin) and tachykininergic (substance P) systems in the alpaca diencephalon

Pablo Sánchez[1], Manuel Lisardo Sánchez[1*], Arturo Mangas[1, 2], Luís Ángel Aguilar[3], Rafael Coveñas[1]

[1]Institute of Neuroscience of Castilla y León (INCYL), Laboratory of Neuroanatomy of the Peptidergic Systems (Lab. 14), University of Salamanca, Salamanca, Spain
[2]PolyNeuroS, Villenave d'Ornon, France
[3]San Ignacio de Loyola University (USIL), Faculty of Health Sciences, Lima, Peru

Abstract

Introduction. In the alpaca diencephalon, the distribution of immunoreactive cell bodies and fibers containing methionine-enkephalin (MET) or substance P (SP) has been studied.

Material and methods. The immunohistochemical study was performed by standard method on the diencephalon of four male alpacas that lived at sea level.

Results. Nerve fibers containing MET or SP were widely distributed in the thalamus and hypothalamus. MET- and SP-immunoreactive fibers showed a similar distribution in the whole diencephalon. Immunoreactive cell bodies containing MET or SP were only observed in the hypothalamus. The distribution of MET-immunoreactive cell bodies was more widespread than that observed for cell bodies containing SP.

Conclusions. A close neuroanatomical relationship between the tachykininergic (SP) and enkephalinergic (MET) systems was observed in the whole diencephalon suggestive of the existence of multiple physiological interactions between both systems. *(Folia Histochemica et Cytobiologica 2020, Vol. 58, No. 2, 135–146)*

Key words: *Lama pacos*; hypothalamus; thalamus; methionine-enkephalin; substance P; IHC

Introduction

The ungulate alpaca (*Lama pacos*) (family: Camelidae; order: Artiodactyla) can live from 5,000 m altitude to the sea level and this means that these animals have unique special physiological adjustment mechanisms in which neuroactive substances could be involved [1]. The diencephalon plays important physiological functions: the thalamus, among other functions, is closely related to the relay of sensory information and regulation of sleep and wakefulness, whereas the hypothalamus plays a crucial role as a neuroendocrine center. Substance P (SP) (an undecapeptide member of the tachykinin family of peptides) and methionine-enkephalin (MET) (a pentapeptide that belongs to the opioid family of peptides) (Fig. 1) are widely distributed throughout the mammalian central nervous system (CNS). It is known that SP and MET are involved in functional and pathophysiological activities (*e.g.*, inflammation, feeding behavior, immune response, neuroendocrine and visual mechanisms, learning, cancer, pain, depression, stress) [2–9]. These actions are mediated by neurokinin and opiate receptors which are transmem-

Correspondence address: Dr. Manuel Lisardo Sánchez
Universidad de Salamanca
Instituto de Neurociencias de Castilla y León (INCYL)
Laboratorio de Neuroanatomía de los Sistema Peptidérgicos (Lab. 14)
c/ Pintor Fernando Gallego, 1
37007-Salamanca, Spain
phone: +34 923294400 ext. 1856
fax: +34 923294549
e-mail: lisardosanchez8@gmail.com

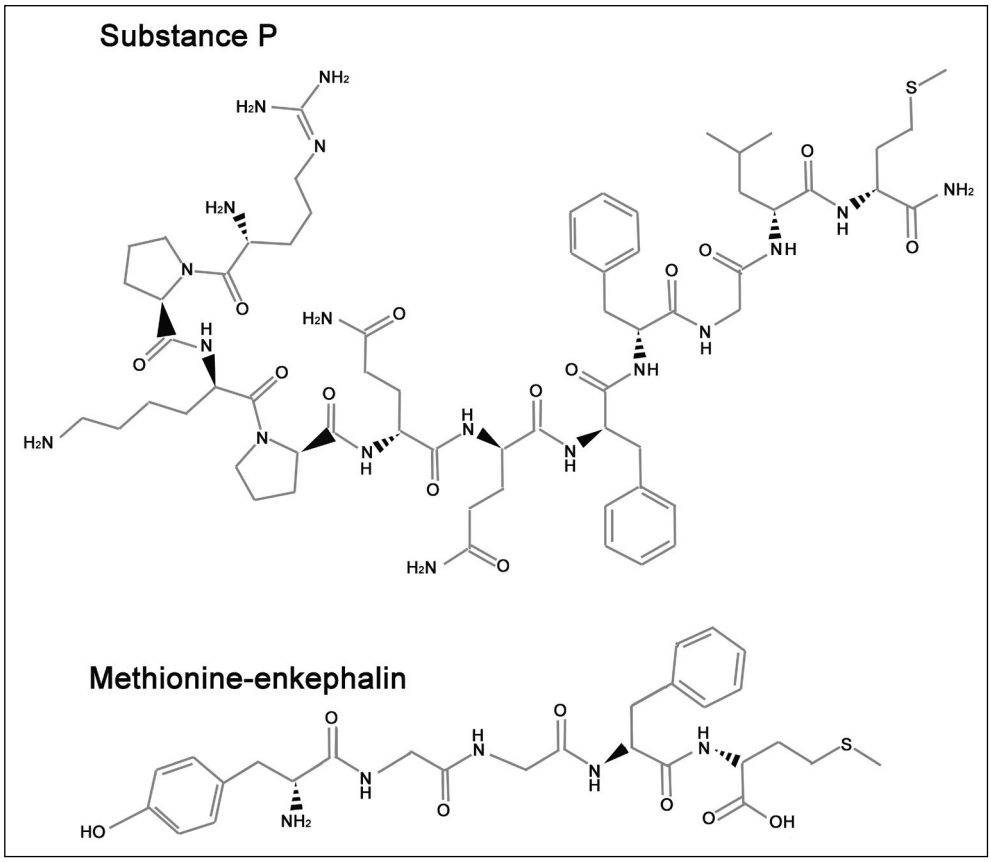

Figure 1. Chemical structures of substance P and methionine-enkephalin.

brane G-protein coupled receptors. The neurokinin-1 receptor shows a preferential affinity for SP, whereas MET is a potent agonist of the delta opioid receptor and to a lesser extend of the mu receptor [2].

Our group has previously studied the distribution of several neuropeptides in the alpaca diencephalon (somatostatin-28) (1–12), calcitonin gene-related peptide (CGRP), adrenocorticotropic hormone (18–39), ACTH, alpha-melanocyte-stimulating hormone (alpha MSH), beta-endorphin (1–27), alpha-neo-endorphin, leucine-enkephalin, and neurotensin) [10–14]. In this study we aimed to describe for the first time, the distribution of immunoreactive cell bodies and fibers containing MET or SP in the alpaca diencephalon since in other mammals (*e.g.*, rat, cat, monkey) a neuroanatomical relationship between SP and MET in the CNS has been previously reported [15–20].

Material and methods

Animals and tissue preparation. As previously reported [14], the study was carried out according to Spanish and Peruvian laws and under the supervision of the Research Commission of the Cayetano Heredia Peruvian University (Lima, Peru). Four male adult alpacas (70–80 kg) were always kept at sea level and were obtained from the Cayetano Heredia Peruvian University (Faculty of Veterinary Medicine and Animal Sciences) [14]. As previously described [14], alpacas were deeply anaesthetized (ketamine (10 mg/kg) and xylazine (4 mg/kg), *i.v.*), heparinized and perfused *via* the carotid artery with cold NaCl (0.9%) and followed by perfusion with cold paraformaldehyde (4% in 0.15 M phosphate-buffered saline (PBS), pH 7.2). Diencephalons were dissected out, post-fixed overnight in paraformaldehyde and cryoprotected by immersion in increasing (10–30%) concentrations of sucrose solution until they sank. Using a cryostat, serial frontal sections (50 μm thick) were obtained. Two of five sections were used for immunohistochemistry: section 1, for anti-SP staining; section 2, for histological control or to be stained with cresyl violet to delineate/identify the diencephalic nuclei; section 3, for anti-MET staining; sections 4–5 were kept for other experimental purposes. The distance between sections 1 and 6 (and so on, kept in the same container) was about 200 μm. Thus, sections kept in slide container 1 were used for anti-SP and those kept in container 3 for anti-MET. In each container, 25–30 frontal sections/animal were collected. Sections were kept in PBS at 4° C for 2–6 days.

Immunohistochemistry and specificity of the antisera. Free-floating immunohistochemistry was performed as previously reported [14, 21]. Sections were washed in PBS and incubated in PBS containing Triton X-100 (0.3%, Panreac, Barcelona, Spain) and normal horse serum (1%, Sigma-Aldrich, Madrid, Spain) for 30 min. Then, sections were incubated overnight (4°C) in the latter PBS solution containing anti-Met-5 antiserum (1/3,000) or anti-SP antiserum (1/3,000). Later, sections were washed in PBS and incubated in biotinylated anti-rabbit IgG (1:200) (Vector Laboratories, Burlingame, CA, USA) for 1 h. Then, sections were rinsed with PBS and treated with Vectastain ABC reagent (1:100) (Vector Laboratories) for 1 h. Sections were washed in PBS (30 min) and Tris-HCL buffer (10 min) (Panreac). Using 3, 3'-diaminobenzidine (Sigma-Aldrich) as chromogen and H_2O_2 the tissue bound peroxidase was developed. Finally, sections were washed with PBS and coverslipped with glycerol/PBS (1:1).

As formerly reported [22–24], the polyclonal primary antibodies (anti-SP; anti-MET) used in this study were raised in rabbits against immunogens assembled by coupling the full synthetic MET or SP to a carrier protein (human serum albumin) with glutaraldehyde. Both antibodies were obtained at the laboratory of Professor Gérard Tramu (University of Bordeaux I, Talence, France). Moreover, the immunological properties of the anti-MET and anti-SP antisera have been previously published [22–24]. To confirm the specificity of both antisera, histological controls were carried out: 1) in the first incubation bath, the first antiserum was omitted; 2) the primary antiserum was preabsorbed with an excess of the antigen (100 μg/mL of diluted antiserum; *e.g.* anti-SP with SP); and 3) the primary antiserum was preabsorbed with an excess (10^{-7} M) of heterologous antigens (*e.g.* anti-MET with leucine-enkephalin). In all cases, the results confirmed the specificity of the immunoreactivity observed in the alpaca diencephalon. Moreover, as previously reported [14] and to avoid interference by endogenous peroxidase, sections were treated with H_2O, NaOH and NH_3 (Panreac) before the immunohistochemical technique was performed.

Mapping. Mapping was carried out according to the frontal planes of the alpaca diencephalon (the brain atlas used in this study is available from the Mammalian Brain Collections of the University of Wisconsin, Madison, WI, U.S.A.) and according to the alpaca diencephalic frontal sections published in previous papers [10–14]. For nomenclature of the diencephalic nuclei, we followed the nomenclature used in previously published works carried out in the alpaca [10–14]. Using an Olympus DP-50 digital camera (Olympus, Tokyo, Japan) attached to a Kyowa Unilux 12 microscope (Kyowa, Tokyo, Japan), photomicrographs were taken and Adobe Photoshop CS6 software was used to adjust brightness and contrast.

As previously published [10–14], the density of the immunoreactive fibers was considered as high, moderate, low and single. Sections were viewed at constant magnification with reference to photographs in which high, moderate or low densities had been previously determined [10–14]. The density of the immunoreactive cell bodies was considered as high (> 20 perikarya/section), moderate (10–20 perikarya/section) and low (< 10 perikarya/section). Moreover, cell bodies were classified into three categories: large (> 25 μm diameter), medium sized (15–25 μm) and small (< 15 μm) [14]. The size was measured using a micrometer grid with the nucleus in the focal plane.

Results

General considerations

Figures 2–5 show the density and distribution of the immunoreactive structures (cell bodies and fibers) for MET/SP found in the alpaca diencephalon. In this region, 40/42 tracts/nuclei (95%) contained SP-immunoreactive (-Ir) cell bodies and/or fibers, whereas the same percentage was observed for MET-Ir structures. In all thalamic tracts/nuclei (25 in total), SP- and MET-Ir structures were observed (100%), whereas in 15/17 (88%) of nuclei of the hypothalamus immunoreactivity for both neuropeptides was found.

SP- and MET-Ir fibers showed a widespread distribution in the alpaca diencephalon. Except for the optic tract and optic chiasm, in the diencephalon SP and MET immunoreactive fibers were observed in almost all diencephalic tracts/nuclei (40/42, 95%) and hence the distribution of both immunoreactive fibers was similar (Fig. 2; Table 1). In addition, in the alpaca diencephalon the density of both immunoreactive fibers was similar (Fig. 2; Table 1).

In the diencephalon, no SP- or MET-immunoreactive cell body was observed in the thalamus, whereas in the hypothalamus cell bodies containing SP were only visualized in one nucleus (6%) and those containing MET in six hypothalamic nuclei (35%). Thus, in the alpaca hypothalamus the distribution and number of cell bodies containing MET was higher than those containing SP. The morphological characteristics of the SP- and MET-immunoreactive cell bodies are shown in Table 2.

Finally, it is important to remark that in different regions of the same diencephalic nucleus, high and moderate densities of the studied structures were observed (Table 1). In these cases, to obtain the percentages appearing below the highest density was chosen.

Thalamus

No cell body containing SP or MET was found, but all thalamic tracts/nuclei (25 in total) showed SP- and MET-Ir nerve fibers (Fig. 2; Table 1). Thus, a similar distribution for SP- and MET-immunoreactive

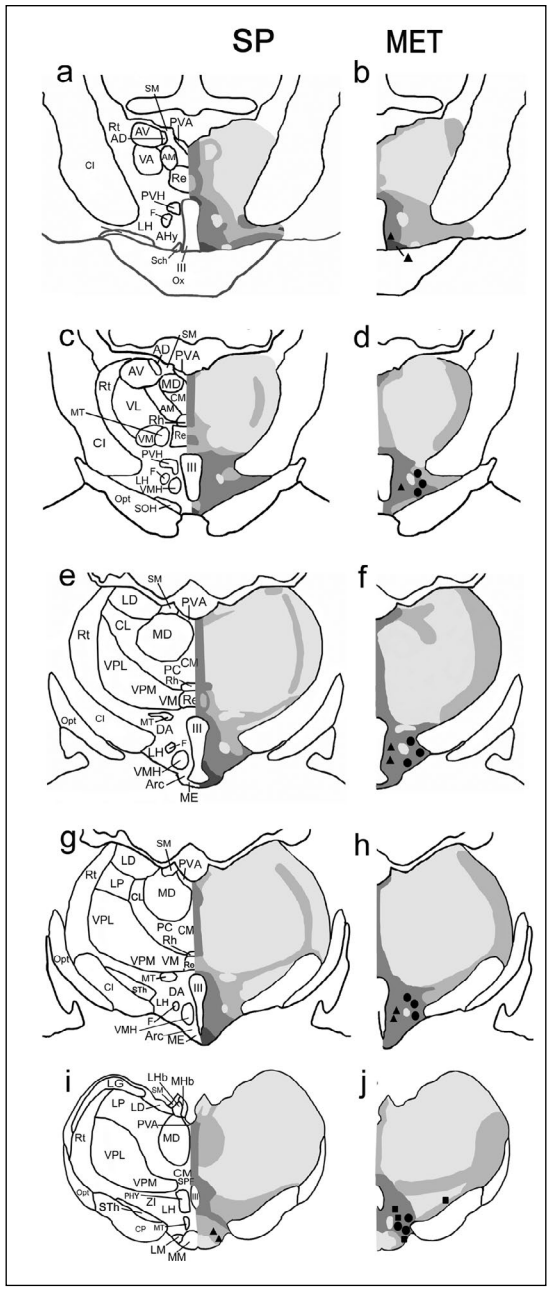

Figure 2. Distribution of substance P- (SP) and methionine-enkephalin (MET)-immunoreactive fibers and cell bodies in frontal planes of the alpaca diencephalon (**a–j**) from rostral (**a**) to caudal (**j**) levels. Cell bodies containing the peptides are represented by closed circles (high density), triangles (moderate density) and squares (low density), whereas immunoreactive fibers are represented by slightly dark (single axons), moderately dark (low density), strongly dark (moderate density), and dark (high density). Abbreviations: III — third ventricle; AD — anterodorsal thalamic nucleus; AHy — anterior hypothalamic area; AM — anteromedial thalamic nucleus; Arc — arcuate nucleus; AV — anteroventral thalamic nucleus; CI — capsula interna; CL — centrolateral thalamic nucleus; CM — central medial thalamic nucleus; CP — cerebral peduncle; DA — dorsal hypothalamic area; F — fornix; IP — interpeduncular nucleus; LD — laterodorsal thalamic nucleus; LG — lateral geniculate nucleus; LH — lateral hypothalamic nucleus; LHb — lateral habenular nucleus; LM — lateral mammillary nucleus; LP — lateroposterior thalamic nucleus; MD — mediodorsal thalamic nucleus; ME — median eminence; MHb — medial habenular nucleus; MM — medial mammillary nucleus; MT — mammillothalamic tract; Opt — optic tract; Ox — optic chiasm; PC — paracentral thalamic nucleus; PHy — posterior hypothalamic nucleus; PVA — paraventricular thalamic nucleus; PVH — paraventricular hypothalamic nucleus; Re — reuniens thalamic nucleus; Rh — rhomboid thalamic nucleus; Rt — reticular thalamic nucleus; Sch — suprachiasmatic nucleus; SM — stria medullaris; SOH — supraoptic hypothalamic nucleus; SPF — subparafascicular thalamic nucleus; STh — subthalamic nucleus; VA — ventroanterior thalamic nucleus; VL — ventrolateral thalamic nucleus; VM — ventromedial thalamic nucleus; VMH — ventromedial hypothalamic nucleus; VPL — ventroposterior thalamic nucleus, lateral part; VPM — ventroposterior thalamic nucleus, medial part; ZI — zona incerta.

Table 1. Alpaca diencephalon: distribution and density of SP- and MET-immunoreactive cell bodies and fibers

Thalamus				
	SP		**MET**	
Nucleus	**CB**	**Fibers**	**CB**	**Fibers**
AD	–	s/+	–	s
AM	–	s/+	–	s
AV	–	s/+	–	s
CL	–	s	–	s
CM	–	++	–	s/++
CP	–	s/+	–	s
LD	–	s	–	s/+
LG	–	s	–	s
LHb	–	s/+	–	s
LP	–	s	–	s
MD	–	s/+	–	s/+
MHb	–	s/+	–	+
PC	–	s	–	s
PVA	–	+/++	–	++
Re	–	+/++	–	s/++
Rh	–	+/++	–	s/++
Rt	–	s/+	–	s/+
SM	–	s	–	s/+
SPF	–	++	–	++
STh	–	+	–	+
VA	–	s	–	s
VL	–	s	–	s
VM	–	s/+	–	s
VPL	–	s	–	s
VPM	–	s	–	s
Hypothalamus				
	SP		**MET**	
Nucleus	**CB**	**Fibers**	**CB**	**Fibers**
AHy	–	++/+++	+	+/+++
Arc	–	+++	–	++
DA	–	++	–	+/++
F	–	s/+	–	s
LH	–	+/++	+++	++
LM	+	+/++	++	++
ME	–	+++	–	++
MM	–	s/+	–	s/+
MT	–	s/+	–	s
Opt	–	–	–	–
Ox	–	–	–	–
PHy	–	++/+++	++	++
PVH	–	++	–	++
Sch	–	+++	+	+++
SOH	–	++	–	+
VMH	–	++	+	++
ZI	–	s/+	–	s

CB — cell bodies (+++: high density; ++: moderate density; +: low density; –: no immunoreactivity). Nerve fibers (+++: high density; ++: moderate density; +: low density; s: single; –: no immunoreactivity). For nomenclature of the nuclei, see list of abbreviations in the description of Figure 2.

fibers was visualized (Figs. 4d–g; 5b–d). The density observed for both neuropeptides ranged from single fibers to moderate (Table 1). Single immunoreactive fibers for SP and MET were found in 10 (40%) and 14 (56%) thalamic tracts/nuclei, respectively; a low density in 10 (40%) and 6 (24%) tracts/nuclei, and a moderate density in 5 nuclei (for both SP and MET, 20%) (Table 1).

Hypothalamus

SP-Ir cell bodies were found in the lateral mammillary nucleus (Fig. 5f) and MET-Ir perikarya in the anterior hypothalamic area (Fig. 3e), lateral mammillary nucleus (Fig. 5e–g), lateral hypothalamic nucleus (Fig. 4c), posterior hypothalamic nucleus, suprachiasmatic nucleus and ventromedial hypothalamic nucleus (Fig. 2; Tables 1, 2).

Fibers containing SP (Figs. 3b, d, f; 4b) or MET (Figs. 3c, e, g; 4c) were observed in all hypothalamic tracts/nuclei studied, except for the optic tract and optic chiasm and hence these fibers showed a similar distribution (Table 1). Single SP-immunoreactive fibers were not observed, whereas single fibers containing MET were found in 3 hypothalamic nuclei (18%). A low density of SP- and MET-Ir fibers were respectively visualized in 4 (24%) and 2 (12%) tract/nuclei; a moderate density in 6 (35%) and 8 (47%) hypothalamic nuclei, and a high density in 5 (29%) and 2 (12%) nuclei (Table 1).

Discussion

SP and MET immunoreactivity in the alpaca diencephalon

For the first time, this study demonstrates the distribution of the MET- and SP-immunoreactive fibers and cell bodies in the alpaca diencephalon. In the hypothalamus the distribution of MET-Ir perikarya is more widespread than that observed for cell bodies containing SP. Our results have also shown a close neuroanatomical relationship between the enkephalinergic (MET) and tachykininergic (SP) systems in the alpaca diencephalon, suggesting that a functional relationship between both systems also occur. Currently, the mechanisms of possible intercellular communication between both systems are unknown and further studies are needed to explain them. However, this relationship could occur *via* volume transmission (paracrine) mechanisms and/or synaptic contacts [25, 26]. Volume transmission is a slow mode of communication showing a high degree of divergence. In this mode of communication, peptides are released into the extracellular fluid and diffuse longer distances to reach high-affinity recep-

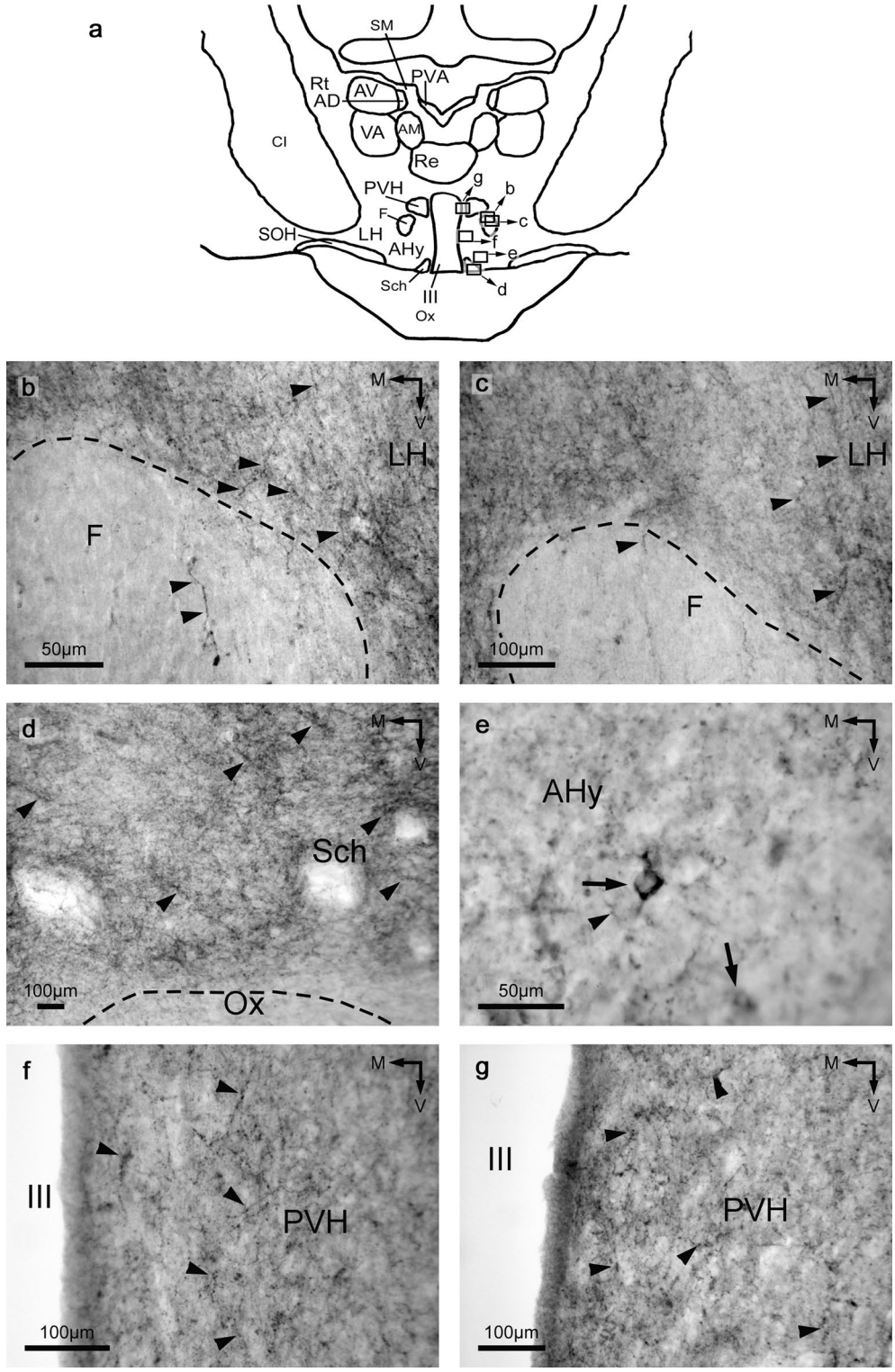

Figure 3. SP- and MET-immunoreactive cell bodies and fibers in the alpaca diencephalon. (**a**) Frontal section of the alpaca diencephalon. For the nomenclature of the nuclei, see Figure 2 (abbreviations). The photographs shown in b–g were taken from the regions delimited by the rectangles in a (indicated as b, c, d, e, f and g). (**b**) SP-immunoreactive fibers (arrowheads) located in the lateral hypothalamic area (LH) and fornix (F). (**c**) MET-immunoreactive fibers (arrowheads) located in the lateral hypothalamic area (LH) and fornix (F). (**d**) SP-immunoreactive fibers (arrowheads) located in the suprachiasmatic nucleus (Sch). Ox — optic chiasm. (**e**) MET-immunoreactive perikarya (arrows) in the anterior hypothalamic area (AHy). (**f**) SP-immunoreactive fibers (arrowheads) in the paraventricular hypothalamic nucleus (PVH). III — third ventricle. (**g**) MET-immunoreactive fibers (arrowheads) in the paraventricular hypothalamic nucleus (PVH). M — medial. V — ventral.

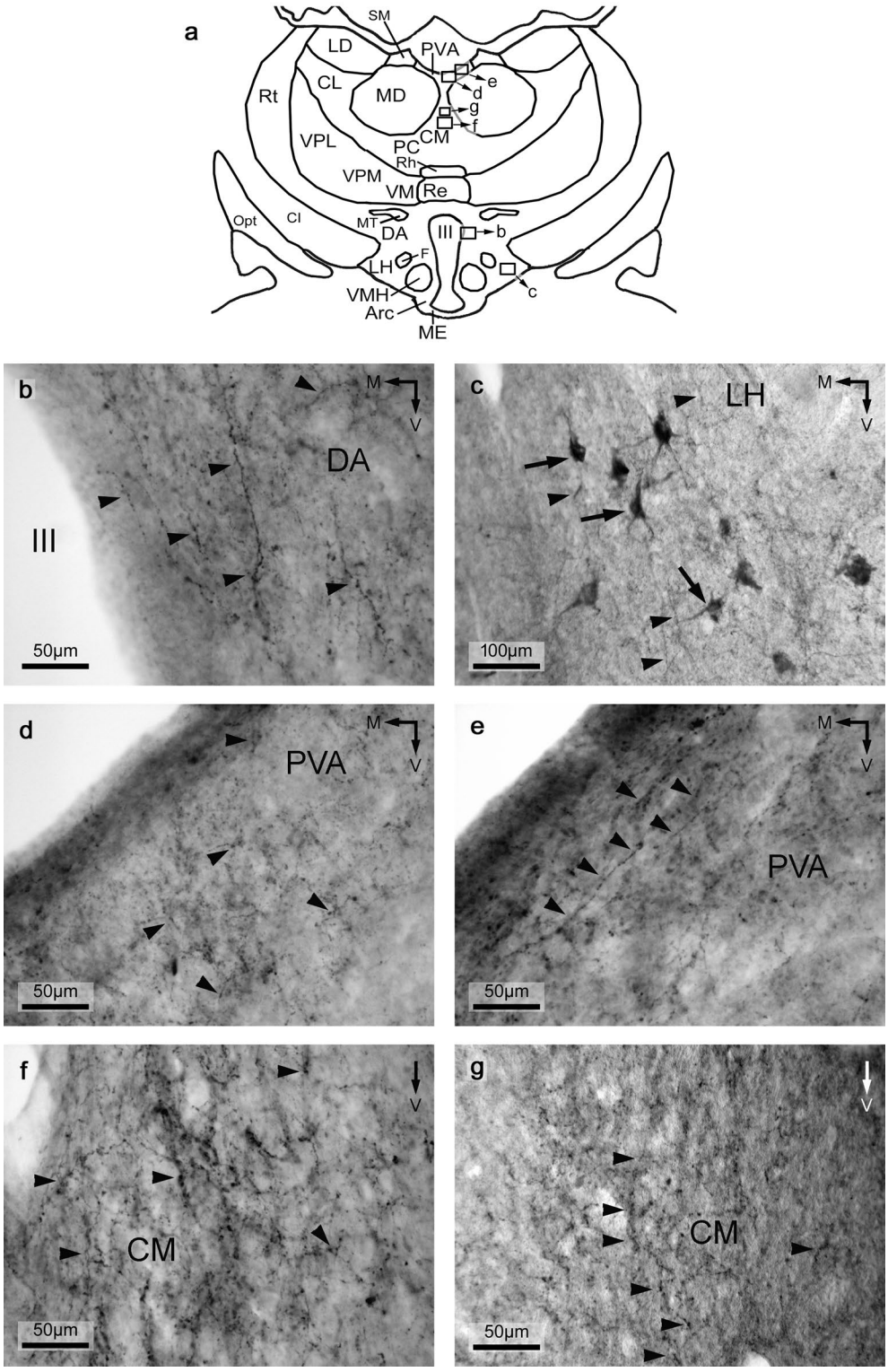

Figure 4. Immunoreactive fibers and cell bodies containing SP or MET in the alpaca diencephalon. (**a**) Frontal section of the alpaca diencephalon. For the nomenclature of the nuclei, see Figure 2 for abbreviations. The photographs shown in b–g were taken from the regions delimited by the rectangles in a (indicated as b, c, d, e, f and g). (**b**) SP-immunoreactive fibers (arrowheads) located in the dorsal hypothalamic area (DA). III — third ventricle. (**c**) MET-immunoreactive cell bodies (arrows) in the lateral hypothalamic area (LH). Arrowheads: immunoreactive fibers. (**d**) SP-immunoreactive fibers (arrowheads) located in the paraventricular thalamic nucleus (PVA). (**e**) MET-immunoreactive fibers (arrowheads) located in the paraventricular thalamic nucleus (PVA). (**f**) SP-immunoreactive fibers (arrowheads) in the central medial thalamic nucleus (CM). (**g**) MET-immunoreactive fibers (arrowheads) in the central medial thalamic nucleus (CM). M — medial. V — ventral.

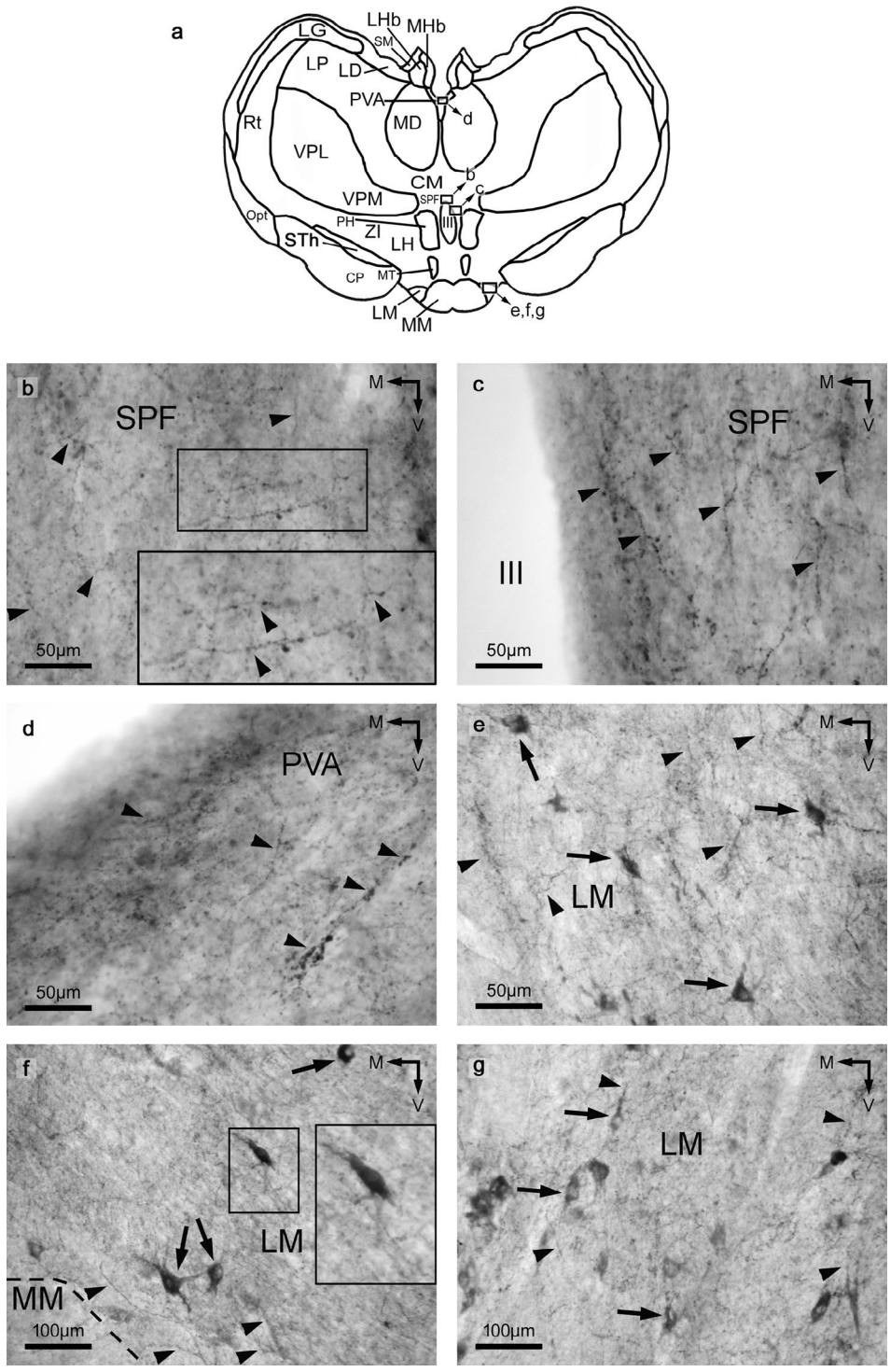

Figure 5. SP- and MET-immunoreactive fibers and cell bodies in the alpaca diencephalon. (**a**) Frontal section of the alpaca diencephalon. For the nomenclature of the nuclei, see Figure 2 (abbreviations). The photographs shown in b–g were taken from the regions delimited by the rectangles in a (indicated as b, c, d, e, f and g). (**b**) SP-immunoreactive fibers (arrowheads) located in the subparafascicular thalamic nucleus (SPF). The region delimited by the small rectangle is showed at higher magnification. (**c**) MET-immunoreactive fibers (arrowheads) in the subparafascicular thalamic nucleus (SPF). III — third ventricle. (**d**) SP-immunoreactive fibers (arrowheads) located in the paraventricular thalamic nucleus (PVA). (**e**) MET-immunoreactive cell bodies (arrows) located in the lateral mammillary nucleus (LM). Arrowheads: immunoreactive fibers. (**f**) SP-immunoreactive cell bodies (arrows) in the lateral mammillary nucleus (LM). The region delimited by the small rectangle is showed at higher magnification. Arrowheads show immunoreactive fibers or dendrites. (**g**) MET-immunoreactive cell bodies (arrows) in the lateral mammillary nucleus (LM). Arrowheads show immunoreactive fibers or dendrites. M — medial. V — ventral.

Table 2. Alpaca diencephalon: morphological characteristics of the MET- and SP-immunoreactive cell bodies

Nucleus	Density	Size	Shape	Dendritic processes
MET- immunoreactive cell bodies				
AHy	+	Medium	Polygonal	2–3
LH	+++	Large	Polygonal	2–4
LM	++	Large	Polygonal	2–4
PHy	++	Large	Polygonal, oval	2–3
Sch	+	Large	Polygonal	2–5
VMH	+	Medium	Pyriform, oval	1
SP- immunoreactive cell bodies				
LM	+	Large	Polygonal, oval	2–4

+++: high density; ++: moderate density; +: low density. For nomenclature of the nuclei, see list of abbreviations.

tors (*e.g.* neurokinin-1 and delta receptors) located in cell membranes [25, 27]. Moreover, both peptides could exert an autocrine action.

Our results show a neuroanatomical basis for future physiological investigations to study activities in which SP and MET are involved in the alpaca diencephalon. These actions are currently unknown, but the widespread distribution of SP- and MET-immunoreactive structures in the alpaca diencephalon suggests that both neuropeptides are involved in many physiological actions, in which SP and MET could interact. In mammals, it is known that SP regulates the release of prolactin, luteinizing hormone, dopamine and ACTH and that this undecapeptide is involved in vascular permeability, blood pressure and respiratory mechanisms, whereas MET has been involved in visual mechanisms, inhibition of the release of acetylcholine, dopamine, vasopressin and SP and controls the hypophysis [2]. For example, the presence of immunoreactive fibers containing SP or MET in the alpaca diencephalic nuclei involved in the transmission of pain signals suggests that SP is involved in this transmission and MET in the control of the pain transmission [28, 29]. Moreover, according to the neuroanatomical distribution of both peptides in the alpaca diencephalon and to the known actions in which the diencephalic nuclei are involved in other mammals, more physiological actions for SP/MET can be suggested in the camelid. Thus, in mammals, the lateral hypothalamic nucleus has been involved in feeding behavior, sleep and arousal, [30, 31]; the arcuate and paraventricular hypothalamic nuclei in neuroendocrine and stress mechanisms [32], and the suprachiasmatic nucleus in the circadian rhythm [33]. MET has been observed in the alpaca lateral hypothalamic nucleus and this suggests that in the camelid the peptide could be involved in the previous mentioned actions observed in other mammals. Moreover, it is known that the lateral mammillary nucleus is involved in the control of special localization of head and angular velocity [34]. The observation of cell bodies containing SP or MET in the latter nucleus suggests that in alpaca both peptides could be involved in this action.

Neuropeptides in the alpaca diencephalon

Using immunohistochemical techniques, the distribution of several neuropeptides in the alpaca diencephalon (somatostatin, CGRP, ACTH, αMSH, beta-endorphin, alpha-neo-endorphin, leucine-enkephalin, neurotensin) has been previously published [10–12, 14]. Thus, in the alpaca diencephalon, the presence of peptidergic-immunoreactive fibers has been studied for ten neuropeptides (including SP and MET) [10–12, 14]. In all cases, the distribution of the peptidergic-immunoreactive fibers containing the mentioned ten neuropeptides in the alpaca thalamus and hypothalamus was widespread and, in the same diencephalic nuclei (*e.g.* anterior hypothalamic area, arcuate nucleus, central medial thalamic nucleus, paraventricular thalamic nucleus, reuniens and rhomboid thalamic nuclei), the presence of all ten neuropeptides in fibers has been demonstrated. This means, in general, that: (i) a close neuroanatomical relationship occurs between the neuropeptides studied [10–12, 14], (ii) the peptidergic systems show the same/similar distribution, (iii) the coexistence of neuropeptides is possible, and (iv) in most of the alpaca diencephalic nuclei, an elaborate modulation of the functions of many neuropeptides occurs. It is important to note that the distribution of immunoreactive fibers containing SP, MET, somatostatin, CGRP, beta-endorphin, αMSH, alpha-neo-endorphin or neurotensin was similar and that the distribution of fibers containing

ACTH or leucine-enkephalin, although widespread, was lesser than the previous eight neuropeptides [10–12, 14]. Regarding the peptidergic cell bodies found in the alpaca diencephalon, these perikarya were only observed in the hypothalamus [10–12, 14]. No immunoreactive cell body for ACTH was found in the hypothalamus, whereas the other neuropeptides showed a very restricted distribution: beta-endorphin and SP were observed in 1 nucleus; leucine-enkephalin in 2 nuclei; somatostatin in 3 nuclei; αMSH in 5 nuclei and MET, CGRP, alpha-neo-endorphin and neurotensin in 6 nuclei [10–12, 14]. In the lateral and ventromedial hypothalamic nuclei, the presence of six neuropeptides (CGRP, somatostatin, αMSH, alpha-neo-endorphin, neurotensin and MET) has been reported in perikarya; four neuropeptides (CGRP, αMSH, neurotensin and MET) in cell bodies located in the anterior hypothalamic area and arcuate nucleus; three neuropeptides (CGRP, alpha-neo-endorphin and neurotensin) in the dorsal hypothalamic area and paraventricular and supraoptic hypothalamic nuclei and two of them in the lateral mammillary nucleus, posterior hypothalamic nucleus and suprachiasmatic nucleus. The possible coexistence of these neuropeptides in the hypothalamic cell bodies must be studied in the future. Finally, it is important to remark that in this and the previous studies performed in the alpaca, for ethical considerations no colchicine was administered to animals [10–12, 14]. This could explain the restricted distribution of the peptidergic perikarya in the alpaca diencephalon, since it is known that in general the administration of colchicine increases the number and distribution of the peptidergic cell bodies.

SP and MET in the mammalian diencephalon

Many immunohistochemical studies regarding the distribution of SP and MET in the mammalian diencephalon have been performed [15, 16, 22, 35–45]. In general, the widespread distribution of the MET-immunoreactive fibers found in the alpaca diencephalon is quite similar to the distribution reported in other mammals. However, some differences occur. For example, in the cat/dog thalamus, MET-immunoreactive fibers were mainly observed in the midline nuclei [16, 22], whereas in alpaca these fibers were also observed in the lateral thalamic nuclei. In the hypothalamus, the dog and alpaca showed the same distribution and this was a slight more widespread than that found in the cat hypothalamus [17, 22]. By contrast, many differences can be observed when comparing the distribution of the MET-immunoreactive perikarya in the mammalian diencephalon. These differences are due to the methodology applied (administration of colchicine; as indicated above, this drug is used to increase the number of peptidergic cell bodies). In general, in animals treated with colchicine a widespread distribution of immunoreactive cell bodies was observed [17, 22, 37, 38]. For example, in rats, cats and dogs treated with the drug, a widespread distribution of cell bodies containing MET was observed in the thalamus and hypothalamus [17, 22, 37, 38]. However, this widespread distribution was not observed here in the diencephalon of alpacas because they were not treated with colchicine. In summary, in comparison with other mammals, the distribution of MET-immunoreactive cell bodies in the alpaca diencephalon is very restricted.

In general, the distribution of the SP-immunoreactive fibers observed in the diencephalon of the alpaca is similar to that reported in other mammalian species (*e.g.* rat, human) [15, 36, 43]. Thus, in the hypothalamus of the three species a widespread distribution of SP-immunoreactive fibers was observed, whereas in the rat and human thalamus these fibers were mainly located in the midline nuclei but in the alpaca fibers containing SP were observed in both midline and lateral thalamic nuclei [15, 36, 43]. Regarding the distribution of the SP-immunoreactive perikarya in the mammalian diencephalon, a more widespread distribution (in both thalamus and hypothalamus) was observed in rats than in alpacas and humans [36, 43]. This was due to the administration of colchicine to rats. In both alpacas and humans, SP-immunoreactive cell bodies showed a very restricted distribution in the diencephalon.

In summary, this study increases the knowledge on the neuroanatomical distribution of the tachykininergic (SP) and enkephalinergic (MET) peptidergic systems in the alpaca diencephalon. SP- and MET-immunoreactive fibers showed a widespread and similar distribution in the diencephalon. A close neuroanatomical relationship between SP- and MET-immunoreactive fibers was found, suggestive of multiple physiological interactions between both neuropeptides. The distribution of the cell bodies containing SP is very restricted, whereas MET-immunoreactive perikarya show a moderately widespread distribution in the hypothalamus.

Acknowledgements

The authors wish to thank Professor Gérard Tramu (Université de Bordeaux I, France) for the gift of primary antibodies and the Language Service of the Universidad de Salamanca (Spain) for supervising the English text. This work has been supported by "Programa XI: Financiación de Unidades de Excelencia de la Universidad de Salamanca" (Spain).

References

1. Bux F, Bhagwandin A, Fuxe K, et al. Organization of cholinergic, putative catecholaminergic and serotonergic nuclei in the diencephalon, midbrain and pons of sub-adult male giraffes. J Chem Neuroanat. 2010; 39(3): 189–203, doi: 10.1016/j.jchemneu.2009.09.006, indexed in Pubmed: 19808092.
2. Coveñas R, Mangas A, Narváez JA. Introduction to neuropeptides. In: Coveñas R, Mangas A, Narváez JA, eds. Focus on Neuropeptide Research. Trivandrum: Transworld Research Network; 2007: 1-26.
3. Ebner K, Singewald N. The role of substance P in stress and anxiety responses. Amino Acids. 2006; 31(3): 251–272, doi: 10.1007/s00726-006-0335-9, indexed in Pubmed: 16820980.
4. Ebner K, Muigg P, Singewald G, et al. Substance P in stress and anxiety: NK-1 receptor antagonism interacts with key brain areas of the stress circuitry. Ann N Y Acad Sci. 2008; 1144: 61–73, doi: 10.1196/annals.1418.018, indexed in Pubmed: 19076365.
5. Graefe S, Mohiuddin SS. Biochemistry, substance P. Treasure Island (FL): StatPearls Publishing; 2020. PMID: 32119470.
6. Hertler B, Hosp JA, Blanco MB, et al. Substance P signalling in primary motor cortex facilitates motor learning in rats. PLoS One. 2017; 12(12): e0189812, doi: 10.1371/journal.pone.0189812, indexed in Pubmed: 29281692.
7. Mashaghi A, Marmalidou A, Tehrani M, et al. Neuropeptide substance P and the immune response. Cell Mol Life Sci. 2016; 73(22): 4249–4264, doi: 10.1007/s00018-016-2293-z, indexed in Pubmed: 27314883.
8. Ribeiro-da-Silva A, Hökfelt T. Neuroanatomical localisation of substance P in the CNS and sensory neurons. Neuropeptides. 2000; 34(5): 256–271, doi: 10.1054/npep.2000.0834, indexed in Pubmed: 11049730.
9. Ebrahimi S, Javid H, Alaei A, et al. New insight into the role of substance P/neurokinin-1 receptor system in breast cancer progression and its crosstalk with microRNAs. Clin Genet. 2020 [Epub ahead of print], doi: 10.1111/cge.13750, indexed in Pubmed: 32266968.
10. Coveñas R, Mangas A, Medina LE, et al. Mapping of somatostatin-28 (1-12) in the alpaca diencephalon. J Chem Neuroanat. 2011; 42(1): 89–98, doi: 10.1016/j.jchemneu.2011.06.006, indexed in Pubmed: 21729751.
11. Coveñas R, Sánchez ML, Mangas A, et al. Mapping of CGRP in the alpaca diencephalon. J Chem Neuroanat. 2012; 45(1-2): 36–44, doi: 10.1016/j.jchemneu.2012.07.004, indexed in Pubmed: 22922318.
12. Manso B, Sánchez ML, Medina LE, et al. Immunohistochemical mapping of pro-opiomelanocortin- and pro-dynorphin-derived peptides in the alpaca (Lama pacos) diencephalon. J Chem Neuroanat. 2014; 59-60: 36–50, doi: 10.1016/j.jchemneu.2014.06.001, indexed in Pubmed: 24956196.
13. Marcos P, Arroyo-Jiménez MM, Lozano G, et al. Mapping of tyrosine hydroxylase in the diencephalon of alpaca (Lama pacos) and co-distribution with somatostatin-28 (1-12). J Chem Neuroanat. 2013; 50-51: 66–74, doi: 10.1016/j.jchemneu.2013.02.006, indexed in Pubmed: 23474224.
14. Sánchez ML, Mangas A, Medina LE, et al. Immunohistochemical mapping of neurotensin in the alpaca diencephalon. Folia Histochem Cytobiol. 2018; 56(1): 49–58, doi: 10.5603/FHC.a2018.0003, indexed in Pubmed: 29516445.
15. Palkovits M. Neuropeptides in the brain. In: Ganong WF, Martini L, eds. Frontiers in Neuroendocrinology. New York: Raven Press. ; 1988: 1–44.
16. Conrath M, Covenas R, Romo R, et al. Distribution of Met-enkephalin immunoreactive fibres in the thalamus of the cat. Neurosci Lett. 1986; 65(3): 299–303, doi: 10.1016/0304-3940(86)90278-8, indexed in Pubmed: 3520398.
17. Coveñas R, Burgos C, Conrath M. Immunocytochemical study of met-enkephalin-like cell bodies in the cat hypothalamus. Neurosci Res. 1988; 5(4): 353–360, doi: 10.1016/0168-0102(88)90037-5, indexed in Pubmed: 3374865.
18. Burgos C, Aguirre JA, Alonso JR, et al. Immunocytochemical study of substance P-like fibres and cell bodies in the cat diencephalon. J Hirnforsch. 1988; 29(6): 651–657, indexed in Pubmed: 2466889.
19. Duque-Díaz E, Díaz-Cabiale Z, Narváez JA, et al. Mapping of enkephalins and adrenocorticotropic hormone in the squirrel monkey brainstem. Anat Sci Int. 2017; 92(2): 275–292, doi: 10.1007/s12565-016-0333-2, indexed in Pubmed: 26897373.
20. Duque-Díaz E, Coveñas R. Distribution of somatostatin-28 (1-12), calcitonin gene-related peptide, and substance P in the squirrel monkey brainstem: an immunocytochemical study. Anat Sci Int. 2019; 94(1): 86–100, doi: 10.1007/s12565-018-0453-y, indexed in Pubmed: 30051271.
21. Mangas A, Yajeya J, Gonzalez N, et al. Detection of pantothenic acid-immunoreactive neurons in the rat lateral septal nucleus by a newly developed antibody. Folia Histochem Cytobiol. 2016; 54(4): 186–192, doi: 10.5603/FHC.a2016.0024, indexed in Pubmed: 27966211.
22. Pesini P, Pego-Reigosa R, Tramu G, et al. Distribution of met-enkephalin immunoreactivity in the diencephalon and the brainstem of the dog. J Chem Neuroanat. 2000; 19(4): 243–258, doi: 10.1016/s0891-0618(00)00071-5, indexed in Pubmed: 11036241.
23. Samsam M, Coveñas R, Csillik B, et al. Depletion of substance P, neurokinin A and calcitonin gene-related peptide from the contralateral and ipsilateral caudal trigeminal nucleus following unilateral electrical stimulation of the trigeminal ganglion; a possible neurophysiological and neuroanatomical link to generalized head pain. J Chem Neuroanat. 2001; 21(2): 161–169, doi: 10.1016/s0891-0618(01)00088-6, indexed in Pubmed: 11312057.
24. Sánchez ML, Vecino E, Coveñas R. Distribution of methionine-enkephalin in the minipig brainstem. J Chem Neuroanat. 2013; 50-51: 1–10, doi: 10.1016/j.jchemneu.2013.03.002, indexed in Pubmed: 23538385.
25. Fuxe K, Agnati LF, Coveñas R, et al. Volume transmission in transmitter peptide costoring neurons in the medulla oblongata. In: Barraco IRA, ed. Nucleus of the Solitary Tract. Boca Raton: CRC Press. ; 1994: 74–89, doi: 10.1201/9780429277214.
26. Fuxe K, Borroto-Escuela DO. Volume transmission and receptor-receptor interactions in heteroreceptor complexes: understanding the role of new concepts for brain communication. Neural Regen Res. 2016; 11(8): 1220–1223, doi: 10.4103/1673-5374.189168, indexed in Pubmed: 27651759.
27. Nusbaum M, Blitz D, Marder E. Functional consequences of neuropeptide and small-molecule co-transmission. Nat Rev Neurosci. 2017; 18(7): 389–403, doi: 10.1038/nrn.2017.56.
28. Ralston HJ. Pain and the primate thalamus. Prog Brain Res. 2005; 149: 1–10, doi: 10.1016/S0079-6123(05)49001-9, indexed in Pubmed: 16226572.
29. Li JN, Sun Yi, Ji SL, et al. Collateral projections from the medullary dorsal horn to the ventral posteromedial thalamic nucleus and the parafascicular thalamic nucleus in the rat. Neuroscience. 2019; 410: 293–304, doi: 10.1016/j.neuroscience.2019.04.050, indexed in Pubmed: 31075313.
30. Urstadt KR, Berridge KC. Optogenetic mapping of feeding and self-stimulation within the lateral hypothalamus of the rat. PLoS One. 2020; 15(1): e0224301, doi: 10.1371/journal.pone.0224301, indexed in Pubmed: 31986148.
31. Szymusiak R, McGinty D. Hypothalamic regulation of sleep and arousal. Ann N Y Acad Sci. 2008; 1129: 275––286, doi: 10.1196/annals.1417.027, indexed in Pubmed: 18591488.

32. Coveñas R, de León M, Cintra A, et al. Coexistence of c-Fos and glucocorticoid receptor immunoreactivities in the CRF immunoreactive neurons of the paraventricular hypothalamic nucleus of the rat after acute immobilization stress. Neurosci Lett. 1993; 149(2): 149–152, doi: 10.1016/0304-3940(93)90758-d, indexed in Pubmed: 8474689.
33. Koinuma S, Asakawa T, Nagano M, et al. Regional circadian period difference in the suprachiasmatic nucleus of the mammalian circadian center. Eur J Neurosci. 2013; 38(6): 2832–2841, doi: 10.1111/ejn.12308, indexed in Pubmed: 23869693.
34. Blair HT, Cho J, Sharp PE. Role of the lateral mammillary nucleus in the rat head direction circuit: a combined single unit recording and lesion study. Neuron. 1998; 21(6): 1387–1397, doi: 10.1016/s0896-6273(00)80657-1, indexed in Pubmed: 9883731.
35. Bouras C, Taban CH, Constantinidis J. Mapping of enkephalins in human brain. An immunohistofluorescence study on brains from patients with senile and presenile dementia. Neuroscience. 1984; 12(1): 179–190, doi: 10.1016/0306-4522(84)90146-5, indexed in Pubmed: 6379499.
36. Bouras C, Vallet PG, Dobrinov H, et al. Substance P neuronal cell bodies in the human brain: complete mapping by immunohistofluorescence. Neurosci Lett. 1986; 69(1): 31–36, doi: 10.1016/0304-3940(86)90409-x, indexed in Pubmed: 2427977.
37. Covenas R, Romo R, Cheramy A, et al. Immunocytochemical study of enkephalin-like cell bodies in the thalamus of the cat. Brain Res. 1986; 377(2): 355–361, doi: 10.1016/0006-8993(86)90881-4, indexed in Pubmed: 3524752.
38. Coveñas R, Alonso JR, Conrath M. Immunocytochemical study of enkephalin-like cell bodies in the thalamus of the rat. Brain Res Bull. 1989; 23(4-5): 277–281, doi: 10.1016/0361-9230(89)90209-8, indexed in Pubmed: 2590840.
39. Finley JC, Maderdrut JL, Petrusz P. The immunocytochemical localization of enkephalin in the central nervous system of the rat. J Comp Neurol. 1981; 198(4): 541–565, doi: 10.1002/cne.901980402, indexed in Pubmed: 7019273.
40. Haber SN, Wolfe DP, Groenewegen HJ, et al. The distribution of enkephalin immunoreactive fibers and terminals in the monkey central nervous system: an immunohistochemical study. Neuroscience. 1982; 7(5): 1049–1095, doi: 10.1016/0306-4522(82)91118-6, indexed in Pubmed: 7050764.
41. Hökfelt T, Elde R, Johansson O, et al. The distribution of enkephalin-immunoreactive cell bodies in the rat central nervous system. Neurosci Lett. 1977; 5(1-2): 25–31, doi: 10.1016/0304-3940(77)90160-4, indexed in Pubmed: 19604966.
42. Inagaki S, Parent A. Distribution of enkephalin-immunoreactive neurons in the forebrain and upper brainstem of the squirrel monkey. Brain Res. 1985; 359(1-2): 267–280, doi: 10.1016/0006-8993(85)91437-4, indexed in Pubmed: 3907752.
43. Ljungdahl A, Hökfelt T, Nilsson G. Distribution of substance P-like immunoreactivity in the central nervous system of the rat-I. Cell bodies and nerve terminals. Neuroscience. 1978; 3(10): 861–943, doi: 10.1016/0306-4522(78)90116-1, indexed in Pubmed: 366451.
44. Merchenthaler I, Maderdrut JL, Altschuler RA, et al. Immunocytochemical localization of proenkephalin-derived peptides in the central nervous system of the rat. Neuroscience. 1986; 17(2): 325–348, doi: 10.1016/0306-4522(86)90250-2, indexed in Pubmed: 3517687.
45. Sar M, Stumpf WE, Miller RJ, et al. Immunohistochemical localization of enkephalin in rat brain and spinal cord. J Comp Neurol. 1978; 182(1): 17–37, doi: 10.1002/cne.901820103, indexed in Pubmed: 359601.

Submitted: 10 January, 2020
Accepted after reviews: 29 April, 2020
Available as AoP: 2 June, 2020

FOLIA HISTOCHEMICA ET CYTOBIOLOGICA
Vol. 58, No. 2, 2020
pp. 147–155

ORIGINAL PAPER

VIA MEDICA

Reactivity of astrocytes in the periaqueductal gray matter of rats treated with monosodium glutamate

Aleksandra Krawczyk, Jadwiga Jaworska-Adamu

Department of Animal Anatomy and Histology, University of Life Sciences, Lublin, Poland

Abstract

Introduction. The astrocytic S100β calcium-binding protein performs numerous intra- and extracellular functions, promoting the survival of central nervous system (CNS) structures. Its increased synthesis and release are a manifestation of reactive glial behavior, crucial for the maintenance of proper neuronal function, particularly under the pathological conditions. The periaqueductal gray matter (PAG) is a mindbrain area composed of four parts dorsomedial (dm), dorsolateral (dl), lateral (l) and ventrolateral (vl)) which are involved in pain sensing and defensive reactions of the body. The aim of this study was to evaluate the S100β protein immunoreactive (S100β-IR) astrocytes in adult rats after administration of monosodium glutamate (MSG).

Material and methods. The animals were administered the saline solution (group C), 2 g/kg b.w. MSG (group I) and 4 g/kg b.w. MSG (group II). The study was carried out on the brain sections stained by immunohistochemical peroxidase-antiperoxidase method with a primary mouse antibody against the S100β protein.

Results. The analyses showed the presence of the S100β-immunoreactive cells in dm, dl, l, vl PAG of all animals. In the C and I group animals, the PAG astrocytes were characterized mainly by the presence of the studied protein in the nucleus and cytoplasm of the cell body. In the group II rats in all parts of PAG, the S100β-IR cells with numerous, thicker and branched processes were observed. A decrease in the number of the S100β-IR cells was found in dm, dl and l PAG in the MSG-treated animals, particularly with the larger dose. The number of cells with the S100β expression was comparable in vl PAG in all rats.

Conclusions. MSG administered parenterally to the higher dose to adult rats affects the immunoreactivity of S100β protein in PAG. Phenotypic changes of the studied cells may indicate reactivity of glial cells and increased expression of the studied protein whereas a decrease in their number may result from the increased protein secretion into the extracellular space or cytotoxic death of glial cells. *(Folia Histochemica et Cytobiologica 2020, Vol. 58, No. 2, 147–155)*

Key words: rat; monosodium glutamate; periaqueductal gray matter; S100β; astrocytes

Introduction

Astrocytes are glial cells responsible for maintenance and control of neural homeostasis in the central nervous system (CNS). These cells provide a structural-metabolic support for neurons, protecting them against various types of damage. They also play an active role in the synaptic transmission, including the neurotransmitter metabolism, and are a source of many active gliotrophic and neurotrophic substances [1–3]. Astrocytes play a key role in the pathogenesis of numerous neurological and CNS disorders. Moreover, their dysfunction may affect neuronal survival [2, 4]. The activity of glial cells changes dynamically depending on the functional state of the neuronal microenvironment. In order to protect neurons, astrocytes become activated in many types of CNS disorders and damage. The reactivity of astrocytes to various CNS insults is recognized to be a pathological feature of structural changes in the nervous system. In the course of the so-called reactive astrogliosis, numerous changes at the molecular, cellular and functional levels are observed including hypertrophy of cell body and cell processes, increased expression and synthesis of various proteins as well as the increased

Correspondence address: Aleksandra Krawczyk, DVM, PhD
Department of Animal Anatomy and Histology
Faculty of Veterinary Medicine, University of Life Sciences
Akademicka St. 12, 20–950 Lublin, Poland
e-mail: aleksandra.krawczyk@up.lublin.pl

amplitude, duration and frequency of intracellular calcium signals [2–7].

Calcium ions take an active part in the intracellular signaling and communication. The maintenance of their homeostasis is essential for proper cell functioning. A sudden increase in cellular Ca^{2+} concentration may lead to the activation of a number of enzymatic reactions and consequently, to the induction of apoptotic cell death [8]. A rapid increase in Ca^{+2} levels in astrocytes was observed, among others, in the pilocarpine model of epilepsy [9]. During the kainate-induced seizures in the murine hippocampus a similar glial reaction was shown [10]. Kainic acid, as a cyclic analog of L-glutamate (Glu), is a strong agonist of Glu-specific ionotropic receptors [11]. Glu is the main excitatory neurotransmitter in CNS. It is present in the extracellular space at a low concentration. However, in the pathological states an increase in the extracellular Glu level is observed. This phenomenon results in the excessive stimulation of Glu-specific ionotropic receptors. Such activity can lead to excitotoxicity death caused by a rapid influx of calcium ions into the cell [12, 13]. Excitotoxicity is of significant importance for the pathogenesis of many pathological CNS conditions, *e.g.* ischemia [14], stroke [15], trauma [16], epilepsy [17], as well as neurodegenerative diseases [18–20]. In such pathological states, reactivity of astrocytes manifested by hypertrophy of their bodies and processes was observed [6, 7, 21]. Glu is also the main component of monosodium glutamate (MSG) which is used worldwide as a flavor enhancer. MSG is often used in experimental studies due to its toxicity [22–24]. In animals treated with MSG some brain lesions were observed [25–28].

There are many mechanisms that lead to a decrease in intracellular of Ca^{2+} levels. One of them is the presence of calcium-binding proteins that belong to the S100 family representing 25 relatively small proteins. Engaged in numerous intracellular and extracellular functions, they take part in the regulation of proliferation, differentiation, cell migration, apoptosis, energy metabolism and protein phosphorylation [29, 30]. Astrocytes exhibit the presence of S100β protein, which is an acid homodimer composed of two β subunits. It leads to the intracellular changes in the calcium ion levels and reduces their concentration acting as a buffer [31, 32]. Moreover, in the course of numerous acute and chronic disorders of the nervous system, presence of this protein in the extracellular space is demonstrated [33, 34].

The elevated level of S100β in the body fluids (peripheral blood, cerebrospinal fluid, urine, saliva) is observed during the traumatic brain injury [35, 36], Alzheimer's disease [37], Parkinson's disease [38], Down syndrome [39], schizophrenia [40] and mood disorders [41, 42]. Therefore, S100β is considered to be a biomarker of pathological states in the nervous system [32–34].

The periaqueductal gray matter (PAG) is a midbrain area. In rat it consists of four parts: dorsomedial (dm), dorsolateral (dl), lateral (l) and ventrolateral (vl). Through numerous descending and ascending pathways, PAG is connected with other CNS areas, participating in pain sensing and defensive reactions of the organism with characteristic autonomic symptoms in the respiratory and cardiovascular systems. Activity of this area depends on the appropriate level of neurotransmitters including Glu [43–46]. The proper concentration of this amino acid is controlled by astrocytes [2, 3]. Taking into account important functions and numerous PAG connections in CNS, it seems to be essential to estimate the astroglial activity under the conditions of the elevated Glu level in the extracellular space.

The aim of this study was to evaluate the effects of monosodium glutamate (MSG) on the morphology, distribution and density of immunoreactive S100β astrocytes in the periaqueductal gray matter of adult rats.

Material and methods

Animals and material collection. The experiments were approved by the 2nd Local Ethical Commission for Animal Experiments in Lublin (No. 7/2011). The study was performed on fifteen 60-day-old male Wistar rats. They were kept in metal cages at the temperature of 20–22°C, 60% air humidity, in a 12h:12h day/night cycle with continuous access to food and water. The rats were randomly divided into three groups of 5 animals each control (C), I and II. Rats of the C group were administered saline solution, whereas animals in groups I and II received monosodium glutamate (MSG) (Sigma-Aldrich, St. Louis, MO, USA) in the doses of 2 g/kg b.w. and 4 g/kg b.w., respectively, subcutaneously for 3 consecutive days. All animals were euthanized 24 h after the last injection of MSG or saline solution. Thereafter brains were immediately collected for examination. The material was fixed in the buffered 10% formalin and embedded in the paraffin blocks by the routine histological technique. Next, the frontal, 4 μm-thick sections were obtained and placed on the SuperFrost Plus slides.

Immunohistochemistry. The brain sections containing PAG from each animal were stained with indirect peroxidase-antiperoxidase (PAP) method using the antibodies and reagents from Sigma-Aldrich. The reaction was performed with dilutions in 0.5M TBS (Tris-buffered saline) at pH 7.6 according to the manufacturer's recommendations. In the

first stage, all sections were dewaxed and rehydrated. Next, they were treated with 3% H_2O_2 at room temperature (RT) for 30 min and then with the goat serum (G9023, 1:10) for 20 min. Then incubation with the primary mouse antibody against the S100β protein (S2532, 1:2000) was performed at 4°C for 16 hours. Later the secondary goat antibody against the mouse IgG conjugated with the peroxidase–antiperoxidase complex (A9917, 1:150) was used at room temperature for 1 hour. To visualize the reaction, the DAB chromogen (RT, 30 min.) was applied. At the final stage, all sections were stained with Mayer's hematoxylin, and slip-covered using DPX (Fluka, Buchs, Switzerland). At the same time, negative control of the immunohistochemical reactions by omission of the primary antibody was performed. The specificity of the primary antibody was confirmed on the rat brain sections in our earlier study [47]. The stained sections were analyzed and microphotographs were obtained in Olympus BX40 microscope connected to the digital Olympus Color View III camera (Olympus, Tokyo, Japan).

Microscopic and morphometric analyses. The morphology and distribution of immunoreactive cells for S100β (S100β--IR) were evaluated on the brain sections of each animal. The measurements of 50 sections from each group of rats (10 sections/animal) were made based on the microscopic observations. The number of S100β-IR astrocytes identified by the presence of brown reaction product was measured in the individual parts of PAG (dm, dl, l and vl) of each animal from all groups (C, I, II). The measurements were conducted in 100 squares (2.0×10^{-2} mm^2) using the grid. The analyses were made in 20 randomly selected fields per animal (2 fields/section) using the Cell ^ D program. The obtained results from the dm, dl, l and vl PAG of rats of each group were presented as the average number of S100β-IR cells (N) in the area of 2.0×10^{-2} mm^2.

Statistical analysis. The data were subjected to the statistical analyses using the Statistica software (version 12.5, StatSoft, Krakow, Poland). The normal distribution of data was verified using the Shapiro-Wilk test. The Friedman test was applied to compare the results between the individual parts of PAG within one group. The data obtained from the groups were compared using the Kruskal-Wallis test. The post-hoc Dunn test was applied in both cases. A value of $p < 0.05$ was considered as statistically significant.

Results

The microscopic analyses showed that in all animals in the studied groups S100β-IR cells were present in PAG. In all parts of the studied area of the control animals and in dorsomedial, dorsolateral and lateral part of PAG of the rats treated with the lower dose of MSG a brown reaction product was observed in the nucleus and cytoplasm of astrocytes. However, in ventrolateral part of PAG of animals from group I astrocytes containing brown reactivity product in the initial parts of processes were more frequent. These immunoreactive processes were usually less intensely stained, thin and did not branched. In all parts of PAG of rats treated with the higher dose of MSG, the S100β-IR cells with the brown nucleus, cell body cytoplasm and numerous thick and branched processes were present. The remaining S100β-IR cells showed a similar location of studied protein to that in the control (Figs. 1, 2).

The morphometric analyses proved the largest density of S100β-IR cells in dorsomedial part of PAG in the control group of animals. In rats which received MSG at both doses, astrocytes with the brown product of reaction were the most numerous in ventrolateral part of PAG. The average number of cells with the expression of the S100β protein was comparable in this part of PAG in both control and MSG-treated rats (Fig. 3). In dorsomedial part of PAG of groups I and II, a statistically significant decrease in the S100β-IR density of astrocytes was observed in comparison to the control group. In dorsolateral and lateral part of PAG, the mean number of S100β-IR cells in groups C and I animals was comparable and statistically significantly higher than in the group II (Fig. 4).

Discussion

Our studies showed that PAGs of all animals had nuclear-cytoplasmic immunoreactive cells for S100β protein. Additionally, in the MSG administered animals, a phenotypically different S100β-IR type of astrocyte was observed. The cells presented S100β immunoreactivity in nucleus, cell body cytoplasm and cellular processes. Such morphology may indicate the increased protein synthesis being a sign of reactive astrogliosis. This phenomenon is most likely to occur in response to the intracellular calcium ion levels increase due to the enhanced activation of glutamate specific ionotropic receptors [48]. In the cell S100β protein controls calcium-dependent processes and regulates enzymatic activity. Its interactions with other molecules influence, among others, the growth, differentiation and proliferation of astrocytes. This protein modulates cytoskeleton remodeling, which allows for dynamic changes in cell morphology [32]. In group II rats, the phenotypically modified cells occurred in all parts of PAG while in group I they were present only in vl PAG. This may be related to the increased loss of calretinine (CR) immunoreactive neurons being affected by MSG in this part of PAG as has been shown by us recently [49]. The CR-positive cells are

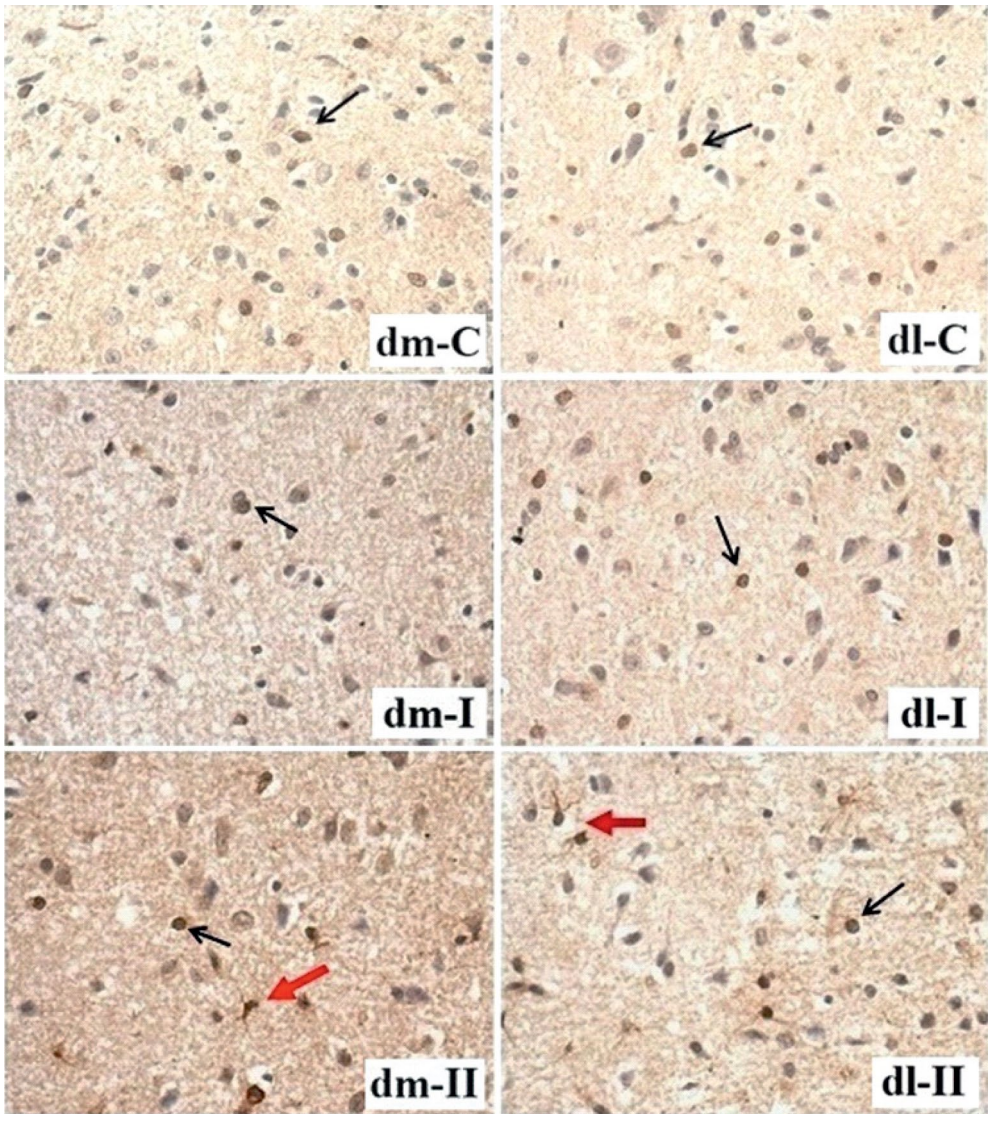

Figure 1. S100β-immunoreactive cells in the dorsomedial (dm) and dorsolateral (dl) parts of periaqueductal gray matter (PAG) in rats from the control group (C) and rats treated *sc* with monosodium glutamate (MSG) in the dose of 2 g/kg b.w. (group I) and 4 g/kg b.w. (group II). Black arrows show non-reactive astrocytes. Red arrows show reactive astrocytes. S100β-immunoreactivity was detected as described in Material and methods. Objective magnification: 40×.

probably a subpopulation of inhibitory GABA-ergic interneurons. Their reduced number may lead to the increased activity of glutamatergic neurons due to a lack of GABA-dependent inhibition. This process increases further the glutamate (Glu) amount in the extracellular space which enhances the glial response [50].

Numerous studies have proved harmful influence of MSG on the nervous system [25–28, 51, 52]. The intraperitoneal administration of MSG at the dose of 3.5 mg/g b.w. caused a decrease in number of Purkinje cells in rat cerebellum [27]. Neurotoxic effect of MSG leads to degenerative changes and death of Purkinje cells in the cerebellar cortex of the rats which were administered 3 g/kg b.w. of MSG orally for 14 days [26]. Astrocytes are less sensitive to the Glu-induced damage than neurons [53]. However, some authors suggest that the excess of this neurotransmitter in the extracellular space may also lead to the death of these glial cells [1, 26]. This process has been observed in both *in vitro* and *in vivo* studies. The cortical cultured astrocytes treated with glutamate for 24 hours (50–100 mM) showed changes in nucleus morphology, DNA fragmentation and activation of the caspase pathway, indicating apoptosis induction [1]. Death of astroglial cells, probably due to the oxidative stress, was also found in the cerebellar cortex of the rats which were administered 3 g/kg b.w. of MAG orally for 14 days

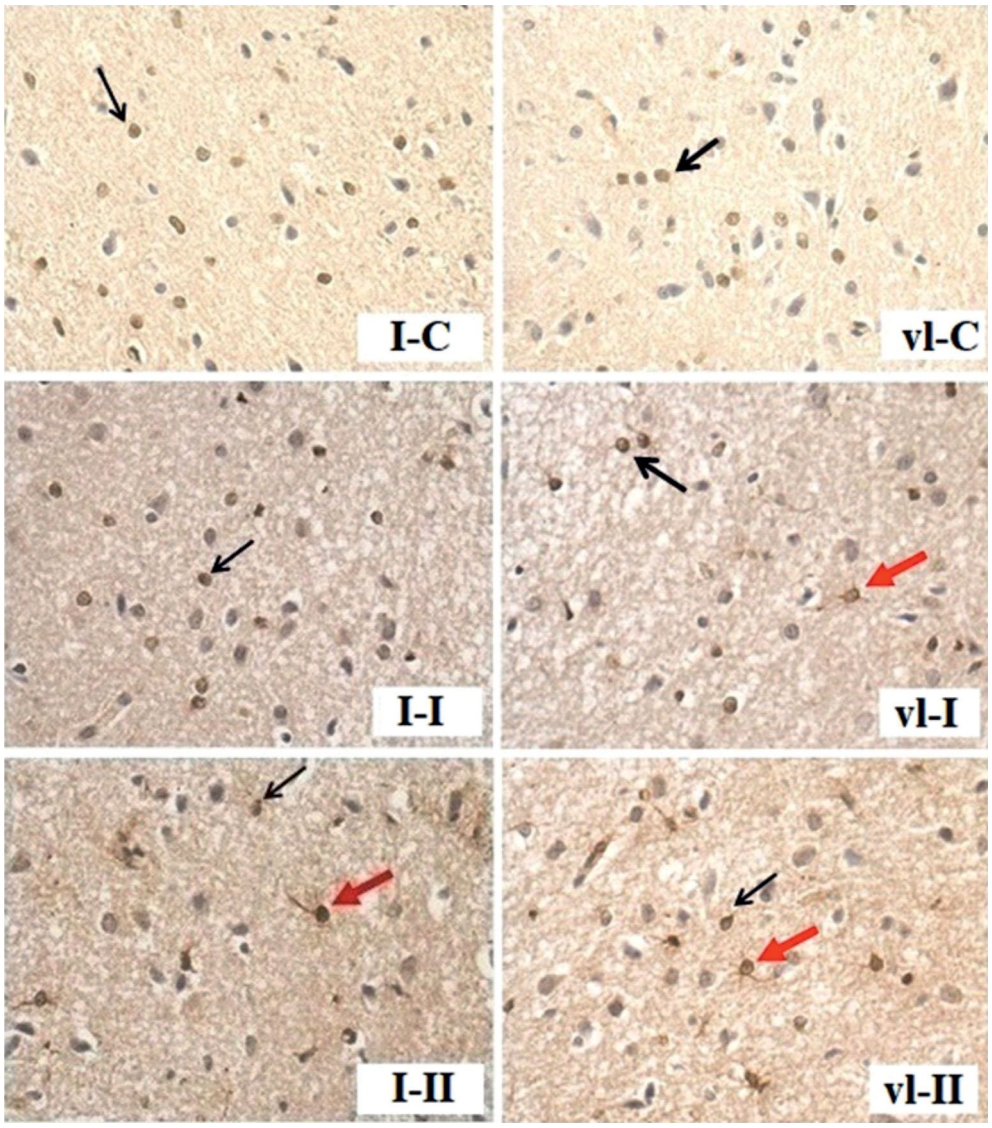

Figure 2. S100β-immunoreactive cells in the lateral (l) and ventrolateral (vl) parts of PAG in the control (C) and monosodium glutamate-treated (I, II) rats. Black arrows show non-reactive astrocytes. Red arrows show reactive astrocytes. S100β-immunoreactivity was detected as described in Material and methods. Objective magnification: 40×.

[26]. Cytotoxic glial damage may be also the cause of decrease in the S100β-IR density of astrocytes in PAG of the MSG treated animals as found in our study (group I and II). High concentration of Glu in the extracellular space leads to intracellular exhaustion of glutathione and accumulation of reactive oxygen species [54]. As a consequence, mitochondrial DNA damage and cell death may occur [1, 14, 23, 26, 55]. However, a decrease in the number of S100β-IR astrocytes may also be associated with the increased protein secretion into the extracellular space. This phenomenon is, among others, a result of the activation of metabotropic Glu receptors [48, 56]. The increased secretion of S100β protein into the extracellular space occurs also after stimulation of astrocytic serotonin receptors (5HT1A). In the dorsal part of PAG, there are numerous serotonergic endings of the dorsal raphe nucleus neurons. Their activity increases in response to the increased Glu concentration [32, 50, 57, 58]. This may account for the greatest reduction in S100β-IR in dm PAG cells of the MSG administered rats observed in our study. Moreover, some authors suggest that the S100β protein present in the extracellular space can intensify apoptotic changes in neurons and glial, as it is toxic at the micromolecular concentrations [29, 30, 32]. Therefore, further studies are necessary to determine whether the decrease in the number of S100β-IR cells observed in our study

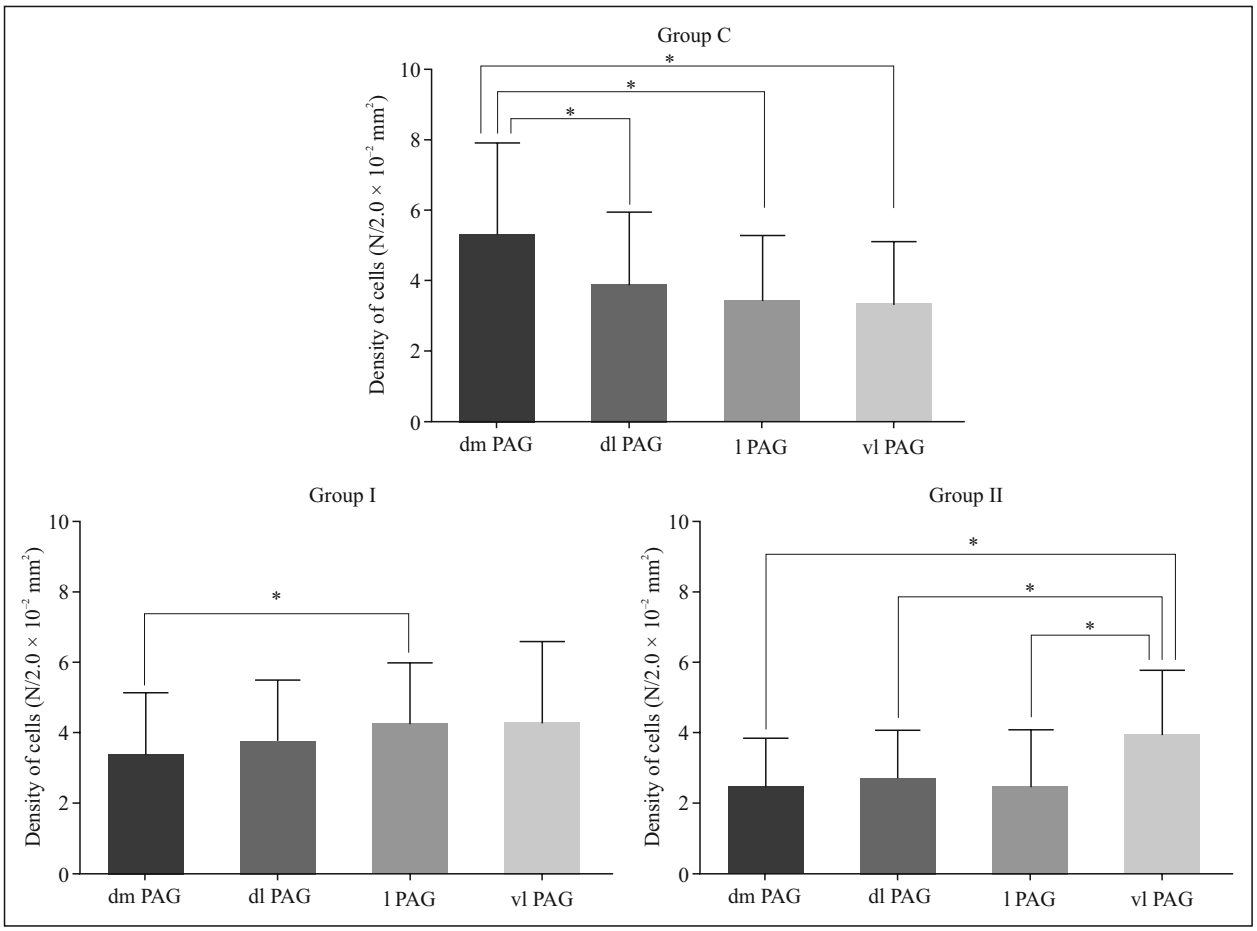

Figure 3. The density of S100β-immunoreactive (S100β-IR) cells in the dorsomedial (dm), dorsolateral (dl), lateral (l) and ventrolateral (vl) parts of PAG in the control (C) and MSG-treated rats (groups I and II). The bars show the mean density of S100β-IR cells in the area of 2.0×10^{-2} mm^2 and the whiskers represent standard deviation. *$p < 0.05$ — statistically significant differences between the parts of PAG related to the same group (Friedman test).

is the result of increased S100β protein secretion into the extracellular space and/or cell death.

In conclusion, the administration of MSG to the adult rats, particularly in large doses, affects the immunoreactivity of S100β protein in the PAG astrocytes. Phenotypic changes of these cells may indicate reactivity of glial cells and increased expression of the studied protein whereas a decrease in their number may result from the increased S100β secretion into the extracellular space and/or cytotoxic glial death.

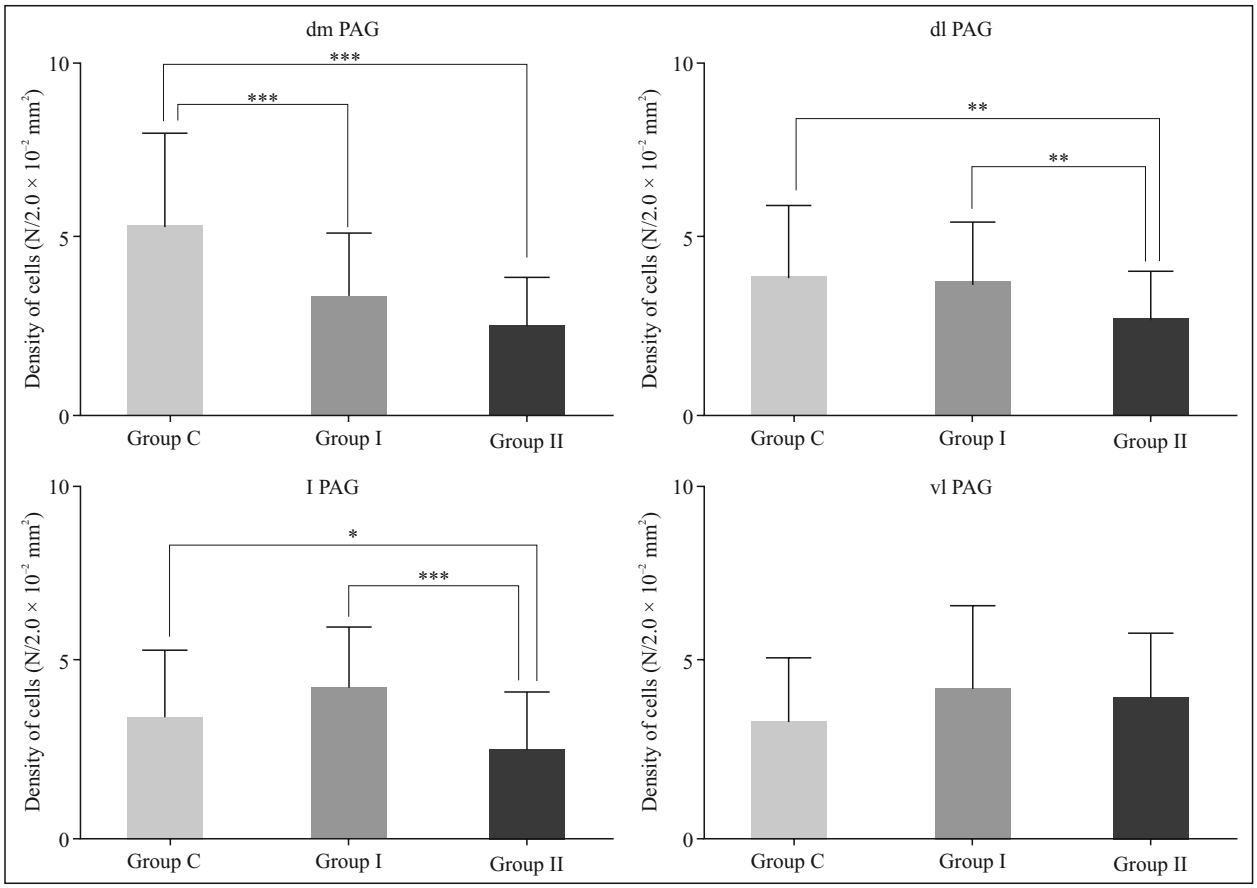

Figure 4. The density of S100β-immunoreactive cells in the dorsomedial (dm), dorsolateral (dl), lateral (l) and ventrolateral (vl) parts of PAG in control rats (group C) and MSG-treated rats (groups I and II). The bars show the mean density of S100β-IR cells in the area of 2.0 $\times 10^{-2}$ mm^2 and the whiskers represent standard deviation. *p < 0.05, **p < 0.01, ***p < 0.001 — statistically significant differences between the control rats and the MSG-treated animals in relation to the same part of PAG (Kruskal-Wallis test).

References

1. Szydlowska K, Zawadzka M, Kaminska B. Neuroprotectant FK506 inhibits glutamate-induced apoptosis of astrocytes in vitro and in vivo. J Neurochem. 2006; 99(3): 965–975, doi: 10.1111/j.1471-4159.2006.04136.x, indexed in Pubmed: 17076660.
2. Sofroniew MV, Vinters HV. Astrocytes: biology and pathology. Acta Neuropathol. 2010; 119(1): 7–35, doi: 10.1007/s00401-009-0619-8, indexed in Pubmed: 20012068.
3. Verkhratsky A, Nedergaard M. Physiology of Astroglia. Physiol Rev. 2018; 98(1): 239–389, doi: 10.1152/physrev.00042.2016, indexed in Pubmed: 29351512.
4. Mizuno GO, Wang Y, Shi G, et al. Aberrant Calcium Signaling in Astrocytes Inhibits Neuronal Excitability in a Human Down Syndrome Stem Cell Model. Cell Rep. 2018; 24(2): 355–365, doi: 10.1016/j.celrep.2018.06.033, indexed in Pubmed: 29996097.
5. Shigetomi E, Saito K, Sano F, et al. Aberrant Calcium Signals in Reactive Astrocytes: A Key Process in Neurological Disorders. Int J Mol Sci. 2019; 20(4), doi: 10.3390/ijms20040996, indexed in Pubmed: 30823575.
6. Pekny M, Pekna M. Astrocyte reactivity and reactive astrogliosis: costs and benefits. Physiol Rev. 2014; 94(4): 1077–1098, doi: 10.1152/physrev.00041.2013, indexed in Pubmed: 25287860.
7. Pekny M, Pekna M. Reactive gliosis in the pathogenesis of CNS diseases. Biochim Biophys Acta. 2016; 1862(3): 483–491, doi: 10.1016/j.bbadis.2015.11.014, indexed in Pubmed: 26655603.
8. Fairless R, Williams SK, Diem R. Calcium-Binding Proteins as Determinants of Central Nervous System Neuronal Vulnerability to Disease. Int J Mol Sci. 2019; 20(9), doi: 10.3390/ijms20092146, indexed in Pubmed: 31052285.
9. Álvarez-Ferradas C, Morales JC, Wellmann M, et al. Enhanced astroglial Ca2+ signaling increases excitatory synaptic strength in the epileptic brain. Glia. 2015; 63(9): 1507–1521, doi: 10.1002/glia.22817, indexed in Pubmed: 25980474.
10. Heuser K, Nome CG, Pettersen KH, et al. Ca2+ Signals in Astrocytes Facilitate Spread of Epileptiform Activity. Cereb Cortex. 2018; 28(11): 4036–4048, doi: 10.1093/cercor/bhy196, indexed in Pubmed: 30169757.
11. Lévesque M, Avoli M. The kainic acid model of temporal lobe epilepsy. Neurosci Biobehav Rev. 2013; 37(10 Pt 2): 2887–2899, doi: 10.1016/j.neubiorev.2013.10.011, indexed in Pubmed: 24184743.
12. Pinky NF, Wilkie CM, Barnes JR, et al. Region- and Activity-Dependent Regulation of Extracellular Glutamate.

J Neurosci. 2018; 38(23): 5351–5366, doi: 10.1523/JNEUROSCI.3213-17.2018, indexed in Pubmed: 29760178.
13. Mahmoud S, Gharagozloo M, Simard C, et al. Astrocytes Maintain Glutamate Homeostasis in the CNS by Controlling the Balance between Glutamate Uptake and Release. Cells. 2019; 8(2), doi: 10.3390/cells8020184, indexed in Pubmed: 30791579.
14. Belov Kirdajova D, Kriska J, Tureckova J, et al. Ischemia-Triggered Glutamate Excitotoxicity From the Perspective of Glial Cells. Front Cell Neurosci. 2020; 14: 51, doi: 10.3389/fncel.2020.00051, indexed in Pubmed: 32265656.
15. Lai TW, Zhang S, Wang YuT. Excitotoxicity and stroke: identifying novel targets for neuroprotection. Prog Neurobiol. 2014; 115: 157–188, doi: 10.1016/j.pneurobio.2013.11.006, indexed in Pubmed: 24361499.
16. van Landeghem FKH, Weiss T, Oehmichen M, et al. Decreased expression of glutamate transporters in astrocytes after human traumatic brain injury. J Neurotrauma. 2006; 23(10): 1518–1528, doi: 10.1089/neu.2006.23.1518, indexed in Pubmed: 17020486.
17. Barker-Haliski M, White HS. Glutamatergic Mechanisms Associated with Seizures and Epilepsy. Cold Spring Harb Perspect Med. 2015; 5(8): a022863, doi: 10.1101/cshperspect.a022863, indexed in Pubmed: 26101204.
18. Tannenberg RK, Scott HL, Westphalen RI, et al. The identification and characterization of excitotoxic nerve-endings in Alzheimer disease. Curr Alzheimer Res. 2004; 1(1): 11–25, doi: 10.2174/1567205043480591, indexed in Pubmed: 15975081.
19. Roze E, Saudou F, Caboche J. Pathophysiology of Huntington's disease: from huntingtin functions to potential treatments. Curr Opin Neurol. 2008; 21(4): 497–503, doi: 10.1097/WCO.0b013e328304b692, indexed in Pubmed: 18607213.
20. Caudle WM, Zhang J. Glutamate, excitotoxicity, and programmed cell death in Parkinson disease. Exp Neurol. 2009; 220(2): 230–233, doi: 10.1016/j.expneurol.2009.09.027, indexed in Pubmed: 19815009.
21. Burda JE, Sofroniew MV. Reactive gliosis and the multicellular response to CNS damage and disease. Neuron. 2014; 81(2): 229–248, doi: 10.1016/j.neuron.2013.12.034, indexed in Pubmed: 24462092.
22. Niaz K, Zaplatic E, Spoor J. Extensive use of monosodium glutamate: A threat to public health? EXCLI J. 2018; 17: 273–278. doi: 10. 17179/excli2018-1092, index in Pubmed: 29743864, doi: 10.17179/excli2018-1092.
23. Rosa SG, Chagas PM, Pesarico AP, et al. Monosodium glutamate induced nociception and oxidative stress dependent on time of administration, age of rats and susceptibility of spinal cord and brain regions. Toxicol Appl Pharmacol. 2018; 351: 64–73, doi: 10.1016/j.taap.2018.05.019, indexed in Pubmed: 29782962.
24. Chakraborty SP. Patho-physiological and toxicological aspects of monosodium glutamate. Toxicol Mech Methods. 2019; 29(6): 389–396, doi: 10.1080/15376516.2018.1528649, indexed in Pubmed: 30273089.
25. Tanaka K, Shimada M, Nakao K, et al. Hypothalamic lesion induced by injection of monosodium glutamate in suckling period and subsequent development of obesity. Exp Neurol. 1978; 62(1): 191–199, doi: 10.1016/0014-4886(78)90050-x, indexed in Pubmed: index in Pubmed: 729669.
26. Hashem HE, El-Din Safwat MD, Algaidi S. The effect of monosodium glutamate on the cerebellar cortex of male albino rats and the protective role of vitamin C (histological and immunohistochemical study). J Mol Histol. 2012; 43(2): 179–186, doi: 10.1007/s10735-011-9380-0, indexed in Pubmed: 22143495.
27. Prastiwi D, Djunaidi A, Partadiredja G. High dosage of monosodium glutamate causes deficits of the motor coordination and the number of cerebellar Purkinje cells of rats. Hum Exp Toxicol. 2015; 34(11): 1171–1179, doi: 10.1177/0960327115572706, indexed in Pubmed: 25697849.
28. Shah SA, Yoon GHo, Kim HO, et al. Vitamin C neuroprotection against dose-dependent glutamate-induced neurodegeneration in the postnatal brain. Neurochem Res. 2015; 40(5): 875–884, doi: 10.1007/s11064-015-1540-2, indexed in Pubmed: 25701025.
29. Heizmann C. S100 proteins structure functions and pathology. Frontiers in Bioscience. 2002; 7(4): d1356–1368, doi: 10.2741/a846, indexed in Pubmed: 11991838.
30. Donato R, Cannon BR, Sorci G, et al. Functions of S100 Proteins. Curr Mol Med. 2012; 13(1): 24–57, doi: 10.2174/1566524011307010024, indexed in Pubmed: 22834835..
31. Donato R, Sorci G, Riuzzi F, et al. S100B's double life: intracellular regulator and extracellular signal. Biochim Biophys Acta. 2009; 1793(6): 1008–1022, doi: 10.1016/j.bbamcr.2008.11.009, indexed in Pubmed: 19110011.
32. Michetti F, D'Ambrosi N, Toesca A, et al. The S100B story: from biomarker to active factor in neural injury. J Neurochem. 2019; 148(2): 168–187, doi: 10.1111/jnc.14574, indexed in Pubmed: 30144068.
33. Kleindienst A, Hesse F, Bullock M, et al. The neurotrophic protein S100B: value as a marker of brain damage and possible therapeutic implications. Progr Brain Res. 2007: 317–325, doi: 10.1016/s0079-6123(06)61022-4, indexed in Pubmed: 17618987.
34. Yardan T, Erenler AK, Baydin A, et al. Usefulness of S100B protein in neurological disorders. J Pak Med Assoc. 2011; 61(3): 276–281, indexed in Pubmed: 21465945.
35. Kellermann I, Kleindienst A, Hore N, et al. Early CSF and Serum S100B Concentrations for Outcome Prediction in Traumatic Brain Injury and Subarachnoid Hemorrhage. Clin Neurol Neurosurg. 2016; 145: 79–83, doi: 10.1016/j.clineuro.2016.04.005, indexed in Pubmed: 27101088.
36. Thelin EP, Nelson DW, Bellander BM. A review of the clinical utility of serum S100B protein levels in the assessment of traumatic brain injury. Acta Neurochir (Wien). 2017; 159(2): 209–225, doi: 10.1007/s00701-016-3046-3, indexed in Pubmed: 27957604.
37. Chaves ML, Camozzato AL, Ferreira ED, et al. Serum levels of S100B and NSE proteins in Alzheimer's disease patients. J Neuroinflammation. 2010; 7: 6, doi: 10.1186/1742-2094-7-6, indexed in Pubmed: 20105309.
38. Schaf DV, Tort ABL, Fricke D, et al. S100B and NSE serum levels in patients with Parkinson's disease. Parkinsonism Relat Disord. 2005; 11(1): 39–43, doi: 10.1016/j.parkreldis.2004.07.002, indexed in Pubmed: 15619461.
39. Tort ABL, Portela LV, da Purificação Tavares M, et al. Specificity and sensitivity of S100B levels in amniotic fluid for Down syndrome diagnosis. Life Sci. 2004; 76(4): 379–384, doi: 10.1016/j.lfs.2004.09.003, indexed in Pubmed: 15530500.
40. Lara DR, Gama CS, Belmonte-de-Abreu P, et al. Increased serum S100B protein in schizophrenia: a study in medication-free patients. J Psychiatr Res. 2001; 35(1): 11–14, doi: 10.1016/s0022-3956(01)00003-6, indexed in Pubmed: 11287051.
41. Schroeter ML, Sacher J, Steiner J, et al. Serum S100B represents a new biomarker for mood disorders. Curr Drug Targets.

2013; 14(11): 1237–1248, doi: 10.2174/1389450113149990014, indexed in Pubmed: 23701298.
42. da Rosa MI, Simon C, Grande AJ, et al. Serum S100B in manic bipolar disorder patients: Systematic review and meta-analysis. J Affect Disord. 2016; 206: 210–215, doi: 10.1016/j.jad.2016.07.030, indexed in Pubmed: 27475892.
43. Vianna DML, Brandão ML. Anatomical connections of the periaqueductal gray: specific neural substrates for different kinds of fear. Braz J Med Biol Res. 2003; 36(5): 557–566, doi: 10.1590/s0100-879x2003000500002, indexed in Pubmed: 12715074.
44. Barbaresi P, Quaranta A, Amoroso S, et al. Immunocytochemical localization of calretinin-containing neurons in the rat periaqueductal gray and colocalization with enzymes producing nitric oxide: a double, double-labeling study. Synapse. 2012; 66(4): 291–307, doi: 10.1002/syn.21509, indexed in Pubmed: 22121011.
45. Menant O, Andersson F, Zelena D, et al. The benefits of magnetic resonance imaging methods to extend the knowledge of the anatomical organisation of the periaqueductal gray in mammals. J Chem Neuroanat. 2016; 77: 110–120, doi: 10.1016/j.jchemneu.2016.06.003, indexed in Pubmed: 27344962.
46. Ajayi I. Neuroanatomical and Physiological Considerations for the role of the Periaqueductal gray in expressing emotions. MOJ Anatomy & Physiology. 2017; 3(5), doi: 10.15406/mojap.2017.03.00107.
47. Krawczyk A, Jaworska-Adamu J. Influence of the age of rats treated with the sodium salt of glutamate acid on the reactivity of astroglia of the infundibular nucleus. Medycyna Weterynaryjna. 2017; 73(4): 234–238, doi: 10.21521/mw.5675.
48. Sakatani S, Seto-Ohshima A, Shinohara Y, et al. Neural-activity-dependent release of S100B from astrocytes enhances kainate-induced gamma oscillations in vivo. J Neurosci. 2008; 28(43): 10928–10936, doi: 10.1523/JNEUROSCI.3693-08.2008, indexed in Pubmed: 18945900.
49. Krawczyk A, Jaworska-Adamu J, Rycerz K. Immunohistochemical evaluation of calretinin in the periaqueductal gray matter of rats treated with monosodium glutamate. Pak Vet J. 2020; 40(1): 93–97, doi: 10.29261/pakvetj/2019.118.
50. Quintero JE, McMahon DG. Serotonin modulates glutamate responses in isolated suprachiasmatic nucleus neurons. J Neurophysiol. 1999; 82(2): 533–539, doi: 10.1152/jn.1999.82.2.533, indexed in Pubmed: 10444653.
51. Beas-Zárate C, Pérez-Vega M, González-Burgos I. Neonatal exposure to monosodium l-glutamate induces loss of neurons and cytoarchitectural alterations in hippocampal CA1 pyramidal neurons of adult rats. Brain Research. 2002; 952(2): 275–281, doi: 10.1016/s0006-8993(02)03252-3.
52. Rojas-Castañeda JC, Vigueras-Villaseñor RM, Chávez-Saldaña M, et al. Neonatal exposure to monosodium glutamate induces morphological alterations in suprachiasmatic nucleus of adult rat. Int J Exp Pathol. 2016; 97(1): 18–26, doi: 10.1111/iep.12157, indexed in Pubmed: 26799547.
53. Panickar KS, Norenberg MD. Astrocytes in cerebral ischemic injury: morphological and general considerations. Glia. 2005; 50(4): 287–298, doi: 10.1002/glia.20181, indexed in Pubmed: 15846806.
54. Chen CJ, Liao SL, Kuo JS. Gliotoxic action of glutamate on cultured astrocytes. J Neurochem. 2000; 75(4): 1557–1565, doi: 10.1046/j.1471-4159.2000.0751557.x, indexed in Pubmed: 10987836.
55. Girling KD, Demers MJ, Laine J, et al. Activation of caspase-6 and cleavage of caspase-6 substrates is an early event in NMDA receptor-mediated excitotoxicity. J Neurosci Res. 2018; 96(3): 391–406, doi: 10.1002/jnr.24153, indexed in Pubmed: 29193273.
56. Ciccarelli R, Iorio PDi, Bruno V, et al. Activation of A1 adenosine or mGlu3 metabotropic glutamate receptors enhances the release of nerve growth factor and S-100beta protein from cultured astrocytes. Glia. 1999; 27(3): 275–281, doi: 10.1002/(sici)1098-1136(199909)27:3<275::aid-glia9>3.0.co;2-0.
57. Tao R, Auerbach SB. Regulation of serotonin release by GABA and excitatory amino acids. J Psychopharmacol. 2000; 14(2): 100–113, doi: 10.1177/026988110001400201, indexed in Pubmed: 10890306.
58. Oliveira LC, Broiz AC, de Macedo CE, et al. 5-HT2 receptor mechanisms of the dorsal periaqueductal gray in the conditioned and unconditioned fear in rats. Psychopharmacology (Berl). 2007; 191(2): 253–262, doi: 10.1007/s00213-006-0653-3, indexed in Pubmed: 17205316.

Submitted: 27 November, 2019
Accepted after reviews: 26 May, 2020
Available as AoP: 4 June, 2020

FOLIA HISTOCHEMICA ET CYTOBIOLOGICA
Vol. 58, No. 2, 2020
pp. 156–161

ORIGINAL PAPER

VIA MEDICA

The effect of dental gel formulation on human primary fibroblasts — an *in vitro* study

Barbara Sterczala[1], Julita Kulbacka[2], Jolanta Saczko[2], Marzena Dominiak[1]

[1]Department of Dental Surgery, Wroclaw Medical University, Wroclaw, Poland
[2]Department of Molecular and Cellular Biology, Wroclaw Medical University, Wroclaw, Poland

Abstract

Introduction. In ordinary dental practice, the dentist often meets with patients suffering from ulcers, aphtha with edema, bleeding gums, bothersome burning, and dry mouth. These are prosthetic, orthodontic patients, after surgery, in various age ranges. Protefix® gel is a soothing and regenerating preparation aimed at patients with mucosal problems. The aim of our study was to evaluate the protective properties and the safety of Protefix® gel application after dental procedures *in vitro.*

Material and methods. Human gingival fibroblasts (HGFs) were isolated from normal gingival tissues, cultured to full monolayer and exposed to Protefix® gel in the concentration from 1 to 100%. The viability of cells was examined by MTT assays. Cell migration as a response of treated cells was assessed. The expression of collagen III was estimated by immunocytochemistry after 20 minutes or 24 hours incubation with Protefix® gel.

Results. The obtained results indicated that the verified gel significantly stimulated fibroblasts' proliferation, and mitochondrial activity determined by MTT assay increased almost two-fold for lower gel concentrations. The immunohistochemical detection of collagen III revealed an increased expression after incubation with 5% gel.

Conclusions. The results proved that the gel is safe for cells derived from human gingiva and moreover has regenerative properties, which can be of great importance in the treatment of gingivitis after retraction and surgical procedures, or even ordinary daily injuries of oral cavity. *(Folia Histochemica et Cytobiologica 2020, Vol. 58, No. 2, 156–161)*

Key words: Protefix® gel; human gingival fibroblasts; cell proliferation; collagen III

Introduction

In everyday dental practice, the dentist often meets with patients suffering from ulcers, aphthae with edema, bleeding gums, bothersome burning, and dry mouth. These are prosthetic, orthodontic patients, after surgery, in various age ranges. The etiology of oral mucosal damage is variable. Protefix® gel is a gentle and redeveloping preparation, which can be effectively applied by patients with mucosal problems.

It is considered that orthodontic appliances and moveable prosthetic restorations can cause numerous mucosal injuries, chronically irritating sharp gingival edges of the gum-bone surface. Other problems occur when the denture is not properly adjusted and this leads to proliferative lesions in the form of fibromuscular hypertrophic changes of the oral mucosa. Then, the treatment consists of the surgical removal of pathological granulomatous hyperplasia [1, 2]. Such procedures are often conducted in elderly patients, who very often suffer from other systemic diseases. Therefore, the healing process of extensive wounds of gingival tissues is sustained and painful. An unadjusted adaptation of prosthetic restorations to short-circuit conditions is the reason for residual debris and for reasons apart from mechanical irritation of the mucosa, bacteria and fungi develop.

As a result of chemical-toxic factors such as dental materials and solutions, for example mercury, nickel, and paraformaldehyde, allergic reactions may occur in the form of redness or burning. Among the systemic factors that can irritate the oral mucosa, we can dis-

Correspondence address: Barbara Sterczala,
Department of Dental Surgery, Wroclaw Medical University,
Krakowska 26, 50–425 Wroclaw, Poland
tel.: +48 502 932 269
e-mail: barbara.sterczala@umed.wroc.pl

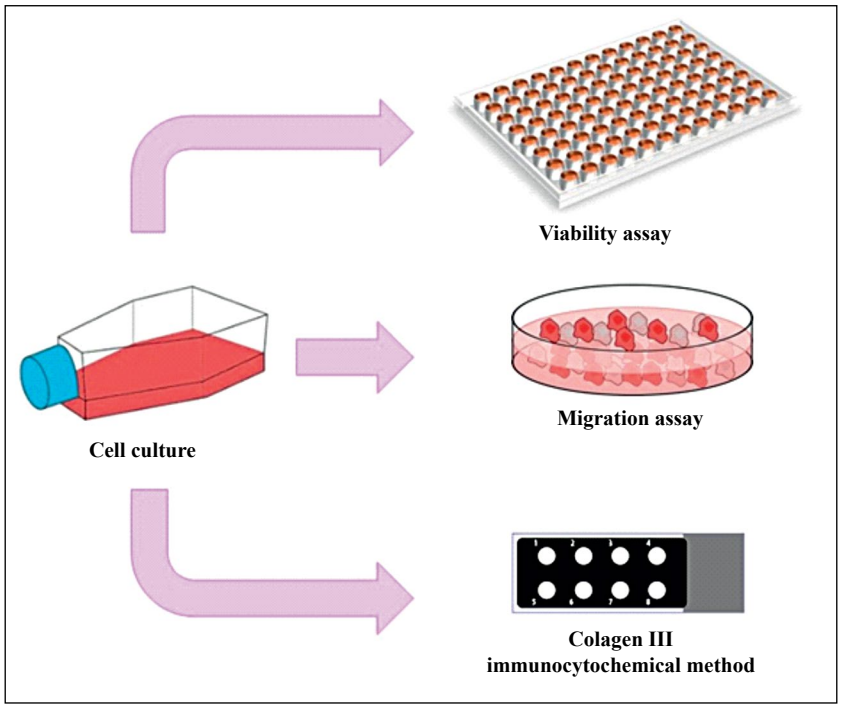

Figure 1. Schematic representation of Protefix® gel experimental verification by MTT, migration assay and immunocytochemistry.

tinguish: psychosomatic diseases like hypertension or diabetes, hormonal changes, deficiency diseases of the oral mucosa like anemia or Sjogren syndrome that can provoke symptoms such as dry mouth and burning mucous. Therefore, drug-induced gingival papillae are exposed to injuries even at brushing, and the resulting pain discourages patients from regular daily hygiene which further escalates the problem of inflammation [2–4].

Protefix® gel, by dint of its gel form, is easy to apply and effects the extended penetration time of active substances into the tissue. The glyceroloxydtriester contained in the composition forms a lipid film on the gum with a protective and regenerating effect. Therefore, Protefix® gel is mainly targeted at patients suffering from abrasions or minor wounds of the oral mucosa. Additionally, the clove oil contained in Protefix® gel may minimize postoperative pain. In addition to its anesthetic properties, clove oil also exhibits antibacterial properties and eliminates bacteria including *Escherichia coli*, *Mycobacterium phlei*, *Bacillus subtillis*, and *Streptoccocus ureus* [5, 6]. The oil also acts antiseptically, antivirally and against fungal infection. The clove oil speeds up circulation, which results in better wound healing [3, 7–9]. Untreated changes in the oral mucosa may initiate the formation of periodontal disease, bone loss, loss of teeth, or cancer. Besides, the discomfort of painful lesions on the oral mucosa impedes the proper functioning of patients in society.

The aim of our study was to evaluate the protective properties and the safety of Protefix® gel application in human gingival fibroblasts from primary culture after the simulation of dental procedures *in vitro*.

Materials and methods

Cell culturing. Human gingival fibroblasts (HGFs) were used for the experimental protocols. The HGFs were isolated from healthy gingival tissues according to a procedure described previously (Patent No: P 3812045) [10]. Cells were cultured in Dulbecco's Modified-Eagle Medium (DMEM, Sigma-Aldrich, Poznan, Poland) containing 10% fetal bovine serum (Gibco-ThermoFisher, Warsaw, Poland) and enriched in 5% antibiotic/antimycotic solution (Sigma-Aldrich). The cultured medium was changed twice a week. The cell culture and all procedures were performed under sterile conditions using laminar flow hood. Cells were kept in a humidified atmosphere at 37°C and 5% CO_2. For further experiments fibroblast cells (Fig. 1) were detached from the cell culture flask by trypsin (0.25% Trypsin-EDTA, Sigma-Aldrich) and resuspended in appropriate cell culture dishes.

Cell viability assay. HGFs were seeded into transparent 96-well plates. After 24 h, Protefix® gel (Quiesser Pharma

Poland Sp z o.o., Warsaw, Poland) was added at various dilutions (1, 5, 10, 25, 50, 75 and 100%) for 20 min or 24 h incubation. Gel dilutions (1–75%) were prepared in cell culture medium and added in volume of 200 μl/well to the 96-well plate. Control cells were incubated for the same time in the presence of the complete cell culture medium. All experiments were performed in triplicate. After the incubation, an MTT assay (Sigma-Aldrich) was performed to determine the cell viability. The method is based on the detection of activity of the mitochondrial enzyme succinate dehydrogenase. This converts the orange, water-soluble tetrazole salt (3-(4,5-dimethylthiazol-2-yl)-2,5-diphenyltetrazolium bromide) to formazan. This product has the form of dark purple, insoluble crystals. Due to their dissolution with isopropanol (they are not soluble in water), a colored solution is formed. The intensity of the colored reaction is verified spectrophotometrically at 570 nm. The amount of the resulting colored product indicates the oxidative activity of the mitochondria in the cells, and thus the number of viable cells in the entire population (the more reduced the MTT, the greater the number of metabolically active cells). The measurements were performed on a Multiskan™ FC microplate photometer (Thermo Scientific, Alab, Warsaw, Poland).

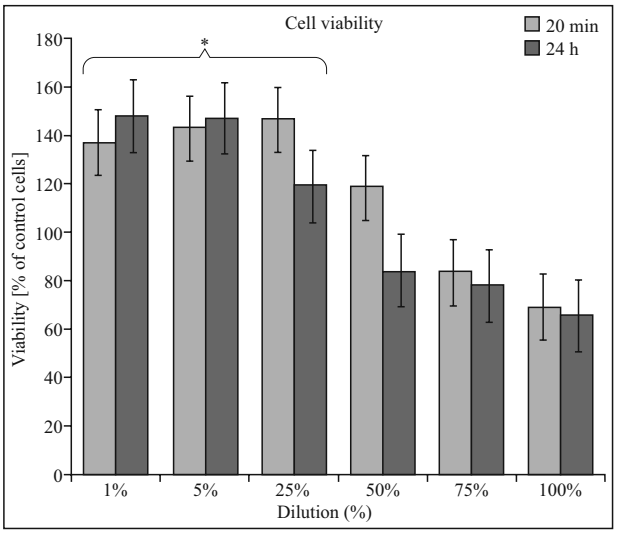

Figure 2. The impact of Protefix® gel in various dilutions on human gingival fibroblasts after exposure for 20 min and 24 h time. X-axis: dilution level of used gel, Y-axis cell viability expressed as a percentage of control cells. The results are presented as mean values of the percentage of the untreated control cells. Data represent mean values of a minimum of triplicate repetitions *$p \leq 0.05$.

Evaluation of cellular migration. The evaluation of cell migration was performed on Nunc 35 mm Petri dishes (Biokom, Janki, Poland). Protefix® gel drops (100% concentration) were applied to sterile dishes. The plate was then covered with a fibroblast suspension at the density of 5×10^3 cells. All observations of cell migration in the presence of the gel were carried out after 24 and 48 hours using an Olympus CX41 (Olympus, Tokyo, Japan) inverted light microscope.

Immunocytochemical evaluation of collagen III. Human normal fibroblasts were placed onto 10-well microscopic slides (Menzel, Equimed, Wroclaw, Poland). After 24 h when the cells were attached to the surface, Protefix® gel dilutions were added to the cells. The expression of collagen III was estimated using immunocytochemistry after 20 minutes and 24 hours incubation with Protefix gel and fixed in 4% fresh paraformaldehyde (Roth, Karlsruhe, Germany). Cells were stained using rabbit polyclonal collagen III (cat. No.: sc-271249, Santa Cruz, CA, USA). Collagen type III and I are the main ingredients of the interstitial matrix and play the main role in remodeling and reconstruction of the external matrix while type III collagen together with type I collagen are the main constituents of the interstitial matrix. Type III is especially responsible for wound healing [11]. The antibody was diluted with PBS buffer in the proportion 1:200. The detailed protocol was performed according to our previous study [12]. The quantification of the level of stained reaction in treated cells that revealed immunocytochemical reaction was estimated as a percentage values. The stained cells' counting was performed by two independent investigators. The intensity of immunoassayed reaction was evaluated as (–) negative (no reaction), (–/+) pattern reaction; (+) weak, (++) moderate, and (+++) strong.

Statistical analysis. The statistical significance was calculated by two-way ANOVA test using the control group of the untreated fibroblasts incubated as a reference. Values were presented as a mean ± SD; n = 3 and judged as a statistically significant for $p < 0.05$.

Results

Cell viability by MTT assays

The results of cell viability after exposition to gel in various concentrations are shown in Figure 2. We observed a tendency to a slight, statistically not significant decrease in cell viability after exposition to 100% and 75% gel concentration. The lower concentrations (1–25%) of the examined gel showed significantly stimulating properties in terms of cell proliferation which increased by more than 50% in relation to untreated control cells (where the level of control cells was 100%).

Evaluation of cellular migration

In another experiment, cell migration ability was tested in the presence of Protefix® gel (Fig. 3). These observations showed a fairly high cell affinity for the

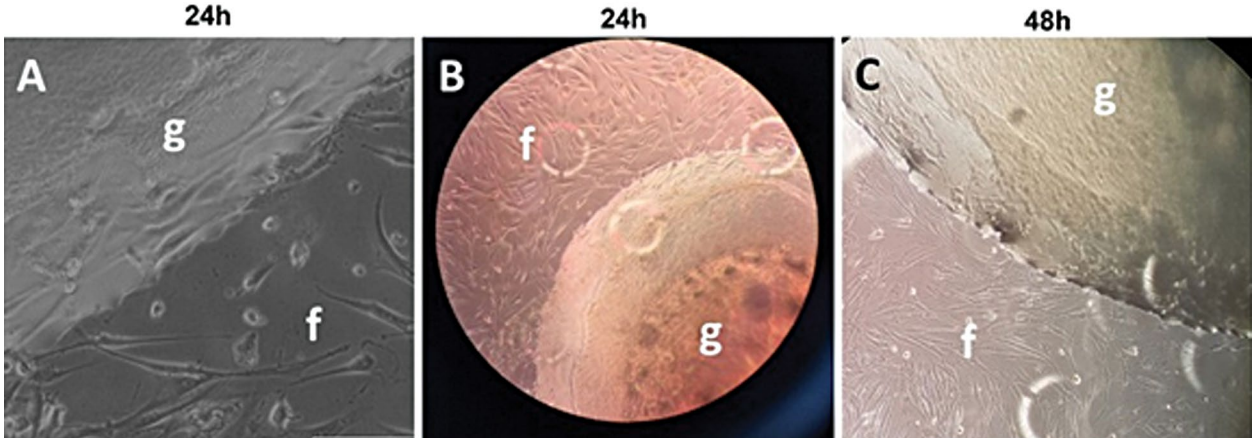

Figure 3. The effect of Protefix® gel in 100% concentration (placed on the culture plate) on human gingival fibroblasts migration ability after 24 h (**A** and **B**) and 48 h (**C**) time of exposure. Symbols: g — gel; f — fibroblasts.

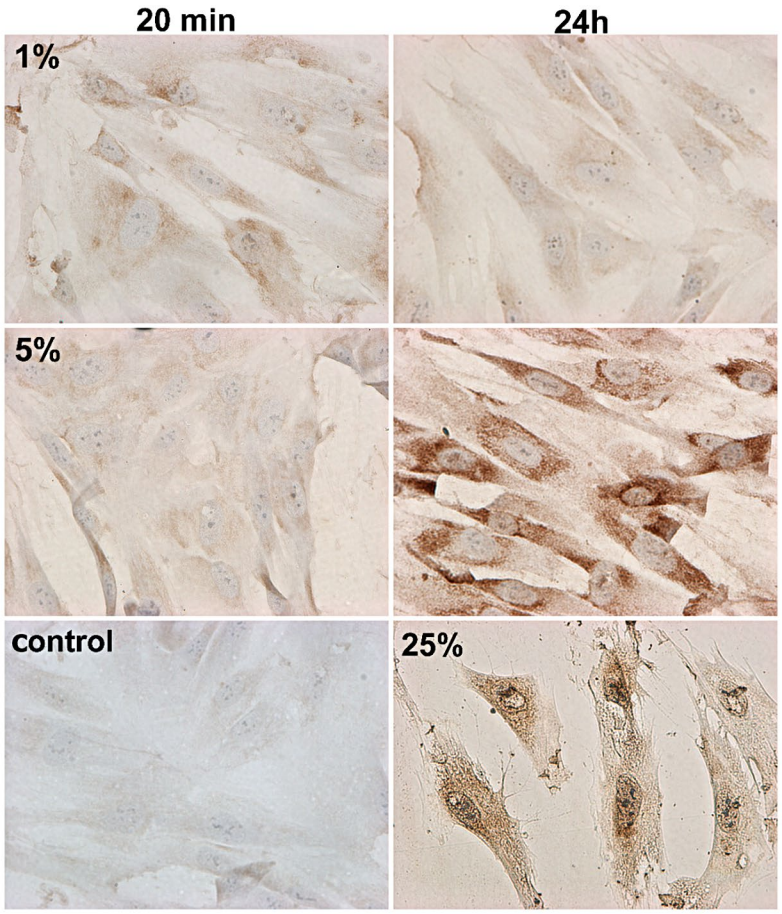

Figure 4. Immunohistochemical visualization of collagen III expression in human gingival fibroblasts after exposure to Protefix® gel in concentrations of 1%, 5% and 25% for 20 min and 24 h.

gel. Here we could observe that fibroblasts grew rapidly to form a full monolayer in the gel-coated area on the Petri dish. Even prolonged observations of up to 48 hours showed that the presence of the gel had a positive rather than inhibitory effect on cell growth.

Estimation of Collagen III by the immunocytochemical method

The results of the immunostained reaction are presented in Figure 4. In Table 1 is shown the quantification of the percentage values of the cells characterized

Table 1. Semi-quantitative assessment of collagen III expression in human gingival fibroblasts after exposure to Protefix® gel in concentrations of 1%, 5% and 25% for 20 min and 24 h. The results were classified as positive if staining was observed in more than 5% of cells. The intensity of immunohistochemical reaction was evaluated as (−) negative (no reaction); (–/+) pattern reaction; (+) weak, (++) moderate, and (+++) strong

Sample	20 min	24 h
1% gel	++ 100%	++ 100%
5% gel	++ 95%	+++ 100
25% gel	++/+++ 100%	+++ 100
Untreated control	–/+ 90%	–/+ 100%

by stained reaction demonstrating collagen III. The obtained results revealed the trace expression of this protein in control cells. After the exposure to Protefix® gel in concentrations of 1%, 5%, and 25%, a significant increase of the reaction intensity was observed, especially after 24 h.

Discussion

Currently, in prosthetic practice it is extremely important to carefully select preparations for adhesive dentures so as not to provoke any injuries or allergic reaction. In the present study, Protefix® gel was verified in an *in vitro* approach on human fibroblasts derived from primary gingival tissue. This therapeutic gel is designed in particular for those patients who have problems with mucosa, recurrent aphthous stomatitis (RAS) and other mucosa gingival problems. Moreover, triester glycerol oxide is the topical agent which has the property of adherence to the oral mucosa by forming a lipid film which protects against mechanical trauma and may help to reduce oral tissue moisture loss and inflammation [13–15]. Many clinical randomized investigations have been conducted to assess the efficiency of Protefix® gel for patients suffering for various problems with gingival mucosa such as recurrent aphthous stomatitis (RAS) [16]. However, there have not been any investigations in which the safety for surrounding gingival tissue has been confirmed *in vitro*. Our *in vitro* study showed that Protefix® gel activated proliferation of human gingival fibroblasts. Cell viability slightly decreased only after incubations of HGF with 100 and 75% gel concentrations. The lower concentrations of evaluated gel were involved in significant stimulating properties of HGF cells. The observed increase even exceeded 50% in relation to untreated control cells. This was also confirmed by another experiment in which cell migration ability was tested. Our prolonged observations of up to 48 hours demonstrated the positive effect of Protefix® gel on human gingival fibroblasts growth. The expression of collagen III was also examined semi-quantitatively by the immunocytochemical method. The expression of collagen III in control, untreated cells revealed only pattern expression. However, after exposure to Protefix® gel in concentrations of 1, 5 or 25% human gingival fibroblasts demonstrated significant increases in the color reaction, especially after 24 hours. The results showed that Protefix® gel was involved in regeneration, due to increased collagen III expression in treated cells. This type of collagen is mainly present in the tissue formed from fibroblasts before type I collagen is produced. Its significant expression is observed during wound healing, where it forms fibers of connective tissue and proper connective tissue. Collagen III is produced by fibroblasts and is primarily involved in the formation of the peptide scaffolds of collagen I. This process could play the main role *inter alia* in wound healing promotion and especially in periodontal ligament tissue regeneration [17].

In conclusion, the results of our study suggest that the proper selection of the regeneration materials for gingival tissue used in everyday prosthetic practice is essential. Our results prove that the tested gel has regenerative properties, which can be of great importance in the treatment of gingivitis after retraction, surgical procedures, or even with ordinary daily injuries.

Acknowledgments

This research was partially performed in the Screening Laboratory of Biological Activity Testing and Collection of Biological Material, Faculty of Pharmacy and the Division of Laboratory Diagnostics, Wrocław Medical University, supported by the ERDF Project within the Innovation Economy Operational Program POIG.02.01.00-14-122/09.

References

1. Yu GY. Oral and maxillofacial surgery: Current and future. Ann Maxillofac Surg. 2013; 3(2): 111–112, doi: 10.4103/2231-0746.119209, indexed in Pubmed: 24205468.
2. Wolf DL, Lamster IB. Contemporary concepts in the diagnosis of periodontal disease. Dent Clin North Am. 2011; 55(1): 47–61, doi: 10.1016/j.cden.2010.08.009, indexed in Pubmed: 21094718.
3. Góra J, Lis A, Kula J, et al. Chemical composition variability of essential oils in the ontogenesis of some plants. Flavour Fragrance J. 2002; 17(6): 445–451, doi: 10.1002/ffj.1126.

4. Sterczała B, Kulbacka J, Saczko J, et al. : Evaluation of keratinized gingival fibroblast proliferation after Protefix® gel application, in the aspect of wound healing in elderly patients, J Stoma 2019; 72. ; 1: 8–11.
5. Upadhay RK. : Plant natural products: Their pharmaceutical potential against disease and drug resistant microbial pathogens, J Pharm Res. 2011; 4(4): 1179–1185.
6. Sakagami H, Tomomura M. Dental Application of Natural Products. Medicines (Basel). 2018; 5(1), doi: 10.3390/medicines5010021, indexed in Pubmed: 29443874.
7. Cimanga K, Kambu K, Tona L, et al. Correlation between chemical composition and antibacterial activity of essential oils of some aromatic medicinal plants growing in the Democratic Republic of Congo. J Ethnopharmacol. 2002; 79(2): 213–220, doi: 10.1016/s0378-8741(01)00384-1, indexed in Pubmed: 11801384.
8. Park MJ, Gwak KS, Yang I, et al. Effect of citral, eugenol, nerolidol and alpha-terpineol on the ultrastructural changes of Trichophyton mentagrophytes. Fitoterapia. 2009; 80(5): 290–296, doi: 10.1016/j.fitote.2009.03.007, indexed in Pubmed: 19345255.
9. Omidbeygi M, Barzegar M, Hamidi Z, et al. Antifungal activity of thyme, summer savory and clove essential oils against Aspergillus flavus in liquid medium and tomato paste. Food Control. 2007; 18(12): 1518–1523, doi: 10.1016/j.foodcont.2006.12.003.
10. Dominiak M, Łysiak-Drwal K, Saczko J, et al. A simple and established method of tissue culture of human gingival fibroblasts for gingival augmentation. Folia Histochem Cytobiol. 2008; 46(1): 117–119, doi: 10.2478/v10042-008-0017-4, indexed in Pubmed: 18296274.
11. Volk SW, Wang Y, Mauldin EA, et al. Diminished type III collagen promotes myofibroblast differentiation and increases scar deposition in cutaneous wound healing. Cells Tissues Organs. 2011; 194(1): 25–37, doi: 10.1159/000322399, indexed in Pubmed: 21252470.
12. Drąg-Zalesińska M, Rembiałkowska N, Borska S, et al. A New Betulin Derivative Stimulates the Synthesis of Collagen in Human Fibroblasts Stronger than its Precursor. In Vivo. 2019; 33(4): 1087–1093, doi: 10.21873/invivo.11577, indexed in Pubmed: 31280196.
13. Jurge S, Kuffer R, Scully C, et al. Mucosal disease series. Number VI. Recurrent aphthous stomatitis. Oral Dis. 2006; 12(1): 1–21, doi: 10.1111/j.1601-0825.2005.01143.x, indexed in Pubmed: 16390463.
14. Scully C, Porter S. Oral mucosal disease: Recurrent aphthous stomatitis. Br J Oral Maxillofac Surg. 2008; 46(3): 198–206, doi: 10.1016/j.bjoms.2007.07.201.
15. Baccaglini L, Lalla RV, Bruce AJ, et al. Urban legends: recurrent aphthous stomatitis. Oral Dis. 2011; 17(8): 755–770, doi: 10.1111/j.1601-0825.2011.01840.x, indexed in Pubmed: 21812866.
16. Ofluoglu D, Ergun S, Warmakulasuiriya S, et al.: Triester Glycerol Oxide gel in the treatment of minor RAS. Med Oral Patol Oral Cir Bucal. 2017; 22(2): 159–66.
17. Kumada Y, Zhang S. Significant type I and type III collagen production from human periodontal ligament fibroblasts in 3D peptide scaffolds without extra growth factors. PLoS One. 2010; 5(4): e10305, doi: 10.1371/journal.pone.0010305, indexed in Pubmed: 20421985.

Submitted: 6 March, 2019
Accepted after reviews: 9 June, 2020
Available as AoP: 22 June, 2020

INSTRUCTIONS FOR AUTHORS

MANUSCRPIT SUBMISSION

Folia Histochemica et Cytobiologica accepts manuscripts (original articles, short communications, review articles) from the field of histochemistry, as well as cell and tissue biology. Each manuscript is reviewed by independent referees. Book reviews and information concerning congresses, symposia, meetings etc., are also published.

All articles should be submitted to FHC electronically online at www.fhc.viamedica.pl where detailed instruction regarding submission process will be provided.

AUTHOR'S STATEMENT

The manuscript must be accompanied by the author's statement that it has not been published (or submitted to publication) elsewhere.

GHOSTWRITTING

Ghostwriting and guest-authorship are forbidden. In case of detecting ghost written manuscripts, their actions will be taking involving both the submitting authors and the participants involved.

The corresponding author must have obtained permission from all authors for the submission of each version of the paper and for any change in authorship. Submission of a paper that has not been approved by all authors may result in immediate rejection.

COST OF PUBLICATION

The cost of publication of accepted manuscript is 800 Euro.

OFFPRINTS

PDF file of each printed paper is supplied for the author free of charge. Orders for additional offprints should be sent to the Editorial Office together with galley proofs.

ORGANIZATION OF MANUSCRIPT

The first page must include: the title, name(s) of author(s), affiliation(s), short running head (no more than 60 characters incl. spaces) and detailed address for correspondence including e-mail. Organization of the manuscript: 1. Abstract (not exceeding one typed page — should consist of the following sections: Introduction, Material and methods, Results, Conclusions); 2. Key words (max. 10); Introduction; Material and methods; Results; Discussion; Acknowledgements (if any); References; Tables (with legends); Figures; Legends to figures.

In a short communication, Results and Discussion should be written jointly. Organization of a review article is free.

TECHNICAL REQUIREMENTS

Illustrations (line drawings and halftones) — either single or mounted in the form of plates, can be 85 mm, 125 mm, or 175 mm wide and cannot exceed the size of 175 × 250 mm. The authors are requested to plan their illustrations in such a way that the printed area is eco-nomically used. Numbers, inscriptions and abbreviations on the figures must be about 3 mm high. In case of micrographs, magnification (*e.g.* × 65 000) should be given in the legend. Calibration bars can also be used. For the best quality of illustrations please provide images in one of commonly used formats e.g. *.tiff, *.png, *pdf (preferred resolution 300 dpi). Color illustrations can be published only at author's cost and the cost estimate will be sent to the author after submission of the manuscript. Tables should be numbered consecutively in Arabic numerals and each table must be typed on a separate page. The authors are requested to mark the places in the text, where a given table or figure should appear in print. Legends must begin on a new page and should be as concise as necessary for a self-sufficient explanation of the illustrations. PDF file of each paper is supplied free of charge.

CITATIONS

In References section of article please use following American Medical Association 9th Ed. citation style. Note, that items are listed numerically in the order they are cited in the text, not alphabetically. If you are using a typewriter and cannot use italics, then use underlining.

Authors: use initials of first and second names with no spaces. Include up to six authors. If there are more than six, include the first three, followed by et al. If no author is given, start with the title. **Books:** include the edition statement (ex: 3rd ed. or Rev ed.) between the title and place if it is not the first edition. **Place:** use abbreviations of states, not postal codes. **Journals:** abbreviate titles as shown in *Index Medicus*. If the journal does not paginate continuously through the volume, include the month (and day). **Websites:** include the name of the webpage, the name of the entire website, the full date of the page (if available), and the date you looked at it. The rules concerning a title within a title are *not* displayed here for purposes of clarity. See the printed version of the manual for details. For documents and situations not listed here, see the printed version of the manual.

EXAMPLES

Book:

1. Okuda M, Okuda D. *Star Trek Chronology: The History of the Future.* New York: Pocket Books; 1993.

Journal or Magazine Article (with volume numbers):

2. Redon J, Cifkova R, Laurent S et al. Mechanisms of hypertension in the cardiometabolic syndrome. *J Hypertens.* 2009; 27(3):441–451. doi: 10.1097/HJH.0b013e32831e13e5.

Book Article or Chapter:

3. James NE. Two sides of paradise: the Eden myth according to Kirk and Spock. In: Palumbo D, ed. *Spectrum of the Fantastic*. Westport, Conn: Greenwood; 1988:219–223.

When the manufacturers of the reagents etc. are mentioned for the first time, town, (state in the US) and country must be provided wheras for next referral only the name of the firm should be given.

Website:

4. Lynch T. DSN trials and tribble-ations review. Psi Phi: Bradley's Science Fiction Club Web site. 1996. Available at: http://www.bradley.edu/campusorg/psiphi/DS9/ep/503r.htm. Accessed October 8, 1997.

Journal Article on the Internet:

5. McCoy LH. Respiratory changes in Vulcans during pon farr. *J Extr Med* [serial online]. 1999;47:237–247. Available at: http:// //infotrac.galegroup.com/itweb/nysl_li_liu. Accessed April 7, 1999.